

**A measurement of the jet multiplicity in di-lepton  
final states of  $t\bar{t}$  events.**

**Dustin Urbaniec**

Submitted in partial fulfillment of the  
requirements for the degree  
of Doctor of Philosophy  
in the Graduate School of Arts and Sciences

**COLUMBIA UNIVERSITY**

2013

©2013

Dustin Urbaniec

All Rights Reserved

# ABSTRACT

## A measurement of the jet multiplicity in di-lepton final states of $t\bar{t}$ events.

Dustin Urbaniec

A measurement of the jet multiplicity in di-leptonically decaying  $t\bar{t}$  events (i.e.  $t\bar{t} \rightarrow (ee, \mu\mu, e\mu) + E_{\text{T}}^{\text{miss}} + \text{jets}$ ) is presented, using  $4.66 \text{ fb}^{-1}$  of data collected from  $\sqrt{s} = 7$  TeV  $pp$  collisions at the CERN Large Hadron Collider. In order to mitigate the effects of systematic uncertainties associated with jet energy measurements, a measurement of the ratio of the number of di-lepton  $t\bar{t}$  events with  $N + 2$  jets to  $Z \rightarrow \ell\ell + N$  jet events is also determined. The results are unfolded for detector effects and compared to the particle-level predictions of several Monte Carlo generators, showing generally good agreement.

# Table of Contents

<b>1</b>	<b>Introduction</b>	<b>1</b>
1.1	The Standard Model . . . . .	1
1.2	High energy physics experiments and the goal of this analysis . . . . .	5
1.3	Outline . . . . .	8
<b>2</b>	<b>Theoretical considerations</b>	<b>9</b>
2.1	Quantum Chromodynamics and its predictions . . . . .	11
2.1.1	Historical introduction . . . . .	11
2.1.2	Hadron structure . . . . .	12
2.1.3	$t\bar{t}$ production . . . . .	14
2.1.4	The parton shower approximation . . . . .	16
2.1.5	Hadronization . . . . .	18
2.2	Jet physics . . . . .	19
2.3	Monte Carlo event generators . . . . .	22
<b>3</b>	<b>Description of the experiment</b>	<b>29</b>
3.1	The Large Hadron Collider . . . . .	29
3.2	The ATLAS experiment . . . . .	33
3.2.1	The Inner Detector . . . . .	34
3.2.2	Calorimetry . . . . .	37
3.2.3	The Muon System . . . . .	45
3.2.4	Luminosity systems . . . . .	48
3.2.5	The ATLAS trigger system . . . . .	51

3.2.6	Data quality and detector simulation . . . . .	53
<b>4</b>	<b>Object reconstruction</b>	<b>56</b>
4.1	Tracking . . . . .	56
4.2	Electrons . . . . .	57
4.3	Muons . . . . .	60
4.4	Jets . . . . .	63
4.4.1	Reconstruction . . . . .	63
4.4.2	Calibration . . . . .	64
4.4.3	Jet selection . . . . .	66
4.5	Overlap Removal . . . . .	69
4.6	Missing transverse momentum . . . . .	69
<b>5</b>	<b>Event selections and background estimation</b>	<b>71</b>
5.1	Event selections . . . . .	71
5.2	Estimation of background contributions . . . . .	74
5.2.1	Fake leptons in $t\bar{t}$ events . . . . .	75
5.2.2	Drell-Yan contribution to $t\bar{t}$ events . . . . .	83
5.2.3	Multi-jet background in $Z$ +jets events . . . . .	85
5.3	Reconstruction-level results . . . . .	86
5.3.1	$t\bar{t}$ signal region . . . . .	86
5.3.2	$Z$ +jets signal region . . . . .	94
<b>6</b>	<b>Extraction of the particle-level results</b>	<b>97</b>
6.1	Particle-level object and event selections . . . . .	98
6.2	Unfolding method . . . . .	101
6.2.1	Efficiency effects . . . . .	101
6.2.2	Migrations . . . . .	102
6.2.3	Closure . . . . .	109
6.2.4	$Z$ +jets unfolding . . . . .	111

<b>7</b>	<b>Systematic Uncertainties on the Measurement</b>	<b>112</b>
7.1	Sources of uncertainty . . . . .	112
7.2	Propagation of uncertainties . . . . .	116
<b>8</b>	<b>Results and Conclusions</b>	<b>118</b>
8.1	$t\bar{t}$ measurement . . . . .	118
8.2	Ratio to $Z$ +jets . . . . .	129
8.3	Combination of all channels . . . . .	134
8.4	Conclusions . . . . .	143
<b>I</b>	<b>Appendices</b>	<b>144</b>
<b>A</b>	<b>Data/MC agreement</b>	<b>145</b>
A.1	General discussion . . . . .	145
A.2	Reconstructed jet multiplicity results and modeling . . . . .	157
<b>B</b>	<b>Unfolding</b>	<b>162</b>
<b>C</b>	<b>Details of systematic uncertainties</b>	<b>164</b>
C.1	Jet Energy Scale . . . . .	164
C.2	Full systematic uncertainty tables . . . . .	169
<b>II</b>	<b>Bibliography</b>	<b>174</b>
	<b>Bibliography</b>	<b>175</b>

# List of Figures

1.1	Comparison of the $p_T$ and $\eta$ distributions in $t\bar{t}$ and $Z$ boson events passing truth-level kinematic selections which are similar to those used in this analysis.	7
2.1	Leading order Feynman diagrams for $t\bar{t}$ production in hadron-hadron collisions.	9
2.2	The structure of a hadron-hadron collision as implemented in QCD predictions. A valence quark and a sea anti-quark annihilate into a vector boson producing a $q\bar{q}$ pair. The hard sub-process final state $q\bar{q}$ pair showers into more partons which eventually hadronize, and unstable hadrons decay into stable particles. Not shown is initial state radiation, described by higher order corrections in the hard sub-process, or more commonly via a parton shower algorithm. Since the hard sub-process is electro-weak, the final state is not color connected to the initial state as it is in $t\bar{t}$ production. . . . .	11
2.3	PDFs and their uncertainties for two energy scales, fitted by MSTW. . . . .	14
2.4	Illustration of collinear safety (left) and collinear unsafety in a cone type algorithm (right) together with its implication for perturbative calculations. Partons are vertical lines, their height is proportional to their transverse momentum, and the horizontal axis indicates rapidity. Figure taken from Ref. [1]. . . . .	21

2.5	A sample parton-level event (generated with HERWIG, an MC generator using an angular ordered PS algorithm), together with additional random soft radiation, clustered with four different jets algorithms, illustrating the areas of the resulting hard jets. The top left configuration was clustered using the $k_T$ algorithm (with $n = 2$ in Equation 2.3). The top right uses the Cambridge-Aachen algorithm ( $n = 0$ ). The bottom left uses the seedless infrared safe cone algorithm (SISCone). The anti- $k_T$ algorithm shown in the bottom right clusters jets into ideal conical structures with equal active areas in all non-overlapping jets. Figure taken from Ref. [1] . . . . .	28
3.1	Schematic of the injection complex servicing the LHC. . . . .	31
3.2	Schematic of each experimental and utility insertion region of the LHC. . .	32
3.3	Cut-away view of the ATLAS detector. . . . .	34
3.4	Detailed schematic showing positions of the various components of the Inner Detector relative to the origin. . . . .	35
3.5	Cut-away view of the ATLAS calorimeters. . . . .	38
3.6	Accordion geometry of the LAr EM calorimeter (left) and configuration of the scintillating tile configuration hadronic barrel calorimeter (right). Note that the coordinate system for the tile diagram is different than the one shown in the LAr schematic. For the tile diagram, the radial direction is vertical and the axial direction is perpendicular to the tiles. . . . .	40
3.7	Geometry of the HEC and FCal systems. The solid circle labeled $R_M$ indicates the size of a cylinder containing on average 90% of the energy of an electromagnetic shower. . . . .	41
3.8	Schematic of one of the end-cap cryostats. . . . .	42
3.9	Triangular shape of a typical raw pulse in a cell of the LAr calorimeters, and the shaped output of the LAr FEBs. The points on the shaped output are at the 40 MHz sampling frequency. The total readout time for a cell is about 450 ns and about 125 ns for the first 5 samples. The timing resolution using the optimal filtering method is about 1 ns. . . . .	43

3.10	Schematic of the Muon System showing the magnet system and each of the four tracking technologies used for both precision tracking and the trigger decision. . . . .	46
3.11	Cumulative luminosity versus day delivered to (green), and recorded by (yellow) ATLAS during stable beams and for pp collisions at 7 TeV center-of-mass energy in 2011. The delivered luminosity accounts for the luminosity delivered from the start of stable beams until the LHC requests ATLAS to turn the sensitive detector off to allow a beam dump or beam studies. Given is the luminosity as determined from counting rates measured by the luminosity detectors. These detectors have been calibrated with the use of the van der Meer beam-separation method. . . . .	49
3.12	Efficiencies for the trigger chain used for (top) electrons and (bottom) muons for part of the 2011 data-taking period as a function of offline transverse energy.	54
4.1	A comparison of the simulated and measured electron efficiencies as a function of the number of reconstructed vertices (left) and a comparison of the simulated and measured energy resolution on $Z \rightarrow ee$ events using a fit to the di-electron invariant mass. . . . .	60
4.2	A comparison of the simulated and measured muon efficiencies as a function of the reconstructed muon $p_T$ (left) and $\eta$ (right) and the resulting scale factors (lower panels). . . . .	61
4.3	A comparison of measured momentum resolution in data and simulation as a function of the reconstructed muon $\eta$ for standalone tracks in the Muon System (left) and tracks in the Inner Detector (right). Smearing is applied independently to reconstructed tracks in both systems before combining tracks.	62
4.4	The MC based calibration corrections (left) and the residual <i>in situ</i> corrections (right) used to calibrate calorimeter jets to the particle-level. . . . .	65
4.5	The measured asymmetry $A$ for jets with $20\text{GeV} < p_T < 30\text{GeV}$ used to extract the JER in the di-jet balance method (left) and a schematic of the jet configuration and coordinate system used to extract the JER in the bisector method (right). . . . .	66

4.6	The jet vertex fraction (JVF) distributions for jets originating from the primary and pile-up vertices as predicted by MC simulation in QCD di-jet events (left) and a comparison of the JVF distribution of all jets in $Z$ boson events before corrections are applied (right). . . . .	68
5.1	Efficiencies for real (left) and fake (right) electrons that pass the loose selection criteria to also pass the tight ones, parametrized in electron $\Delta R(e, \text{nearest jet})$ . The $3 < \Delta R < 5$ bin includes all leptons for which $\Delta R > 3$ . The $5 < \Delta R < 6$ bin includes leptons for which there is no jet in the event. . . . .	78
5.2	Real electron efficiencies parametrized in electron $\eta$ (left) and $\Delta R(e, \text{nearest jet})$ (right) with a non-isolated medium identification definition (including the photon conversion veto) on several MC samples for processes contributing to the di-lepton signal region. The average of the $t\bar{t}$ and $Z$ +jets efficiencies is calculated and the difference between the average and the $Z$ +jets efficiency is applied to the data measured rates as a correction. . . . .	78
5.3	Multiplicities of jets with $p_T > 25\text{GeV}$ for same-sign lepton events passing all other signal selections for the the $ee$ (top left), $\mu\mu$ (top right), and $e\mu$ (bottom) channels. . . . .	81
5.4	Multiplicities of jets with $p_T > 25\text{GeV}$ for events where one lepton fails the tight selection criteria for the $ee$ (top left), $\mu\mu$ (top right), and $e\mu$ (bottom) channels. . . . .	82
5.5	Multiplicity of jets with $p_T > 25\text{GeV}$ for events in the $Z/\gamma^* \rightarrow ee$ (left) and $Z/\gamma^* \rightarrow \mu\mu$ (right) control regions. . . . .	84
5.6	$E_T^{\text{miss}}$ distributions for the $ee$ (top left), $\mu\mu$ (top right), and $e\mu$ (bottom) channels. Note that the last bin includes overflow of events in the distribution (i.e. events with $E_T^{\text{miss}} > 300\text{GeV}$ ). . . . .	87
5.7	Reconstructed jet multiplicities with $p_T > 25\text{GeV}$ for the $ee$ (top left), $\mu\mu$ (top right), and $e\mu$ (bottom) channels for events passing all selections, except the jet multiplicity cut. . . . .	90

5.8	Reconstructed jet multiplicities with $p_T > 40\text{GeV}$ for the $ee$ (top left), $\mu\mu$ (top right), and $e\mu$ (bottom) channels for events passing all selections, including the jet multiplicity cut. . . . .	91
5.9	Reconstructed jet multiplicities with $p_T > 60\text{GeV}$ for the $ee$ (top left), $\mu\mu$ (top right), and $e\mu$ (bottom) channels for events passing all selections, including the jet multiplicity cut. . . . .	92
5.10	Reconstructed jet multiplicities with $p_T > 80\text{GeV}$ for the $ee$ (top left), $\mu\mu$ (top right), and $e\mu$ (bottom) channels for events passing all selections, including the jet multiplicity cut. . . . .	93
5.11	Reconstructed di-lepton invariant mass $M_{\ell\ell}$ for all $ee$ (left) and $\mu\mu$ (right) candidates. . . . .	94
5.12	Reconstructed jet multiplicities with $p_T > 25\text{GeV}$ for the $Z \rightarrow ee$ (left) and $Z \rightarrow \mu\mu$ (right) channels. . . . .	95
6.1	The acceptance correction, $f_{\text{accept}}$ as a function of $N_{\text{jets}}^{\text{reco}}$ for the $ee$ (top left), $\mu\mu$ (top right), and $e\mu$ (bottom) channels as estimated from the ALPGEN+HERWIG generator for the $p_T > 25\text{GeV}$ threshold. The error bars show the MC statistical uncertainties. . . . .	103
6.2	The migration correction made before unsmearing, $(1 - f_{\text{reco part}})$ as a function of $N_{\text{jets}}^{\text{reco}}$ for the $ee$ (top left), $\mu\mu$ (top right), and $e\mu$ (bottom) channels for the $p_T > 25\text{GeV}$ threshold, as estimated using the ALPGEN+HERWIG generator. . . . .	104
6.3	The migration matrix for the $p_T > 25\text{GeV}$ threshold for events with at least two particle-level and reconstruction-level jets, used for the unsmearing algorithm for the $ee$ (top left), $\mu\mu$ (top right), and $e\mu$ (bottom) channels, as estimated using the ALPGEN+HERWIG generator. . . . .	106
6.4	The $f_{\text{part reco}}$ scale factors as a function of $N_{\text{jets}}^{\text{part}}$ for the $ee$ (top left), $\mu\mu$ (top right), and $e\mu$ (bottom) channels for the $p_T > 25\text{GeV}$ threshold. . . . .	108
6.5	Closure tests for unfolding of $p_T > 25\text{GeV}$ jet multiplicity distributions for the $ee$ (top left), $\mu\mu$ (top right), and $e\mu$ (bottom) channels. The distribution after each individual correction is also shown. . . . .	110

6.6	Closure tests for unfolding of $p_T > 25\text{GeV}$ jet multiplicity distributions for the $ee$ (left) and $\mu\mu$ (right) channels. The distribution after each individual correction is also shown. . . . .	111
8.1	The unfolded di-electron $t\bar{t}$ particle-level jet multiplicity differential cross-sections for the (a) 25, (b) 40, (c) 60, and (d) 80 GeV $p_T$ -thresholds. . . . .	120
8.2	The unfolded di-muon $t\bar{t}$ particle-level jet multiplicity differential cross-sections for the (a) 25, (b) 40, (c) 60, and (d) 80 GeV $p_T$ -thresholds. . . . .	123
8.3	The unfolded $e\mu$ -channel $t\bar{t}$ particle-level jet multiplicity differential cross-sections for the (a) 25, (b) 40, (c) 60, and (d) 80 GeV $p_T$ -thresholds. . . . .	126
8.4	The unfolded $Z \rightarrow ee$ (left) and $Z \rightarrow \mu\mu$ (right) results. . . . .	130
8.5	The unfolded ratio of the $t\bar{t}$ to $Z$ +jets jet multiplicities for the $ee$ (top left), $\mu\mu$ (top right), and $e\mu$ (bottom) channels. . . . .	133
8.6	The unfolded $t\bar{t}$ particle-level jet multiplicity normalized differential cross-sections for the combination of all channels for the (a) 25, (b) 40, (c) 60, and (d) 80 GeV $p_T$ -thresholds. The predictions of the ALPGEN, MC@NLO, POWHEG, and SHERPA generators are also shown. . . . .	136
8.7	The unfolded $t\bar{t}$ particle-level jet multiplicity normalized differential cross-sections for the combination of all channels for the (a) 25, (b) 40, (c) 60, and (d) 80 GeV $p_T$ -thresholds. The predictions of the nominal ALPGEN+PYTHIA generator as well as its tunings for more or less radiation also shown. . . . .	137
8.8	The bin-to-bin correlation matrices for the uncertainty on the unfolded $t\bar{t}$ particle-level jet multiplicity cross-sections for the combination of all channels for the (a) 25, (b) 40, (c) 60, and (d) 80 GeV $p_T$ thresholds. . . . .	140
8.9	The unfolded ratio of the $t\bar{t}$ to $Z$ +jets jet multiplicities ( $p_T > 25\text{GeV}$ ) for the all channel combination compared to the predictions of the multi-leg (left) and NLO (right) generators. . . . .	141
8.10	The bin-to-bin correlation matrices for the uncertainty on the unfolded $t\bar{t}$ particle-level jet multiplicity ratio to $Z$ +jets. . . . .	142
A.1	$H_T$ distributions for the $ee$ (left), $\mu\mu$ (center), $e\mu$ (right) channels. . . . .	146

A.2	Di-lepton mass distributions for the $ee$ (left), $\mu\mu$ (center), $e\mu$ (right) channels.	146
A.3	Leading lepton $p_T$ distributions for the $ee$ (left), $\mu\mu$ (center), $e\mu$ (right) channels. . . . .	147
A.4	Leading lepton $\eta$ distributions for the $ee$ (left), $\mu\mu$ (center), $e\mu$ (right) channels.	147
A.5	Sub-leading lepton $p_T$ distributions for the $ee$ (left), $\mu\mu$ (center), $e\mu$ (right) channels. . . . .	148
A.6	Sub-leading lepton $\eta$ distributions for the $ee$ (left), $\mu\mu$ (center), $e\mu$ (right) channels. . . . .	148
A.7	The $E_T^{\text{miss}}$ distribution of the di-electron channel for the exclusive (a) 2, (b) 3, (c) 4, (d) 5, and (e) inclusive 6 jet bins for a $p_T > 25\text{GeV}$ jet threshold. . .	150
A.8	The $E_T^{\text{miss}}$ distribution of the di-muon channel for the exclusive (a) 2, (b) 3, (c) 4, (d) 5, and (e) inclusive 6 jet bins for a $p_T > 25\text{GeV}$ jet threshold. . .	151
A.9	The $E_T^{\text{miss}}$ distribution of the $e\mu$ channel for the exclusive (a) 2, (b) 3, (c) 4, (d) 5, and (e) inclusive 6 jet bins for a $p_T > 25\text{GeV}$ jet threshold. . . . .	152
A.10	The $E_T^{\text{miss}}$ distributions of the di-electron channel with the requirement that at least two jets pass the $b$ -tagging selections in place of a $E_T^{\text{miss}}$ cut for the exclusive (a) 2, (b) 3, (c) 4, (d) 5, and (e) inclusive 6 jet bins for a $p_T > 25\text{GeV}$ jet threshold. . . . .	153
A.11	The $E_T^{\text{miss}}$ distribution of the di-muon channel with the requirement that at least two jets pass the $b$ -tagging selections in place of a $E_T^{\text{miss}}$ cut for the exclusive (a) 2, (b) 3, (c) 4, (d) 5, and (e) inclusive 6 jet bins for a $p_T > 25\text{GeV}$ jet threshold. . . . .	154
A.12	The $p_T$ distributions for all channels combined for the (a) leading, (b) sub-leading, (c) 3 <sup>rd</sup> , (d) 4 <sup>th</sup> , (e) 5 <sup>th</sup> , and (f) 6 <sup>th</sup> (inclusive) jets. . . . .	155
A.13	The $\eta$ distributions for all channels combined for the (a) leading, (b) sub-leading, (c) 3 <sup>rd</sup> , (d) 4 <sup>th</sup> , (e) 5 <sup>th</sup> , and (f) 6 <sup>th</sup> (inclusive) jets. . . . .	156
A.14	Statistical covariance matrix for the $e\mu$ channel. Cross-referencing bins in separate jet multiplicity distributions with different $p_T$ thresholds shows the number of events that are in both bins. . . . .	158

A.15	Probability distribution for the largest statistical fluctuation in a given pseudo-experiment (left) and the corresponding $p$ -value for a given fluctuation (right). The red line shows statistical significance of the observed deviation in the four 60GeV jet bin in the $e\mu$ channel, the largest deviation of the ATLAS dataset with respect to the ALPGEN+HERWIG $t\bar{t}$ MC plus backgrounds in this analysis.	159
A.16	Probability distribution for the largest statistical plus systematic fluctuation in a given pseudo-experiment (left) and the corresponding $p$ -value for a given fluctuation (right). The red line shows significance of the observed deviation in the four 60GeV jet bin in the $e\mu$ channel, the largest deviation of the ATLAS dataset with respect to the ALPGEN+HERWIG $t\bar{t}$ MC plus backgrounds in this analysis. . . . .	159
A.17	Probability distribution for the $\chi^2$ test statistic for a given pseudo-experiment (left) and the corresponding $p$ -value (right). The vertical lines show the observed $\chi^2$ test statistics for each model with respect to the ATLAS dataset.	161
B.1	Estimated unfolding biases for the $ee$ (left), $\mu\mu$ (center), and $e\mu$ channels for the $p_T > 25\text{GeV}$ threshold, for different numbers of iterations, as well as the matrix inversion method for comparison. The dashed line represents the estimated relative error on the measurement due to the unfolding bias and the dotted line is the statistical uncertainty. The solid line is the two uncertainties added in quadrature. . . . .	163
C.1	The gluon fraction estimate used in the di-lepton $t\bar{t}$ jet multiplicity for events with (a) 2, (b) 3, (c) 4, and (d) $\geq 5$ jets, used for the JES uncertainty. . . .	166
C.2	The gluon fraction uncertainty estimate used in the di-lepton $t\bar{t}$ jet multiplicity for events with (a) 2, (b) 3, (c) 4, and (d) $\geq 5$ jets, used for the JES uncertainty. . . . .	167
C.3	The default JES uncertainty by component as a function of jet $p_T$ for jets with $\eta < 0.8$ . . . . .	167

C.4 The JES uncertainty by component using the estimated flavor fraction inputs,  
as a function of jet  $p_T$  for events with (a) 2, (b) 3, (c) 4, and (d)  $\geq 5$  jets,  
and for jets with  $\eta < 0.8$ . . . . . 168

# List of Tables

1.1	Fundamental interactions of the Standard Model and their force carriers. $A_\mu^a$ and $B_\mu$ are the $SU(2)$ and $U(1)$ generators (respectively) and $g = \sin\theta_W/e$ and $g' = \cos\theta_W/e$ , where $\theta_W$ is the weak mixing angle and $e$ is the charge of the electron. . . . .	2
1.2	Fundamental fermions of the Standard Model, their masses and their gauge quantum numbers. Note that electric charge $Q$ relates to weak isospin $I_3$ and hypercharge $Y$ via the equation $Q = I_3 + \frac{1}{2}Y$ . . . . .	3
3.1	Intrinsic accuracy and coverage of each component of the Inner Detector. . .	37
3.2	Main parameters of the calorimeter system. . . . .	39
3.3	Main parameters of the tracking technologies used for tracking and triggering in the Muon System. . . . .	47
5.1	The number of Monte Carlo events in the control region for both DY sources and other processes, the number of observed events in data, and the calculated scale factor. . . . .	84
5.2	Fraction of the total yields attributed to multi-jet events as determined from the template fit for the $Z \rightarrow ee$ and $Z \rightarrow \mu\mu$ signal regions. . . . .	85
5.3	Yields as a function of reconstructed jet multiplicity for the di-electron channel. The total systematic uncertainty is shown for the expected numbers of events. . . . .	86
5.4	Yields as a function of reconstructed jet multiplicity for the di-muon channel. The total systematic uncertainty is shown for the expected numbers of events.	88

5.5	Yields as a function of reconstructed jet multiplicity for the $e\mu$ channel. The total systematic uncertainty is shown for the expected numbers of events. . . . .	88
5.6	Yields as a function of reconstructed jet multiplicity for the $Z \rightarrow ee$ sample. The total systematic uncertainty is shown for the expected numbers of events. . . . .	95
5.7	Yields as a function of reconstructed jet multiplicity for the $Z \rightarrow \mu\mu$ sample. The total systematic uncertainty is shown for the expected numbers of events. . . . .	96
8.1	Relative uncertainties (in %) for the $ee$ -channel for the $p_T > 25\text{GeV}$ threshold measurement. . . . .	121
8.2	Relative uncertainties (in %) for the $ee$ -channel for the $p_T > 40\text{GeV}$ threshold measurement. . . . .	121
8.3	Relative uncertainties (in %) for the $ee$ -channel for the $p_T > 60\text{GeV}$ threshold measurement. . . . .	122
8.4	Relative uncertainties (in %) for the $ee$ -channel for the $p_T > 80\text{GeV}$ threshold measurement. . . . .	122
8.5	Relative uncertainties (in %) for the $\mu\mu$ -channel for the $p_T > 25\text{GeV}$ threshold measurement. . . . .	124
8.6	Relative uncertainties (in %) for the $\mu\mu$ -channel for the $p_T > 40\text{GeV}$ threshold measurement. . . . .	124
8.7	Relative uncertainties (in %) for the $\mu\mu$ -channel for the $p_T > 60\text{GeV}$ threshold measurement. . . . .	125
8.8	Relative uncertainties (in %) for the $\mu\mu$ -channel for the $p_T > 80\text{GeV}$ threshold measurement. . . . .	125
8.9	Relative uncertainties (in %) for the $e\mu$ -channel for the $p_T > 25\text{GeV}$ threshold measurement. . . . .	127
8.10	Relative uncertainties (in %) for the $e\mu$ -channel for the $p_T > 40\text{GeV}$ threshold measurement. . . . .	127
8.11	Relative uncertainties (in %) for the $e\mu$ -channel for the $p_T > 60\text{GeV}$ threshold measurement. . . . .	128
8.12	Relative uncertainties (in %) for the $e\mu$ -channel for the $p_T > 80\text{GeV}$ threshold measurement. . . . .	128

8.13	Relative uncertainties (in %) broken down by source for the $ee$ -channel for ratio of the $t\bar{t}$ to $Z$ +jets jet multiplicities. . . . .	131
8.14	Relative uncertainties (in %) broken down by source for the $\mu\mu$ -channel for ratio of the $t\bar{t}$ to $Z$ +jets jet multiplicities. . . . .	131
8.15	Relative uncertainties (in %) broken down by source for the $e\mu$ -channel for ratio of the $t\bar{t}$ to $Z$ +jets jet multiplicities. . . . .	132
8.16	Relative uncertainties (in %) for the combination for the $p_T > 25\text{GeV}$ threshold measurement. . . . .	138
8.17	Relative uncertainties (in %) for the combination for the $p_T > 40\text{GeV}$ threshold measurement. . . . .	138
8.18	Relative uncertainties (in %) for the combination for the $p_T > 60\text{GeV}$ threshold measurement. . . . .	139
8.19	Relative uncertainties (in %) for the combination for the $p_T > 80\text{GeV}$ threshold measurement. . . . .	139
8.20	Relative uncertainties (in %) for the combination of all channels for the ratio of the $t\bar{t}$ to $Z$ +jets jet multiplicities ( $p_T > 25\text{GeV}$ ). . . . .	142
A.1	Table showing the observed generalized $\chi^2$ test statistics of each fully simulated model used in this analysis with respect to the ATLAS dataset, as well as the $p$ -value that the dataset is consistent with each model. The $p$ -value in each case is determined using the pseudo-experiment method described in this section, with the exception of MC@NLO which is estimated assuming a standard $\chi^2$ distribution with 60 degrees of freedom for each bin considered in this analysis. . . . .	161
C.1	Statistical uncertainties (in %) for the combination of all channels for the $p_T > 25\text{GeV}$ threshold. . . . .	169
C.2	Background specific uncertainties (in %) for the combination of all channels for the $p_T > 25\text{GeV}$ threshold. . . . .	169
C.3	Lepton specific uncertainties (in %) for the combination of all channels for the $p_T > 25\text{GeV}$ threshold. . . . .	170

C.4	$E_T^{\text{miss}}$ -specific uncertainties (in %) for the combination of all channels for the $p_T > 25\text{GeV}$ threshold. . . . .	170
C.5	Jet specific uncertainties (in %) for the combination of all channels for the $p_T > 25\text{GeV}$ threshold. . . . .	171
C.6	Unfolding/signal modeling specific uncertainties (in %) for the combination of all channels for the $p_T > 25\text{GeV}$ threshold. . . . .	172
C.7	Jet specific uncertainties (in %) for the combination of all channels for the $p_T > 25\text{GeV}$ threshold ratio measurement. . . . .	173

# Acknowledgments

First and foremost, I would like to extend my deepest appreciation for my advisor, Gustaaf Brooijmans. The completion of this dissertation would not have been possible without his excellent advice and near endless patience throughout my career as a graduate student. I am also grateful for the many useful discussions I had with Francesco Spano. His attentive feedback was a source of confidence and inspiration for me. It was also a pleasure to work closely with William Bell, who deserves a significant amount of credit for many of the strategies implemented in this analysis.

I would like to thank my colleagues and friends, Konrad Jende, Alex Penson, Eric Williams, and Evan Wulf for helping and encouraging me throughout this analysis, and for making what little free time I did have fun. I owe a debt of gratitude to Emily Thompson and John Parsons for their advice and guidance as well. I would also like to thank the rest of the current and former Columbia University ATLAS group including Tim Andeen, Andrew Altheimer, Seth Caughron, Mark Cooke, Kathy Copic, Thomas Gadfort, Heather Gray, Jun Guo, Diedi Hu, Emlyn Hughes, David Lopez Mateos, Zach Marshall, Nikiforos Nikiforou, Kerstin Perez, Valeria Perez Reale, Max Scherzer, Feng Tian, Mike Tuts, Lei Zhou, Ning Zhou, and Lidija Zivkovic. It was a pleasure to work with all of them.

I am indebted to my undergraduate advisors, David Kirkby and Mario Bondioli, for inspiring me to pursue research in particle physics. I would not have been able to perform this research without the excellent instruction of the Columbia University Physics Department faculty, as well as the administrative support of the staff of Nevis Laboratories and the Columbia University Physics Department. I should also thank the ATLAS collaboration, for laying the experimental foundation upon which this analysis was built.

It would take an entire thesis to describe how lucky I feel and how thankful I am to have the support of so many friends and family members. To my parents, thank you for

always pushing me to succeed and for letting me know that even if I didn't, you would be there for me. To Nicole, Alex, Bella, Elizabeth, Eric, Jason, Julie, Christopher, and Kelly, thank you for always making me feel like I never left whenever I visit home. To Grandma Pauline, thank you for looking after me and keeping me on track in school in my younger years. To Grandpa Gene and Grandma Elaine, thanks for always being interested in my work. To my grandparents, aunts, uncles, and cousins who I haven't mentioned by name, I am truly grateful for your support. To Omar, thanks for being a true friend, and for sharing about your experiences of life as a graduate student and for listening to mine. Finally to my girlfriend Sofia, thank you for your love, patience, and support throughout the last few challenging years. To all of you, thank you. Your support undoubtedly carried me through the more difficult times of my graduate studies, so I dedicate this work to all of you.

for my family

# Chapter 1

## Introduction

### 1.1 The Standard Model

Particle physics is the science which seeks to describe the fundamental constituents of the universe and their interactions. At present, the Standard Model of Particle Physics (SM) is the most successful attempt to that end. It is a relativistic quantum field theory describing the interactions of fermions (particles of half-integer spin) mediated by gauge bosons (particles of integer spin). The theory, its successes, and some of its shortcomings will briefly be described here. Detailed discussions of relativistic quantum field theory and the SM can be found in several excellent textbooks [2, 3, 4, 5].

The SM is understood as an  $SU(3) \times SU(2) \times U(1)$  gauge theory of interactions mediated by vector bosons, which mathematically transform as generators of the groups corresponding to the underlying symmetries of the theory. The strength of the interactions depends on quantum numbers represented by eigenvalues of the adjoint representation of the gauge symmetry group carried by the interacting fermions. Fermions therefore transform as eigenvectors.

The  $SU(2) \times U(1)$  component of the SM is spontaneously broken to  $U(1)$ . The prevailing method in the SM accomplishes this through a process called the Higgs mechanism. In this process, the generators of the  $SU(2) \times U(1)$  component of the SM are presumed to couple to a scalar field known as the Higgs field. This coupling leads to one massless (the photon,  $\gamma$ ) and three massive (the  $W^\pm$  and  $Z$  bosons) vector bosons which are linear combinations

of the generators of  $SU(2) \times U(1)$ . This mechanism necessitates the existence of at least one scalar particle known as the Higgs boson. Though a recently discovered particle [6, 7] appears to be consistent with the SM Higgs boson, further analysis of its couplings to the particles in the SM will be needed for confirmation.

The unbroken  $SU(3)$  component of the SM is known as Quantum Chromodynamics (QCD) or the strong interaction [8, 9]. There are 8 types of massless vector bosons (called “gluons” and usually represented by the symbol  $g$ ) corresponding to the 8 generators of the  $SU(3)$  symmetry of QCD. The quantum number associated with QCD is called color. QCD forms the dominant interacting component of the theoretical predictions specific to this analysis. A detailed description of QCD will be provided in Chapter 2. All force carriers in the SM are summarized in Table 1.1 along with their masses<sup>1</sup> and descriptions of their gauge symmetries.

Table 1.1: Fundamental interactions of the Standard Model and their force carriers.  $A_\mu^a$  and  $B_\mu$  are the  $SU(2)$  and  $U(1)$  generators (respectively) and  $g = \sin\theta_W/e$  and  $g' = \cos\theta_W/e$ , where  $\theta_W$  is the weak mixing angle and  $e$  is the charge of the electron.

Force	Force Carrier	Mass (GeV)	$SU(2) \times U(1)$ Combination	$SU(3)$ Symmetry
Strong	gluon ( $g$ )	0	-	<b>8</b>
Charged Weak	$W^\pm$	80.4	$\frac{1}{\sqrt{2}}(A_\mu^1 \mp iA_\mu^2)$	<b>1</b>
Neutral Weak	$Z$	91.2	$\frac{1}{\sqrt{g^2+g'^2}}(gA_\mu^3 - g'B_\mu)$	<b>1</b>
Electromagnetic	photon ( $\gamma$ )	0	$\frac{1}{\sqrt{g^2+g'^2}}(g'A_\mu^3 + gB_\mu)$	<b>1</b>

The two types of fermions in the SM, leptons and quarks, are listed in Table 1.2. Leptons appear to come in three generations. In each generation there is a charged (the electron, muon, and tau) and neutral lepton (their corresponding neutrinos), all of which are colorless and therefore do not interact through the strong force. Each lepton also has its own anti-particle which has the same mass, but different quantum numbers (most important is their

<sup>1</sup>In this thesis, mass and momentum are always expressed as energies in units of electron-volts (eV), while speed of light  $c$  is set to 1.

opposite electric charge  $Q$ ).

Table 1.2: Fundamental fermions of the Standard Model, their masses and their gauge quantum numbers. Note that electric charge  $Q$  relates to weak isospin  $I_3$  and hypercharge  $Y$  via the equation  $Q = I_3 + \frac{1}{2}Y$ .

Type of Particle	Name	Mass (GeV)	Particle (Anti-particle) Hypercharge, Isospin, $SU(3)$ Symmetry
Leptons	electron ( $e$ )	0.000511	$-1/2, -1, \mathbf{1}$ ( $0, +2, \mathbf{1}$ )
	electron neutrino ( $\nu_e$ )	$< 0.46 \times 10^{-6}$	$+1/2, -1, \mathbf{1}$ ( $0, 0, \mathbf{1}$ )
	muon ( $\mu$ )	0.105	$-1/2, -1, \mathbf{1}$ ( $0, +2, \mathbf{1}$ )
	muon neutrino ( $\nu_\mu$ )	$< 0.19 \times 10^{-3}$	$+1/2, -1, \mathbf{1}$ ( $0, 0, \mathbf{1}$ )
	tau lepton ( $\tau$ )	1.777	$-1/2, -1, \mathbf{1}$ ( $0, +2, \mathbf{1}$ )
	tau neutrino ( $\nu_\tau$ )	$< 18.2 \times 10^{-3}$	$+1/2, -1, \mathbf{1}$ ( $0, 0, \mathbf{1}$ )
Quarks	up quark ( $u$ )	0.0017-0.0031	$+1/2, +1/3, \mathbf{3}$ ( $0, -4/3, \bar{\mathbf{3}}$ )
	down quark ( $d$ )	0.0041-0.0057	$-1/2, +1/3, \mathbf{3}$ ( $0, +2/3, \bar{\mathbf{3}}$ )
	charm quark ( $\mu$ )	1.29	$+1/2, +1/3, \mathbf{3}$ ( $0, -4/3, \bar{\mathbf{3}}$ )
	strange quark ( $s$ )	0.1	$-1/2, +1/3, \mathbf{3}$ ( $0, +2/3, \bar{\mathbf{3}}$ )
	top quark ( $t$ )	172.9	$+1/2, +1/3, \mathbf{3}$ ( $0, -4/3, \bar{\mathbf{3}}$ )
	bottom quark ( $b$ )	4.19	$-1/2, +1/3, \mathbf{3}$ ( $0, +2/3, \bar{\mathbf{3}}$ )

Quarks also come in three generations with each generation containing an up-type quark and a down-type quark. The names of the quarks are “up” and “down” in the first generation, “charm” and “strange” in the second, and “top” and “bottom” in the third, with up-type quarks listed first in each generation here. Like leptons, quarks are charged with up-type quarks having charge  $+2|e|/3$  and down-type  $-|e|/3$ , where  $e$  is the charge of the electron. Unlike leptons, they do possess color and interact with the gluon field. In addition quarks are never observed in isolation, always confined in color-singlet bound-states called hadrons of either one valence quark and one valence anti-quark (the anti-matter counterpart of a quark with opposite charge and carrying anti-color),  $q\bar{q}$  (known as mesons), or three

valence quarks,  $qqq$  (called baryons). Protons and neutrons, making up most of the baryonic matter of the universe, are examples of such bound states with the proton (neutron) being  $uud$  ( $udd$ ) in a simplified picture.

The SM has been incredibly successful at describing a wide range of phenomena. Its predictions have been verified by experiment to an unprecedented degree of accuracy in many cases. As an example, experiments measuring the anomalous magnetic di-pole moment of the muon agree with the theoretical predictions of Electro-weak theory to within one part in  $10^8$ .

Despite its many successes, the SM has several limitations necessitating either its continued verification, and/or its supersession by a higher theory. The most outstanding challenge to the SM is the complete understanding of electro-weak symmetry breaking, though there has been progress in this regard. Additionally, fermions acquire mass in the SM only through the arbitrary values of Yukawa couplings to the Higgs field. This, in addition to several other input parameters to the SM which cannot be calculated from first principles (such as the gauge coupling constants and the CKM mixing angles [10, 11]), leads the SM to often be regarded as an “effective field theory”.

Though the SM accurately describes a wide range of physical phenomena, it is not yet a “theory of everything.” Perhaps most obvious is its non-incorporation of gravity, the most familiar of the physical forces, but presumed weak enough to be ignored up to the Planck scale ( $\sim 10^{18}$  GeV). Another major issue with the SM is the so called “hierarchy problem.” If the recently discovered particle turns out to be the SM Higgs boson, one can question why its mass (around 125 GeV) is so much lower than the scale of grand unification, which is the scale at which the coupling strengths of the fundamental forces appear to converge ( $\sim 10^{16}$  GeV), potentially unifying the strong and electro-weak forces under a theory of a higher symmetry. Since the calculation of the Higgs boson mass should include loop corrections up to this scale, either a very delicate cancellation is required to keep the Higgs boson mass low, or new processes which become relevant close to the electro-weak scale are necessary to stabilize its mass.

Other outstanding problems include astro-physical observations, including anomalous motions of galaxies, clusters, and super-clusters, that have hinted at the existence of stable

weakly interacting or non-interacting massive particles (i.e. Dark Matter). Such particles have not been discovered. Finally, several experiments have measured oscillations of neutrino flavors which violate lepton number and necessitate neutrino mass. Though nothing in the SM forbids these features, their complete understanding is pending.

## 1.2 High energy physics experiments and the goal of this analysis

In many cases, experiments in particle physics involve searching for or studying the properties of massive, unstable particles. In order to produce such particles, large amounts of energy are needed, making use of Einstein's famous equation  $E = mc^2$ . In addition, detectors are needed to measure the signatures of the decays of these particles. For this analysis, this is accomplished using the high energy collisions at the Large Hadron Collider (LHC, see Section 3.1).

The top quark ( $t$ ) is the heaviest particle in the SM with a mass of 172.9 GeV, the closest of all known particles to the scale of electro-weak symmetry breaking. This hints that the top quark may couple strongly to processes responsible for this phenomenon (i.e. the Higgs field in the SM, or possibly to other new physics processes beyond the SM), making the detailed study of its properties essential. The top quark was discovered in 1995 by the Tevatron experiments at Fermilab in Batavia, Illinois [12, 13]. Since then, several of its properties have been studied at both the Tevatron and LHC [14, 15, 16, 17, 18]. The subject of this thesis is the multiplicity of jets produced in association with top quark pair ( $t\bar{t}$ ) events in 7 TeV  $pp$ -collisions, a well-defined measurable property which can be compared to the theoretical predictions through programs called Monte Carlo (MC) generators. These programs implement SM calculations and predict the outcomes of collisions. In addition, since several new physics models include processes which couple strongly to the top quark and include extra jets in the final state [?, 19, 20, 21], this analysis is also potentially sensitive to new physics.

Top quarks are unique in that they do not hadronize. Instead they decay via the weak force on a time-scale of about  $10^{-25}$  s, much shorter than the time-scale in which QCD

becomes non-perturbative ( $\Lambda_{QCD}^{-1}$ ), which is also the regime where quarks amalgamate into hadrons. In the SM top quarks decay to a  $W$  boson and a down-type quark. The probability for a top quark to decay to a  $W$  boson and quark  $q$  is proportional to  $|V_{tq}|^2$  where  $|V_{tq}|$  is the corresponding element of the CKM matrix:

$$\begin{aligned}
 V_{CKM} &= \begin{bmatrix} |V_{ud}| & |V_{us}| & |V_{ub}| \\ |V_{cd}| & |V_{cs}| & |V_{cb}| \\ |V_{td}| & |V_{ts}| & |V_{tb}| \end{bmatrix} \\
 &= \begin{bmatrix} 0.97428 \pm 0.00015 & 0.2253 \pm 0.0007 & 0.00347^{+0.00016}_{-0.00012} \\ 0.2252 \pm 0.0007 & 0.97345^{+0.00015}_{-0.00016} & 0.0410^{+0.0011}_{-0.0007} \\ 0.00862^{+0.00026}_{-0.00020} & 0.0403^{+0.0011}_{-0.0007} & 0.999152^{+0.000030}_{-0.000045} \end{bmatrix}.
 \end{aligned} \tag{1.1}$$

With the  $|V_{tb}|$  element very close to unity, top quarks decay almost exclusively to a  $W$  boson and a  $b$  quark, with  $b$  quarks usually evolving into collimated streams of hadrons: a jet (the details of this process will be discussed in Chapter 2).  $W$  bosons can then decay to either quarks, or a lepton and a neutrino.  $t\bar{t}$  events are usually characterized experimentally by the number of leptons in the final state coming from  $W$  boson decays, including via leptonic  $\tau$  decays. Since  $\tau$  leptons decay very close to the interaction point,  $\tau$  decays to hadrons are observed as a jet and are not considered leptonic from an experimental point of view. This thesis focuses on  $t\bar{t}$  events decaying to a di-leptonic final state. Since neutrinos are neutral and colorless, they escape the detector and their presence can only be inferred from missing transverse momentum,  $E_T^{\text{miss}}$ . Therefore, the experimental signature of interest in this thesis will be  $t\bar{t} \rightarrow \ell\ell + E_T^{\text{miss}} + \text{jets}$ , where  $\ell$  is an electron ( $e$ ) or muon ( $\mu$ ).

The dominant systematic uncertainty in this analysis is expected to be the uncertainty associated with the measurement and calibration of jet energies (i.e. the jet energy scale or JES), as it has been in previous jet multiplicity measurements [22, 23, 24]. The effect can be mitigated by instead measuring a bin-by-bin ratio of the jet multiplicity distribution in  $t\bar{t}$  events to the same distribution in leptonically decaying  $Z$  boson events. The reason for

this mitigation is that the extra<sup>2</sup> hard jets produced in association with  $t\bar{t}$  pairs have similar kinematic properties to those produced in  $Z$  boson events as can be seen in Figure 1.1. As will be discussed in Chapter 4, the jet energy scale and its uncertainty are primarily functions of the jet kinematics (transverse momentum,  $p_T$ , and pseudorapidity,  $\eta$ ). Biases, e.g. due to miscalibrations, which are present in the measurement of the multiplicity of extra jets in  $t\bar{t}$  events should also be present in the same measurement in  $Z$  boson events. Since  $t\bar{t}$  events usually include at least two jets induced by the  $b$ -quarks, any bias should partially cancel in the bin-by-bin ratio of  $(N+2)$ -jets in  $t\bar{t}$  events to  $N$ -jets in  $Z$  boson events. With the ratio in hand, one can extrapolate to the  $t\bar{t}$  distribution using the theoretical  $Z$ +jet cross-section, which has a smaller uncertainty than that associated with the JES [25]. Alternatively, the ratio itself is a quantity that a model can predict and be compared with this measurement.

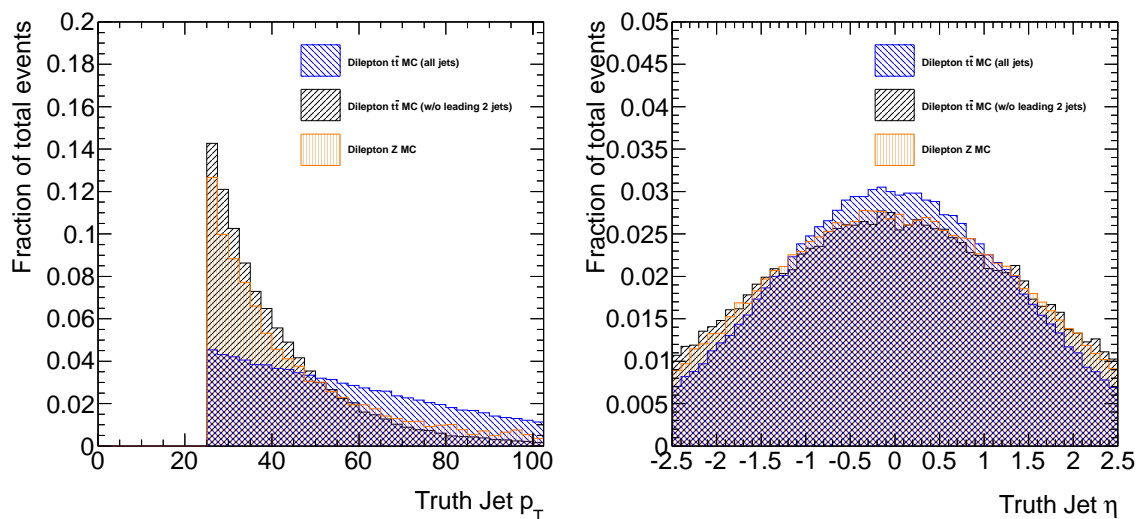


Figure 1.1: Comparison of the  $p_T$  and  $\eta$  distributions in  $t\bar{t}$  and  $Z$  boson events passing truth-level kinematic selections which are similar to those used in this analysis.

Figure 1.1 compares the predictions for the  $p_T$  and  $\eta$  distributions of MC truth jets for both di-lepton  $t\bar{t}$  events and leptonically decaying  $Z$  boson events. Both the distribution of

---

<sup>2</sup>With regard to  $t\bar{t}$  events, the term “extra” is used loosely here. From a theoretical perspective, labeling a jet in a  $t\bar{t}$  event as “extra” (i.e. not originating from the  $t\bar{t}$  system) is difficult to define. Here, “extra” means all but the leading two jets, since the experimental selection of  $t\bar{t}$  events requires the presence of at least two jets.

all jets in the event and the all but the leading two jets are shown for  $t\bar{t}$  events for comparison. The kinematics of all but the leading two jets in  $t\bar{t}$  events are similar enough to the kinematics of jets produced in  $Z$  boson events that a significant reduction in the uncertainty of the ratio<sup>3</sup> compared to the direct measurement is expected. Several other important systematic uncertainties, such as uncertainties on the luminosity or the lepton trigger and reconstruction efficiency estimates, will also be reduced in the ratio measurement.

### 1.3 Outline

This thesis is outlined as follows: Chapter 2 will discuss several aspects of QCD and Monte Carlo simulations, particularly in the context of  $t\bar{t}$  production. Chapter 3 describes the machinery used to produce and measure top quark events for this analysis, namely the Large Hadron Collider and the ATLAS detector. Chapter 4 describes the details of the reconstruction and selection of leptons, jets, and missing transverse momentum. Chapter 5 discusses the selection of  $t\bar{t}$  events and the estimation of backgrounds. Once events are selected and the background subtracted, in principle jet counting is trivial. However, detector effects can lead to migrations between bins, smearing the distributions. In order to compare the results of this measurement to results from other experiments, or to predictions which have not been processed through the ATLAS detector simulation, attempts have been made to “unsmear” detector effects through a process called unfolding. This is described in Chapter 6. Chapter 7 discusses systematic uncertainties associated with this measurement and Chapter 8 summarizes the final results and concludes the thesis.

---

<sup>3</sup>Note that some residual uncertainty is expected due to differences in jet flavors (i.e. the flavors of the quarks inducing the jets) between the  $t\bar{t}$  and  $Z$ +jets processes, as well as other smaller effects such as effects of nearby jets.

## Chapter 2

# Theoretical considerations

The inclusive cross-section for  $t\bar{t}$  production in 7 TeV proton-proton collisions has been measured [26] and compared to the approximate next-to-next-to-leading order (aN<sup>2</sup>LO) theoretical predictions [27, 28], and good agreement has been observed. This analysis aims to measure the effects of additional radiation in  $t\bar{t}$  production by measuring the differential cross-section  $d\sigma_{t\bar{t}}/dN_{\text{jets}}$ . Fixed order calculations lead to theoretical uncertainties of order 10% for the inclusive cross-section, but are inadequate for predicting the jet multiplicity of  $t\bar{t}$  events due to the large number of final state particles involved. This chapter will discuss the Monte Carlo methods used to make these predictions.

At leading order in perturbative QCD,  $t\bar{t}$  production at the LHC proceeds via the following Feynman diagrams:

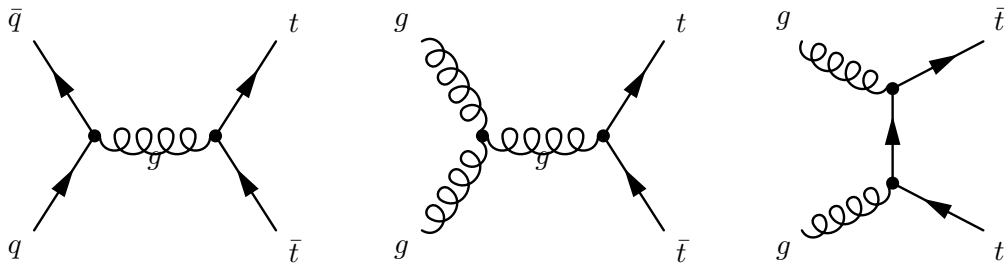


Figure 2.1: Leading order Feynman diagrams for  $t\bar{t}$  production in hadron-hadron collisions.

This highly idealized picture does not completely describe phenomena associated with  $t\bar{t}$  production in the framework of the SM:

- First, the isolated quarks and gluons (collectively called “partons” in this thesis) in

the initial state do not exist in nature. Instead interactions must occur within hadrons (protons in the case of the LHC) and the remnants of protons which are not part of the hard collision can also have effects on the final state.

- Second, top quarks decay weakly as discussed in Section 1.2. As already mentioned, this analysis focuses on di-leptonic final states. With this in mind, the diagrams above should be expanded by adding vertices for each top quark decaying as  $t \rightarrow bW(\rightarrow \ell\nu)$ .
- Third and perhaps most crucial to this analysis is that these diagrams are not what happens in the space-time picture of the process. They are calculational tools used in a perturbation series and only the leading order contribution to that series is shown. More precise calculations include higher orders of perturbation theory, summing additional diagrams with extra vertices, each QCD vertex corresponding to an extra factor  $\alpha_s$  which should be considerably less than 1 if the series is to converge. As will be discussed in this chapter, higher order corrections predict additional soft and collinear radiation of the initial and final state partons as well as additional hard final state partons which can also radiate. It is the amount of this additional hard radiation that this analysis will measure, but as with the first bullet point, the direct observation of final state isolated partons is unphysical.
- Fourth, the unphysical final state quarks and gluons must undergo the strictly non-perturbative effect of hadronization into physical, stable particles.

With the exception of the weak decay of top quarks, all of these interactions are QCD phenomena [8, 9]. Taking all of the necessary QCD effects into account, a more complete picture of the anatomy of a hadron collision as understood by the SM is shown in Figure 2. The figure shows an electro-weak multi-jet process instead of strong  $t\bar{t}$  production, but the most salient features of the QCD structure of the final state are the same.

The chapter is outlined as follows: first, a description of how QCD is used to make predictions for each stage in the evolution of hadron collisions is given in the next section. This is followed by a section on important considerations regarding the precise definition of the final state jets of hadrons. Finally, the specific Monte Carlo methods used to predict the properties of typical  $t\bar{t}$  events are discussed.

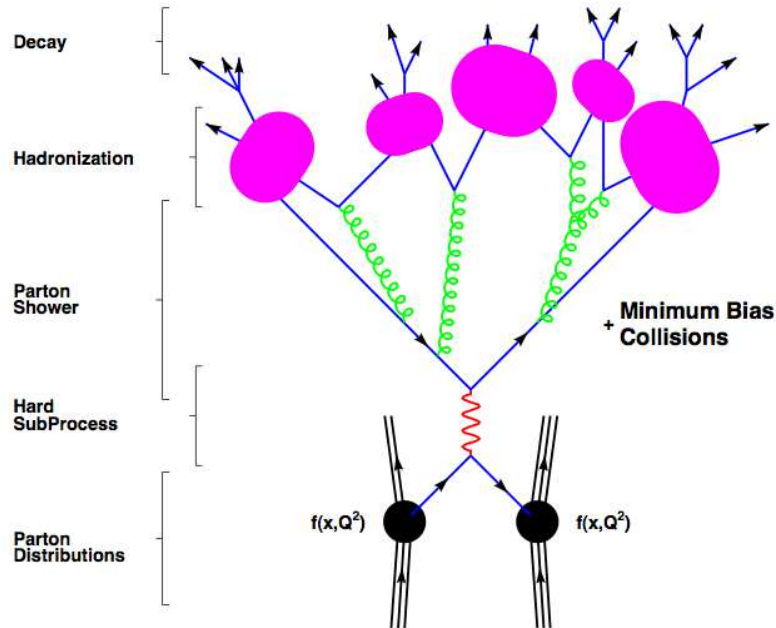


Figure 2.2: The structure of a hadron-hadron collision as implemented in QCD predictions. A valence quark and a sea anti-quark annihilate into a vector boson producing a  $q\bar{q}$  pair. The hard sub-process final state  $q\bar{q}$  pair showers into more partons which eventually hadronize, and unstable hadrons decay into stable particles. Not shown is initial state radiation, described by higher order corrections in the hard sub-process, or more commonly via a parton shower algorithm. Since the hard sub-process is electro-weak, the final state is not color connected to the initial state as it is in  $t\bar{t}$  production.

## 2.1 Quantum Chromodynamics and its predictions

### 2.1.1 Historical introduction

The theory of the strong force originally developed as an attempt to explain the confinement of protons and neutrons in the nuclei of atoms. In 1934, the first successful model [29] proposed that this interaction should occur through the exchange of a massive (100 MeV) scalar particle in order to explain the short range of the force inferred from the size of the atomic nucleus. The pi meson (pion) discovered over a decade later [30, 31, 32] seemed to fit the bill, however it was later discovered that pions themselves were composite particles held together by the strong force. From then up until the 1960s, dozens of other hadrons were

discovered, and to organize them the quark model [33, 34] was proposed, motivated by an approximate  $SU(3)$ -flavor symmetry exhibited by these hadrons. The model postulated that baryons were composed of bound states of three quarks, and mesons composed of a quark–anti-quark pair. Quarks are held strongly together inside baryons and mesons through the exchange of a particle called the gluon. In order to avoid the existence of baryons with a totally symmetric (under quark exchange) wave function such as the  $\Delta^{++}(uuu)$ , which is forbidden for fermions by the spin-statistics theorem, an additional quantum number, called “color” and transforming under  $SU(3)$  (not to be confused with the aforementioned  $SU(3)$ -flavor), was introduced and assigned to each quark [35, 36].

Experimental measurements of deep inelastic scattering [37, 38] in the 1960s and 1970s seemed to confirm that hadrons were indeed composed of point-like particles. However, it was observed that quarks inside hadrons behaved like free particles in high energy collisions, which led to the development of the parton model [39, 40]. This implied that the strong force becomes weak at high energy, a phenomenon referred to as “asymptotic freedom” in quantum field theory [41, 42]. The only class of renormalizable asymptotically free quantum field theories are non-abelian gauge theories [43, 44, 45, 46, 47]. All that was needed was to determine the gauge group. The  $SU(3)$  color symmetry, originally an *ad hoc* introduction, was the natural choice and color was understood to be the gauge quantum number of the theory, thus forming QCD [48, 49, 50].

Calculationally, asymptotic freedom divides QCD into a perturbative high energy regime, where the strong coupling  $\alpha_s$  is small and the perturbation series converges, and a non-perturbative low energy regime, where perturbation theory breaks down and other methods must be used to make predictions. In the transition region, an impractically large number of terms in the perturbation series is needed for a meaningful prediction, so in general approximation methods are used. The next few sections describe how QCD makes predictions for  $t\bar{t}$  production in each of these regimes.

### 2.1.2 Hadron structure

Since quarks are confined inside hadrons, studying the fundamental properties of QCD in the high energy regime (including  $t\bar{t}$  production) necessitates high energy collisions of

composite hadrons. Understanding the details of the structure of hadrons is vital for making predictions about the hard-scatter of partons. At present, a description of the distribution of quarks and gluons within hadrons cannot be calculated. This may one day be possible using lattice QCD methods [51, 52].

The current best method of describing the structure inside hadrons involved in high energy collisions is through the use of the factorization theorem [53], where a hard collision involving a parton in a hadron is calculated via a convolution of the expression for the hard scatter with a function describing the probability that the parton carries a momentum fraction  $x$  of the total hadron momentum. These functions are called parton distribution functions (PDFs) and are usually written as  $f_i(x, Q^2)$ , where  $i$  denotes the flavor of the parton and  $Q^2$  is the invariant momentum transfer of the hard process, that is, the scale (energy/distance) at which the hadron is being probed.

PDFs are empirically determined using global fits to data from several experiments [54, 55, 56]. Experimental datasets are chosen based on their ability to constrain PDFs and involve a range of physical processes sensitive to different components. The evolution of the PDFs with energy scale is slow and described by the Dokshitzer-Gribov-Lipatov-Altarelli-Parisi (DGLAP) equations [57, 58, 59]. Thus, the fit can involve experiments probing different energy scales, and PDFs measured at energies below those which the LHC probes can be evolved to LHC energies. The DGLAP equations, together with the Balitsky-Fadin-Kuraev-Lipatov (BFKL) equation [60, 61] which describes the low  $x$  behavior ( $x < 10^{-4}$ ), form the basis of the current understanding of hadron structure in high energy collisions.

Figure 2.3 shows the proton PDF at two different scales as evaluated by Martin, Stirling, Thorne, and Watt (MSTW) [56]. Though protons are often thought of as bound states of two up quarks and a down quark ( $uud$ ), the proton PDF contains contributions from other quarks, anti-quarks, and gluons. The down and two up quarks of the proton are usually called “valence quarks” because they determine its quantum numbers and, as shown in Figure 2.3, make up the largest contribution to the proton PDF at high  $x$ .

Hadron structure can influence the hard collision in other ways. Hard collisions of partons in a hadron by definition involve a large momentum transfer and, to first approximation, these partons can be treated as free particles. However, they are still color connected to the

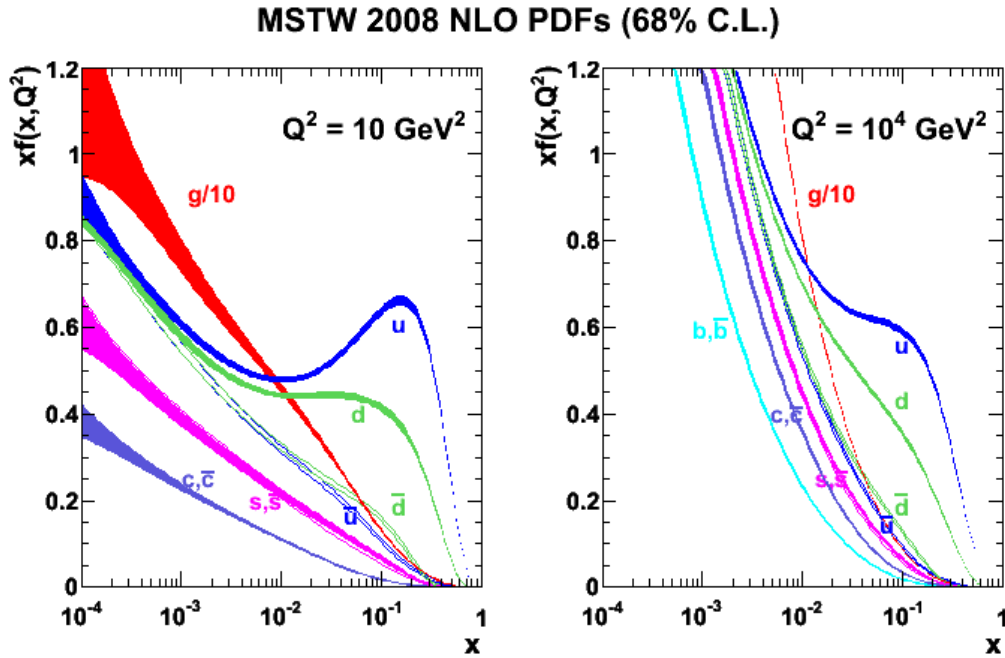


Figure 2.3: PDFs and their uncertainties for two energy scales, fitted by MSTW.

proton remnants from the collision which can influence the hadronization process. In addition, the remnants from one proton can undergo additional interactions with the remnants from the other. These are called multiple parton interactions and should be distinguished from pile-up interactions, which are separate proton-proton collisions. The effects of the proton remnants and multiple parton interactions on the final state are referred to as the “underlying event”, and these effects should be accounted for in QCD predictions [62].

### 2.1.3 $t\bar{t}$ production

Due to the high mass of the top quark,  $t\bar{t}$  production inevitably involves large momentum transfer and, therefore, can be described by perturbative methods. Using the factorization theorem, the cross-section for  $t\bar{t}$  production at the LHC can be computed by [62, 63]:

$$\begin{aligned} \sigma_{t\bar{t}+X} &= \sum_{a,b} \int_0^1 dx_a \int_0^1 dx_b \int d\Omega f_a(x_a, \mu_F) f_b(x_b, \mu_F) \\ &\times \frac{1}{2x_a x_b s} |\mathcal{M}_{ab \rightarrow t\bar{t}+X}(\Omega; \mu_F, \mu_R)|^2, \end{aligned} \quad (2.1)$$

where the possible initial state partons  $a$  and  $b$  are summed over and their PDFs are convolved with the matrix element (ME) of the hard sub-process  $ab \rightarrow t\bar{t} + X$ , where  $s$  is the center-of-mass energy squared of the colliding protons, and the phase space  $\Omega$  of the outgoing particles is integrated over. The MEs  $\mathcal{M}(\Omega; \mu_F, \mu_R)$  must be evaluated for the process of interest, in this case the production of a  $t\bar{t}$  pair inclusive of additional partons in the final state. There are several methods for doing this depending on the number of final state partons and the formal accuracy desired. These will be briefly discussed in Section 2.3. Textbook methods for their calculation involve a sum over all Feynman diagrams up to a given order in perturbation theory.

In addition to the phase space of the outgoing particles, the calculation of the MEs also depends on the choice of factorization scale  $\mu_F$  (i.e. the scale at which the PDFs are evaluated) and renormalization scale  $\mu_R$ . Since loop diagrams contributing to this process contain propagators whose momenta must be integrated to infinity, their calculation leads to logarithmic divergences called “ultraviolet divergences.” At high enough energies, new physics processes may eventually take over that could alter these integrals or cancel their divergences. Even in the absence of knowledge of the physics in this regime, QCD can still make predictions using the theorem of renormalization. This theorem states that the short time/high energy effects of these loops can be absorbed into the parameters of the theory such as the coupling constant,  $\alpha_s$  in QCD. In the modified minimal subtraction renormalization scheme (or  $\overline{\text{MS}}$ ) [64, 65, 66], this is accomplished by introducing an ultraviolet cut-off in the integral called the renormalization scale,  $\mu_R$ . The effects of not integrating above this scale are included by using a “running coupling,”  $\alpha_s(\mu_R)$ . The running coupling is evaluated using a differential equation called the renormalization group equation, which is also evaluated in a perturbation series of terms of increasing order in  $\log(\mu_R^2/M^2)$ , where  $M$  is a choice of boundary condition. At leading order, the solution to the renormalization group equation is:

$$\alpha_s(\mu_R) \approx \frac{\alpha_s(M)}{1 + (\beta_0/\pi)\alpha_s(M)\log(\mu_R^2/M^2)}, \quad (2.2)$$

where  $\beta_0 = (11 - 2N_f)/12 < 0$  if the number of quark flavors  $N_f = 6$ . The parameter  $\alpha_s(M)$  is not known and must be determined by experiment.

In principle, the cross-section should not depend on the choice of renormalization scale. However, since calculations are always made at some finite order of perturbation theory, calculations of the cross section do depend on this choice. One can see from Equation 2.2 that  $\alpha_s(\mu_R)$  decreases with increasing  $\mu_R$ , leading to the property of asymptotic freedom. This practically limits the choice of  $\mu_R$  used in Equation 2.1. If it is chosen to be too small, higher order terms in the perturbation series used to calculate the MEs in Equation 2.1 become increasingly important and the series may not converge. However, if it's chosen too large, the perturbation series solution to the renormalization group equation will not converge. In practice, the choice  $\mu_R^2 = \mu_F^2 = Q^2$  is often chosen, and varied to determine theoretical uncertainties associated with the scale dependence [8].

#### 2.1.4 The parton shower approximation

In addition to the ultraviolet divergences discussed above, infrared (IR) divergences are also present in QCD predictions. These logarithmic divergences occur for soft or collinear radiation of initial and final state partons. Radiated quarks or gluons can themselves radiate or pair-produce additional soft (low energy/transverse momentum) and collinear quarks and gluons, and so on. The result is a collinear stream of quarks and gluons called a parton shower (PS). In Equation 2.1, IR divergences are handled one of several ways, depending on the formal accuracy desired for the ME calculation (see Section 2.3). One way to handle them is to apply phase space cuts so that scales below a cut-off are not integrated over.

Before describing the parton shower approximation used in QCD calculations, the physical meaning of the divergences in the soft and collinear regime should be understood. Final state quarks and gluons ultimately hadronize into stable particles. Additional emissions from a given parton with momentum transfer below some scale do not change the final state configuration, and further emissions are said to be unresolvable. An analogous situation occurs in quantum electrodynamics [67]. Therefore, a cut-off above this scale which

renders calculations finite is physically meaningful. In addition, virtual corrections to the real emission cancel the divergences in this regime [62], though the explicit calculation is often not needed since unitarity arguments can be used to determine the probability of no emissions above the resolvable scale.

Because of IR divergences, large logarithmic terms at all orders in the perturbation series are present in soft and collinear regions of phase space. Fixed order calculations would involve very large uncertainties due to terms which were left out. The parton shower approximation attempts to include the effects of the large logarithmic terms at all orders in perturbation theory while ignoring less important effects. This is accomplished through the use of parton shower algorithms, which are Markov Chain processes that make use of the so-called Sudakov form factors [68, 69, 70]  $\Delta_i(T, t) = \rho$ , where  $i$  is the  $i^{\text{th}}$  parton,  $T$  and  $t$  are variables proportional to the relative angle of the emitted parton with respect to the emitter (such as the angle itself  $\theta$ , the virtuality  $q$ , or the transverse momentum  $p_T$ ), and  $\rho$  gives the probability that no emissions between  $T$  and  $t$  will occur for the  $i^{\text{th}}$  parton. The Sudakov form factors are determined from approximations to the perturbative solution. Their explicit form involves a variable  $z$  which is loosely the momentum fraction carried away by the emitted parton with respect to the emitter, and some variable corresponding to  $t$ . The  $\Delta_i$  suggest an iterative approach starting at a hardness value  $T$  corresponding to the hard interaction scale  $Q^2$  and evolving downward to some hardness  $t_0$ , below which emissions are considered unresolvable (usually this is some factor above the hadronization scale of order 1 GeV). At each stage in the evolution, a random number  $\rho$  is selected and the equation  $\Delta_i(T, t) = \rho$  is solved for  $t$ . If  $t$  is above  $t_0$ , an emission with hardness  $t$  is added to the final state and iteration continues, with  $T \rightarrow t$  for the next iteration. Once  $t$  falls below  $t_0$ , iteration stops and the hadronization process begins.

The results of the parton shower approach are illustrated in Figure 2.2. The figure splits the collision process into several regimes including one for the hard sub-process and one for the parton shower. After the hard sub-process, the parton shower algorithm iteratively adds quarks and gluons to the final state until hadronization begins. Since additional partons can be added to the event at both the hard sub-process stage and at the parton shower stage, care must be taken to avoid double counting of event phase space. This is accomplished by

ME/PS matching algorithms and will be discussed in some detail in Section 2.3. Though Figure 2.2 does not show initial state radiation, the parton shower approach is used to describe it as well, though for practical reasons the evolution downward in the hardness scale proceeds backward in time starting from the hard interaction.

One of the main differences between different parton shower algorithms is the choice of variable  $t$ . In this thesis, two main algorithms are used. The  $t = \theta$  (i.e. “angular ordered”) shower has the advantage of easily accounting for color coherence effects in soft emissions [69], but has the disadvantage of complicating ME/PS matching. In order to implement color coherence, the  $t = p_T$  (i.e. “ $p_T$  ordered”) shower must formulate the shower as a successive emission of color dipoles by pairs of emitters [71]. This is somewhat more complicated than the angular ordered shower, but is often easier to match with the matrix element calculation.

### 2.1.5 Hadronization

After the parton shower, the non-physical colored quarks and gluons hadronize into physical color singlet mesons and baryons. Since this cannot yet be calculated from first principles, it is accomplished using one of two main classes of models informed by QCD: string methods and cluster methods.

String models [72] transform systems of partons directly into hadrons using the principle of linear confinement. In this model, as a quark  $q$  and anti-quark  $\bar{q}$  move apart, their potential, often thought of as a QCD “string” connecting the  $q$  and  $\bar{q}$ , increases linearly with distance until it becomes energetically favorable to produce a new  $q'\bar{q}'$  pair, breaking the string and forming two new color singlets,  $q\bar{q}'$  and  $q'\bar{q}$ . Di-quark–anti-di-quark systems can also be produced at the endpoints of strings in order to form color singlet baryons. Additionally, gluons are included in color singlet  $q\bar{q}g$  systems as energy-momentum “kinks” in a string with  $q$  and  $\bar{q}$  endpoints, or as closed  $ggg$  strings. If the new string systems (e.g.  $q\bar{q}'$ ) have enough invariant mass, they too can move apart until their strings independently break, forming new color singlets. This string fragmentation process continues until only low invariant mass mesons and baryons are left.

Cluster models [73] are based on preconfinement of quarks and gluons produced by

the parton shower algorithm into color singlet clusters of partons with a mass distribution depending only on the parton shower cut-off scale  $t_0$ . Clusters are formed from color-connected quarks after splitting gluons into  $q\bar{q}$  or di-quark–anti-di-quark pairs. Most clusters hadronize by pseudo-two-body decays into mesons and baryons depending mostly on masses and spins of the decay products and initial cluster. Occasionally, clusters in the high tail of the mass distribution need special treatment, similar to procedures used in string models.

The effects of these hadronization models tend to preserve the overall structure of the partonic event after parton showering, with the final state having some number of collimated streams of hadrons instead of partons. This is also what is observed in hadron collisions in the data. Though string models tend to perform slightly better than cluster models, cluster models typically have fewer parameters which need to be measured from the data. It should be noted that cluster models, when paired with angular ordered parton shower algorithms, do describe the data well [62].

Regardless of the hadronization model used, final state hadrons that are unstable on collider time-scales as well as tau-leptons must decay to stable particles. This is accomplished using sophisticated decay algorithms [74, 75] which include most modes which are likely to occur at an appreciable rate and take into account spin, mass smearing, and even CP violating effects. Decay rates are based on a combination of experimental measurements and theoretical predictions.

## 2.2 Jet physics

The final state of QCD events in hadron collisions includes collimated streams of outgoing hadrons called jets. Since jets are not fundamental objects, a precise definition is needed which must satisfy certain theoretical requirements in order to allow for consistent, well-defined predictions [1]. The most important theoretical necessity is the idea of infrared and collinear safety. An observable is infrared and collinear safe if its predictions are independent of additional soft or collinear QCD radiation. Ideally, it should also be well suited for experimental measurements. The precise collinear and infrared safe definition of a jet is the subject of this section. Jet definitions are algorithms that decide which particles belong to

which jet as well as how to compute the four-momentum of the jet. In this thesis, the four-momentum of the jet is always computed by adding the four-momenta of its constituent particles. This is called the four-momentum recombination scheme.

Broadly speaking, there are two main classes of jet definitions: cone and sequential recombination algorithms. Cone algorithms have often been used at hadron colliders mainly because they are fast, easy to implement, and they reflect an intuitive notion of a jet (observed deposition energies in calorimeters of collider detectors tend to be conical). The first cone algorithms [76] began with seed particles around which a cone was defined and all particles in the cone were added to the jet four-momentum. Many algorithms would iterate from there by recalculating the center of the jet based on kinematic properties of the particles and then forming a new cone around the center [77]. This process repeats until a stable cone is formed. Cone algorithms also have to deal with overlapping jets and do this a number of ways [78, 79, 80]. Seeded cone algorithms are not collinear safe because they usually use the hardest particle(s) as seeds. If a seed particle were to have undergone an additional resolvable collinear splitting, a different seed may have been chosen potentially leading to a different configuration of jets. This is illustrated in Figure 2.4. Soft radiation can also lead to problems with infrared safety when dealing with overlapping jets. For example, split-merge procedures [78] can cause two jets close together to merge if one of the jets radiates a soft parton or particle in between them. Recently, a cone algorithm (the Seedless Infrared Safe or SIScone algorithm) has been developed which is both infrared/collinear safe and is practical to use [81].

Sequential recombination algorithms [82, 83, 84] start with  $N$  particles and classify them as “pseudo-jets.” Based on a particular prescription, the algorithm combines the pair pseudo-jet  $i$  and pseudo-jet  $j$  which has the smallest “distance”  $d_{ij}$  by adding their four-momenta, leaving  $N - 1$  pseudo-jets. The definition of the distance depends on the sequential recombination algorithm used. This iteration continues until the algorithm terminates depending on certain specified parameters. The anti- $k_T$  sequential recombination algorithm [85] is used to classify jets in this thesis. This definition uses a distance defined as

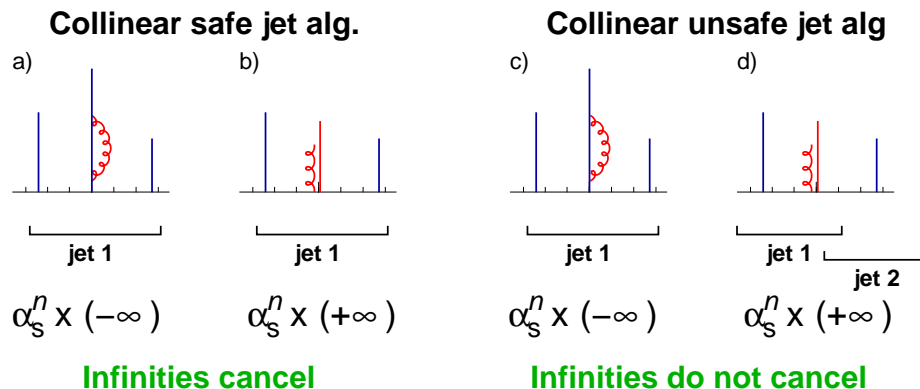


Figure 2.4: Illustration of collinear safety (left) and collinear unsafety in a cone type algorithm (right) together with its implication for perturbative calculations. Partons are vertical lines, their height is proportional to their transverse momentum, and the horizontal axis indicates rapidity. Figure taken from Ref. [1].

$$d_{ij} = \min(k_{T,i}^n, k_{T,j}^n) \frac{\Delta R_{ij}^2}{R^2}, \quad (2.3)$$

where  $k_{T,i}$  is the transverse momentum of pseudo-jet  $i$ ,  $R$  is a parameter roughly corresponding to the allowed radius of the jets, and  $\Delta R_{ij}$  is the distance in rapidity-azimuth ( $y$ - $\phi$ ) space between pseudo jet  $i$  and  $j$  defined by:

$$\Delta R_{ij}^2 = (y_i - y_j)^2 + (\phi_i - \phi_j)^2. \quad (2.4)$$

For the anti- $k_T$  algorithm, the exponent  $n = -2$ . Some other sequential recombination algorithms exist which differ only in their values for  $n$  (See 2.5).

The algorithm also defines a “beam-jet” distance by:

$$d_{iB} = k_{T,i}^n. \quad (2.5)$$

If the smallest distance at any stage in the iteration is a  $d_{ij}$ , pseudo-jets  $i$  and  $j$  are combined into a new pseudo-jet before iteration continues. If the smallest distance is a  $d_{iB}$ , pseudo-jet  $i$  is removed and called a jet before the next iteration. The algorithm continues until no pseudo-jets are left.

The anti- $k_T$  jet clustering algorithm is infrared and collinear safe [85]. A hard collinear splitting will be clustered first due to the  $\Delta R_{ij}^2$  factor in Equation 2.3, recovering the hard pseudo-jet before the split. It is also infrared safe because it naturally handles overlapping jets. If a soft pseudo-jet resides between two harder pseudo-jets (due to soft radiation, for example), the hardest of the two pseudo-jets will absorb the soft one between them, which doesn't change the two jet configuration into one, as can happen in split-merge procedures for cone algorithms. In addition to being infrared and collinear safe, anti- $k_T$  jets also have very stable areas allowing for easier understanding of their calibration in experimental measurements. Figure 2.5 illustrates the final jet configuration for a sample partonic event showered using HERWIG for several different jet definitions including the anti- $k_T$  algorithm.

### 2.3 Monte Carlo event generators

Due to the complexity of a typical  $t\bar{t}$  interaction and the necessity of using a parton shower to describe additional radiation, the best way to make predictions of jet production in association with  $t\bar{t}$  events is to use Monte Carlo event generators [62, 63]. These programs attempt to simulate typical high energy collision events, such as proton-proton collisions at the LHC. Often they are built around a particular process such as  $pp \rightarrow t\bar{t} + X$ . The basic procedure implemented in event generators starts with calculating a probability for a hard sub-process with a particular phase space configuration (particle 1 with momentum  $p_1$ , particle 2 with momentum  $p_2$ , etc.) to occur based on an acceptance-rejection method. The first step is to sample the phase space in order to determine  $d\sigma_{t\bar{t}+X}^{\max}$ , that is, the most probable phase space configuration. From there, random numbers are drawn to determine a new phase space configuration and its cross-section  $d\sigma$  is calculated. Then the quantity  $d\sigma/d\sigma_{\max}$  is compared to a random number  $R \in [0, 1]$ . If  $d\sigma/d\sigma_{\max} > R$ , the event is kept and if not, the event is rejected. This procedure generates events with uniform weights with the same kinematic distributions as predicted at finite order by perturbative QCD.

Due to practical limitations, the ME calculation can only calculate  $2 \rightarrow N$  hard sub-processes, where  $N$  is typically less than 7 for a leading order calculation. After the hard sub-process for a particular event is accepted, a parton shower algorithm is used to prob-

abolistically add initial and final state radiation to the event and then hadronize the final state partons, as described above. Several Monte Carlo event generators are used in this thesis to predict the  $t\bar{t}$  jet multiplicity. These generators differ in many respects such as the order in perturbation theory in which they calculate the ME, the parton shower algorithm used, the way in which they handle overlapping final state configurations which can occur after showering an  $N$  hard parton final state into an  $N + 1$  hard parton final state, and the hadronization and decay algorithms used. The most important generators used in this analysis will be described below. Event generators are also used as part of the background estimation and in order to derive corrections for the reconstruction-level jet multiplicity to the particle-level. These details will be discussed in Chapter 6.

After simulating the hard sub-process, a suitable parton shower algorithm is used for initial and final state radiation. A few general purpose generators exist which both calculate matrix elements and shower the resulting final states. Examples of this type of generator are PYTHIA [86], HERWIG [87], and SHERPA [88]. Several other specialized generators perform only the ME calculation and must be interfaced to one of these generators for the parton showering. Though PYTHIA and HERWIG are not used for ME calculations in this analysis, their parton shower and hadronization algorithms are interfaced to most of the specialized hard sub-process generators. PYTHIA uses a  $p_T$  ordered shower with string model hadronization. HERWIG uses an angular ordered shower with cluster hadronization. PYTHIA simulates the effects of the underlying event as well whereas for generators showered with HERWIG, JIMMY [89] is used for the underlying event. Both PYTHIA and HERWIG/JIMMY are tuned to available data [90, 91, 92].

**Leading Order  $2 \rightarrow 2$  Generators** – ACERMC [93] is the only generator used in this analysis to calculate a leading order  $2 \rightarrow 2$  matrix element, mainly due to its fast, efficient generation of unweighted events. This facilitates generating and simulating several samples with different parameters governing additional radiation, the underlying event, and color reconnection, all within their theoretical uncertainties with the purpose of the studying their effects on the unfolding corrections (see Chapter 6). ACERMC is interfaced with the PYTHIA generator for the parton shower, which merges with the ME calculation by reweighting events such that the first emitted parton is corrected to a  $2 \rightarrow 3$  leading order

ME calculation. However, the ACERMC+PYTHIA predictions for additional jets beyond the first emission must come from hard wide-angle emissions in the parton shower, which are not expected to be accurate.

**Next-to-leading Order Generators** – In order to reduce the effects of theoretical uncertainties on certain quantities such as the final state ME kinematics, several generators provide ME calculations to next-to-leading order (NLO) accuracy, and in doing so they must overcome a number of obstacles. NLO  $t\bar{t}$  production calculations include 1 extra vertex on any of the three diagrams in Figure 2.1. This vertex can lead to a real emission, or a virtual loop. The real, virtual, and “Born” diagrams (i.e. no emission at all) must be summed coherently where appropriate.

The first obstacle that NLO generators must overcome is that the soft and collinear divergences in the ME calculations must be formally handled if the calculation is to retain its NLO accuracy. Both NLO generators considered in this thesis handle these divergences in a similar way. As mentioned in Section 2.1.4, the divergences in the real and virtual parts of the calculation cancel. In an NLO ME calculation, the real and virtual parts involve different phase space integrations due to the extra parton in the real emission part. This poses a problem in, for example, acceptance-rejection integration where a probability is calculated for a particular phase space at a time (either with or without an additional emission). In the NLO event generators used in this thesis, the subtraction method [94] handles this problem by introducing counter terms which are factorized as the Born term convolved with a universal splitting kernel which encodes the divergent structure of the real and virtual terms. One can analytically subtract the counter term from the real term and add it to the virtual term, rendering both calculations finite.

The second obstacle is that the resulting hard scatter events are not straight-forwardly interfaced with PS generators due to overlapping regions in phase space, since a  $t\bar{t} + 1$  hard parton event can arise by both a  $pp \rightarrow t\bar{t} + 1$  hard parton ME and by a  $pp \rightarrow t\bar{t} + 0$  partons ME with a hard wide angle emission from the parton shower. These overlapping regions are removed by so-called matching algorithms. In this analysis, two NLO generators are considered: MC@NLO [95, 96] and POWHEG [97]. Each has essentially the same ME calculation procedure, but they differ in their matching procedures.

The MC@NLO method removes overlapping phase space configurations by modifying the counter terms used to regularize integration of the Born and real emission phase spaces. As a result of this modification, the integration is not guaranteed to be positive, leading to negative weighted events in the acceptance-rejection method (though in the limit of large MC statistics, the contributions to all bins in all distributions are positive). In this analysis, MC@NLO uses CT10 PDFs [55] and is interfaced with the HERWIG generator for the parton shower.

The POWHEG method avoids overlapping regions of phase space by generating the hardest parton first in the ME calculation. The event can then be fed to a parton shower generator which must only add partons to the event which are softer than the first emission from the hard sub-process. This is known as the CKKW(-L) matching algorithm [98, 99, 100]. POWHEG can be interfaced to either HERWIG or PYTHIA. In the  $p_T$ -ordered showers of PYTHIA, the hardest emission is guaranteed to come from the ME as long as the shower starts with  $t = p_T$ , where  $p_T$  is the transverse momentum of the emission from the POWHEG ME. For the angular-ordered showers of HERWIG, the first emission in the shower is often not the hardest. Therefore, the shower must veto emissions that are harder than the POWHEG emission, starting from some  $t = \theta_{\max}$  down to  $t = \theta_1$ , where  $\theta_1$  is the angle of the POWHEG ME emission. The algorithm then replaces the shower emission with the emission from the ME and then continues the shower down to the cutoff  $\theta_0$  where hadronization begins. In this analysis, the POWHEG generator uses CTEQ6.6 [54] for the PDF.

**Tree-level multi-leg generators** – The NLO generators discussed above correct the Born level kinematics to NLO accuracy. Additionally, the first emission is calculated in the matrix element to LO accuracy. However, all subsequent hard wide angle emissions rely on generation from the parton shower, which is only expected to be accurate in the soft and collinear regime. Leading order multi-leg generators generate  $pp \rightarrow t\bar{t} + N$  hard parton events to leading order accuracy, with up to  $N = 5$  additional hard partons in the final state. With more than 1 additional hard parton in the final state, merging a parton shower generator with the ME calculation becomes more challenging. Two multi-leg generators are used in this analysis: ALPGEN [101] and SHERPA [88]. The biggest difference between the algorithms is the ME/PS merging algorithm used.

ALPGEN calculates matrix elements for  $t\bar{t}$  production at the LHC with up to 5 additional hard partons and uses the so-called MLM matching scheme [102] to avoid double-counting of final states. In this matching scheme, an additional energy scale  $p_{T,\min}^{\text{ME}} \sim 10$  GeV is introduced. An exclusive final state ( $t\bar{t} + N_p$ , where  $N_p$  is the number of additional partons) is chosen and the matrix element is calculated for a generated phase space (at fixed  $\alpha_s$  and later corrected to account for the running coupling). All additional partons in the matrix element calculation are required to have  $p_T > p_{T,\min}^{\text{ME}}$ . The resulting hard sub-process is showered and the final state partons are clustered with a cone-based jet clustering algorithm (see Section 2.2). All jets with  $p_T > p_{T,\min}^{\text{jet}}$  (usually with  $p_{T,\min}^{\text{jet}} > p_{T,\min}^{\text{ME}}$ ) are counted and matched to the partons from the ME calculation based on their distance in  $y - \phi$  space, where  $y$  is the rapidity of a parton/jet and  $\phi$  its azimuthal angle. If all jets are matched to a parton and  $N_{\text{jets}} = N_p$ , the event is accepted. For the maximum value  $N_p = 5$ ,  $N_{\text{jets}}$  is allowed to be greater than  $N_p$ .

SHERPA produces  $t\bar{t}$  final states with up to 4 additional partons and, like POWHEG, uses the CKKW(-L) matching algorithm. In the multi-leg matrix element case, the matching algorithm is somewhat more complicated. As with MLM, the ME is calculated for a  $t\bar{t} + N_p$  hard sub-process, also requiring a cut-off scale  $p_{T,\min}^{\text{ME}}$ . An additional correction to the matrix element is applied using Sudakov form factors, which give the probability that a given parton will not produce an emission harder than  $p_{T,\min}^{\text{ME}}$  in order to make the state exclusive. From there the event can be showered, vetoing on emissions harder than the cut-off. Due to additional necessary modifications in the parton shower algorithm, SHERPA also performs the showering (a di-pole based,  $p_T$  ordered shower).

SHERPA is somewhat more elegant in that it only introduces one additional parameter (the cut-off scale  $p_{T,\min}^{\text{ME}}$ ) whereas ALPGEN requires additional parameters related to the jet definition. ALPGEN has been around longer and therefore has been tested more extensively and found to perform well in previous measurements [23]. Because of this, ALPGEN interfaced with HERWIG for the parton shower and using CTEQ6L1 PDFs is the nominal generator used to study detector effects and systematic uncertainties on di-lepton  $t\bar{t}$  events in this analysis. ALPGEN interfaced with PYTHIA and using CTEQ5L PDFs is also used in this analysis. In this configuration,  $\alpha_s$  can effectively be varied up or down (with care

taken to be consistent in both the ME and PS calculations [103]) in order to determine the effects of additional initial and final state radiation on the jet multiplicity predictions. SHERPA uses CT10 PDFs.

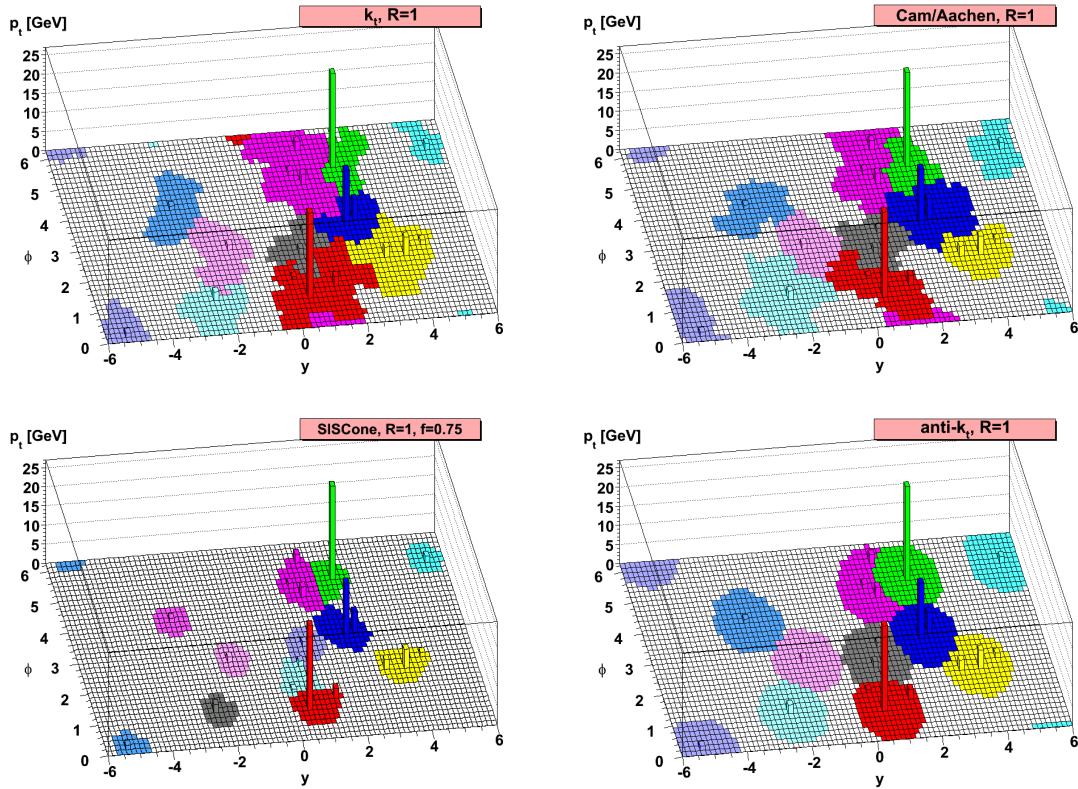


Figure 2.5: A sample parton-level event (generated with HERWIG, an MC generator using an angular ordered PS algorithm), together with additional random soft radiation, clustered with four different jets algorithms, illustrating the areas of the resulting hard jets. The top left configuration was clustered using the  $k_T$  algorithm (with  $n = 2$  in Equation 2.3). The top right uses the Cambridge-Aachen algorithm ( $n = 0$ ). The bottom left uses the seedless infrared safe cone algorithm (SISCone). The anti- $k_T$  algorithm shown in the bottom right clusters jets into ideal conical structures with equal active areas in all non-overlapping jets. Figure taken from Ref. [1]

## Chapter 3

# Description of the experiment

Top quarks decay rapidly and, due to their high mass, must be produced in high energy collisions. The 27 km Large Hadron Collider (LHC) collides two proton beams at TeV energies with the purpose of studying many properties of the fundamental constituents of the universe, and is used to produce top quarks for this analysis.

Several detectors are used to study the proton-proton ( $pp$ ) collisions provided by the LHC. Two general purpose detectors including the Compact Muon Solenoid (CMS) [104] and **A Toroidal LHC ApparatuS** (ATLAS, see Section 3.2) were built to study a broad range of physics processes (both SM and beyond), including processes involving top quarks. There is also the LHCb detector [105] designed to study the decays of  $B$  hadrons produced in  $pp$  collisions and the (ALICE) [106] detector used for studying lead ion collisions. Additionally, two other detectors (TOTEM [107], LHCf [108]) were built to study forward scattering in  $pp$  collisions.

The LHC is briefly discussed in Section 3.1. For this analysis, the ATLAS detector was used for measuring the remnants of  $t\bar{t}$  decays and the jets produced in  $t\bar{t}$  events. The ATLAS detector is discussed in some detail in Section 3.2.

### 3.1 The Large Hadron Collider

The LHC [109] is a proton-proton synchrotron accelerator and collider located at CERN near Geneva, Switzerland. It was designed with several physics goals in mind, most notably

for the search for the SM Higgs boson. It also presents an unprecedented opportunity to study the properties of top quarks. Though the LHC is the highest energy collider in the world, the fact that it collides two protons makes its luminosity reach particularly valuable for the study of processes expected to have low production cross-sections (in this case, di-leptonic  $t\bar{t}$  events with high jet multiplicities). This is in contrast to proton–anti-proton colliders such as the Fermilab Tevatron Collider, which are luminosity-limited by the expensive and time consuming process of producing anti-protons [110]. The time-integrated luminosity<sup>1</sup> is an important quantity which, along with the cross-section, determines the total number of collisions. A convenient choice of unit for cross-sections in particle physics is the “barn” (b), where  $1 \text{ b} = 10^{-28} \text{ m}^2$  (approximately equal to the cross-sectional area of the uranium nucleus). Integrated luminosity is usually measured in units of inverse area, so that a cross-section multiplied by the integrated luminosity gives the expected total number of collisions. With its high luminosity and its TeV collision energies pushing the production cross-section for  $t\bar{t}$  events above 100 pb, the LHC is the world’s first “top factory” and is ideal for this analysis, expected to produce on average roughly one  $t\bar{t}$  pair per second. Though designed for center-of-mass collisions at  $\sqrt{s} = 14 \text{ TeV}$  with a peak luminosity of  $10^{34} \text{ cm}^{-2}\text{s}^{-1}$ , the LHC collided proton beams at  $\sqrt{s} = 7 \text{ TeV}$  throughout the data-taking period used for this analysis (March–October in 2011) with a peak luminosity of  $3.65 \times 10^{33} \text{ cm}^{-2}\text{s}^{-1}$ , with bunches of approximately  $10^{11}$  protons spaced by 50 ns.

A schematic of the LHC injection chain is shown in Figure 3.1. All accelerators in the chain use radio frequency (RF) systems to accelerate protons, with bunches of protons sitting in “buckets” at the halfway point between the peak and the trough of the RF electric field. Bunches are accelerated to a given energy before being transferred to the next accelerator in the chain. The injection chain begins with the Linac2, where large bunches of protons approximately 120  $\mu\text{s}$  long are produced with energies of approximately 50 MeV per proton before being injected into the Proton Synchrotron Booster (PSB), where each bunch is split into four identical rings, boosted to 1.4 GeV, and recombined. Bunches then enter the Proton Synchrotron (PS), which can hold 6 buckets injected from the PSB, plus

---

<sup>1</sup>Both the “time-integrated luminosity” and the “instantaneous luminosity” (or luminosity per unit time) are often called just “luminosity.”

a 7th empty bucket. Bunches can then be split into three, changing the RF harmonic from 7 to 21. Note that the exact numbers of bunches depend on the luminosity configuration of a given LHC fill. The beam is accelerated to 25 GeV before splitting once more into two, to now up to 72 bunches on harmonic 84 with a gap of 12 buckets. Bunches are injected into the Super Proton Synchrotron (SPS) by switching on “fast kicker” dipole magnets while the gap crosses the transfer tunnel. Up to four batches of 72 proton bunches can be injected into the SPS at a time. The SPS accelerates the bunches to 450 GeV and injects into the LHC. The process is repeated several times until the LHC is filled to the desired number of bunches per beam.

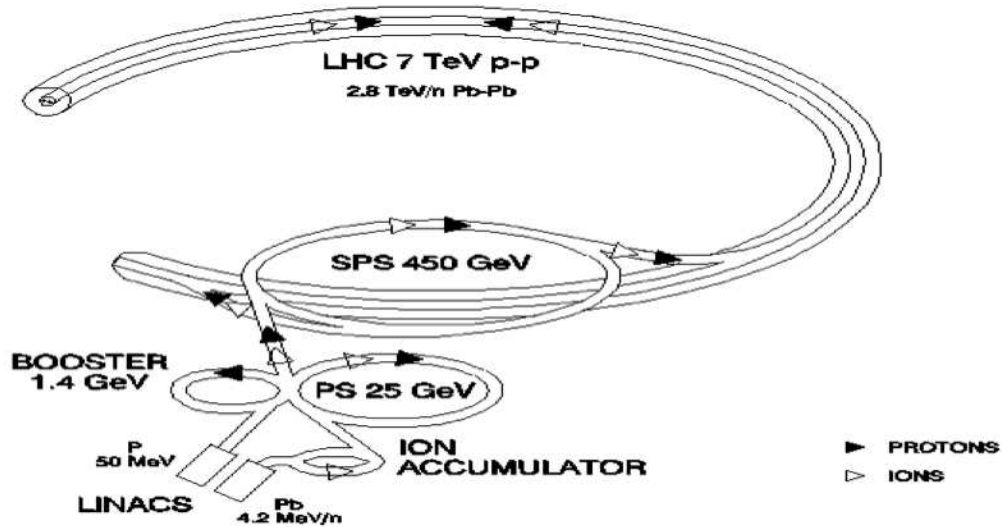


Figure 3.1: Schematic of the injection complex servicing the LHC.

Since the LHC is a  $pp$  collider with two positively charged beams circulating in opposite directions, each beam requires separate magnetic fields and vacuum pipes. The LHC ring is divided into 8 sectors as shown in Figure 3.2, with 8 arcs where the beams are bent and 8 straight sections serving as experimental or utility insertion regions (IR). The beams cross at the insertion regions in sectors 1 and 5 (IR1 and IR5) for the ATLAS and CMS detectors, and at IR2 and IR8 for the ALICE and LHCb detectors. IR2 and IR8 also include the injection systems for Beam 1 and Beam 2. After injection into the LHC rings, the 450 GeV

protons were accelerated to 3.5 TeV during the 2011 run using the 40 MHz RF systems in IR4. IR3 and IR7 are used for beam cleaning, where collimators deflect particles with a large momentum offset and scatter particles with large betatron amplitudes. Sector 6 is used for dumping the beams in case of instrumentation problems, emergencies, or at the end of a fill using fast kicker magnets. The ensuing field forces the beam into an iron septum magnet which deflects the beam vertically away from machine components in order to prevent their damage.

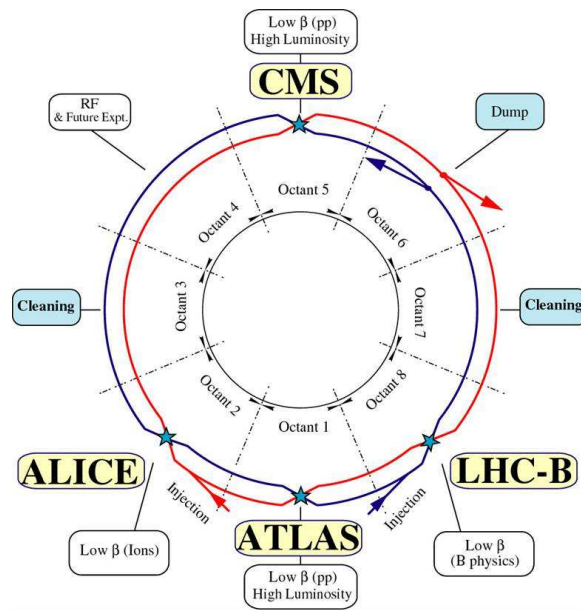


Figure 3.2: Schematic of each experimental and utility insertion region of the LHC.

To generate the large magnetic fields (4.2 T at 3.5 TeV) necessary for bending, focusing, and correcting the LHC beams, superconducting NbTi cables are cooled to below 2 K using superfluid helium. The magnet system consists of over 1200 twin-bore dipoles used to bend the LHC beams in each of the 8 arcs. Additionally, over 3500 multi-pole magnets are placed throughout the LHC rings and are used to focus and stabilize the beams. After ramping the beams to 3.5 TeV, the beams are “squeezed” by the focusing magnets in order to reduce the emittance (the spread in the transverse direction) before final focus magnets at IR1 steer the beams to collide at the interaction point.

Once the beams are colliding at full energy and no further need to be made, the beams

are declared “stable” and physics data taking starts. The instantaneous luminosity decreases over time throughout a run, mostly due to collisions increasing the beam emittance. After typically 10-15 hours, the beams are dumped and the LHC refilled.

## 3.2 The ATLAS experiment

The ATLAS experiment [111, 112] provides physicists with the opportunity to study high energy collisions at the LHC. This section discusses the components of the ATLAS detector, the ATLAS trigger system, and details of the dataset collected.

The detector is positioned about 100 m underground at point 1 on the LHC ring. Like most general purpose collider detectors, it is composed of three coaxial cylindrical sub-detectors built around the beam axis, each designed to measure and identify particles exiting the collision point. The inner detector, used for measuring the momenta of charged particles, is positioned closest to the beam pipe and is surrounded by a solenoidal magnet. Following the inner detector are electromagnetic and hadronic calorimeters used for measuring the energies of photons, electrons, and hadrons. Last, a muon system is used for identifying and tracking muons which traverse the calorimeters.

The coordinate system used in this section and in the rest of this thesis is a right-handed coordinate system with the origin at the geometric center of the detector (i.e. the interaction point), the  $x$ -axis pointing toward the center of the LHC ring and the  $y$ -axis pointing vertically upwards. Therefore, the  $z$ -axis points along the beam direction with the azimuthal angle  $\phi$  (polar angle  $\theta$ ) measured around (with respect to) the beam axis. Transverse energies and momenta are defined in the  $x$ - $y$  plane. The pseudorapidity  $\eta$  defined as  $\eta \equiv -\ln[\tan(\theta/2)]$  depends only on the polar angle and is equal to the traditional definition of rapidity in the massless limit. The  $z > 0$  ( $z < 0$ ) side of the ATLAS detector is often called the A (C) side.

A schematic of the ATLAS detector is shown in Figure 3.3. As a whole, the detector has a diameter of about 25 m, is about 44 m long, and weighs about 7000 metric tons. Each of its sub-detectors are discussed below. Several additional sub-systems were used to measure the integrated and instantaneous luminosity of the dataset and these systems will also be

described here.

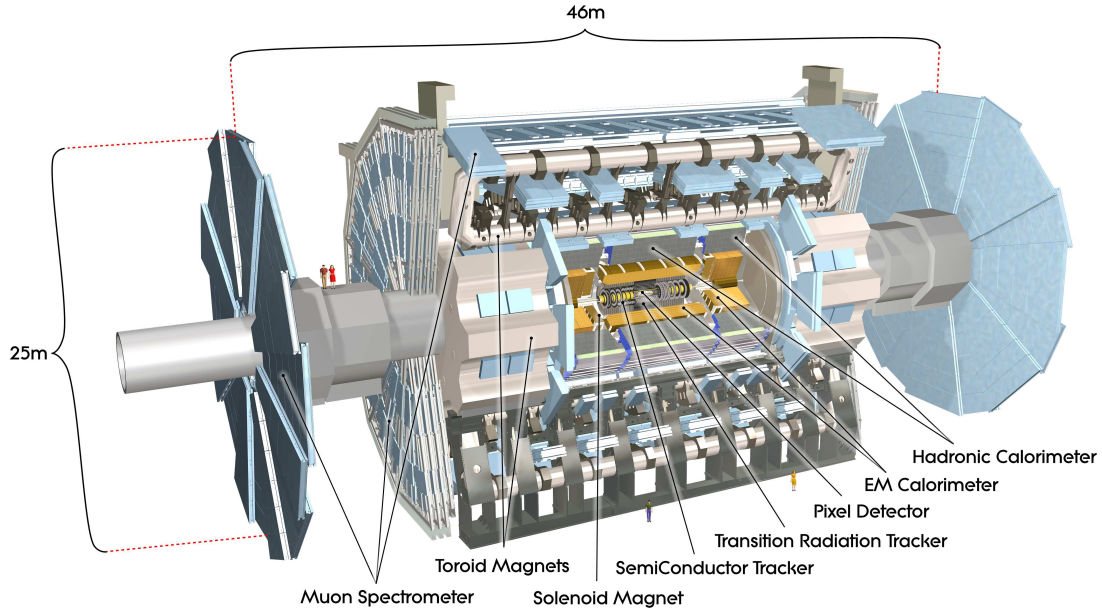


Figure 3.3: Cut-away view of the ATLAS detector.

### 3.2.1 The Inner Detector

The Inner Detector (ID) is divided into three components: the Pixel Detector made of silicon pixel sensors, the Semi-Conductor Tracker (SCT) of essentially the same technology as the Pixel Detector but with silicon strips of different granularity, and the straw tube Transition Radiation Tracker (TRT). The ID is encased in a solenoid which provides a 2 T magnetic field used to bend the trajectories of charged particles as they traverse the detector. The radius of curvature can be used to determine the transverse momentum of the charged particle and the bending direction to identify its charge.

The Pixel Detector consists of three barrel layers arranged in concentric cylinders around the beam axis, and three end-cap layers arranged in disks perpendicular to the beam axis. Each layer contains several segmented modules with 250  $\mu\text{m}$  thick wafers of silicon of size 16.4 mm by 60.8 mm. A detailed schematic of the position of each layer relative to the

beam spot is shown in Figure 3.4. Each module has 46080 readout pixels bump-bonded to the silicon sensor, with most pixels sized  $50 \mu\text{m}$  in  $\phi$  by  $400 \mu\text{m}$  in  $z$ . There are 1744 modules with a total of about 80.4 million channels. Charged particles passing through the silicon in a pixel module create electron-hole pairs which, due to a high voltage applied across the module, collect at its surface registering a hit in the readout electronics. To reduce hits coming from noise, the signal is compared to a threshold and the time over threshold (TOT) is read out by the front end chips. One charged particle can register a hit in multiple neighboring pixels, which are clustered together and treated as a single hit.

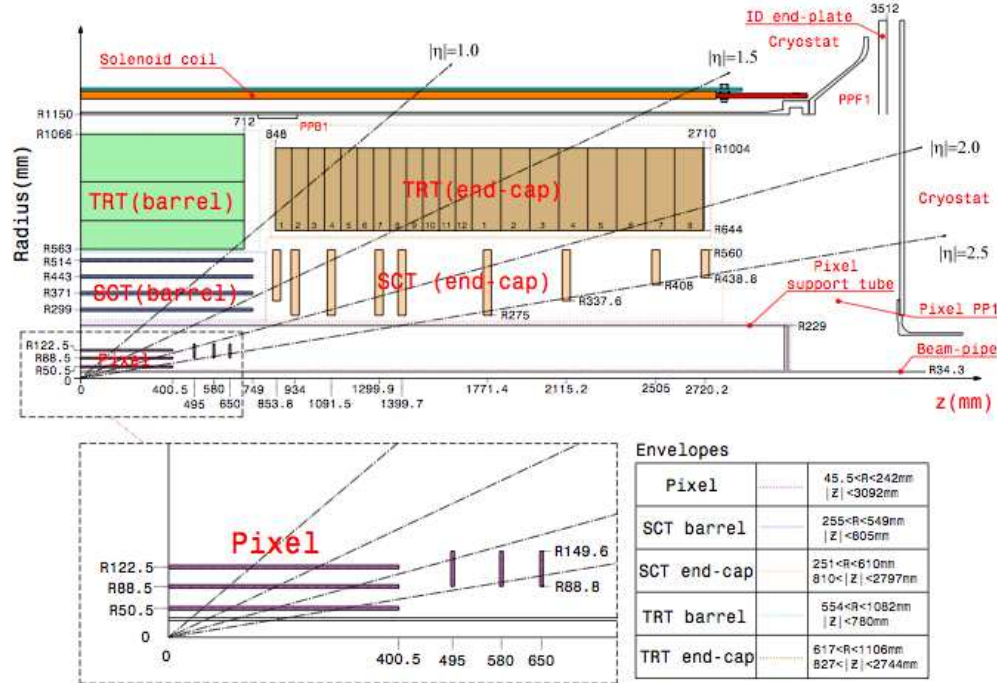


Figure 3.4: Detailed schematic showing positions of the various components of the Inner Detector relative to the origin.

The SCT works essentially the same way as the pixel detector, but with sensors read out by larger micro-strips of size  $80 \mu\text{m}$  by about 12 cm long, thus reducing the number of readout channels. Each module consists of two daisy chained silicon sensors which are slightly thicker than the pixel sensors ( $285 \mu\text{m}$ ). There are four coaxial cylindrical barrel layers, and six disc end-cap layers. Each barrel layer as well as the 1st, 3rd, and 6th end-

cap layers include two sets of strips, one on top of the other with a small angle (40 mrad) between them in order to measure both the  $\phi$  and  $z$  ( $r$ ) coordinates in the SCT barrel (end-cap). The intrinsic accuracy of these configurations along with all sections of the ID is given in Table 3.1. In total there are 6.3 million readout channels in the 15912 modules of the SCT. The precision trackers (both the Pixel Detector and the SCT) each cover the pseudorapidity range  $0 < |\eta| < 2.5$ .

The TRT provides the largest number of hits per track in the ID (typically 36). It is composed of polyimide tubes of diameter 4 mm arranged parallel to the beam axis in the barrel and in perpendicular discs with the tubes along the radial direction for each of the end-caps. Within each cathode tube is a 31  $\mu\text{m}$  thick gold-plated tungsten anode wire. The tubes are filled with a mix of xenon and carbon-dioxide gas. Charged particles passing through the tubes ionize the gas and the freed electrons are collected by the anode wire. Measurement of the drift time improves the  $\phi$  resolution, however, this detector makes no measurement along the  $z$ -axis. Transition radiation emitted when a relativistic charged particle crosses an interface between two media with different dielectric properties in the TRT is used to discriminate between pions and electrons (since electrons have a lower mass and therefore a higher Lorentz factor at the same energy as pions), and is the purpose of using xenon in the gas mixture. The TRT provides coverage in the range  $0 < |\eta| < 2.0$ .

Details of the layout of the various components of the ID are shown in Figure 3.4. In total, the ID is about 7 m long and extends out to a radius of about 1.1 m. The spacial coverage and resolution of each component are summarized in Table 3.1. Details of the performance of the Inner Detector can be found in Ref. [113].

The Inner Detector was used for several purposes in this analysis. First, vertex reconstruction is used to select good collision candidates and reject cosmic background. Track identification and quality are used in both electron and muon definitions. Transition radiation from electrons traversing the TRT is an important part of electron identification in the ATLAS experiment. Finally, jets from pile-up events are rejected by selecting on the jet vertex fraction ( $p_{\text{T}}$ -weighted fraction of tracks in a jet which point to the primary vertex). The details of each of these requirements are discussed in Chapter 4. Vertexing and precision tracking is also vital component of identifying  $B$ -hadron decays in jets (called

Table 3.1: Intrinsic accuracy and coverage of each component of the Inner Detector.

Sub-detector	Coverage	Intrinsic Accuracy ( $\mu\text{m}$ )
Pixel Barrel	$0 <  \eta  < 2.5$	10 ( $R$ - $\phi$ ), 115 ( $z$ )
Pixel End-Cap	$2.0 <  \eta  < 2.5$	10 ( $R$ - $\phi$ ), 115 ( $R$ )
SCT Barrel	$0 <  \eta  < 1.5$	17 ( $R$ - $\phi$ ), 580 ( $z$ )
SCT End-Cap	$1.3 <  \eta  < 2.5$	17 ( $R$ - $\phi$ ), 580 ( $R$ )
TRT Barrel	$0 <  \eta  < 1.0$	130
TRT End-Cap	$0.8 <  \eta  < 2.0$	130

“ $b$ -tagging), however, this procedure was only minimally used in this analysis.

### 3.2.2 Calorimetry

The ATLAS sampling calorimeters cover the range  $|\eta| < 4.9$  and make use of two different technologies. The fine granularity of the electromagnetic (EM) Liquid Argon (LAr) calorimeter is used to identify and measure the energies of electrons and photons. The barrel of the ATLAS scintillating Hadronic Tile Calorimeter has coarser granularity sufficient for the reconstruction of jets of hadrons. The end caps of the hadronic calorimeter and the forward calorimeters use the same liquid argon technology as the EM calorimeter, however, in slightly different configurations. A schematic of the calorimeters is shown in Figure 3.5, while details of their granularity and coverages are shown in Table 3.2. Since the calorimeter is the main system used to measure jets, some detail about its design and performance will be discussed here.

The barrel of the EM calorimeter extends to  $|\eta| < 1.475$  and is composed of two identical halves joining at  $z = 0$  ( $|\eta| = 0$ ). The barrel contains lead absorber plates about 1-1.5 mm thick fixed to two 0.2 mm thick stainless steel sheets for structural support. The plates are arranged in an accordion geometry with small gaps (of about 2 mm) as shown in Figure 3.6. This accordion geometry provides full symmetry in  $\phi$  without any gaps in the absorption/detection material. Between each absorber plate are kapton readout electrodes layered with copper and held in place with honeycomb spacers. Liquid argon fills the space between the electrodes and absorber plates and is used as the active detection medium.

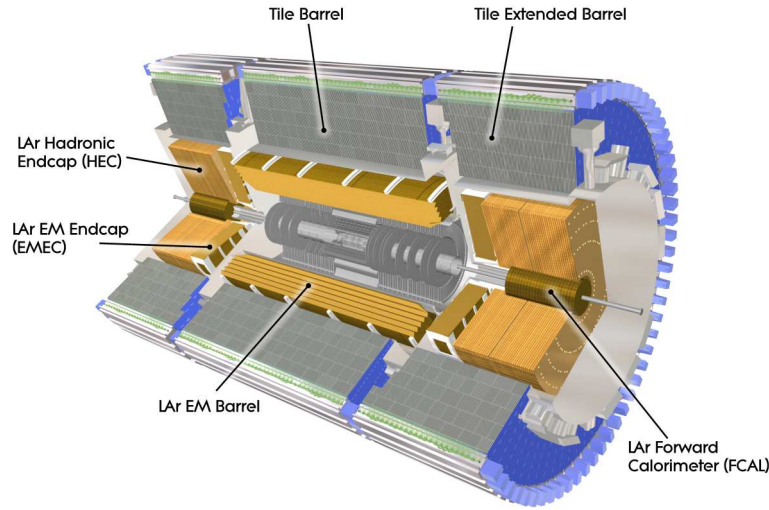


Figure 3.5: Cut-away view of the ATLAS calorimeters.

The barrel is split into 3 separate layers of varying depths, plus a presampler layer closest to the beam used to correct for energy lost upstream of calorimeter. The readout electrodes in each layer are etched into cells of varying granularity.

The EM end-cap covers the range  $1.375 < |\eta| < 3.2$  and uses the same absorber, detection, and readout materials which are also arranged in an accordion geometry.

Particles traversing the LAr calorimeters interact in the lead absorber plates, producing Bremsstrahlung radiation for charged electrons and pair production of electrons for photons. The secondary electrons and photons continue this process of radiation/pair production into an electromagnetic shower. The showering continues until the energy of the particle is completely absorbed. A high voltage is applied across the electrodes, so that electrons from the shower ionize the liquid argon and the resulting electrons and ions drift towards the electrodes, producing a pulse which is measured and shaped in the calorimeter front end electronics. The energy in each cell is determined by the size of the pulse. Hadronic showers are also induced in the LAr calorimeter by pions, kaons, protons, and neutrons, though they are usually wider than the electromagnetic showers induced by electrons and photons. The granularity and layering in the calorimeter aids in determining the shape of the shower, which is used to discriminate between hadrons and electrons or photons. This

Table 3.2: Main parameters of the calorimeter system.

	Barrel	End-cap
<b>EM calorimeter</b>		
Number of layers and $ \eta $ coverage		
Presampler	1 $ \eta  < 1.52$	1 $1.5 <  \eta  < 1.8$
Calorimeter	3 $ \eta  < 1.35$	2 $1.375 <  \eta  < 1.5$
	2 $1.35 <  \eta  < 1.475$	3 $1.5 <  \eta  < 2.5$
		2 $2.5 <  \eta  < 3.2$
Granularity $\Delta\eta \times \Delta\phi$ versus $ \eta $		
Presampler	$0.025 \times 0.1$ $ \eta  < 1.52$	$0.025 \times 0.1$ $1.5 <  \eta  < 1.8$
Calorimeter 1st layer	$0.025/8 \times 0.1$ $ \eta  < 1.40$	$0.050 \times 0.1$ $1.375 <  \eta  < 1.425$
	$0.025 \times 0.025$ $1.40 <  \eta  < 1.475$	$0.025 \times 0.1$ $1.425 <  \eta  < 1.5$
		$0.025/8 \times 0.1$ $1.5 <  \eta  < 1.8$
		$0.025/6 \times 0.1$ $1.8 <  \eta  < 2.0$
		$0.025/4 \times 0.1$ $2.0 <  \eta  < 2.4$
		$0.025 \times 0.1$ $2.4 <  \eta  < 2.5$
Calorimeter 2nd layer	$0.025 \times 0.025$ $ \eta  < 1.40$	$0.050 \times 0.025$ $1.375 <  \eta  < 1.42$
	$0.075 \times 0.025$ $1.40 <  \eta  < 1.475$	$0.025 \times 0.025$ $1.425 <  \eta  < 2.5$
Calorimeter 3rd layer	$0.050 \times 0.025$ $ \eta  < 1.35$	$0.1 \times 0.1$ $2.5 <  \eta  < 3.2$
		$0.050 \times 0.025$ $1.5 <  \eta  < 2.5$
Number of readout channels		
Presampler	7808	1536 (both sides)
Calorimeter	101760	62208 (both sides)
<b>LAr hadronic end-cap</b>		
$ \eta $ coverage		$1.5 <  \eta  < 3.2$
Number of layers		4
Granularity $\Delta\eta \times \Delta\phi$		$0.1 \times 0.1$ $1.5 <  \eta  < 2.5$
		$0.2 \times 0.2$ $2.5 <  \eta  < 3.2$
Readout channels		5632 (both sides)
<b>LAr forward calorimeter</b>		
$ \eta $ coverage		$3.1 <  \eta  < 4.9$
Number of layers		3
Granularity $\Delta x \times \Delta y$ (cm)		Fcal1: $3.0 \times 2.6$ $3.15 <  \eta  < 4.30$
		Fcal1: $\sim$ four times finer $3.10 <  \eta  < 3.15$
		$4.30 <  \eta  < 4.83$
		Fcal2: $3.3 \times 4.2$ $3.24 <  \eta  < 4.50$
		Fcal2: $\sim$ four times finer $3.20 <  \eta  < 3.24$
		$4.50 <  \eta  < 4.81$
Readout channels		Fcal3: $5.4 \times 4.7$ $3.32 <  \eta  < 4.60$
		Fcal3: $\sim$ four times finer $3.29 <  \eta  < 3.32$
		$4.60 <  \eta  < 4.75$
		3524 (both sides)
<b>Scintillating tile calorimeter</b>		
	Barrel	Extended barrel
$ \eta $ coverage	$ \eta  < 1.0$	$0.8 <  \eta  < 1.7$
Number of layers	3	3
Granularity $\Delta\eta \times \Delta\phi$	$0.1 \times 0.1$	$0.1 \times 0.1$
	Last layer $0.2 \times 0.1$	$0.2 \times 0.1$
Readout channels	5670	4092 (both sides)



which produce scintillation photons in the tiles. Fibers placed along the edges of the scintillating tiles guide the photons into photomultiplier tubes (PMTs) and the size of the signal can be used to determine the energy in a cell. The tile calorimeter is supported by a steel girder, which also provides a return yoke for the magnetic field of the central solenoid.

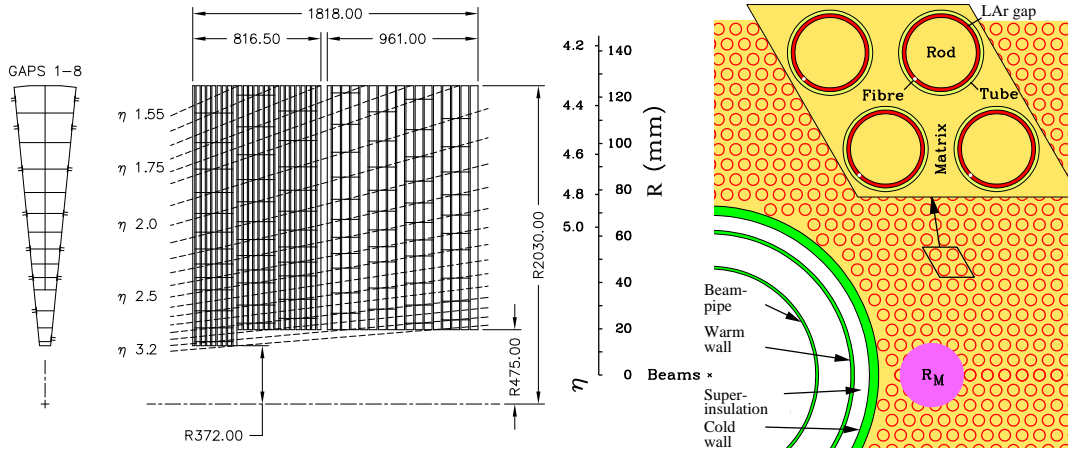


Figure 3.7: Geometry of the HEC and FCal systems. The solid circle labeled  $R_M$  indicates the size of a cylinder containing on average 90% of the energy of an electromagnetic shower.

The two wheels of the Hadronic End-Cap Calorimeters (HEC) also use liquid argon as the detection medium, with 25 mm (50 mm) plates of copper for the absorption material in the first (second) wheel, and with 8.5 mm liquid argon-filled spaces between them. The HEC wheels are housed in the same cryostats as the EM end-cap calorimeters. The plates are arranged perpendicularly to the beam axis and particle detection works in essentially the same way as in the EM calorimeters. The HEC system covers a range  $1.5 < |\eta| < 3.2$ . Housed in the same cryostat are the Forward Calorimeters (FCal), covering  $3.1 < |\eta| < 4.9$ . The FCal contains three wheels, one for EM and two for hadronic calorimetry. The first wheel is made of copper plates stacked one behind the other with small holes drilled into them. Copper rods wrapped in fiber are inserted in the holes and the gap (of about 0.3 mm) between the rod and the hole is filled with liquid argon. This smaller gap prevents build-up of ions and provides the highest possible absorption density necessary to cope with the high particle flux in this region. The two hadronic FCal wheels use tungsten rods instead of copper to reduce the absorption length and reduce the lateral spread of showers. The

geometries of both the HEC and the FCal are shown in Figure 3.7. A schematic of the end-cap configuration can be seen in Figure 3.8.

Each of the three cryostats (one containing the EM calorimeter barrel and two on each end containing the EMEC, HEC, and FCal systems) consist of two concentric cylindrical aluminum vessels, one warm and one cold, with the space between them under vacuum. The central solenoid is supported by the inner cylinder of the warm vessel of the barrel cryostat. Several signal feed-throughs are located at the outer ends of the cryostats. High voltage feed-throughs are located at the highest points of the edges of the cryostats. A schematic of one of the end-cap cryostats is shown in Figure 3.8.

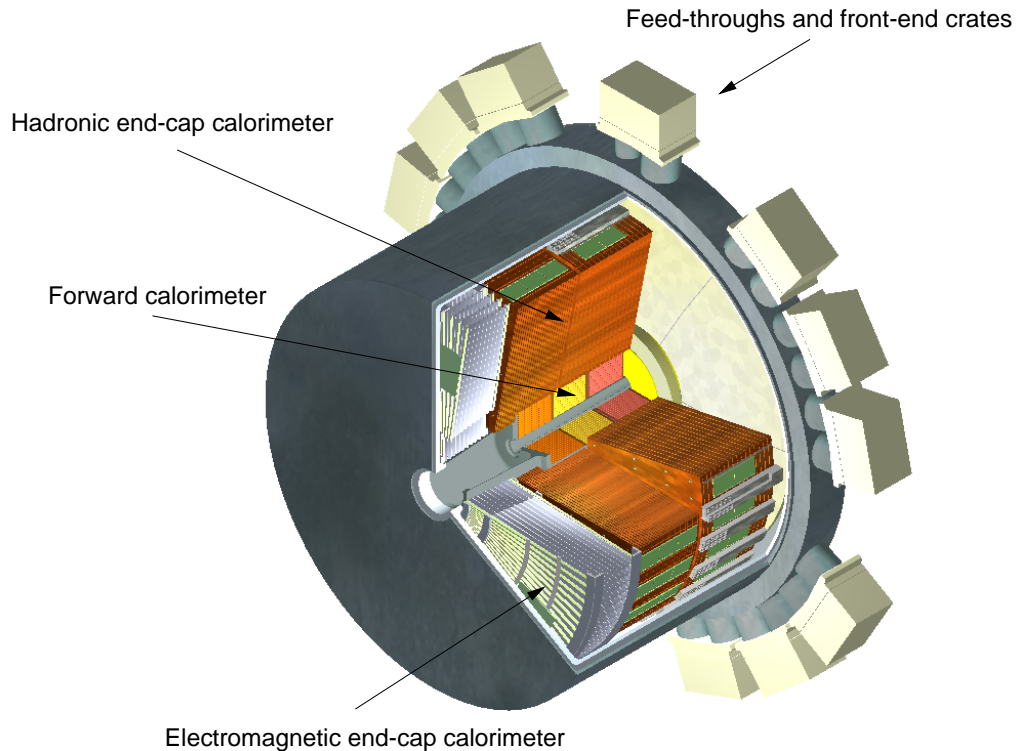


Figure 3.8: Schematic of one of the end-cap cryostats.

Front-end crates positioned on the cryostat provide the first stage of the signal processing for the LAr calorimeters. Two separate readout paths are routed in the front-end crates, one for the Level 1 trigger decision described in Section 3.2.5, and a full, high precision path for the high-level trigger and offline analysis. The analog signals for each cell for triggered

events are processed and digitized in the radiation hard front-end electronics and then sent to the back-end electronics located off-detector for further processing. Additionally, the front-end boards can inject precisely known signals into the calorimeter readout for calibration purposes.

The raw output for a typical energy deposition in a cell of the LAr calorimetry is shown in Figure 3.9. The triangular signal is first amplified with three gain scales, then shaped in order to remove the long tail from the detector response which spans  $\sim 20$  bunch crossings, and reduce electronic and pile-up noise. The shaped signals are then sampled at the LHC bunch crossing frequency of 40 MHz, and for events accepted by the L1 trigger, the sampled signal (usually 5 samples) with the optimal readout gain is transmitted to the back-end electronics using optical links.

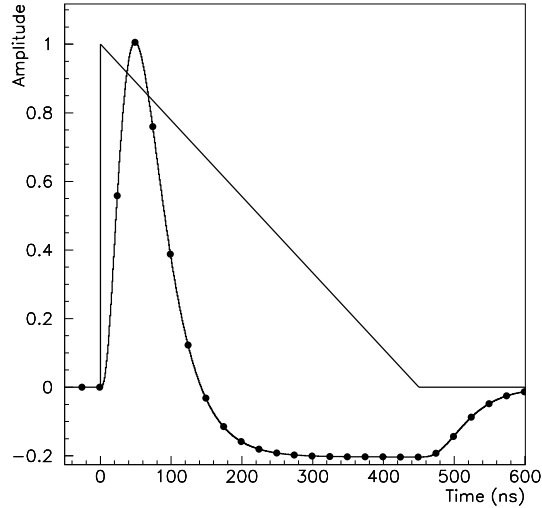


Figure 3.9: Triangular shape of a typical raw pulse in a cell of the LAr calorimeters, and the shaped output of the LAr FEBs. The points on the shaped output are at the 40 MHz sampling frequency. The total readout time for a cell is about 450 ns and about 125 ns for the first 5 samples. The timing resolution using the optimal filtering method is about 1 ns.

The back-end electronics are located in a cavern away from the detector where there are no radiation issues. The digital signals transmitted from the front-end crates are processed using digital signal processor (DSP) chips using an optimal filtering method [114] which

calculates the energy (in GeV), the time (in ns), and a simplified  $\chi^2$ . The energy is given by the following equation:

$$E = \sum_{i=1}^n a_i(s_i - ped), \quad (3.1)$$

where  $n$  is the number of samples,  $a_i$  are the optimal filtering coefficients (OFCs),  $ped$  are the pedestals, and  $s_i$  are the sample amplitudes for a given channel. The energy, time, and  $\chi^2$  are then formatted and sent to the Data Acquisition system. Cell energies here are calibrated to the electromagnetic scale. Cells associated with electrons need only minimal corrections, while cells associated with jets need to be corrected to the hadronic scale. These corrections will be discussed in detail in Chapter 4.

The tile calorimeter electronics begin with the PMT blocks located in drawers on the steel girder support system. Photons from fibers feeding a PMT block first pass through a light mixer, then a PMT, then a voltage divider, and finally a 3-in-1 card. The light mixer ensures uniform illumination of the photomultiplier, which measures the scintillation light. The signal is amplified before entering the 3-in-1 card which shapes the signal in a unipolar form to a pulse width of 50 ns before sampling by a digitizer. The 3-in-1 card also sums the analog signals for the L1 trigger decision. If an event passes the L1 trigger, the digital signal is sent to the back-end electronics. A charge injection system into the 3-in-1 card is used for calibration purposes, along with Cesium sources in the tiles and lasers into the light mixers in order to calibrate at several stages of the signal processing.

The back-end systems for the tile calorimeter also apply the optimal filtering method to determine the energies deposited in their cells. As with the LAr calorimeter, the energy measurement is calibrated to the EM scale, and further corrections are needed to fully calibrate jets to the hadronic scale.

The calorimeter system is used extensively in this analysis. Signals from the calorimeter are used in several stages of the trigger decision. Additionally, electron reconstruction begins in the EM calorimeters and jet reconstruction uses the EM, Tile, and HEC calorimeters. Finally, all systems including the FCal are used for the measurement of missing transverse energy associated with neutrinos in  $t\bar{t}$  events. All of these aspects will be discussed in later sections.

### 3.2.3 The Muon System

The ATLAS Muon System (MS) provides tracking for muons exiting the ATLAS calorimeter systems. In this analysis, the Muon System is used to trigger on and reconstruct muons in di-lepton  $t\bar{t}$  and  $Z$ +jets events.

Due to their larger masses (compared to electrons) and the fact that they don't interact via the strong force, high energy muons traverse the calorimeter with minimal energy loss. The muon system bends and tracks the trajectories of muons to precisely measure their momenta. A schematic of the muon system is shown in Figure 3.10. Three systems of toroidal magnets (one in the barrel and two in the end-cap) generate magnetic fields which are mostly perpendicular to the muon trajectories. Muons are tracked using four different technologies. Monitored Drift Tube (MDT) chambers provide precision tracking throughout most of the detector except in the first layer of the end-cap region, where Cathode Strip Chambers (CSC) do the tracking to cope with the large particle flux. Additionally, Resistive Plate Chambers (RPC) in the barrel and Thin Gap Chambers (TGC) in the end-cap provide fast tracking for the L1 trigger system and make measurements along a direction perpendicular to the precision trackers to measure the coordinate in the non-bending plane. The main parameters of each of the tracking technologies in the Muon System are summarized in Table 3.3. The magnet system, and each of the tracking technologies will be discussed in this section.

There are 8 large toroidal magnets in the barrel region around the calorimeter which generate a magnetic field in the range  $|\eta| < 1.4$  and 8 smaller magnets at each end-cap for the range  $1.6 < |\eta| < 2.7$ . In the transition region  $1.4 < |\eta| < 1.6$ , a combination of the barrel and end-cap toroids is used to generate the fields. About 1800 Hall sensors are positioned throughout the muon system to measure small perturbations in the field due to the tile calorimeter girder and other metallic structures in order to accurately determine the bending power.

The most important tracking system for reconstructing muons consists of the MDT chambers, the basic element of which is a pressurized drift tube filled with Ar/CO<sub>2</sub> gas. The tubes are arranged along the  $\phi$  direction and measure the  $\eta$  coordinate, since the magnetic field bends the muon trajectory in the  $R$ - $z$  plane. This configuration allows the

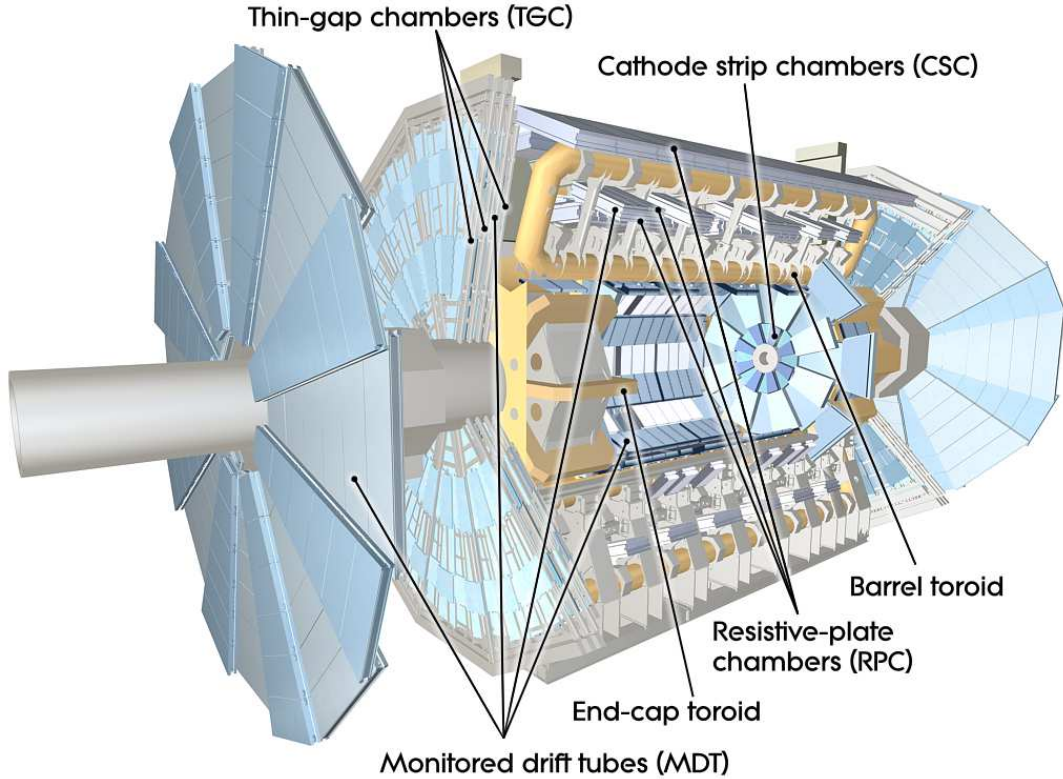


Figure 3.10: Schematic of the Muon System showing the magnet system and each of the four tracking technologies used for both precision tracking and the trigger decision.

tubes to accurately measure the bending sagitta for the best possible momentum resolution. The  $\phi$  coordinate is measured using the RPCs so long as there is only one track in a single MDT-RPC chamber region. Studies have shown a low probability of events with two high  $p_T$  muons in the same MDT-RPC chamber region. However, in the case of such events, the correct coordinates can be determined by matching to tracks from the ID. There are three layers of rectangular chambers of drift tubes in the barrel, and three layers of trapezoidal chambers in the end-caps. The MDT chambers extend out to  $|\eta| < 2.7$  with the exception of the first layer in the end-caps which extends out to  $|\eta| < 2.0$ . Muons traversing the detector ionize the gas in the tubes and electrons are collected on the central high voltage W-Re wire. The drift time (a maximum of about 700 ns) is used to measure the distance from the wire for increased spacial resolution.

Due to the high flux of particles in the forward region, exceeding the limit of safe

operation for the MDTs, the first layer of the end-cap in the region  $2 < |\eta| < 2.7$  uses CSCs for muon tracking. Each chamber contains 4 layers and each layer is composed of copper cathode strips on either side of a gold-plated W/Re anode wire, with one set of strips parallel to the wire and the other perpendicular, providing four independent position measurements in both  $\eta$  and  $\phi$ . Between the two sets of strips is Ar/CO<sub>2</sub> gas. The position of the track is interpolated between neighboring strips. In the event of two tracks in the same chamber, the pulse heights of the strips are compared in order to assign the correct coordinates to a given track.

The RPC and TGC systems provide fast tracking for the trigger decisions in the barrel and end-cap regions of the Muon System. As mentioned above, they also perform the  $\phi$  measurements for most of the muon system, with the MDT system performing the  $\eta$  measurement in the bending plane. Finally, the operating speed of these systems helps tag an event to a given bunch crossing. The RPC measures a range  $|\eta| < 1.05$  and consists of electrode plates spaced 2 mm apart filled with gas (a mixture of C<sub>2</sub>H<sub>2</sub>F<sub>4</sub>/Iso – C<sub>4</sub>H<sub>10</sub>/SF<sub>6</sub>). Electrons and ions resulting from ionized gas are readout on orthogonal strips on the outside of the plates providing an  $\eta$ - $\phi$  measurement. The RPC system contains three layers, two on either side of the middle layer of the MDT system and one on the back side of the last MDT layer. TGCs are made of electrode wires running along  $\phi$  between electrode strips running radially. The 2.8 mm gaps are filled with a mixture of CO<sub>2</sub> and n-C<sub>5</sub>H<sub>12</sub> gas which is ionized by charged particles traversing the detector.

Table 3.3: Main parameters of the tracking technologies used for tracking and triggering in the Muon System.

System	Function	Chamber resolution (RMS)			Measurements/track	
		$z/R$	$\phi$	time	barrel	end-cap
MDT	tracking	35 $\mu\text{m}$ ( $z$ )	-	-	20	20
CSC	tracking	40 $\mu\text{m}$ ( $R$ )	5 mm	7 ns	-	4
RPC	trigger	10 mm ( $z$ )	10 mm	1.5 ns	6	20
TGC	trigger	2-6 mm ( $z$ )	3-7 mm	4 ns	-	9

Precise knowledge of the spacial positions of the detection components of the Muon

System are necessary for determining the trajectories and hence the momentum of the tracks traversing the detector. This is accomplished using an optical alignment system. The muon system has a gap at the center of the detector ( $\eta = 0$ ) of at the largest  $|\eta| < 0.08$  necessary for running services to the ATLAS calorimeter systems. This gap, the optical alignment system, and the Muon System readout electronics are discussed in more detail in Ref. [111].

### 3.2.4 Luminosity systems

An accurate measurement of the luminosity [115] is crucial for absolute cross-section measurements as well as for evaluating backgrounds which must be estimated using simulation. The ATLAS experiment monitors the luminosity by measuring the rate of visible interactions per bunch crossing ( $\mu_{\text{vis}}$ ) with a variety of independent detectors in finite periods of time approximately two minutes long called luminosity blocks (“lumi-blocks”). The interaction rate gives the absolute instantaneous luminosity provided the total visible cross-section  $\sigma_{\text{vis}}$  is known. This cross-section is determined using dedicated beam separation scans called van der Meer scans [116], where the absolute luminosity can be inferred from direct measurements of the beam parameters and compared with the observed  $\mu_{\text{vis}}$  to determine the luminosity scale. Figure 3.11 gives the total integrated luminosity, delivered by the LHC and recorded by the ATLAS detector, throughout the 2011 data-taking period as measured by the ATLAS luminosity systems.

Two main luminosity detectors were used by the ATLAS experiment in 2011 to independently measure the instantaneous luminosity online (i.e. during data-taking). Since the same pairs of bunches always collide with each other throughout a given run (together called a bunch-pair), both detectors measure the instantaneous luminosity independently for each bunch-pair.

The first online luminosity detector is the Beam Conditions Monitor (BCM) [117], which consists of four small diamond sensors arranged in a cross pattern around the beam pipe approximately 2 m away from the center of the detector on both sides. Its main use is to trigger a beam dump in case of beam incidents which could potentially damage the detector, but it is also used to measure  $\mu_{\text{vis}}$  using an “event counting” algorithm, where the number

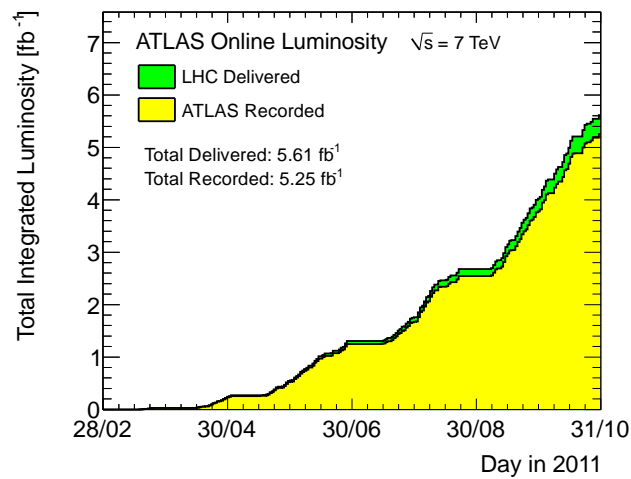


Figure 3.11: Cumulative luminosity versus day delivered to (green), and recorded by (yellow) ATLAS during stable beams and for pp collisions at 7 TeV center-of-mass energy in 2011. The delivered luminosity accounts for the luminosity delivered from the start of stable beams until the LHC requests ATLAS to turn the sensitive detector off to allow a beam dump or beam studies. Given is the luminosity as determined from counting rates measured by the luminosity detectors. These detectors have been calibrated with the use of the van der Meer beam-separation method.

of bunch-crossings passing a certain set of criteria  $N_c$  is counted and compared with the total number of bunch-crossings  $N_{BC}$ . Poisson statistical arguments can be used to relate  $\mu_{vis}$  to the ratio  $N_c/N_{BC}$ , provided the ratio is considerably less than one. The luminosity was increased throughout 2011 by both increases in the number of colliding bunches and in the number of protons per bunch. As the number of protons per bunch increases, the probability that a single bunch crossing can contain more than one  $pp$  interaction (called pile-up) increases. The peak number of interactions per bunch crossing was  $\sim 20$  during the 2011 data taking period. However, due to its low acceptance, even with  $\sim 20$  interactions per bunch-crossing, the ratio  $N_c/N_{BC}$  was always much less than 1 that event counting algorithms were viable throughout 2011.

The other online luminosity detector used in 2011, LUCID (LUMinosity measurement using a Čerenkov Integrating Detector) [118], consists of 16 aluminum tubes filled with  $C_4F_{10}$  gas on each side of the detector 17 m away from the interaction point. Čerenkov photons created by charged particles in the gas are reflected by the polished walls of the tubes until they reach PMTs located at the back of the tubes, separated by a quartz window (which also produces Čerenkov photons). If the number of photons reaching the PMT on a given tube is above a certain threshold, a hit is registered in the tube. The gas can be removed from the tubes so that photons only come from the quartz window, reducing the efficiency of the detector. This was done late in 2011 in order to keep  $N_c/N_{BC}$  low enough for LUCID to use event counting algorithms to estimate  $\mu_{vis}$ . “Hit counting” algorithms have also been used to check the linearity of response. Hit counting algorithms relate  $\mu_{vis}$  to the ratio  $N_{hit}/(N_{BC}N_{ch})$  where  $N_{hit}$  is the number of hits registered and  $N_{ch}$  is the number of channels in the detector.

Both the BCM and LUCID use fast, hardware-based computations of  $\mu_{vis}$  to measure the luminosity online. Several offline analyses have also been used to more precisely measure the luminosity in 2011 and assess its systematic uncertainties. The ID was used to reconstruct and count the number of vertices in randomly selected filled bunch crossings. Calorimeter-based algorithms are also used to measure  $\mu_{vis}$  based on variables sensitive to the particle flux in various regions of the calorimeter along with “particle counting” algorithms, which have an even more linear response than hit counting algorithms in high luminosity environments

(though they require more effort to control systematic uncertainties).

### 3.2.5 The ATLAS trigger system

Due to the amount of information contained in each event, the rate at which collision data can be recorded by the ATLAS data acquisition system is limited to around 200 Hz (that is, 200 events recorded each second on average). At design luminosity, collisions happen every 25 ns or at 40 MHz. The ATLAS trigger system [119] is used to quickly and efficiently filter events so that collisions due to potentially interesting physics processes are kept, while rejecting the majority of low  $p_T$  QCD multijet processes. The system is designed to trigger on events with signals consistent with high  $p_T$  leptons (i.e. electrons or muons), photons, jets, hadronically decaying tau leptons, or on events with large missing transverse energy or large scalar sums of transverse energy. The presence of one or more high  $p_T$  leptons are a good indication of an electro-weak process, such as the semi-leptonic decay of a top quark. Due to the ability to easily estimate the trigger efficiency on “standard candles” such as leptonic decays of  $Z$  bosons, lepton triggers were used in this analysis and are discussed in this section.

The triggering process is divided into three separate steps, together called a “trigger chain.” First, detector signals from each event are stored in front end pipelines where they await a decision from the Level 1 (L1) hardware based trigger system. The L1 hardware algorithms process signals from either calorimeter information for electrons, or from the RPC or TGC muon sub-systems for muons. For electrons, the L1 algorithm searches for trigger towers of size  $0.1 \times 0.1$  in  $\eta$ - $\phi$  in the EM calorimeter with a total deposited transverse energy larger than a predetermined threshold. If such a cluster is found, an L1 accept is issued and the event is transferred to the next step in the trigger chain. A “Region of Interest” (RoI) around the cluster position in the detector is identified. For muons, the L1 trigger algorithm searches for a coincidence between layers of the RPC and/or TGC systems that match a predefined curvature corresponding to a particular momentum threshold. An RoI for muons is also identified. The L1 system is designed to reduce the transfer rate from 40 MHz to  $\sim 75$  kHz.

The next two steps in the trigger chain involve the software-based Level 2 (L2) and

Event Filter (EF) trigger systems, and together comprise the “High-level Trigger” (HLT). In the event of an L1 accept, data from each sub-detector are temporarily stored fragmented in Readout Systems (ROS), where most of it awaits an L2 decision. The L2 system requests and processes the data only from the ROSes corresponding to the RoI identified in the L1 system. For events accepted by the L2 system, data from all Readout Systems are requested by the EF system which further processes the data with algorithms which are similar to the offline reconstruction algorithms to be discussed in Chapter 4. The L2 system was designed to reduce transfers to the EF to about 3 kHz. If the event is accepted by the EF, it will be transferred to the main ATLAS data processing center (Tier0). The Tier0 computing center does the initial offline reconstruction. Beyond that, most ATLAS computing is distributed across the Worldwide LHC Computing Grid [120] in order to cope with the roughly 15 petabytes of data produced annually. If the data are not accepted at any stage in the trigger chain, the data from the event are discarded.

For electrons, a fast clustering algorithm is implemented in the L2 algorithm in the calorimeter RoI(s) determined by the L1 system. The transverse energy deposited in the cluster is determined and compared with a predetermined threshold. Though the EF system has access to data from the entire detector, the electron EF algorithm considers only the RoIs identified by the L1 and L2 systems. The EF algorithm employed for electron clustering and identification is very similar to that used for offline reconstruction including the use of the electron identification algorithms discussed in Section 4.2, with a few exceptions in order to reduce processing time. A minimal amount of identification based on the cluster shape is also employed at L2.

For muons, the L2 system makes use of the precision MDT information around the RoI identified at L1. A fast fitting algorithm is used to reconstruct a stand alone track in the muon system, which is combined with tracks reconstructed in the ID using the L2 tracking algorithms and a  $p_T$  measurement is made and compared with a predetermined threshold. In the EF system, muons are reconstructed around the RoIs determined at L1 and L2 using the offline muon reconstruction software.

This analysis triggers on the presence of at least one high  $p_T$  lepton passing some minimum set of identification requirements. The trigger efficiency on both electrons and

muons is estimated using data from several signal processes such as  $W/Z$ +jets events [121, 122]. In order to avoid large uncertainties on efficiency estimates near selection thresholds, both the  $p_T$ -threshold ( $p_T > 25$  GeV) and the identification algorithms used offline are significantly tighter than those used in the HLT algorithms. Figure 3.12 shows the single lepton trigger efficiency estimated on data as a function of the offline reconstructed transverse momentum for both electrons and muons.

### 3.2.6 Data quality and detector simulation

Several online monitoring systems [123] are used throughout the data taking process to ensure accurate measurements of detector signals. Online data monitoring systems ensure that sub-detector systems are working nominally during data-taking and that no unexpected effects in detector signals (such as a spike in the occupancy of a particular cell of the calorimeter) are present. Further data-quality checks are made offline [124] and data quality “flags” are assigned to each lumi-block for each sub-detector and even for the reconstruction of specific physics objects (electrons, muons, jets, etc.). A green, yellow, or red flag is ultimately assigned for “good,” “questionable,” or “bad” data and only lumi-blocks with green flags for all detector sub-systems and all physics objects relevant to this analysis are used. Of the  $5.2\text{fb}^{-1}$  of data recorded by the ATLAS experiment,  $4.7\text{fb}^{-1}$  pass the data quality requirements of this analysis.

Even with good data quality, several detector effects will influence measurements of physics objects, such as a non-zero jet energy resolution or lepton identification inefficiency. These effects must be accounted for in order to accurately evaluate backgrounds which must be estimated from Monte Carlo event generation, to propagate systematic uncertainties to the jet multiplicity measurement, and to estimate the response of the detector on a given true jet multiplicity configuration in  $t\bar{t}$  MC to unfold detector effects in the data. To account for these effects, MC events are processed with an ATLAS detector simulation [125] implemented using the GEANT4 toolkit [126], which has been tuned and validated using data from test beams and cosmic rays [127, 128]. A small number of samples used only for some uncertainty estimates have been simulated with the ATLAS fast simulation program (ATLFASTII) [129].

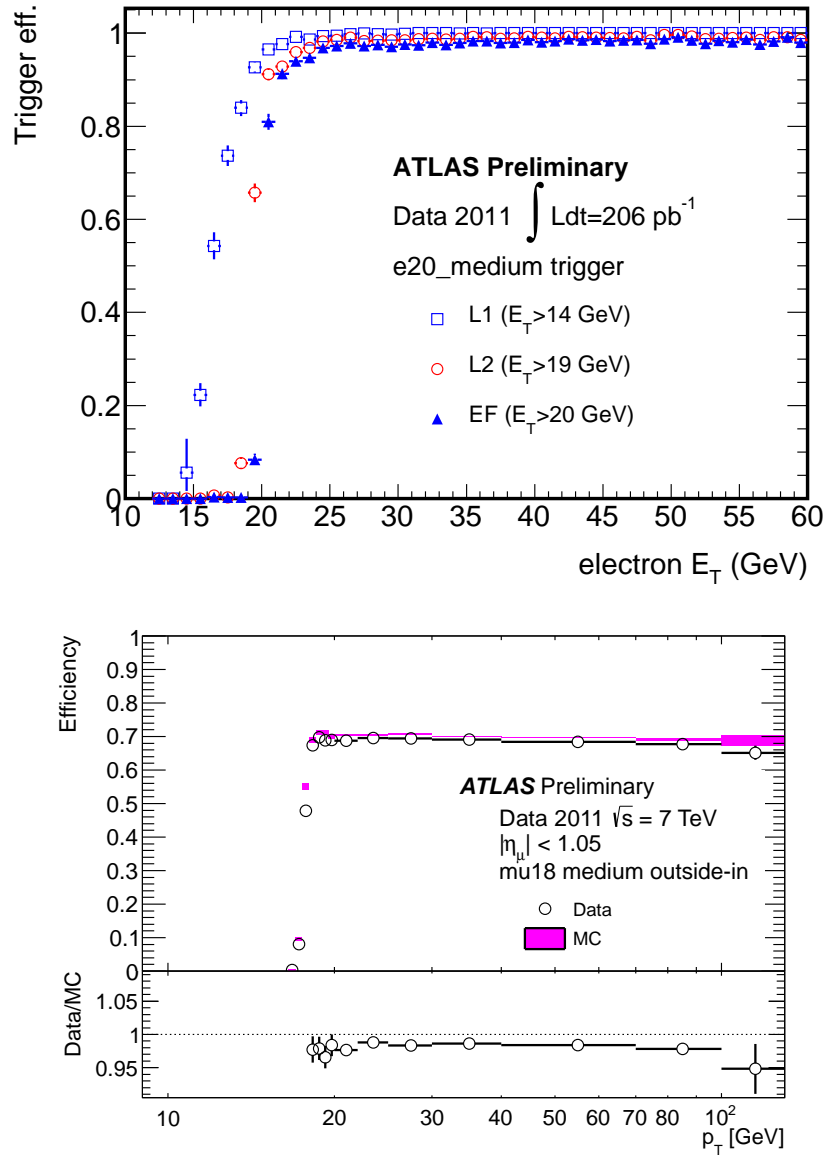


Figure 3.12: Efficiencies for the trigger chain used for (top) electrons and (bottom) muons for part of the 2011 data-taking period as a function of offline transverse energy.

Some of the most important time-dependent dataset conditions have also been included in the ATLAS simulation. Early in the data-taking period, six of the Front End Boards (FEBs) in the LAr Calorimeter stopped transmitting data due to controller problems. Four of the FEBs were later recovered. The loss of these FEBs left a hole in the calorimeter covering the area  $0 < \eta < 1.475$  and  $-0.791 < \phi < -0.595$  which affects reconstruction of electrons and jets. This is included in the simulation for the correct luminosity-weighted fraction of events. Additionally, in order to accurately simulate detector response for real LHC collisions, the effects of pile-up interactions must also be included. Pile-up events are added to the simulation by overlaying MC minimum bias (i.e. not filtered by any trigger or physics process) events generated using PYTHIA on top of physics processes of interest. Pile-up conditions changed throughout 2011 and these conditions have been simulated in the MC. Small additional pile-up corrections are made by reweighting the simulation to match the data for the number of interactions per bunch-crossing. Note that various aspects of the simulation (jet/lepton energy scales/resolution and selection efficiencies) are cross-checked on the data and corrected if necessary, as discussed in Chapter 4.

## Chapter 4

# Object reconstruction

The final state of interest in this analysis consists of two central, high  $p_T$ , oppositely charged leptons, missing transverse momentum, and a number of high  $p_T$  jets. Efficient reconstruction, identification, and calibration of these objects is needed in order to select a pure signal sample and reduce systematic uncertainties on the measurement, and is the subject of this chapter.

### 4.1 Tracking

Hits in the ID are used to reconstruct tracks associated with charged particles traversing the detector. Charged tracks are an essential component for both electron and muon reconstruction, and are used for vertexing as well as for associating reconstructed jets to either the primary or pile-up vertices.

The track reconstruction algorithm [130] begins by clustering hits in the Pixel Detector and SCT and converting the SCT clusters into space points by using both sides of an SCT module. Raw drift time information in the TRT is used to create “drift circles” in each tube. The main tracking algorithm uses an inside out approach whereby tracks are first fitted in the precision silicon trackers and then extended to include TRT information. The combined track is then refitted using the full ID. A complementary back-tracking approach is used for TRT segments not associated to silicon tracks in order to improve efficiency and find tracks resulting from photon conversions or decays of long lived particles. Track quality can be

further improved by making selection cuts on variables such as the reconstructed track  $p_T$  and  $\eta$ , track impact parameters with respect to the primary vertex, the number of outliers in the track fit, the  $\chi^2$  of the track fit, and/or the number of hits in each sub-detector.

In a post-processing phase, the ATLAS tracking software reconstructs primary and pile-up vertices. The primary vertex is defined as the vertex with the highest sum of the  $p_T^2$  of associated tracks. To select collision candidates, events in this analysis are required to have a reconstructed primary vertex with at least four associated tracks. Due to the typically large multiplicity of tracks associated with  $t\bar{t}$  production, this selection has near 100% efficiency.

## 4.2 Electrons

The algorithm used for reconstructing central high  $p_T$  electrons [131, 132] begins by finding seed clusters in the EM calorimeter of size  $3 \times 5$  cells in  $\eta$ - $\phi$  (throughout this section, all cell sizes are based on the granularity of the second layer of the EM calorimeter,  $0.025 \times 0.025$ , unless otherwise specified) and extending in  $r$  throughout the EM calorimeter, which have a total  $p_T > 2.5$  GeV. After overlapping clusters are removed by keeping the cluster with the highest energy, the clusters are loosely matched to tracks by extrapolating their last measured point in the ID to the second layer of the calorimeter and requiring that this extrapolated point and the cluster satisfy  $\Delta\eta < 0.05$  and  $\Delta\phi < 0.1$ . In case of multiple tracks matched to a single cluster, the track with the smallest  $\Delta R$  difference is chosen. Clusters which successfully match to a track are considered electron candidates. These clusters are then rebuilt using cell sizes of  $3 \times 7$  in the barrel and  $5 \times 5$  in the end-caps.

In order to efficiently reject fake electron signals, a number of variables calculated from both calorimeter and tracking information are used for cut-based electron identification. To facilitate studies useful for many analyses in the ATLAS collaboration, three collections of cuts increasing in rejection power have been defined, labeled “loose”, “medium”, and

“tight”<sup>1</sup>.

Loose electrons must pass a minimum set of calorimeter-based requirements. Since the electron cluster is expected to be contained in the EM calorimeter, selections on the ratio of the amount of energy deposited in the hadronic calorimeter to the total energy of the cluster (hadronic leakage) are included on loose electrons. Additionally, showers induced from electrons tend to be narrower than showers induced from hadrons, so cuts on shower shape variables are also included.

Medium electrons must pass all loose cuts plus a number of additional shower shape cuts used to reject high  $p_T$   $\pi^0 \rightarrow \gamma\gamma$  decays (where the photons are collinear due to the boosted pion) by making use of the inner most finely segmented “strip” layer of the calorimeter. Additional track based cuts are also applied including several requirements on track quality such as on the number of hits in the Pixel and SCT trackers as well as a cut on the transverse impact parameter.

Tight electrons must pass all medium selections, plus some additional track based selections. The track-cluster matching is tightened and a cut on the ratio of the reconstructed cluster energy to the reconstructed track momentum is applied. The cut on the transverse impact parameter is also tightened. Tight selections further require a certain number of hits in the TRT, plus a cut on the ratio of the number of high threshold hits (due to transition radiation) to the total number of hits. Finally, electrons originating from converted photons are rejected by requiring at least one hit in the inner layer of the pixel detector as well as by vetoing electrons which match reconstructed photon conversions.

In this analysis, electrons are required to pass all tight selections and have a reconstructed transverse momentum of at least  $p_T > 25$  GeV. The analysis requires that electrons are reconstructed in the central region of the detector ( $|\eta| < 2.47$ ) excluding the transition region between the calorimeter barrel and end-caps ( $1.37 < |\eta| < 1.52$ ). A quality cut rejecting electrons reconstructed near the LAr hole discussed in Section 3.2.6

---

<sup>1</sup>These selections were defined based on MC studies before the data was available. In light of the data, the selections were re-optimized and a new set of selections were derived labeled “loose++”, “medium++”, and “tight++”. The re-optimized selections are described here and used in this analysis, though this thesis has dropped the “++” for the sake of brevity. However, in much of the cited documentation, the labels include the “++” suffix.

is applied during the corresponding data-taking period. The analysis also makes use of isolation algorithms to further reject fake electrons, or electrons resulting from decays of hadrons inside jets. A calorimeter isolation variable is computed by including all energy deposited in all cells inside a cone with opening angle  $\Delta R = 0.2$  centered around the electron, excluding the energy in the electron cluster. A cut is also applied to a track isolation variable consisting of the scalar sum of the  $p_T$  of all tracks with  $p_T > 1$  GeV inside a cone of size  $\Delta R = 0.3$ , excluding the matched electron track. The values of the cuts on each variable depend on the electron  $p_T$ ,  $\eta$ , and pile-up conditions, and are optimized so that each cut independently retains 90% of tight electrons from  $Z$  boson decays. A third isolation selection vetoing electrons which are closer than  $\Delta R = 0.4$  to a good reconstructed jet is also applied (see Section 4.5).

The electron reconstruction, identification, and isolation efficiencies were measured on a variety of signal processes and compared with the simulation. The cleanest measurement takes place using a tag-and-probe method on leptonically decaying  $Z$  boson events, whereby a clean, unbiased sample of probe electron candidates is selected via the presence of a tagged electron in the event (that is, an electron passing tight identification requirements). Small differences between the simulated and measured efficiencies are accounted for by reweighting the MC to match the data. Figure 4.1 shows a comparison of the measured and simulated efficiencies for electrons as a function of the number of reconstructed vertices in the event.

A small MC-based calibration correction is applied by the reconstruction software to account for energy lost upstream of the calorimeter due to absorption in passive material, as well as shower leakage outside of the reconstructed cluster. Small additional corrections are necessary to ensure that the energy scale and resolution in the MC matches the data. The energy scale is calibrated using a template method on data events containing leptonically decaying  $Z$  boson, making use of its well known mass of 91 GeV, as well as on events containing  $W \rightarrow e\nu$  decays by comparing the electron energy measured in the calorimeter to the momentum measured in the ID. These corrections are applied to electrons in the data and are at the percent level. The electron energy resolution is also measured on  $Z$  boson events by fitting the di-lepton mass spectra of both the data and MC. The data show a larger resolution than predicted in the MC, so simulated electrons are smeared by the

measured difference. Figure 4.1 shows an example of this fit.

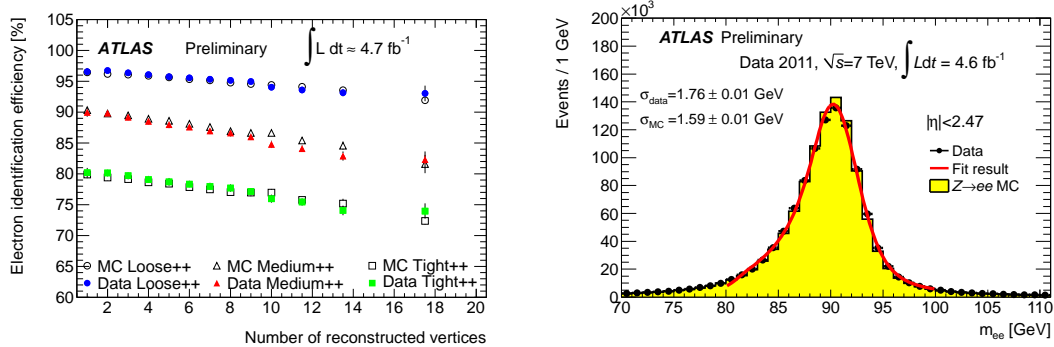


Figure 4.1: A comparison of the simulated and measured electron efficiencies as a function of the number of reconstructed vertices (left) and a comparison of the simulated and measured energy resolution on  $Z \rightarrow ee$  events using a fit to the di-electron invariant mass.

### 4.3 Muons

The “Muid” algorithm [133] is used to reconstruct muons in this analysis. Muons are required to have  $p_T > 25$  GeV and  $|\eta| < 2.5$ . Reconstruction starts by finding standalone tracks in the MS by fitting close hits in the same chamber to a straight line, forming a segment in that chamber. Segments from each chamber station are then used to form the full standalone MS track fit. To efficiently and accurately reconstruct the muon momentum, the standalone track is combined with the track measurement in the ID. Combination of MS standalone and ID tracks is done through a full track refit, using the original hits in both the ID and the MS. The combination takes into account small energy losses in the calorimeter. Selections on the inner detector track quality including cuts on the number of hits and outliers in each ID sub-detector as well as the ID track impact parameter are applied after a combined muon is reconstructed.

Since other charged particles are fully contained in the calorimeter, reconstructed muons have a very high purity. Fake muon signals coming from semi-leptonic decays of  $B$  hadrons close to the interaction point can be rejected using isolation requirements. As with electrons, a calorimeter based cut on an isolation cone of size  $\Delta R = 0.2$  and a track based cut on an

isolation cone of size  $\Delta R = 0.3$  are applied. The cuts were optimized to achieve a good rejection of the fake backgrounds while retaining an efficiency which has small dependence on pile-up conditions. Muons are also removed if they are closer than  $\Delta R = 0.4$  to a good reconstructed jet.

Muons from cosmic events can fake a di-muon signal. Events are rejected if two oppositely charged muons are reconstructed, both with impact parameters satisfying  $|d_0| > 0.5$  mm, and  $\Delta\phi$  between the selected muons is greater than 3.10. This selection combined with the vertex requirement discussed in Section 4.1 reduces this background to negligible levels.

The muon reconstruction and isolation efficiencies are measured using a tag-and-probe method on  $Z \rightarrow \mu\mu$  events [134]. A scale factor is applied to correct the simulation to match the data. The measured efficiencies for the data and simulation and the resulting scale factors are shown in Figure 4.2.

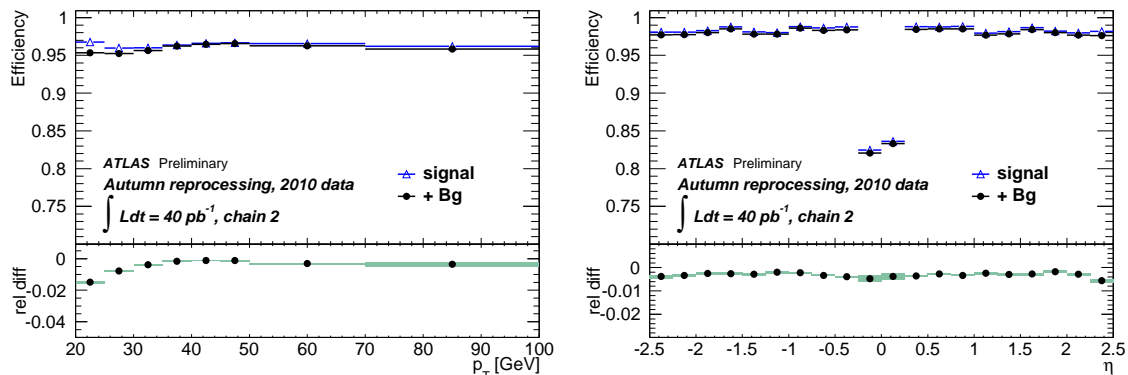


Figure 4.2: A comparison of the simulated and measured muon efficiencies as a function of the reconstructed muon  $p_T$  (left) and  $\eta$  (right) and the resulting scale factors (lower panels).

The muon momentum resolution is also measured on  $Z \rightarrow \mu\mu$  events by fitting the di-muon mass distribution in data and simulation and comparing the measured width [135]. This is done separately for tracks associated with muons in the ID and the MS. The results are shown in Figure 4.3. As with electrons, a small smearing is needed on muons in the simulation to match the resolution observed in the data. The momentum scale difference is estimated by comparing the fitted di-muon mass in the data and simulation. A small shift

of order 1.5% is observed in the forward region of the C side of the detector. A correction is applied to the simulation to match this observation in the data. The resolution is also be measured by comparing the ID and MS standalone tracks associated with muons in  $W \rightarrow \mu\nu$  events in data. The final resolution smearing factors take both estimates into account [135].

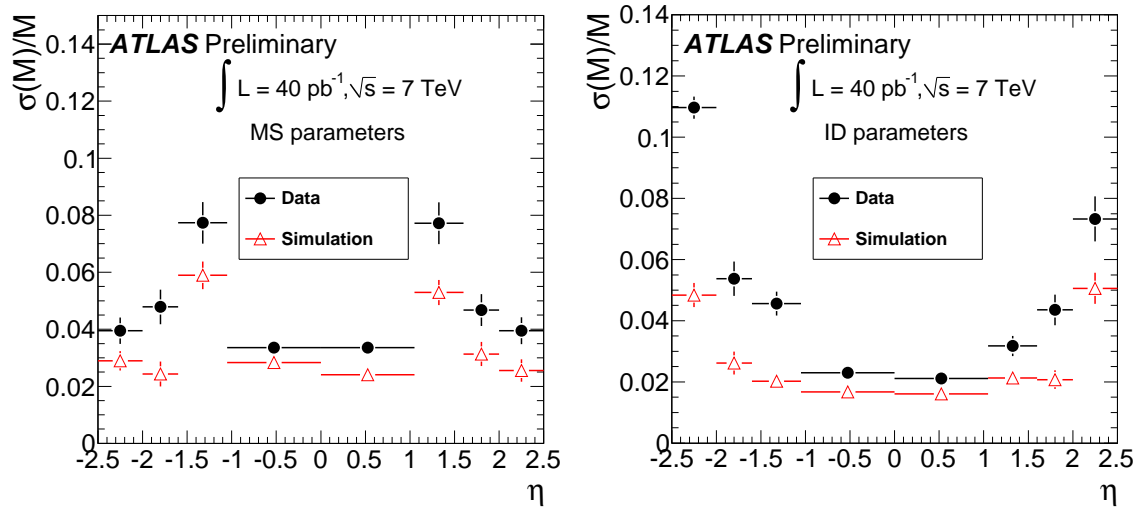


Figure 4.3: A comparison of measured momentum resolution in data and simulation as a function of the reconstructed muon  $\eta$  for standalone tracks in the Muon System (left) and tracks in the Inner Detector (right). Smearing is applied independently to reconstructed tracks in both systems before combining tracks.

## 4.4 Jets

The reconstruction and measurement of the kinematic properties of jets are crucial to this analysis. The largest systematic uncertainties in this analysis are those associated with jet energy measurements. For these reasons, this section will discuss jet reconstruction, calibration, and efficiency measurements in some detail.

### 4.4.1 Reconstruction

Jet reconstruction starts with an algorithm which clusters topologically connected cells in the calorimeter. This includes only cells containing a significant amount of deposited energy, above predetermined thresholds, in order to remove pile-up and electronic noise [136, 137]. The algorithm starts with seed cells that have a signal-to-noise ratio above a large threshold  $S_{\text{seed}}$ . All neighboring cells (defined as the 8 adjacent cells in the same layer, plus the overlapping cells in  $\eta$ - $\phi$  in adjacent layers) are added to the cluster. If a neighboring cell is above a lower threshold  $S_{\text{neighbor}}$ , then its neighboring cells can also be added. A cluster splitting algorithm is applied at this stage which is optimized to separate showers of close-by particles. The energy of the cluster is taken to be the sum of the energies deposited in all cells of the cluster, and it is assumed to have 0 mass. Its  $\eta$ - $\phi$  position is estimated from an energy-weighted average of the positions of its constituent cells. The resulting clusters (called topological clusters or topo-clusters) are of variable size as opposed to the fixed-sized sliding window clusters of the electron reconstruction algorithm. Having clusters of variable size reduces sensitivity to noise and out-of-cluster effects and therefore improves the energy resolution.

The anti- $k_T$  sequential recombination algorithm [85] with radial distance parameter  $R = 0.4$  (Section 2.2) is used to cluster jets in this analysis. A radial parameter of  $R = 0.6$  is also used in several ATLAS jet measurements, however, it has been shown that  $R = 0.4$  jets perform better in high jet multiplicity environments [112]. The inputs to the algorithm are the topo-clusters defined in the previous paragraph, with no additional corrections. These clusters are calibrated to the EM scale. That is, since calorimeter response for hadrons is lower than for electrons or photons, the energy measured by the calorimeter in

hadron induced showers is lower than the energy of the hadron traversing the calorimeter. This is known as “non-compensation.” Additional corrections are needed to fully calibrate jets to the hadronic scale. Clustering takes place in rapidity-azimuth ( $y$ - $\phi$ ) space, while corrections applied to the reconstructed jets are performed based on jet pseudorapidity  $\eta$ . Jet kinematics are calculated using the four-momenta recombination scheme.

#### 4.4.2 Calibration

The first step in jet calibration is to correct for pile-up effects [138]. Particles from pile-up events (low energy multijet collisions of other protons) can add extra energy to cells included in the jet clustering and this additional energy must be subtracted. Pile-up is divided into two categories: in-time and out-of-time pile. In-time pile-up comes from other protons colliding in the same bunch as the two protons from which the event being analyzed originated. Out-of-time pile-up comes from collisions in bunches which collided before the event being analyzed which can leave residual signals in the detector. The pile-up correction is derived from MC simulation and validated using *in situ* techniques on data. The correction is applied as an offset function of pile-up activity, characterized by the number of primary and pile-up vertices  $N_{PV}$  (which provides a good characterization of the amount of in-time pile-up) and the average number of interactions per bunch-crossing  $\mu$  at the time the event was recorded (which gives a good indication of the amount of out-of-time pile-up). The offset can be subtracted from the EM scale measurement  $p_{T, \text{reco}}^{\text{EM}}$  before the next stage of the calibration. A correction to the jet direction is applied at this stage so that the jet points back to the primary vertex, rather than the center of the detector ( $z = 0$ ), which is in general different by a small amount.

Since constituent topo-clusters are calibrated at the EM scale, jets are also initially calibrated at the same scale. In addition to non-compensation, several other effects necessitate corrections, including energy losses upstream of the calorimeter, out-of-cone effects (charged particles whose initial four-momenta should be included in jet but bend out of the jet cone), out-of-cluster effects (particles whose showers are not fully contained in the cluster), and inefficiencies in the clustering process. An MC-based calibration scheme [139] is used to correct jets to the hadronic scale by comparing MC truth jets and reconstructed jets in the

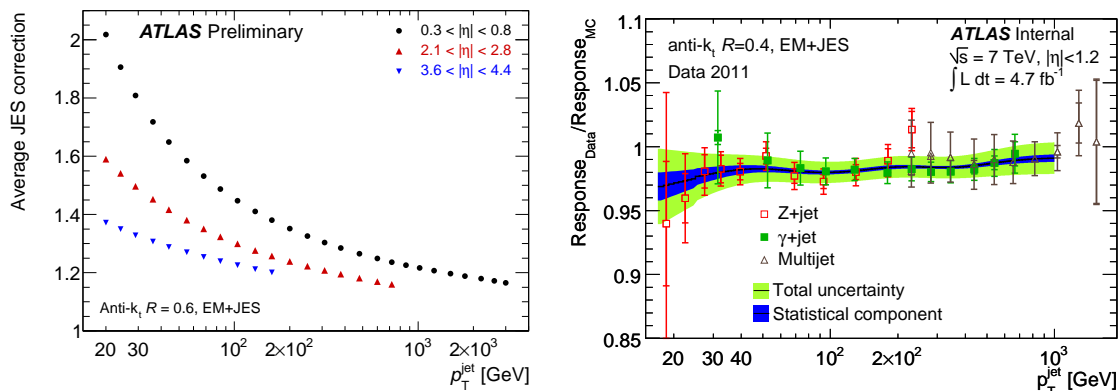


Figure 4.4: The MC based calibration corrections (left) and the residual *in situ* corrections (right) used to calibrate calorimeter jets to the particle-level.

simulation. Only isolated jets are considered, where no additional jet is within  $\Delta R < 1.0$ . A numerical inversion technique is used to determine the jet correction factor as a function of the reconstructed EM scale transverse momentum ( $p_{T,\text{reco}}^{\text{EM}}$ ) and pseudorapidity. Jets at this stage are said to be calibrated to the EM+JES level. This calibration is applied only to jets with an EM scale transverse momentum satisfying  $p_{T,\text{reco}}^{\text{EM}} > 3$  GeV. The size of the applied correction is shown as a function of jet  $p_{T,\text{reco}}^{\text{EM+JES}}$  in Figure 4.4. Though the figure shows anti- $k_T$  jets with  $R = 0.6$ , the response is similar for jets with  $R = 0.4$ .

Additional corrections measured using *in situ* techniques are applied [140] to jets in the data. These corrections are mainly derived using  $p_T$  balance methods in events with a photon or  $Z$  boson recoiling against a jet (or system of jets). The  $Z$ +jet ( $\gamma$ +jet) method calibrates light quark induced jets up to  $p_T \sim 200$  GeV (800 GeV). For higher jet transverse momenta, an intercalibration scheme is used, whereby a high  $p_T$  jet is balanced against a system of lower  $p_T$  jets. The full *in situ* calibration scheme is applied to jets down to  $p_{T,\text{reco}}^{\text{EM+JES}} > 15$  GeV. The size of this additional correction is shown in Figure 4.4. There are a number of uncertainties in the jet calibration method which need to be propagated to the jet multiplicity measurement. These uncertainties are discussed in Chapter 7.

As with leptons, the simulated jet energy resolution is also compared with that observed in the data [141] using di-jet balance and bisector techniques. In the di-jet balance technique, di-jet events are selected and the asymmetry  $A$  defined as:

$$A(p_{T,1}, p_{T,2}) \equiv \frac{p_{T,1} - p_{T,2}}{p_{T,1} + p_{T,2}} \quad (4.1)$$

is measured and fit to a Gaussian shape. The width of the fitted Gaussian determines the resolution. Figure 4.5 compares the asymmetry between the data and simulation. The bisector technique measures the jet energy resolution (JER) on di-jet events by first measuring an imbalance transverse vector  $\mathbf{P}_T$ , which is just the vector sum of the transverse momenta of both jets. A coordinate system is determined by an axis which bisects the jet transverse momenta vectors in the  $xy$ -plane, and an axis perpendicular to the bisector. The components of the  $\mathbf{P}_T$  vector are measured in this coordinate system and, since the component along the axis perpendicular to the bisector is more sensitive to resolution effects than the bisecting axis, the widths of the two components can be used to extract the JER. The JER extracted from the data agrees with the simulation within its uncertainty. No additional corrections are applied to the simulation. The resolution varies from  $\sim 20\%$  at  $p_T = 25$  GeV down to  $< 10\%$  for  $p_T > 100$  GeV.

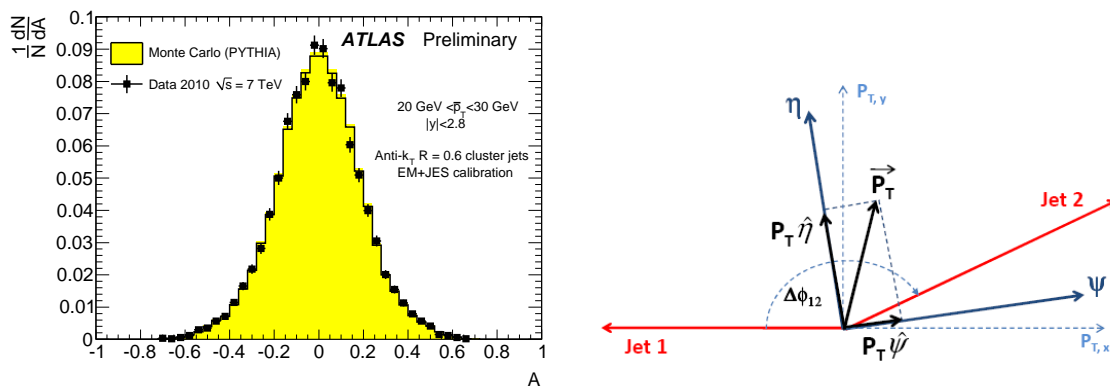


Figure 4.5: The measured asymmetry  $A$  for jets with  $20 \text{ GeV} < p_T < 30 \text{ GeV}$  used to extract the JER in the di-jet balance method (left) and a schematic of the jet configuration and coordinate system used to extract the JER in the bisector method (right).

### 4.4.3 Jet selection

Jets are required to have a calibrated transverse momentum of at least  $p_T > 25 \text{ GeV}$  and detector-level pseudorapidity  $|\eta| < 2.5$ . The jet reconstruction efficiency is estimated

on data by comparing calorimeter jets (reconstructed as defined in this section) to jets reconstructed using the same clustering algorithm with tracks in the ID as inputs. Excellent agreement between the data and simulation is observed for jets with  $p_T > 20$  GeV, so no additional corrections are needed. To reject jets coming from pile-up events, the jet vertex fraction (JVF), defined as the  $p_T$ -weighted fraction of tracks originating from the primary vertex which are associated to the jet (that is, tracks for which  $\Delta R(\text{track}, \text{jet}) < 0.4$ ), is required to satisfy  $|\text{JVF}| > 0.75$ . Jets with no associated tracks are assigned a value  $\text{JVF} = -1$  and therefore pass this selection. Disagreements between the simulation of this variable and the data are estimated using jets reconstructed in  $Z$  boson events. In these events, either a) the reconstructed  $p_T$  of the  $Z$  boson is small, indicating no hadronic recoil so that reconstructed high  $p_T$  jets must come from pile-up interactions, or b) the  $Z$  boson and jet transverse momenta mutually balance and the jet can be assumed to come from the primary vertex. Differences are corrected in the simulation in order to match the data. Figure 4.6 shows the JVF pile-up discriminating power in QCD events as well as the data/MC agreement of this distribution in  $Z$  boson events before the correction.

Selections on jet quality [139] are also made on all jets with a calibrated  $p_T > 20$  GeV. These selections reject the event if low quality jets are found since these jets are likely to be poorly measured and can have adverse effects on the  $E_T^{\text{miss}}$  measurement. Quality cuts are made on variables such as the fractions of energy deposited in the EM or hadronic calorimeter, or in specific layers of the calorimeters. Events with low quality jets are included in the simulation and are found to be rare in this analysis. Events are also rejected if jets were reconstructed near the LAr hole.

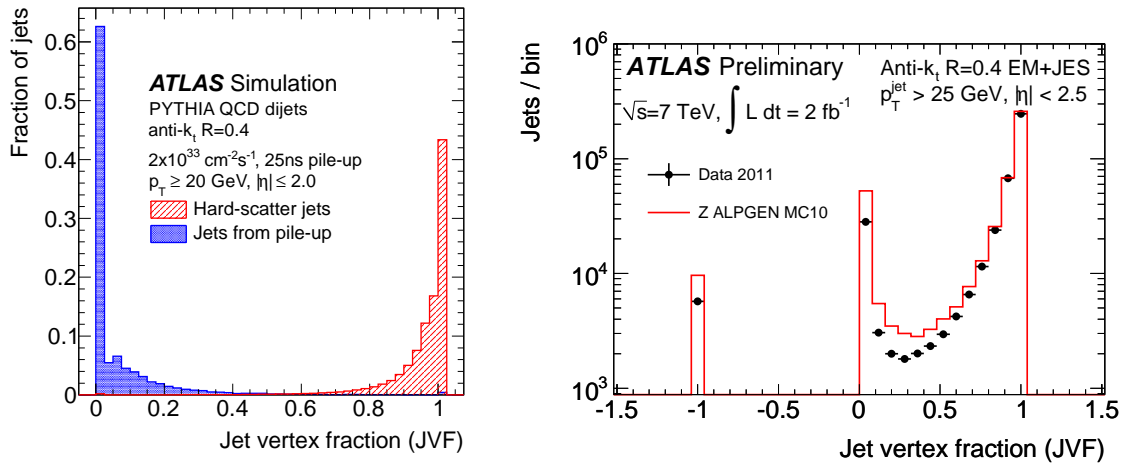


Figure 4.6: The jet vertex fraction (JVF) distributions for jets originating from the primary and pile-up vertices as predicted by MC simulation in QCD di-jet events (left) and a comparison of the JVF distribution of all jets in  $Z$  boson events before corrections are applied (right).

## 4.5 Overlap Removal

Overlapping objects are removed in the following order:

- Since clusters associated with electrons are not removed before jet reconstruction, high  $p_T$  electrons are also clustered as jets. Therefore, exactly one jet is removed from the event if its  $\eta$ - $\phi$  distance to a selected electron is less than  $\Delta R = 0.2$ . If there are two such jets, the one with the smallest  $\Delta R$  is removed.
- Electromagnetic showers in the EM calorimeter induced from bremsstrahlung radiation from high  $p_T$  muons can be associated with the muon ID track, faking an electron signal. If an event contains a selected muon with a track matching a selected electron ( $\Delta\theta < 0.005$  and  $\Delta\phi < 0.005$ ), the event is removed.
- As mentioned in Sections 4.2 and 4.3, to reject leptons from leptonically decaying  $B$  hadrons, any selected lepton is vetoed if it is found to be within  $\Delta R < 0.4$  from any selected jet not removed in the first bullet point of this section.

## 4.6 Missing transverse momentum

Missing transverse momentum ( $E_T^{\text{miss}}$ ) is measured by balancing the vector sum of the total transverse momentum reconstructed in an event. The total transverse momentum is determined using an algorithm which associates topological clusters in the calorimeter to electrons, jets, and soft jets (that is, jets with  $7 \text{ GeV} < p_T < 20 \text{ GeV}$ ) in that order and corrects the clusters to the scale of the objects [142]. Muons are also included in the algorithm. Clusters which are not associated with any of these reconstructed objects are included in the algorithm at the EM scale (the cell-out term). All cluster energies are added vectorially in the transverse direction and the  $E_T^{\text{miss}}$  is determined to be equal and opposite to the resulting vector.

For practical reasons, the selections, calibrations, and energy thresholds used for the objects are slightly different than those used in the above described definitions and are summarized as follows:

- Electrons are required to pass the tight identification requirements and have  $p_T > 10$  GeV. The electron energy uses all corrections except the out-of-cluster correction since it is included in a separate term in the  $E_T^{\text{miss}}$  calculation.
- As discussed in Section 4.4, jet reconstruction uses the anti- $k_T$  algorithm with a radial parameter of size  $R = 0.4$  and all jets (including soft jets) are calibrated to the EM+JES scale. For the purposes of the  $E_T^{\text{miss}}$  calculation, clusters associated with jets with  $p_T > 20$  GeV are corrected to the same EM+JES scale while clusters associated with soft jets are left at the EM scale.
- The momenta of all combined muons with  $|\eta| < 2.5$  are included in the algorithm. Energy deposited in the calorimeter associated with muons is included in either the jet, soft jet, or cell-out terms depending on muon isolation.

## Chapter 5

# Event selections and background estimation

### 5.1 Event selections

After reconstructing and selecting objects, several event-level selection cuts are applied to the data in order to reduce backgrounds. The  $t\bar{t}$  selections were optimized by the Top Working Group of the ATLAS collaboration for the best significance ( $S = N_{\text{signal}}/\sqrt{N_{\text{background}}}$ ) for the ATLAS inclusive cross-section measurement [143]. In order to facilitate comparisons and to use common prescriptions for systematic uncertainty and background estimations, those same selections were used in this analysis (i.e. they were not re-optimized for this analysis):

- **Cut 1 (Data)** Runs and lumi-blocks are required to have “green” data quality flags (Section 3.2.6), which indicates that all sub-detectors and object reconstruction algorithms were performing well.
- **Cut 1 (Signal MC)** Since several  $t\bar{t}$  Monte Carlo (MC) samples used in this analysis include single lepton events, signal MC is required to have two truth leptons originating from  $W$  boson decays (where the  $W$  boson is assumed to originate from a top quark).

- **Cut 2** A single electron (muon) trigger, with  $p_T$  and ID selections looser than those used for the analysis, is required to have fired in the event for the  $ee$  ( $\mu\mu$ ) channel. For the  $e\mu$  channel, a logical OR of the electron and muon triggers is used.
- **Cut 3** At least one primary vertex is required to be reconstructed with at least four tracks.
- **Cut 4** Events with muon signals consistent with cosmic rays are vetoed (see Section 4.3).
- **Cut 5** At least two leptons passing all lepton selections defined in Sections 4.2 and 4.3 are required.
- **Cut 6** At least one of the leptons is required to match a trigger lepton so that the trigger efficiency corrections discussed in Section 3.2.5 and applied to the MC are correctly accounted for.
- **Cut 7** Events are removed if a selected electron and muon share a track, in order to remove fake electron signals due to muon bremsstrahlung.
- **Cut 8** Events are removed if any reconstructed jets with  $p_T > 20$  GeV fail the quality selections discussed in Section 4.4.3.
- **Cut 9** In  $ee$  and  $\mu\mu$  events, the  $E_T^{\text{miss}}$  of the event is required to exceed 60 GeV. This significantly reduces the background from  $Z/\gamma^* + \text{jets}$  events. In  $e\mu$  events, the  $H_T$  (defined as the scalar sum of the  $p_T$  of all selected leptons and jets in the event) is required to be greater than 130 GeV. This mostly reduces the  $Z \rightarrow \tau\tau$  contribution where both  $\tau$ -leptons decay leptonically.
- **Cut 10** At least two jets with  $p_T > 25$  GeV are required. The  $p_T$  threshold for this selection is independent of the threshold used for the jet multiplicity measurement. Due to the two  $b$ -quark induced jets originating in most  $t\bar{t}$  decays, the  $t\bar{t}$  jet multiplicity distribution peaks at two jets. In events with less than two jets, background uncertainties become dominant, so no attempt to measure these events is made.

- **Cut 11** Exactly two good leptons in the event are required. Leptons originating from semi-leptonic decays in  $b$ -jets are typically not well isolated and therefore fail the lepton selections. Such leptons are included as part of the fake hypothesis in the fake estimation, so events with two leptons, one of which comes from a  $b$ -jet, are counted as “fakes”, even if they are  $t\bar{t}$  events.
- **Cut 12** The leptons must have opposite charge since they originate from oppositely charged  $W$  bosons.
- **Cut 13** For the  $ee$  and  $\mu\mu$  channels, the di-lepton invariant mass  $M_{\ell\ell}$  is required to be more than 15 GeV. This is to reduce the contribution of low mass di-leptonic resonances ( $J/\psi$ ,  $\Upsilon$ , etc.)
- **Cut 14** For the  $ee$  and  $\mu\mu$  channels, the di-lepton invariant mass  $M_{\ell\ell}$  is required to be more than 10 GeV away from the  $Z$  boson pole ( $M_{\ell\ell} < 81$  GeV OR  $M_{\ell\ell} > 101$  GeV). This further reduces the contribution from events with di-lepton decays of  $Z$  bosons.
- **Cut 15** In MC events, both leptons are required to match true leptons in the truth record. This is to avoid double counting the contribution from events including one or more fake leptons with the data driven estimate described in Section 5.2.
- **Cut 16** As an additional data quality requirement, events with a `LArError` flag value greater than 1 (indicating data integrity errors) are removed.

No  $b$ -tagging requirements are made in the signal region in this analysis. In principle,  $b$ -tagging could increase the purity of the signal at the expense of additional uncertainties due to estimation of the  $b$ -tagging efficiency. As will be shown in Section 5.3, the purity of  $t\bar{t}$  events using the above selections (especially at high jet multiplicity) is more than sufficient. The background uncertainties at high jet multiplicity are much less than the uncertainty associated with  $b$ -tagging. Thus, adding this selection would reduce the sensitivity of this analysis.

Selection of  $Z \rightarrow \ell\ell$  events proceeds using the same event quality cuts and object definitions as described in Chapter 4. This ensures a partial canceling of the systematic

uncertainties associated with selecting objects and facilitates the estimation of their effects on the ratio measurement.

The  $Z \rightarrow ee$  and  $Z \rightarrow \mu\mu$  event selections differ from the  $t\bar{t} ee$  and  $\mu\mu$  channel selections described above in only the following four cuts:

- **Cut 1 (Signal MC)** No truth requirements are made since  $Z$ +jets event generators are already filtered by decay process.
- **Cut 9** No selections on the  $E_{\text{T}}^{\text{miss}}$  are made.
- **Cut 10** No jet multiplicity requirements are imposed.
- **Cut 14** The invariant mass of the two selected leptons in the event is required to be within 10 GeV of the  $Z$  boson mass ( $81 \text{ GeV} < M_{\ell\ell} < 101 \text{ GeV}$ ).

Since the  $Z$ +jets part of this analysis has a much lower background, no rigorous optimization of these selections was performed. Instead, these selections were chosen in order to be mutually exclusive to the  $t\bar{t}$  signal selection cuts. Due to the high  $Z$  boson cross-section combined with excellent purity and efficiency of the ATLAS calorimeter, the  $Z$  boson signal region is heavily signal dominated, with less than 1% contamination from background processes (see the following sections).

## 5.2 Estimation of background contributions

This section describes the methods used for background estimation for this analysis. Fake lepton events in the  $t\bar{t}$  signal region from  $W$ +jets or QCD multi-jet events have relatively high production cross-sections and it is difficult to model the fake lepton efficiency accurately. Estimates based on simulation would have large statistical and systematic uncertainties. Therefore, these contributions are estimated using data-driven methods. In addition, Drell-Yan  $Z/\gamma^*$ +jets events with two real leptons and large  $E_{\text{T}}^{\text{miss}}$  due to instrumental effects have potential modeling difficulties in the simulation, so they are also estimated in a data-driven way.

In addition to those background sources, several other processes with two real leptons in the final state (di-boson, single top,  $Z \rightarrow \tau\tau$ ) contribute events to the signal regions.

These are estimated from simulation. The production cross-sections are relatively small and therefore the contributions are also small. Conservative systematic uncertainties are used for these backgrounds.

### 5.2.1 Fake leptons in $t\bar{t}$ events

The contribution of events with one or more fake leptons to the  $t\bar{t}$  signal region is estimated using the matrix method. In this method, “loose” and “tight” leptons are defined (where tight must use the same selections as in the analysis) and the loose-to-tight efficiencies for real ( $r$ ) and fake ( $f$ ) leptons are measured in control regions in data. Note that real leptons from hadron decays are included in the “fake” category.

Events with two leptons which pass at least the loose requirements are selected. At the reconstruction-level, these events can be characterized as events with two tight leptons ( $N_{TT}$ ), two loose (not tight) leptons ( $N_{LL}$ ), or one tight and one loose ( $N_{TL}$  and  $N_{LT}$ )<sup>1</sup> lepton. These configurations can originate from events with two real leptons ( $N_{RR}$ ), two fake leptons ( $N_{FF}$ ), or one real and one fake ( $N_{RF}$  and  $N_{FR}$ ) lepton. These two categorizations are related by the following matrix equation:

$$\begin{bmatrix} N_{TT} \\ N_{TL} \\ N_{LT} \\ N_{LL} \end{bmatrix} = \begin{bmatrix} rr & rf & fr & ff \\ r(1-r) & r(1-f) & f(1-r) & f(1-f) \\ (1-r)r & (1-r)f & (1-f)r & (1-f)f \\ (1-r)(1-r) & (1-r)(1-f) & (1-f)(1-r) & (1-f)(1-f) \end{bmatrix} \begin{bmatrix} N_{RR} \\ N_{RF} \\ N_{FR} \\ N_{FF} \end{bmatrix}. \quad (5.1)$$

The matrix can be inverted and multiplied by the reconstruction-level composition in order to determine the truth-level composition. It should be noted that this estimate includes both events with two fake leptons (QCD), and events with one fake and one real lepton ( $W$ +jets).

---

<sup>1</sup>In the  $ee$  and  $\mu\mu$  channels, the order of the subscripts denotes the higher and lower  $p_T$  lepton, respectively. In the  $e\mu$  channel, the first subscript denotes the electron and the second denotes the muon.

### 5.2.1.1 Electron efficiencies

In order to reduce sensitivity to statistical fluctuations while at the same time controlling the systematics, the loose definition for the matrix method is chosen to be electrons passing the medium definition (see Section 4.2), plus an extra requirement vetoing electrons which match to reconstructed photon conversions. Additionally, isolation requirements applied at the tight-level are dropped for the loose definition. The efficiencies for real electrons are measured using a tag-and-probe method in data on  $Z$  boson events. In order to include the influence of pile-up on the isolation efficiency, the data set is split into a low (periods B-K) and high (periods L-M) samples for the efficiency measurement. It has been observed that the presence of nearby jets has a strong influence on the isolation efficiency, as can be seen in Figure 5.1. To account for this effect, the efficiencies are parametrized in  $\Delta R$  between the electron the nearest jet, as well as electron pseudorapidity. Electron  $p_T$  was also considered, but the statistical uncertainties on the measured rates were too large with a three dimensional parametrization. Due to systematic effects being better understood in electron  $\eta$ , as well as stronger correlations between electron  $\Delta R$  and  $p_T$ , electron  $\eta$  is chosen over  $p_T$ .

Since MC samples show a difference in electron efficiencies between di-lepton  $Z$ +jets and  $t\bar{t}$  (as well as other samples, as can be seen in Figure 5.2), a correction is derived from the MC and applied to the data measured efficiencies. The central value for the correction is taken as the average of the  $Z$ +jets ( $\epsilon_Z$ ) and  $t\bar{t}$  ( $\epsilon_{t\bar{t}}$ ) efficiencies, divided by  $\epsilon_Z$  (the magnitude of this correction is of order 1%). It was checked that all other processes contributing to the  $t\bar{t}$  signal region fall between  $\epsilon_Z$  and  $\epsilon_{t\bar{t}}$ . The spread between  $\epsilon_Z$  and  $\epsilon_{t\bar{t}}$  is therefore taken as a systematic uncertainty attributed to the unknown sample composition. In addition to the sample composition uncertainty on the efficiency, smaller uncertainties come from background subtraction in the tag-and-probe method, as well as statistical uncertainties.

Fake electron efficiencies (or “fake-rates”) are measured in a single electron sample with at least one reconstructed jet and low  $E_T^{\text{miss}}$  ( $E_T^{\text{miss}} < 20$  GeV), using the same parametrization as the efficiencies. Due to lower statistics in some important regions of the phase space, the dataset is not split into low and high pile-up samples for the fake-rate measurement. As with the efficiency measurement, an important aspect of the fake-rate

measurement is the sample composition, which for  $t\bar{t}$ -like fake events includes primarily electrons from  $b$ -jets (jets with at least one  $B$ -hadron), light jets (non- $b$ -jets), and photon conversions (photons which “convert” to electrons due to interactions with the detector material). Additional selections are applied to events in the fake control region to enhance fake electrons from each of these classifications. The fake-enhanced control regions include:

- Requiring at least one  $b$ -tagged<sup>2</sup> jet in the event in order to enhance fake leptons originating in  $b$ -jets.
- Requiring the electron to be reconstructed near a conversion vertex to enhance fake leptons originating from converted photons.
- Requiring no  $b$ -tagged jets and that the electron is reconstructed away from the conversion vertex in order to enhance in events with fake electrons originating in light jets.

The base-line control region (i.e. the single electron sample without any additional selections for fake flavor-enhancement) is referred to as the “pretag” region. Fake-rates are measured in each flavor-enhanced control region and the rate used in the matrix method is calculated from the average of the highest and lowest flavor-enhanced fake electron efficiency in each bin. The uncertainty is taken to be half the difference between the extremes. Additional (smaller) uncertainties on the fake-rates coming from background (real electron) subtraction and limited statistics are also estimated. The fake-rates measured in each flavor-enhanced region as well as the pretag region are shown parametrized in  $\Delta R(e, \text{jet})$  in Figure 5.1.

### 5.2.1.2 Muon efficiencies

Fake muons predominantly originate from semi-leptonic  $B$  and charmed-hadron decays. To enhance fake muons in the loose-not-tight sample, the loose definition is defined to be the same as the tight definition without the isolation requirements.

---

<sup>2</sup>Since  $B$ -hadrons often traverse small distances before decaying ( $\sim 1$  mm), a jet can be “tagged” as including a  $B$ -hadron decay by searching for jets with matched tracks which have a non-zero distance of closest approach to the primary vertex, or by attempting to reconstruct a secondary vertex.

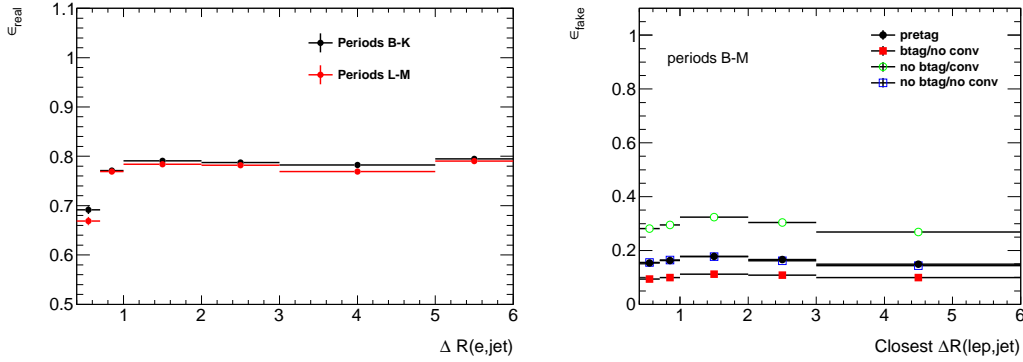


Figure 5.1: Efficiencies for real (left) and fake (right) electrons that pass the loose selection criteria to also pass the tight ones, parametrized in electron  $\Delta R(e, \text{nearest jet})$ . The  $3 < \Delta R < 5$  bin includes all leptons for which  $\Delta R > 3$ . The  $5 < \Delta R < 6$  bin includes leptons for which there is no jet in the event.

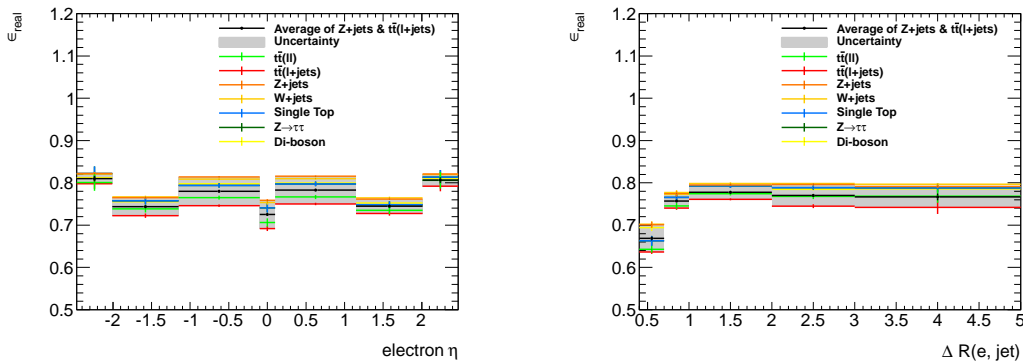


Figure 5.2: Real electron efficiencies parametrized in electron  $\eta$  (left) and  $\Delta R(e, \text{nearest jet})$  (right) with a non-isolated medium identification definition (including the photon conversion veto) on several MC samples for processes contributing to the dilepton signal region. The average of the  $t\bar{t}$  and Z+jets efficiencies is calculated and the difference between the average and the Z+jets efficiency is applied to the data measured rates as a correction.

To handle nearby jet and sample composition effects, the real loose-to-tight muon efficiency is measured in two ways<sup>3</sup>. The first is to estimate the efficiencies parametrized in  $\eta^\mu$  and  $p_T^{\text{lead jet}}$  using the tag-and-probe method on  $Z$  boson events in data. The second is to take the efficiencies from the  $t\bar{t}$  MC simulation and parametrized in  $N_{\text{jets}}$ . For a given event, the efficiencies from each approach are averaged and half the difference between them is taken as the uncertainty. The  $N_{\text{jets}}$  parametrization accounts for nearby jet effects on the muon efficiency while the average of the efficiencies measured on  $Z$  and top events accounts for sample composition effects.

As with electrons, fake muon efficiencies are measured on a low  $E_T^{\text{miss}}$  single muon sample in the data. Sample composition effects are negligible since fake muons originate from a single source (namely hadronic decays in jets). Therefore, uncertainties on the fake muon efficiency are mostly due to real muon subtraction in the control region, limited statistics, and nearby jet effects.

### 5.2.1.3 Fake control regions

The fake lepton modeling is cross-checked using dedicated control regions. One control region is defined by requiring two leptons with the same charge, two jets, and vetoing on events where the di-lepton mass falls within  $81 \text{ GeV} < M_{\ell\ell} < 101 \text{ GeV}$  in order to reject  $Z$ +jets events where the charge of one of the leptons is mis-reconstructed. This control region includes predominantly fake lepton events at both the loose (LL, LT, and TL) and tight (TT) levels, so it is most sensitive to the fake-lepton efficiency estimation. Figure 5.3 shows that good agreement between the data and the predictions of the matrix-method for the  $p_T > 25 \text{ GeV}$  jet multiplicity in each channel. Other distributions are also tested and show good agreement between the data and the fake estimation.

The matrix method is also sensitive to the real lepton efficiency, so a separate control region is also defined by all selections outlined in Section 5.1 except with the requirements

---

<sup>3</sup>Note that this method is different from that used for electrons due to the electron fake rate being significantly higher than for muons necessitating a more critical examination of the method in order to control systematic uncertainties for the real and fake electron efficiency estimations. What's important for this analysis is that both estimates correctly account for nearby jet and sample composition effects.

that both leptons pass the loose selections and at least one of them fails the tight selection. This control region has a significant real lepton contribution, but is enhanced in fake leptons with respect to the tight signal region, and its estimate using the matrix method is sensitive to the real lepton efficiency. Figure 5.4 shows good agreement between the data and the predictions of the simulation for real leptons plus the matrix method for fakes for the  $p_T > 25$  GeV jet multiplicity distribution. As with the same sign control region other distributions have been tested and also show good agreement.

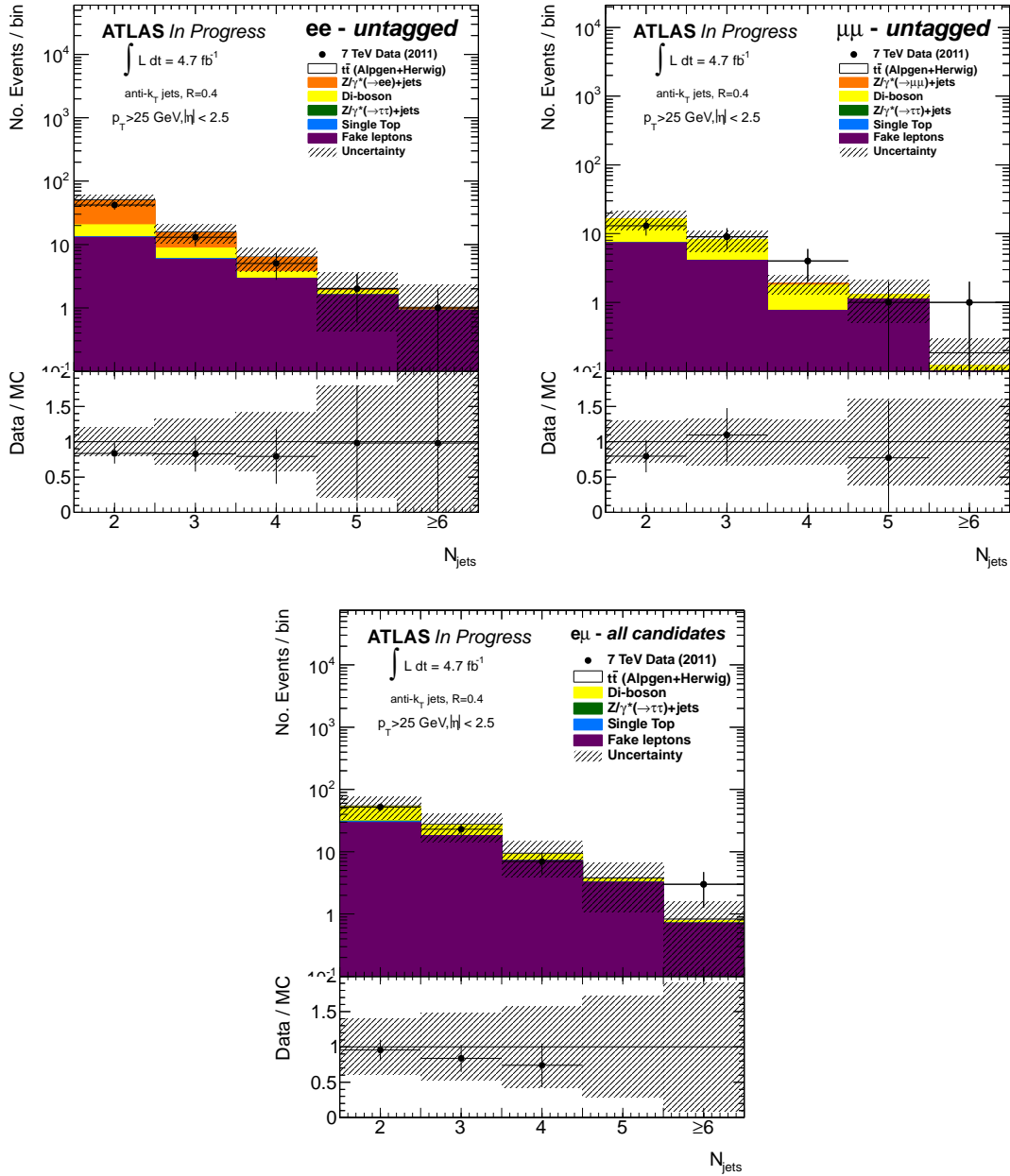


Figure 5.3: Multiplicities of jets with  $p_{\text{T}} > 25 \text{ GeV}$  for same-sign lepton events passing all other signal selections for the the  $ee$  (top left),  $\mu\mu$  (top right), and  $e\mu$  (bottom) channels.

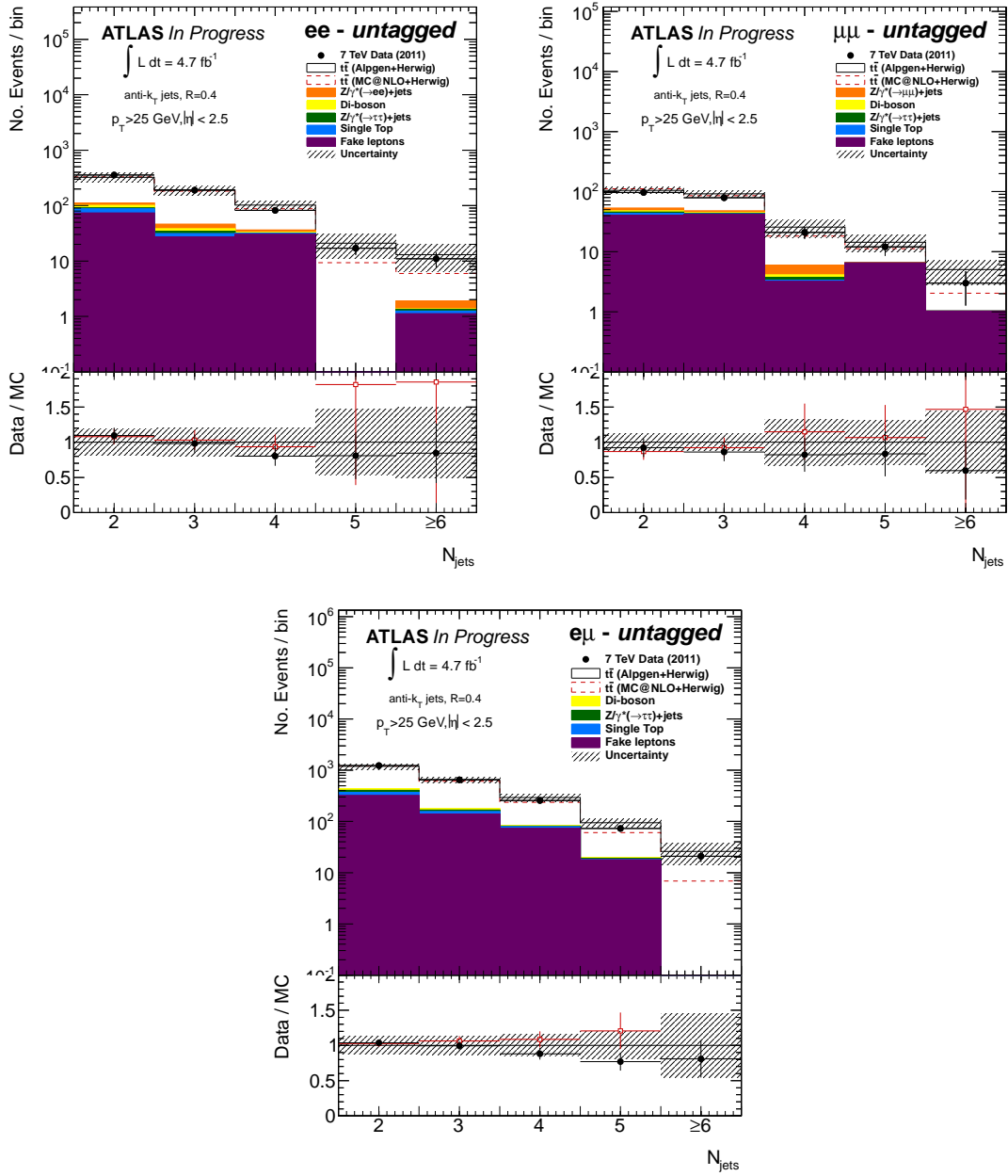


Figure 5.4: Multiplicities of jets with  $p_T > 25 \text{ GeV}$  for events where one lepton fails the tight selection criteria for the  $ee$  (top left),  $\mu\mu$  (top right), and  $e\mu$  (bottom) channels.

## 5.2.2 Drell-Yan contribution to $t\bar{t}$ events

In order to avoid large systematic uncertainties associated with modeling the high  $E_T^{\text{miss}}$  region in Drell-Yan (DY) events, the analysis uses a data driven method to estimate the contribution from this background to the  $t\bar{t}$  signal region. A control region (CR) similar to the  $t\bar{t}$  signal region (SR), but still dominated by  $Z$ +jets, is defined by applying all event selection requirements defined in Section 5.1 except for the following:

- **Cut 8** The  $E_T^{\text{miss}}$  cut is lowered to  $E_T^{\text{miss}} > 30$  GeV.
- **Cut 14** The invariant mass of the two selected leptons in the event is required to be within  $81 \text{ GeV} < M_{\ell\ell} < 101 \text{ GeV}$ . That is, this cut selects  $Z$ +jets events rather than vetoing them.

After selecting events in the control region in data, a scale factor ( $f_{\text{DY}}$ ) is derived from:

$$f_{\text{DY}} = \frac{N_{\text{CR}}^{\text{data}} - N_{\text{CR}}^{\text{bkg}}}{N_{\text{CR}}^{\text{signal}}}. \quad (5.2)$$

where  $N_{\text{CR}}^{\text{data}}$ ,  $N_{\text{CR}}^{\text{bkg}}$ , and  $N_{\text{CR}}^{\text{signal}}$  are the number of events in the control region in data, MC backgrounds, and MC signal, respectively. The scale factor  $f_{\text{DY}}$  is then applied to the ALPGEN  $Z/\gamma^*$ +jets in the  $t\bar{t}$  signal region. The method is not applied to the  $Z/\gamma^* \rightarrow \tau\tau$  contribution (where both  $\tau$  leptons decay leptonically) because the kinematics are different due to the presence of neutrinos resulting from the  $\tau$  decays. This contribution is a small percentage of the signal region and can be estimated from Monte Carlo.

Table 5.1 shows the yields and scale factors for each channel. There is a small difference between the estimates for the scale factors for the  $ee$  and  $\mu\mu$ , however, the values of the scale factors are consistent within their systematic uncertainties. This has been checked by calculating the ratio  $R_{\text{DY}} = f_{\text{DY},ee}/f_{\text{DY},\mu\mu}$  for each source of systematic uncertainty that is expected to be uncorrelated between the two channels. This ratio is found to be  $R_{\text{DY}} = 0.96 \pm 0.05$ , with the dominant components due to electron and muon efficiencies ( $\pm 3.1\%$  and  $\pm 1.6\%$ , respectively) and statistics ( $\pm 2.0\%$ ).

Figure 5.5 shows a comparison between the simulation and data of the jet multiplicity in the control region (after applying the scale factor). The shape is well reproduced by the

simulation indicating that the estimate is reliable.

Table 5.1: The number of Monte Carlo events in the control region for both DY sources and other processes, the number of observed events in data, and the calculated scale factor.

Channel	DY sources		Physics background sources (CR)					$f_{DY}$
	Data(CR)	MC(CR)	$t\bar{t}$	$Z\tau\tau$	W/Z fake	Di-boson	Single top	
$ee$	3153	2720	184	1	3	78	8	1.06
$\mu\mu$	7745	6487	392	1	1	171	16	1.10

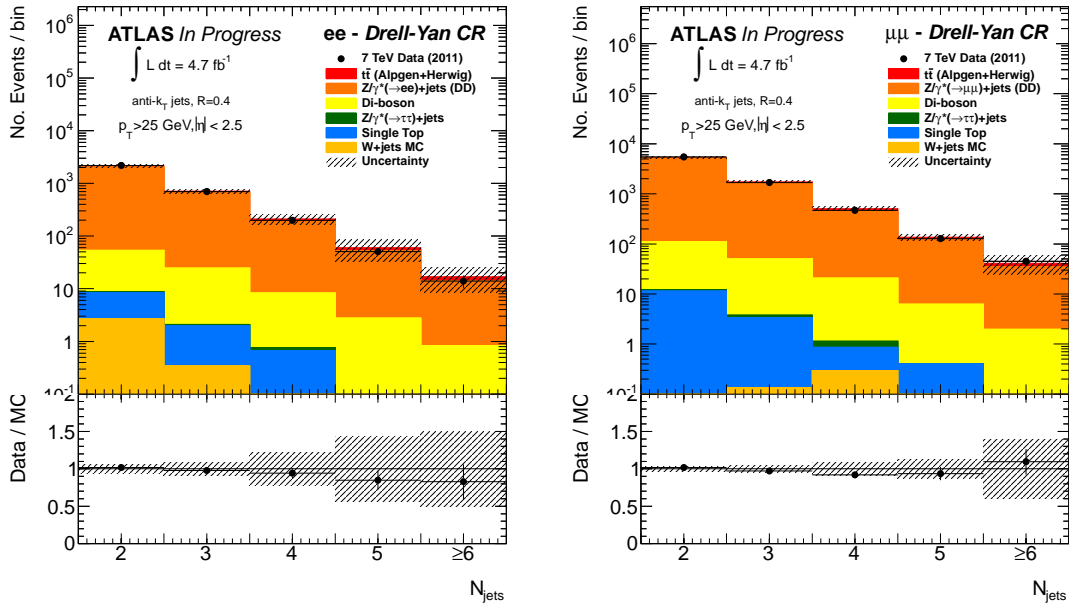


Figure 5.5: Multiplicity of jets with  $p_T > 25$  GeV for events in the  $Z/\gamma^* \rightarrow ee$  (left) and  $Z/\gamma^* \rightarrow \mu\mu$  (right) control regions.

### 5.2.3 Multi-jet background in $Z$ +jets events

Most background contributions to the  $Z$ +jets signal region are determined from the MC. For the same reasons as in the  $t\bar{t}$  signal region, events coming from QCD multi-jet events are estimated using a data-driven method. The method used is the same as the one used in the ATLAS  $Z$ +jets analysis [23]. The general idea is to derive QCD-dominated templates from events with two leptons which fail certain lepton ID requirements and fit the templates to the data along with MC signal templates to derive the fraction of QCD events in the data.

The template for the  $Z \rightarrow ee$  analysis requires that both electrons pass the loose identification selection, but fail the medium criteria. In addition, no isolation requirement is applied. Muons must pass all quality and ID requirements as in the analysis, except for isolation: an inverted isolation selection is applied by requiring that the muon track isolation variable satisfy  $p_{\text{T}}^{\text{cone},0.3}/p_{\text{T}} > 0.1$ .

The QCD templates are derived by applying the same selections as described at the end of Section 5.1 on events with two QCD enhanced leptons instead of the tight analysis leptons. Signal contributions to the multi-jet template are derived from the MC and subtracted. A binned-maximum likelihood template fit is performed on the di-lepton invariant mass distribution over the range  $60 \text{ GeV} < M_{\ell\ell} < 150 \text{ GeV}$  with bins of size 1 GeV. The QCD fractions determined from the fit are shown in Table 5.2. Several checks on the impact of binning, fit range, MC systematic variations, and individual fits as a function of jet multiplicity are performed.

Table 5.2: Fraction of the total yields attributed to multi-jet events as determined from the template fit for the  $Z \rightarrow ee$  and  $Z \rightarrow \mu\mu$  signal regions.

	0 jets	1 jet	2 jets	$\geq 3$ jets	Inclusive
$Z \rightarrow ee$ QCD fractions	0.03%	0.059%	0.071%	0.087%	0.035%
$Z \rightarrow \mu\mu$ QCD fractions	0.08%	0.23%	0.41%	0.68%	0.11%

## 5.3 Reconstruction-level results

### 5.3.1 $t\bar{t}$ signal region

Figure 5.6 shows the  $E_T^{\text{miss}}$  distribution for events passing all selections outlined in Section 5.1 for the  $t\bar{t}$  signal region. Besides showing good agreement between data and MC, the plots show relatively good purity of  $t\bar{t}$  events for the di-lepton channels.

The yields after all selections and their systematic uncertainties, binned in the number of reconstructed jets with  $p_T > 25$  GeV for the  $ee$ ,  $\mu\mu$ , and  $e\mu$  channels are shown in Tables 5.3, 5.4, and 5.5, respectively. The same tables for the higher  $p_T$  thresholds are available in the appendix.

Table 5.3: Yields as a function of reconstructed jet multiplicity for the di-electron channel. The total systematic uncertainty is shown for the expected numbers of events.

	$N_{\text{jets}}^{\text{reco}} = 2$	$N_{\text{jets}}^{\text{reco}} = 3$	$N_{\text{jets}}^{\text{reco}} = 4$	$N_{\text{jets}}^{\text{reco}} = 5$	$N_{\text{jets}}^{\text{reco}} \geq 6$
$Z/\gamma^*(\rightarrow \ell\ell)+\text{jets}$	$13.9 \pm 2.8$	$6.0 \pm 2.4$	$2.1 \pm 1.2$	$0.2 \pm 0.4$	$0.3 \pm 0.5$
$Z/\gamma^*(\rightarrow \tau\tau)+\text{jets}$	$11.6 \pm 3.8$	$5.6 \pm 2.5$	$1.2 \pm 1.0$	$0.3 \pm 0.5$	$0.0 \pm 0.2$
Fake leptons	$11.5 \pm 12.0$	$5.2 \pm 6.9$	$4.3 \pm 4.1$	$0.6 \pm 1.1$	$0.8 \pm 0.7$
Single top	$20.6 \pm 2.8$	$7.6 \pm 2.0$	$2.2 \pm 1.1$	$0.5 \pm 0.4$	$0.1 \pm 0.3$
Dibosons	$15.4 \pm 3.8$	$5.1 \pm 1.8$	$1.7 \pm 0.8$	$0.3 \pm 0.3$	$0.2 \pm 0.1$
Total Background	$73.0 \pm 14.3$	$29.5 \pm 8.9$	$11.5 \pm 4.7$	$1.9 \pm 1.5$	$1.4 \pm 1.2$
$t\bar{t}$	$321.9 \pm 21.4$	$193.9 \pm 14.2$	$78.1 \pm 9.2$	$26.8 \pm 4.7$	$10.5 \pm 2.4$
Expectation	$394.9 \pm 25.0$	$223.4 \pm 19.1$	$89.6 \pm 11.3$	$28.8 \pm 5.5$	$11.9 \pm 3.1$
Data	401	225	73	27	12

The jet multiplicity distributions are shown in Figures 5.7-5.10. In addition to these distributions, the data show fairly good agreement with the Monte Carlo for the ALPGEN  $t\bar{t}$  generator for most distributions important in this analysis, as discussed in Appendix A. Tables showing the break down of systematic uncertainties on the reconstructed distributions are also left for the appendix.

The predictions of the ALPGEN generator agree well with the data within the uncertainties at low jet multiplicity, but show a systematic trend of overestimating the data at

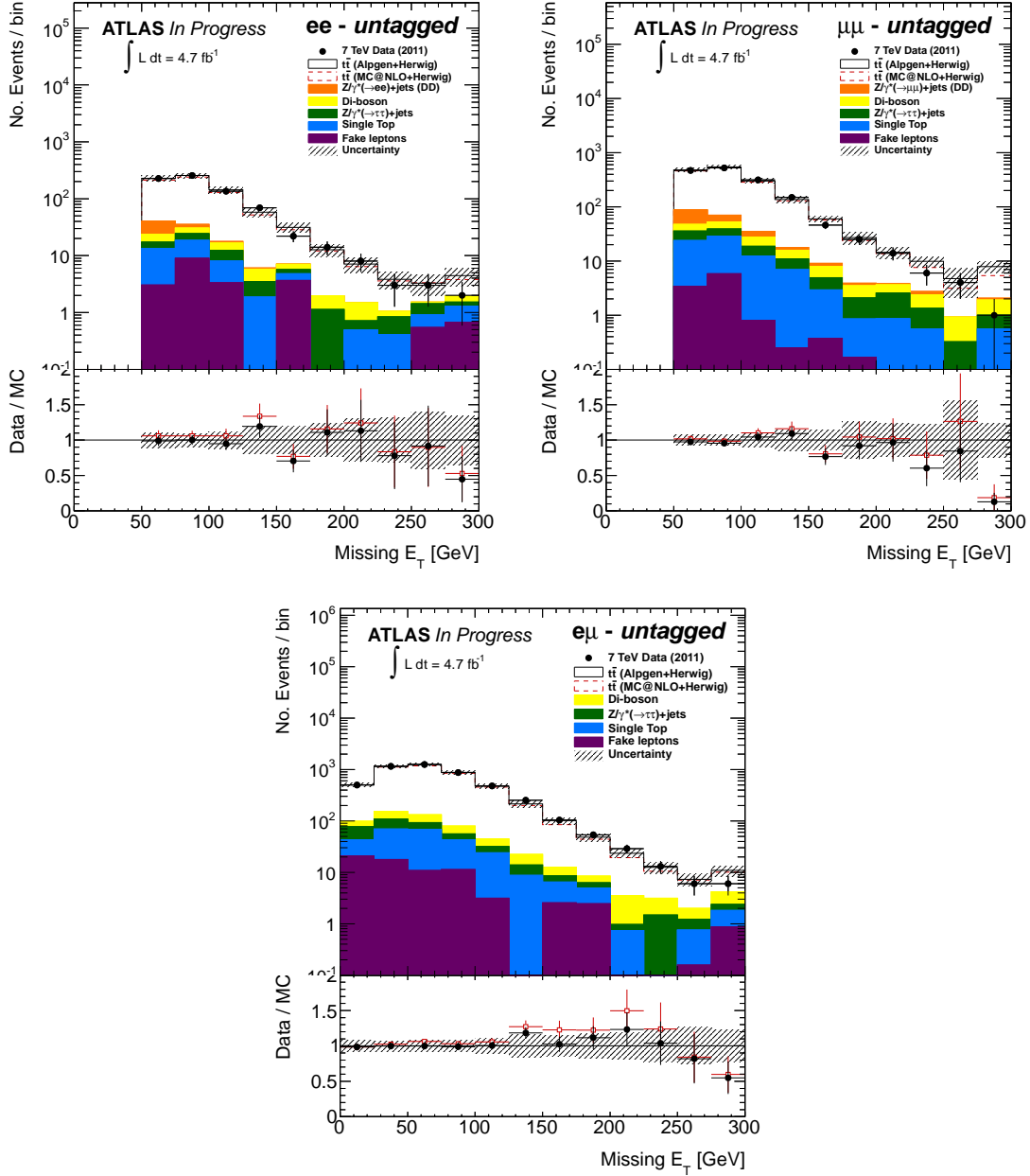


Figure 5.6:  $E_T^{\text{miss}}$  distributions for the  $ee$  (top left),  $\mu\mu$  (top right), and  $e\mu$  (bottom) channels. Note that the last bin includes overflow of events in the distribution (i.e. events with  $E_T^{\text{miss}} > 300$  GeV).

Table 5.4: Yields as a function of reconstructed jet multiplicity for the di-muon channel. The total systematic uncertainty is shown for the expected numbers of events.

	$N_{\text{jets}}^{\text{reco}} = 2$	$N_{\text{jets}}^{\text{reco}} = 3$	$N_{\text{jets}}^{\text{reco}} = 4$	$N_{\text{jets}}^{\text{reco}} = 5$	$N_{\text{jets}}^{\text{reco}} \geq 6$
$Z/\gamma^*(\rightarrow \ell\ell)+\text{jets}$	$38.9 \pm 10.6$	$19.1 \pm 9.8$	$7.2 \pm 3.2$	$3.9 \pm 2.3$	$0.2 \pm 1.1$
$Z/\gamma^*(\rightarrow \tau\tau)+\text{jets}$	$23.8 \pm 6.9$	$9.9 \pm 4.2$	$3.9 \pm 2.3$	$0.7 \pm 0.6$	$0.3 \pm 0.5$
Fake leptons	$4.7 \pm 2.8$	$4.6 \pm 2.7$	$0.4 \pm 0.8$	$0.8 \pm 0.7$	$0.2 \pm 0.3$
Single top	$45.9 \pm 5.1$	$15.4 \pm 2.1$	$4.0 \pm 0.9$	$1.2 \pm 0.6$	$0.7 \pm 0.5$
Dibosons	$34.3 \pm 8.2$	$9.5 \pm 3.4$	$2.4 \pm 1.3$	$1.1 \pm 0.7$	$0.3 \pm 0.4$
Total Background	$147.6 \pm 17.0$	$58.5 \pm 12.1$	$17.9 \pm 5.4$	$7.7 \pm 2.5$	$1.7 \pm 1.9$
$t\bar{t}$	$688.7 \pm 25.5$	$412.8 \pm 20.2$	$173.5 \pm 15.3$	$61.0 \pm 8.3$	$23.3 \pm 4.3$
Expectation	$836.3 \pm 30.0$	$471.3 \pm 24.8$	$191.4 \pm 17.8$	$68.7 \pm 9.2$	$25.0 \pm 5.7$
Data	836	460	181	57	20

Table 5.5: Yields as a function of reconstructed jet multiplicity for the  $e\mu$  channel. The total systematic uncertainty is shown for the expected numbers of events.

	$N_{\text{jets}}^{\text{reco}} = 2$	$N_{\text{jets}}^{\text{reco}} = 3$	$N_{\text{jets}}^{\text{reco}} = 4$	$N_{\text{jets}}^{\text{reco}} = 5$	$N_{\text{jets}}^{\text{reco}} \geq 6$
$Z/\gamma^*(\rightarrow \tau\tau)+\text{jets}$	$86.7 \pm 25.3$	$32.4 \pm 13.4$	$7.9 \pm 4.3$	$2.2 \pm 1.9$	$0.4 \pm 0.4$
Fake leptons	$36.3 \pm 34.3$	$17.4 \pm 21.0$	$13.5 \pm 12.8$	$2.2 \pm 2.9$	$0.5 \pm 0.9$
Single top	$142.2 \pm 14.7$	$46.4 \pm 6.9$	$12.5 \pm 1.8$	$2.0 \pm 0.8$	$1.1 \pm 0.5$
Dibosons	$119.5 \pm 28.3$	$32.5 \pm 11.4$	$8.0 \pm 3.7$	$1.7 \pm 1.0$	$0.5 \pm 0.3$
Total Background	$384.7 \pm 56.0$	$128.7 \pm 29.6$	$41.9 \pm 14.4$	$8.1 \pm 3.8$	$2.5 \pm 1.3$
$t\bar{t}$	$2150.6 \pm 94.5$	$1257.3 \pm 55.9$	$500.3 \pm 40.6$	$160.8 \pm 21.0$	$56.6 \pm 10.6$
Expectation	$2535.3 \pm 109.8$	$1386.0 \pm 70.4$	$542.2 \pm 45.0$	$168.9 \pm 22.4$	$59.1 \pm 11.0$
Data	2629	1404	482	143	60

high jet multiplicity up to 5 jets. In most cases, this is within, or on the outside edge of the uncertainties. The ALPGEN predictions for the inclusive 6 jet bin agree well with the data. In the 4 jet bin of the  $e\mu$  channel for the 60 GeV  $p_T$  threshold, there is a significant disagreement between the data and the predictions of the ALPGEN generator. Since ALPGEN is the main generator used for unfolding and for estimating the systematic uncertainties, it is important to check that this disagreement is not due to a mismodeling problem. Several tests detailed in Appendix A have shown that, when taking into account all bins of interest and their correlations, this deviation is consistent with a fluctuation of the data.

The predictions of the MC@NLO generator are also shown on the reconstructed distributions. These predictions again show good agreement at low jet multiplicity, but badly underestimate the data at high jet multiplicity. Similar tests as those performed addressing the agreement between ALPGEN and the data have also been performed for MC@NLO, showing large disagreement with that generator (see Appendix A).

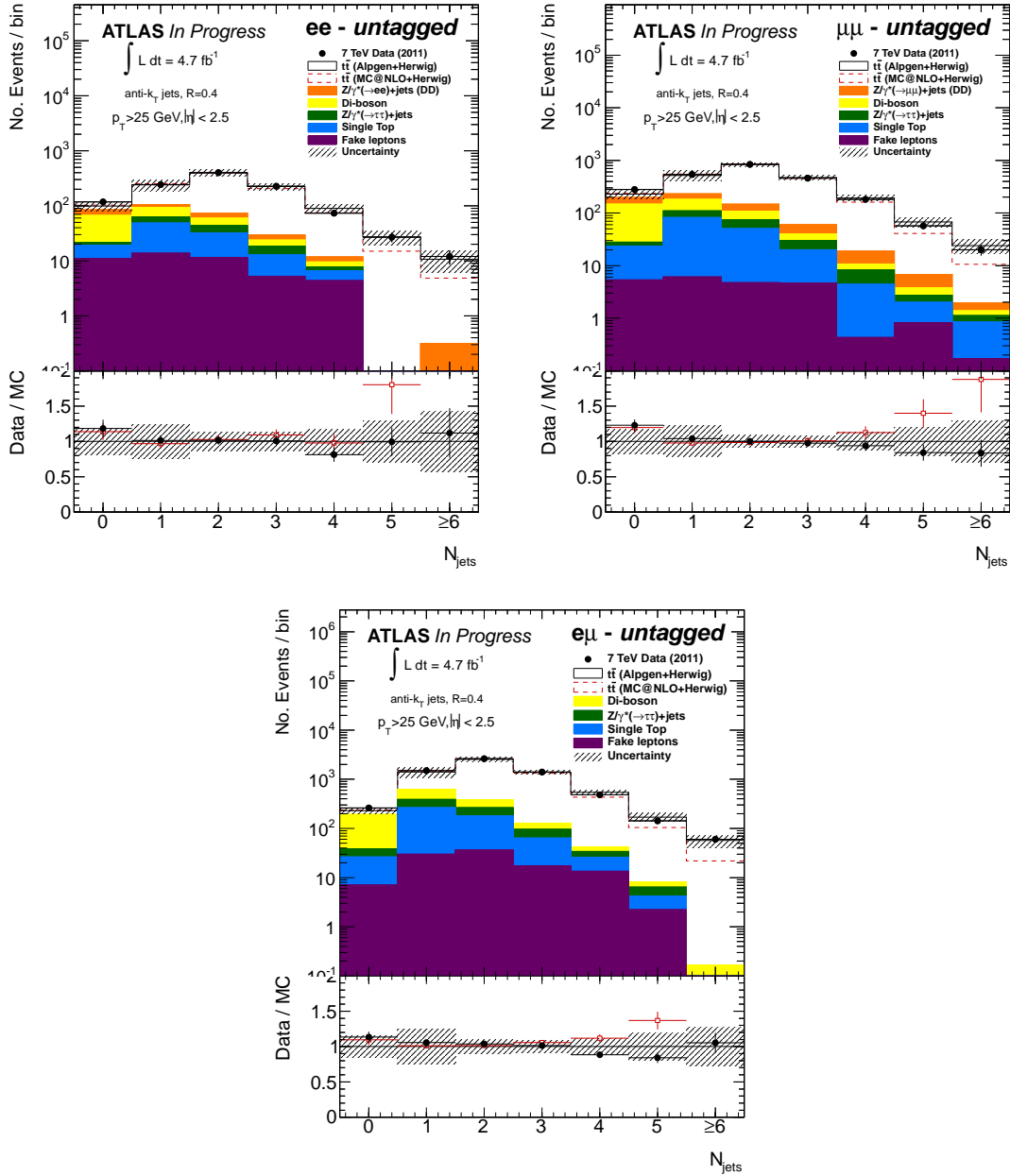


Figure 5.7: Reconstructed jet multiplicities with  $p_T > 25$  GeV for the  $ee$  (top left),  $\mu\mu$  (top right), and  $e\mu$  (bottom) channels for events passing all selections, except the jet multiplicity cut.

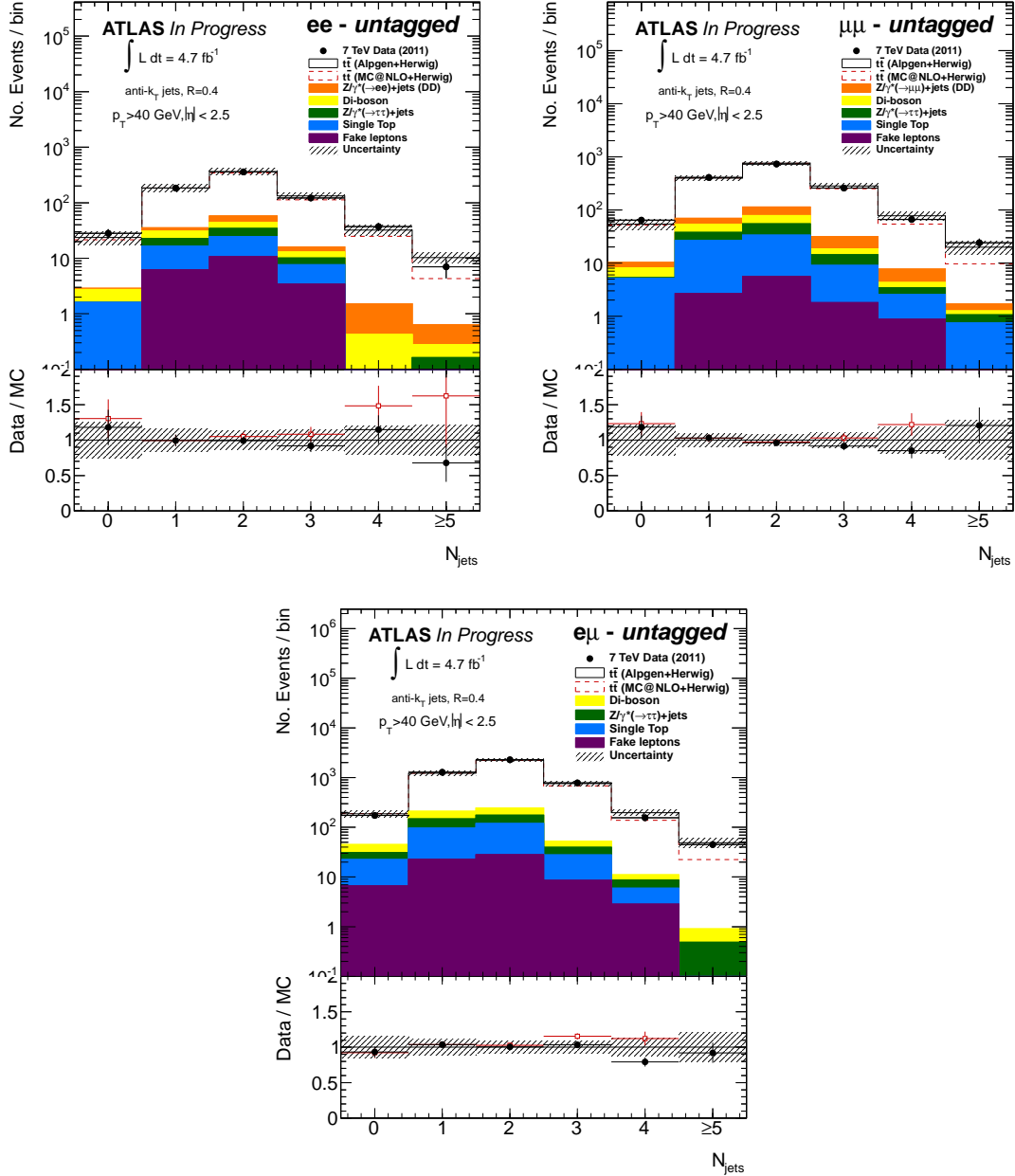


Figure 5.8: Reconstructed jet multiplicities with  $p_T > 40 \text{ GeV}$  for the  $ee$  (top left),  $\mu\mu$  (top right), and  $e\mu$  (bottom) channels for events passing all selections, including the jet multiplicity cut.

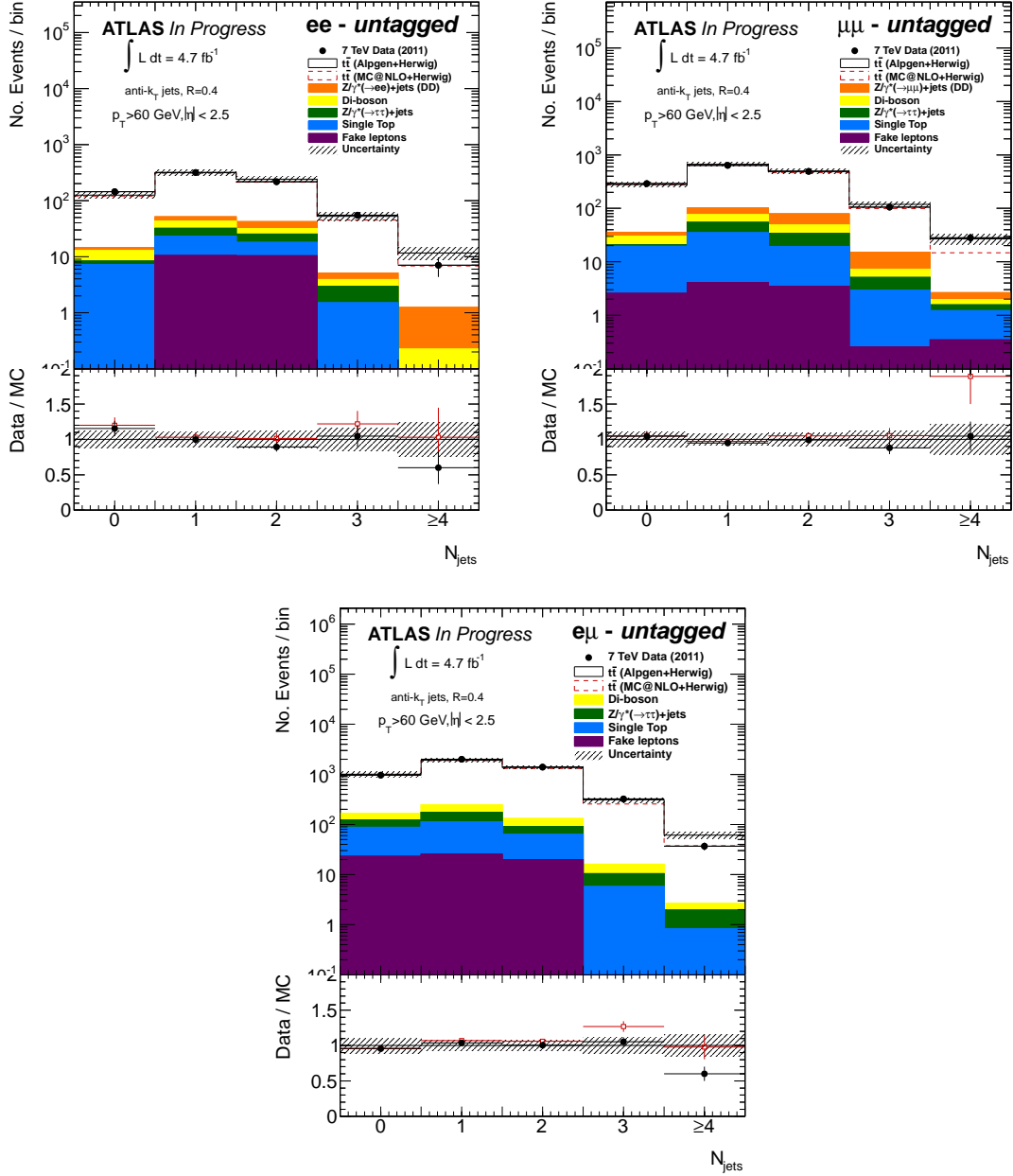


Figure 5.9: Reconstructed jet multiplicities with  $p_T > 60 \text{ GeV}$  for the  $ee$  (top left),  $\mu\mu$  (top right), and  $e\mu$  (bottom) channels for events passing all selections, including the jet multiplicity cut.

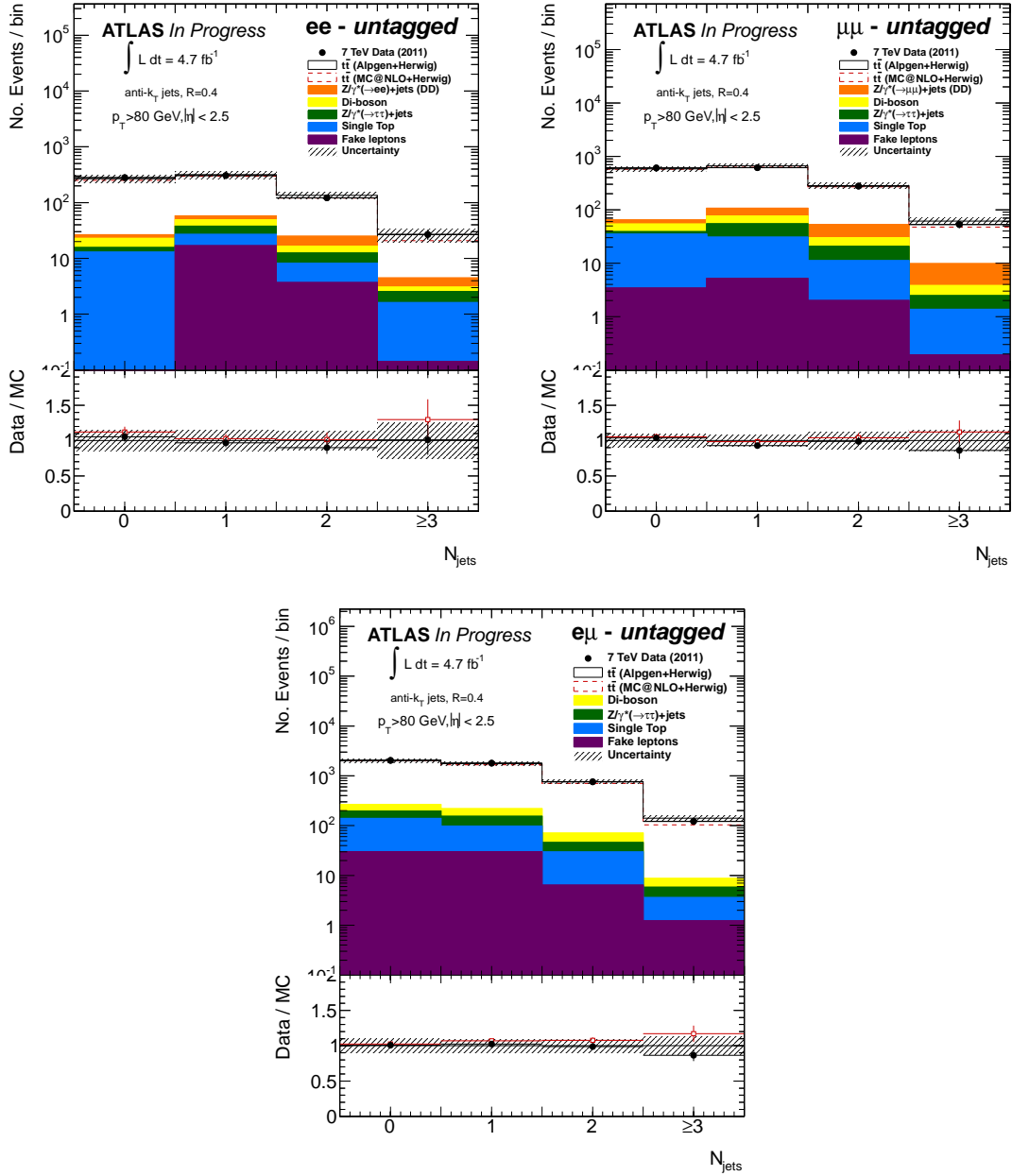


Figure 5.10: Reconstructed jet multiplicities with  $p_T > 80 \text{ GeV}$  for the  $ee$  (top left),  $\mu\mu$  (top right), and  $e\mu$  (bottom) channels for events passing all selections, including the jet multiplicity cut.

### 5.3.2 $Z$ +jets signal region

Figure 5.11 shows the reconstructed di-lepton invariant mass for events passing all  $Z$ +jets selection cuts except the di-lepton mass requirement (**Cut 14**). The sample is completely signal dominated, indicating that background systematic uncertainties will not significantly affect the ratio measurement. The yields in each reconstructed jet multiplicity bin after all selections for  $Z \rightarrow ee$  and  $Z \rightarrow \mu\mu$  events are shown in Tables 5.6 and 5.7, respectively. The distributions are shown in Figure 5.12. They show good agreement with the MC predictions within uncertainties.

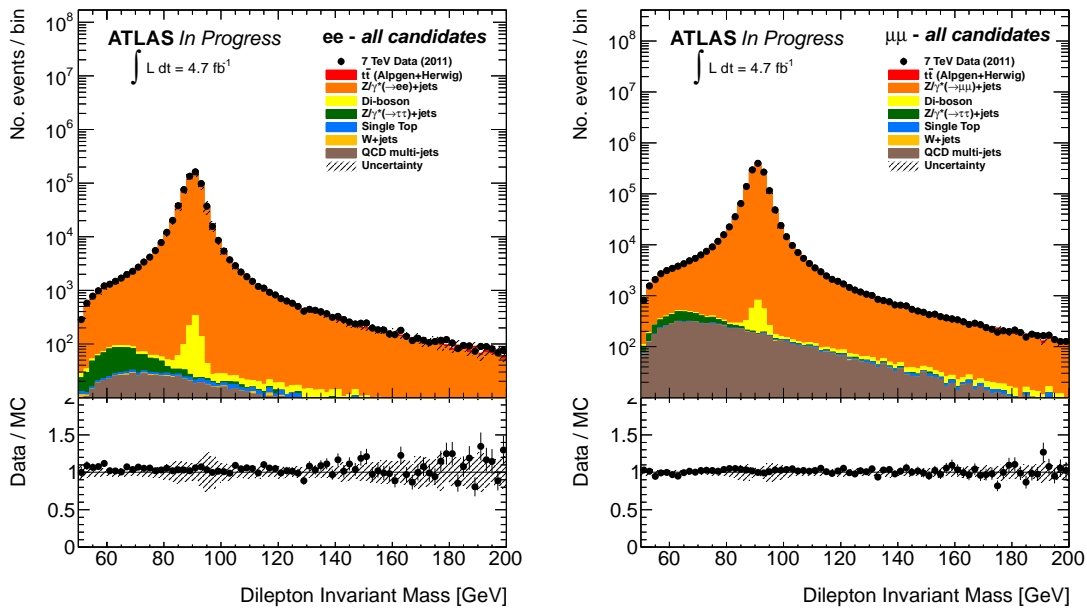


Figure 5.11: Reconstructed di-lepton invariant mass  $M_{\ell\ell}$  for all  $ee$  (left) and  $\mu\mu$  (right) candidates.

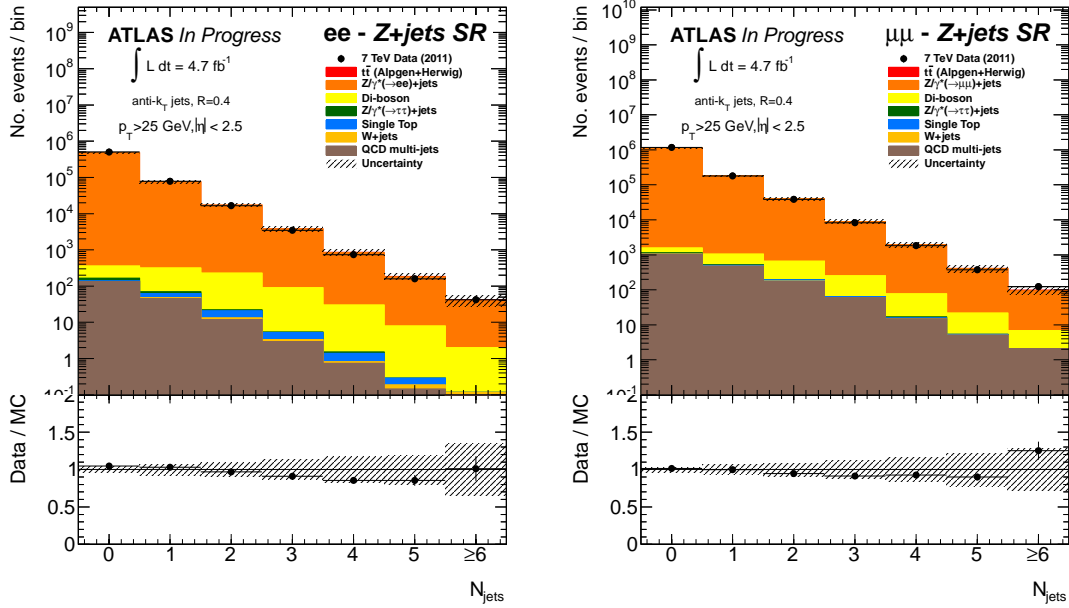


Figure 5.12: Reconstructed jet multiplicities with  $p_T > 25$  GeV for the  $Z \rightarrow ee$  (left) and  $Z \rightarrow \mu\mu$  (right) channels.

Table 5.6: Yields as a function of reconstructed jet multiplicity for the  $Z \rightarrow ee$  sample. The total systematic uncertainty is shown for the expected numbers of events.

	$N_{\text{jets}}^{\text{reco}} = 0$	$N_{\text{jets}}^{\text{reco}} = 1$	$N_{\text{jets}}^{\text{reco}} = 2$	$N_{\text{jets}}^{\text{reco}} = 3$	$N_{\text{jets}}^{\text{reco}} \geq 4$
$t\bar{t}$	$4 \pm 5$	$46 \pm 47$	$116 \pm 118$	$64 \pm 65$	$35 \pm 36$
QCD	$134 \pm 109$	$45 \pm 37$	$12 \pm 10$	$3 \pm 2$	$1 \pm 1$
$W$ +jets	$0.6 \pm 0.8$	$2 \pm 2$	$1 \pm 1$	$0.8 \pm 0.6$	$0.4 \pm 0.3$
$Z \rightarrow \tau\tau$ +jets	$27 \pm 4$	$7 \pm 3$	$1 \pm 1$	$0.1 \pm 0.2$	$0.1 \pm 0.1$
Single Top	$3 \pm 1$	$14 \pm 2$	$8 \pm 2$	$2 \pm 1$	$0.7 \pm 0.6$
Dibosons	$193 \pm 15$	$246 \pm 23$	$206 \pm 50$	$84 \pm 31$	$38 \pm 19$
Total Background	$362 \pm 115$	$360 \pm 66$	$344 \pm 132$	$154 \pm 81$	$75 \pm 43$
$Z \rightarrow \ell\ell$ +jets	$476364 \pm 17643$	$75404 \pm 5314$	$16822 \pm 1480$	$3662 \pm 443$	$1014 \pm 184$
Total Expected	$477726 \pm 17733$	$75764 \pm 5346$	$17166 \pm 1527$	$3816 \pm 501$	$1089 \pm 210$
Observed Events	499503	78107	16615	3475	936

Table 5.7: Yields as a function of reconstructed jet multiplicity for the  $Z \rightarrow \mu\mu$  sample. The total systematic uncertainty is shown for the expected numbers of events.

	$N_{\text{jets}}^{\text{reco}} = 0$	$N_{\text{jets}}^{\text{reco}} = 1$	$N_{\text{jets}}^{\text{reco}} = 2$	$N_{\text{jets}}^{\text{reco}} = 3$	$N_{\text{jets}}^{\text{reco}} \geq 4$
$t\bar{t}$	$11 \pm 11$	$99 \pm 101$	$241 \pm 246$	$133 \pm 135$	$78 \pm 80$
QCD	$1027 \pm 843$	$466 \pm 382$	$174 \pm 143$	$59 \pm 49$	$22 \pm 18$
$W$ +jets	$7 \pm 2$	$2 \pm 1$	$1 \pm 0.6$	$0.1 \pm 0.1$	$0.3 \pm 0.5$
$Z \rightarrow \tau\tau$ +jets	$90 \pm 10$	$14 \pm 3$	$2 \pm 2$	$0.8 \pm 0.6$	$1 \pm 0.9$
Single Top	$6 \pm 1$	$31 \pm 3$	$13 \pm 2$	$4 \pm 0.9$	$1 \pm 1$
Dibosons	$433 \pm 32$	$529 \pm 39$	$459 \pm 110$	$184 \pm 67$	$81 \pm 40$
Total Background	$1574 \pm 844$	$1141 \pm 398$	$890 \pm 307$	$381 \pm 159$	$183 \pm 92$
$Z \rightarrow \ell\ell$ +jets	$1154679 \pm 39031$	$178523 \pm 11712$	$39557 \pm 3362$	$8588 \pm 1021$	$2296 \pm 391$
Total Expected	$1156253 \pm 39030$	$179664 \pm 11759$	$40447 \pm 3413$	$8969 \pm 1056$	$2479 \pm 420$
Observed Events	1174483	179560	38249	8185	2310

## Chapter 6

# Extraction of the particle-level results

The results in Chapter 5.3 show the jet multiplicity of  $t\bar{t}$  events as measured by the ATLAS detector. These results are sensitive to migrations between jet multiplicity bins (i.e. events with a given “true” jet multiplicity can be reconstructed with a different multiplicity due to various detector effects). The results are also sensitive to object and event selection efficiency effects, generally affecting the overall normalization. In the reconstruction-level results shown previously, the magnitude of both of these effects is specific to the ATLAS experiment. The results are therefore not easily compared with other experiments or to generator predictions which have not been processed with the ATLAS detector simulation. To facilitate such comparisons, in a next step detector effects are removed through a process called “unfolding” [144, 145]. The strategy presented here is to unfold the background-subtracted reconstruction-level distributions of the jet multiplicity to truth-level (or particle-level). In general, unfolding algorithms undo detector effects by applying scale factors to account for efficiency effects and undo migrations either by using a migration matrix, which accounts for the probability for an event to migrate from one particular bin to another, or by applying additional bin-by-bin scale factors. Together, the efficiency scale factors and migration matrix are referred to as the response matrix, or just response.

Deriving these corrections necessitates defining how the particle-level jet multiplicity

distribution is determined (how the jets are clustered, what kinematic properties the jets, leptons, and neutrinos should have, etc.). In principle, any reasonable particle-level definition could be used, but there are practical considerations. Corrections for efficiency and migration effects must be estimated using the simulation and therefore have some dependence on the MC model used for their derivation. For example, one particular model may predict more central jets with respect to another and, given that the jet energy scale and resolution depend on the detector pseudorapidity, the choice of model has implications for the response matrix. In order to validate the model dependence of the unfolding corrections, kinematic selections which match closely to the reconstruction-level selections are applied to particle-level events in order to define the particle-level jet multiplicity. For example, by applying the same kinematic requirements on the leptons at the particle-level as in the reconstruction, the scale factors accounting for efficiency effects in the unfolding will not include large extrapolations to regions of phase space that the analysis does not measure, in this case events with low  $p_T$  or very forward leptons. With similar kinematic regions at the particle and reconstruction-levels, one can validate the estimates for the corrections by evaluating the data/MC agreement, which would not be possible in the extrapolation region. The particle-level selections used in this analysis are discussed in Section 6.1.

The main unfolding method used in this analysis first simultaneously corrects for efficiency (events passing the particle-level selections, but failing at the reconstruction-level) and so-called “fake” effects (events passing the reconstruction-level selections, but failing at the particle-level). Then the algorithm corrects for migration effects. Other orders of application of the corrections were also checked and found not to lead to significant differences in the final results, but the order used here allows for the best understanding of the model dependence and statistical uncertainties. Section 6.2 discusses the unfolding corrections in detail.

## 6.1 Particle-level object and event selections

Leptons are required to originate from a  $W$  or  $Z$  boson decay, including via a  $\tau$  lepton from a  $W$  boson. In the case of SHERPA, which does not include  $W/Z$  bosons and instead

evaluates matrix elements after electroweak boson decays, the lepton is required to not originate from a hadron decay. Both leptons are “dressed” to account for collinear photons radiated around the lepton by adding the four-momenta of all photons within  $\Delta R < 0.1$  of the final state lepton to its four-momentum. After dressing the leptons, they are required to have  $p_T > 25$  GeV and  $|\eta| < 2.5$ . This means a small extrapolation occurs in the electron case, where at the reconstruction-level the pseudorapidity cut only extends to  $|\eta| < 2.47$  and a veto is applied in the crack region ( $1.37 < |\eta| < 1.52$ ). The extrapolation is small and validated by checking that the kinematics of muons in di-lepton events are modeled well in the extrapolated regions. Identical cuts are applied for both electrons and muons in order to fully symmetrize the particle-level kinematic regions between each channel considered in this analysis, facilitating a combined measurement of all channels. Leptons are vetoed if their  $\eta$ - $\phi$  distance to the nearest good particle-level jet (defined below) is less than  $\Delta R < 0.4$ . Leptons passing the origin, kinematic, and lepton-jet distance requirements described here are referred to as “good” leptons.

Particle-level jet clustering is performed on all stable final state particles excluding charged leptons and neutrinos originating from  $W/Z$  boson decays, or not originating from hadrons in the case of SHERPA, regardless of the lepton kinematics. FSR dressing photons are also excluded from jet clustering. The same jet clustering algorithm (anti- $k_T$  with  $R = 0.4$  with the four-momentum recombination scheme) as used in the reconstruction is used here as well. Jets satisfying  $p_T > 25$  GeV and  $|\eta| < 2.5$  are called “good” jets.

For  $t\bar{t}$ , the following particle-level event selections are required:

- **Cut 1** Two good leptons are found.
- **Cut 2** At least two good jets are found.
- **Cut 3** For the  $ee$  and  $\mu\mu$  channels, the vector sum of the transverse momentum of all neutrinos originating from  $W$  bosons from top quarks (or not originating from a hadron in the case of SHERPA) must be greater than 60 GeV. For the  $e\mu$  channel the true  $H_T$  is required to be greater than 130 GeV.
- **Cut 4** For the  $ee$  and  $\mu\mu$  channels, the di-lepton invariant mass  $M_{\ell\ell}$  is required to be greater than 15 GeV.

- **Cut 5** For the  $ee$  and  $\mu\mu$  channels, the di-lepton invariant mass is required to satisfy ( $M_{\ell\ell} < 81$  GeV OR  $M_{\ell\ell} > 101$  GeV).

These selections are very similar to those presented in Section 5.1, allowing for easier validation of corrections derived from the ALPGEN+HERWIG generator, and for all other generators used for systematic uncertainties. Once all selections are made, particle-level jets passing the required  $p_T$  threshold are counted in order to estimate the unfolding corrections outlined in the next section.

When combining the results from the individual channels, the event selections outlined above need to be symmetrized between channels in order to avoid differences in the particle-level jet multiplicity due to kinematic effects. This is accomplished by dropping Cuts 3-5 at the particle-level, while retaining their corresponding selections at the reconstruction-level. This results in some extrapolation which is largest in the case of the  $ee$  and  $\mu\mu$  channels after dropping the  $E_T^{\text{miss}}$  selection at the particle-level. This model dependence can be reasonably well validated by comparing the reconstruction-level predictions of each generator with the data in the low  $E_T^{\text{miss}}$  region in the  $e\mu$  channel, where the Drell-Yan contribution is small, and also using a control region in the same-flavor channels where Drell-Yan is rejected using the presence of two  $b$ -tagged jets in place of the  $E_T^{\text{miss}}$  cut. The other smaller extrapolations (i.e. dropping the particle-level  $H_T$  cut for the  $e\mu$  channels and the  $M_{\ell\ell}$  cuts for the same flavor channels) are validated by cross-channel comparisons. These control regions are discussed in Appendix A. Note that this extrapolation is done only for the combination; the individual channel measurements must still pass Cuts 3-5.

For the  $t\bar{t}$ +jets/ $Z$ +jets jet multiplicity ratio measurement, the  $Z$ +jets particle-level selections use the same object definitions as for the  $t\bar{t}$  requirements. The  $Z$ +jets particle-level event selections are similar to the cuts used to select  $t\bar{t}$  events as described above, with the following changes:

- **Cut 2** No cuts are applied on the particle-level jet multiplicity.
- **Cut 3** No cuts are applied on the particle-level  $E_T^{\text{miss}}$  or  $H_T$ .
- **Cut 5** The di-lepton invariant mass is required to satisfy ( $81$  GeV  $< M_{ll} < 101$  GeV).

Since there is no difference between the  $Z \rightarrow ee$  and  $Z \rightarrow \mu\mu$  selections, no changes are necessary for the combination.

## 6.2 Unfolding method

### 6.2.1 Efficiency effects

After subtracting the backgrounds estimated in Section 5.2 from the jet multiplicity distributions measured in data, unfolding starts with an efficiency correction which is applied as a jet multiplicity dependent scale factor. This correction (called  $f_{\text{accpt}}$ ) simultaneously adds events passing at the particle-level but failing at the reconstruction-level, and removes events failing the particle-level selections, but passing at the reconstruction-level. It is derived by dividing the reconstruction-level jet multiplicity distribution of events passing all particle-level selections (save the particle-level jet multiplicity selection) by the same distribution of events passing all reconstruction-level selections. The correction for  $t\bar{t}$  events as estimated from the ALPGEN+HERWIG MC simulation is shown in Figure 6.1. The figure does not show the  $f_{\text{accpt}}$  correction for any of the  $E_{\text{T}}^{\text{miss}}/H_{\text{T}}/M_{\ell\ell}$  extrapolations.

In the case of events with electrons, reconstruction-level inefficiency is primarily due to one or both electrons failing the electron identification or isolation requirements. Since calorimeter clusters from electrons are also included in the jet clustering algorithm at the reconstruction-level and since unidentified electrons will not be used in the overlap removal stage to veto those jets, jets are vetoed if they overlap with any good particle-level electron ( $\Delta R < 0.2$ ) in cases where one or more electrons fails the reconstruction-level selections. This does not cause artificial migrations since particle-level electrons must have  $\Delta R > 0.4$  from the nearest particle-level jet.

The dominant contributions to the  $f_{\text{accpt}}$  factors are to the lepton trigger, reconstruction, identification, and isolation efficiencies at reconstruction-level. The effect is larger for events with electrons due to the lower electron efficiency ( $\sim 60\%$  for tight, isolated electrons). For muons, the efficiency is much closer to unity leading to a smaller correction. Several event quality selections are also applied at the reconstruction-level which are not applied at the particle-level (see Section 5.1), however, their corrections are found to be  $\sim 1$  after requiring

the presence of two particle-level and reconstruction-level leptons. Other event selections on  $E_T^{\text{miss}}$ ,  $H_T$ , and  $M_{\ell\ell}$  are all applied to both the reconstruction and particle-levels, so their contributions to  $f_{\text{accept}}$  are also close to unity. In the extrapolations for the combination, the  $E_T^{\text{miss}}$  extrapolation is largest and found to contribute an additional factor  $\sim 2$  to the  $f_{\text{accept}}$  correction in the same flavor channels.

As observed in the histograms in Figure 6.1, there is a small positive slope in  $f_{\text{accept}}$  with increasing jet multiplicity. This is due to the non-application of selections on track and calorimeter based isolation requirements at the particle-level which are applied at the reconstruction-level, as discussed in Chapter 4. Having more jets increases the likelihood that a jet will radiate out of its clustering cone and into the lepton isolation cone, thereby decreasing the isolation efficiency. Since the  $f_{\text{accept}}$  correction is not flat due to jet multiplicity effects on the lepton efficiency, it is important to validate that the efficiency is well modeled in the simulation in high jet multiplicity environments. This has been checked using a tag-and-probe method on  $Z$  boson events to measure the efficiency as a function of both  $N_{\text{jets}}$  and  $\Delta R(\ell, \text{nearest jet})$ . The measured efficiencies are found to be in good agreement with the predictions of the ALPGEN+HERWIG generator.

### 6.2.2 Migrations

After applying the acceptance correction, the result is a reconstruction-level jet multiplicity distribution which passes all particle-level selections. The distribution is therefore still sensitive to migrations, that is, events with a given particle-level jet multiplicity which are reconstructed with a different multiplicity due to one or more effects:

- Jet energy scale or resolution effects pushing a particle-level jet  $p_T$  above or below the threshold at the reconstruction-level.
- Jet angular resolution pushing a particle-level jet into or out of the pseudorapidity acceptance.
- Jets from the hard scatter failing the jet vertex fraction (JVF) selection used to reject pile-up jets (e.g. by picking up additional tracks from pile-up events).

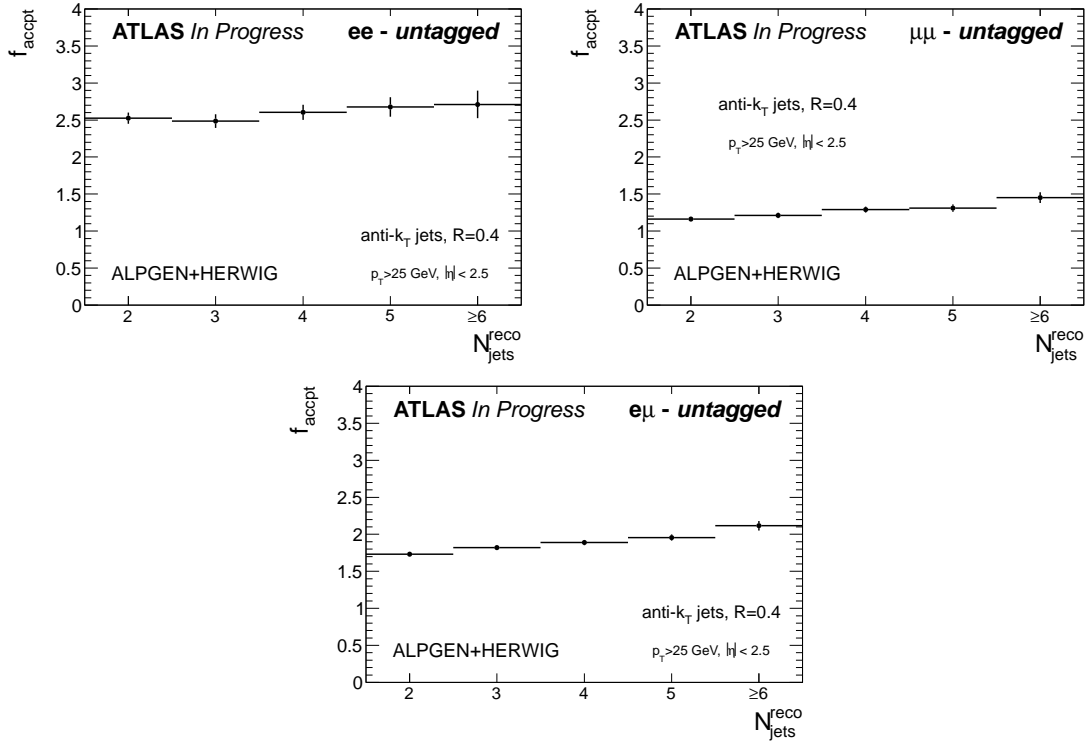


Figure 6.1: The acceptance correction,  $f_{\text{accept}}$  as a function of  $N_{\text{jets}}^{\text{reco}}$  for the  $ee$  (top left),  $\mu\mu$  (top right), and  $e\mu$  (bottom) channels as estimated from the ALPGEN+HERWIG generator for the  $p_T > 25$  GeV threshold. The error bars show the MC statistical uncertainties.

- Jets from pile-up events uncorrelated to the hard scatter passing the jet vertex fraction requirement.
- Jet splitting/merging due to noise or pile-up effects influencing the final clustered jet configuration at the reconstruction-level.

Migrations due to these effects are in general undone in three steps, the most crucial of which involves a migration matrix which specifies the probability for a migration from particle-level bin  $i$  to reconstruction-level bin  $j$ . To facilitate the unsmearing, the migration matrix should be an easily invertible  $n \times n$  matrix, where  $n$  should match the number of bins at the reconstruction-level. For  $t\bar{t}$  events, the analysis requires at least two reconstruction-level jets with  $p_T > 25$  GeV. The reconstruction-level distribution will contain events which originated with less than two particle-level jets which migrated into

the signal region, and a non-square migration matrix would be needed to account for them. Instead, those events are removed before defining a square migration matrix by applying an additional bin-by-bin scale factor called  $(1 - f_{\text{reco|part}})$ . This correction is derived by dividing two distributions, with the numerator being the reconstruction-level distribution passing all particle-level selections including the jet multiplicity, and the denominator passing all particle-level selections excluding the jet multiplicity (i.e. the numerator from the  $f_{\text{accpt}}$  correction). The correction is shown in Figure 6.2.

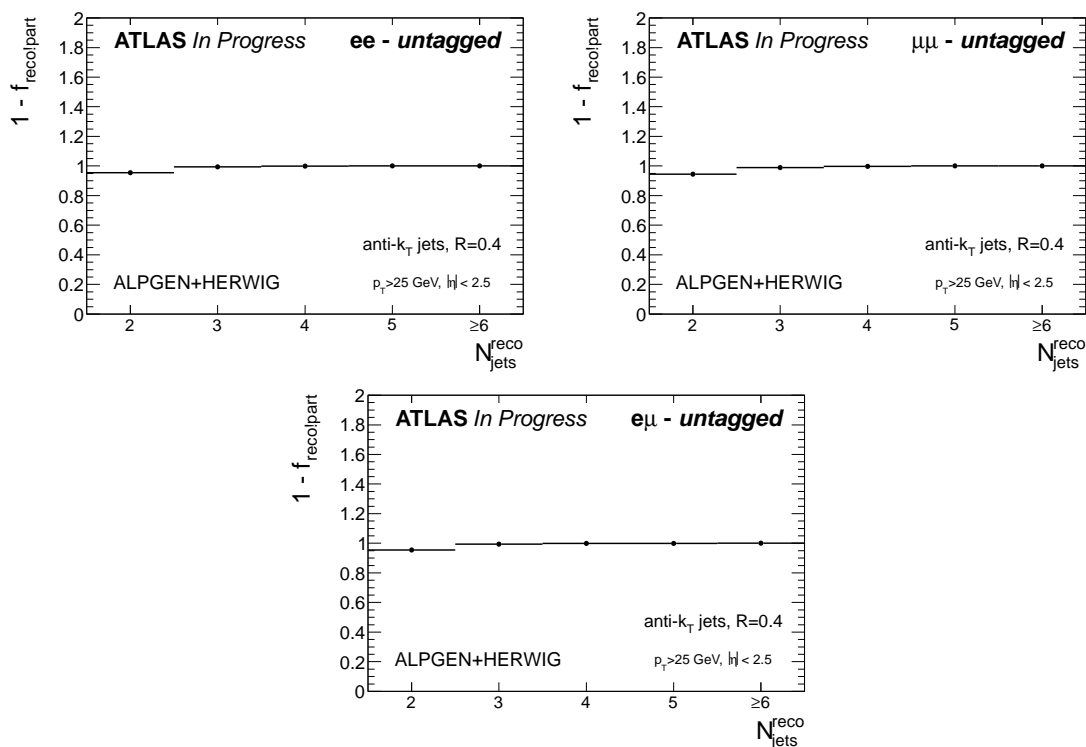


Figure 6.2: The migration correction made before unsmearing,  $(1 - f_{\text{reco|part}})$  as a function of  $N_{\text{jets}}^{\text{reco}}$  for the  $ee$  (top left),  $\mu\mu$  (top right), and  $e\mu$  (bottom) channels for the  $p_T > 25$  GeV threshold, as estimated using the ALPGEN+HERWIG generator.

After the bin-by-bin  $f_{\text{accpt}}$  and  $(1 - f_{\text{reco|part}})$  corrections, the main unsmearing correction can be performed. The migration matrix as estimated using the ALPGEN+HERWIG sample is shown for each channel in Figure 6.3. As seen in the figure, there is a slight bias towards events with fewer reconstructed jets than truth jets. This is largely due to the JVF selection. The inclusion of neutrinos and muons from hadron decays in the particle-

level jet definition also contributes to this bias. An additional feature of the figures is the statistically significant difference between the channels. This is due to the overlap removal between reconstruction-level jets and particle-level electrons in events with unidentified reconstruction-level electrons discussed above. No corresponding veto is needed in events with muons since they are not clustered as jets in the reconstruction. Pile-up jets overlapping with leptons or clustering of additional radiation from around the leptons can lead to extra jets at the reconstruction-level. In events with electrons, such jets are removed in the  $f_{\text{accept}}$  stage whereas in events with muons, the correction is applied in the migration stage.

Several methods were considered for unsmearing in this analysis [146, 147, 148]. The simplest method does not use the migration matrices from Figure 6.3. Instead, a bin-by-bin correction is applied which is derived by dividing the particle-level distribution by the reconstruction-level one. This method is called the “bin-by-bin” method and has the advantage of preserving the relative statistical uncertainties of the reconstruction-level distribution (statistical uncertainties tend to increase in other unfolding methods). However, it has the major disadvantage of biasing the result towards the shape of the predictions of the MC model used to derive the correction, especially if migrations are significant. This is because the method assumes that the ratio of the number of events that migrated into a given bin to the number of events that originated in that bin is the same in both the data and the MC, and this ratio depends on the shape of the true distribution. Since the particle-level jet multiplicity is what the analysis will measure and there would be no way to control this bias or correct it without first knowing how different the particle-level jet multiplicity in the MC is from the data, this method is not used.

Another simple unsmearing method (called matrix inversion) involves inverting the migration matrix and applying it to the reconstruction-level distribution to recover the particle-level one. This method is unbiased because it makes no assumptions about the shape of the particle-level distribution, only the probability that an event will migrate from one bin to another. The method is, however, much more sensitive to statistical fluctuations. This is due to the fact that significant off-diagonal elements lead to factors greater than 1 along the diagonals of the inverse, with some negative off-diagonal elements to preserve the total number of events in the full distribution. The negative elements of the inverse re-

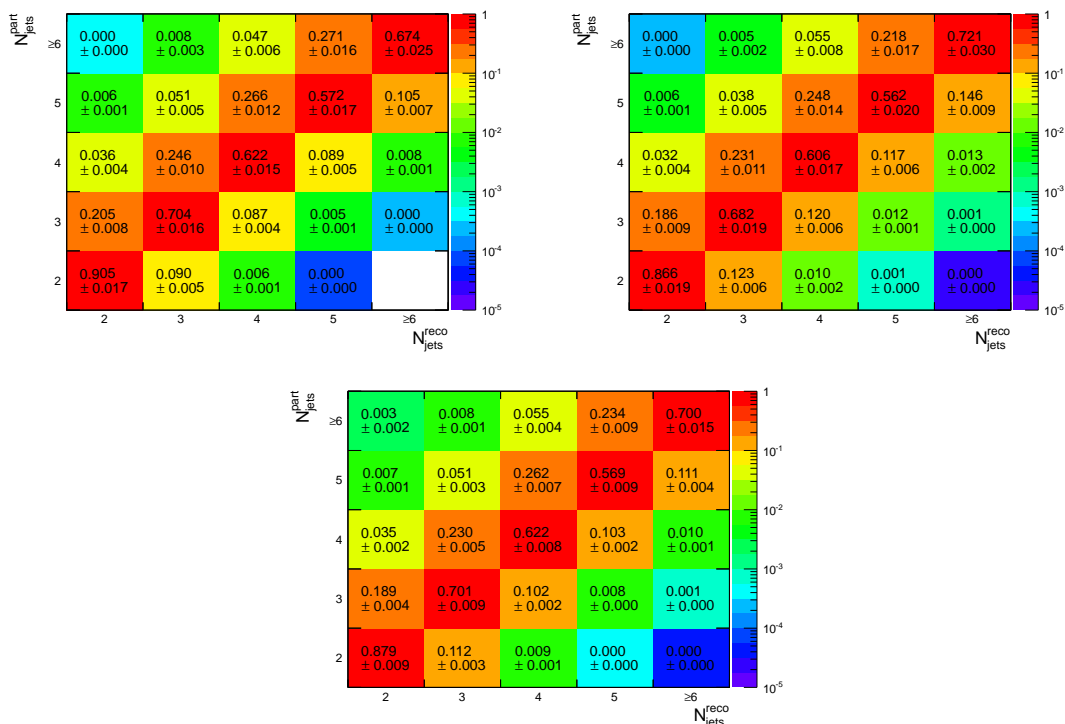


Figure 6.3: The migration matrix for the  $p_T > 25$  GeV threshold for events with at least two particle-level and reconstruction-level jets, used for the unsmearing algorithm for the  $ee$  (top left),  $\mu\mu$  (top right), and  $e\mu$  (bottom) channels, as estimated using the ALPGEN+HERWIG generator.

duce the particle-level estimate in a given bin, but increase the statistical uncertainty. The magnitudes of the elements depend on the size of the migration probabilities (the larger the migrations, the larger the elements of the inverse). The unfolded results of a given bin depend on the contents of all reconstruction-level bins and are therefore sensitive to statistical uncertainties in all bins, which are multiplied by the elements of the inverse. The result is a distribution with correlated, non-Poisson statistical uncertainties which can increase with respect to the reconstruction-level distribution depending on how probable migrations are. An intuitive way to understand this is that matrix inversion unsmearing interprets statistical fluctuations as underlying structure. So if fluctuations have the potential to be large (as they do in this analysis), results unfolded with the matrix inversion method will have large statistical uncertainties. This method is only used in this analysis as a cross-check.

The approach used to calculate the results in this analysis is the so-called iterative ‘‘Bayesian’’ method [146]. This method compromises between a potentially large and uncontrollable bias and large statistical uncertainties. The method starts with a prior probability distribution function (p.d.f.) for the particle-level jet multiplicity distribution and then uses the response matrix along with Bayes’ theorem to construct a probability that an event in reconstruction-level bin  $j$  came from particle-level bin  $i$ . One can then apply this probability to the reconstruction-level jet multiplicity distribution to get an unfolded distribution, which is then used as an updated prior p.d.f. The method can iterate as many times as the user likes, with each iteration bringing the result towards the unbiased but potentially highly fluctuating result.

To be concrete mathematically, consider  $\mathbf{p}$  to be a p.d.f. for the particle-level distribution so that  $N_{\text{events}} \times \mathbf{p}$  would equal the unsmeared jet multiplicity distribution  $\mathbf{d}$ . Then, to estimate the unfolded result for particle-level bin  $i$ , one can use the following equation:

$$d_j = \sum_i P(j|i)n_i. \quad (6.1)$$

where  $n_i$  is an element of the particle-level jet multiplicity distribution vector  $\mathbf{n}$ , the sum is over all jet multiplicity bins, and  $P(j|i)$  gives the probability that an event found in reconstruction-level bin  $j$  came from particle-level bin  $i$ .  $P(j|i)$  is not the same as the migration matrix  $P(i|j)$  which gives the probability for an event originating in bin  $i$  to be reconstructed in bin  $j$ , but it can be related using Bayes’ theorem:

$$P(j|i) = \frac{P(i|j)p_j}{\sum_k P(i|k)p_k}. \quad (6.2)$$

where  $p_j$  is one element of the p.d.f. vector,  $\mathbf{p}$ , and the denominator is just a normalization factor. Inserting Equation 6.2 into Equation 6.1, one arrives at:

$$d_j = \sum_i \frac{P(i|j)p_j}{\sum_k P(i|k)p_k} n_i. \quad (6.3)$$

The iterative approach starts with some initial prior p.d.f.  $\mathbf{p}_{\text{initial}}$  calculated from the MC and applies Equation 6.3 to the reconstruction-level vector  $\mathbf{n}$  to get an unfolded distribution  $\mathbf{d}$ . The vector  $\mathbf{d}$  will be biased, but improved with respect to  $\mathbf{n}$ , and can then be used as an

updated prior for a next iteration. The method limits sensitivity fluctuations by stopping after some number of iterations, at the price of a bias coming from the choice of initial prior. Thus an optimum number of iterations (four in this analysis) can be chosen such that the sensitivity of the result to statistical fluctuations is significantly reduced, while ensuring that the bias is smaller than other uncertainties (see Appendix B).

For the  $p_T > 25$  GeV threshold, unsmearing takes place on events with at least two particle and reconstruction-level jets. After applying the iterative unsmearing procedure, there are still events which pass all particle-level selections with more than two particle-level jets, but fail the reconstruction-level jet multiplicity cut and therefore, weren't in the migration matrix. These events must be added back to the distribution. This is also done with a scale factor applied as a function of  $N_{\text{jets}}^{\text{part}}$  called  $f_{\text{part}|\text{reco}}$  and is shown in Figure 6.4. Since this is also technically a migration correction, there is some structure in the low jet multiplicity region.

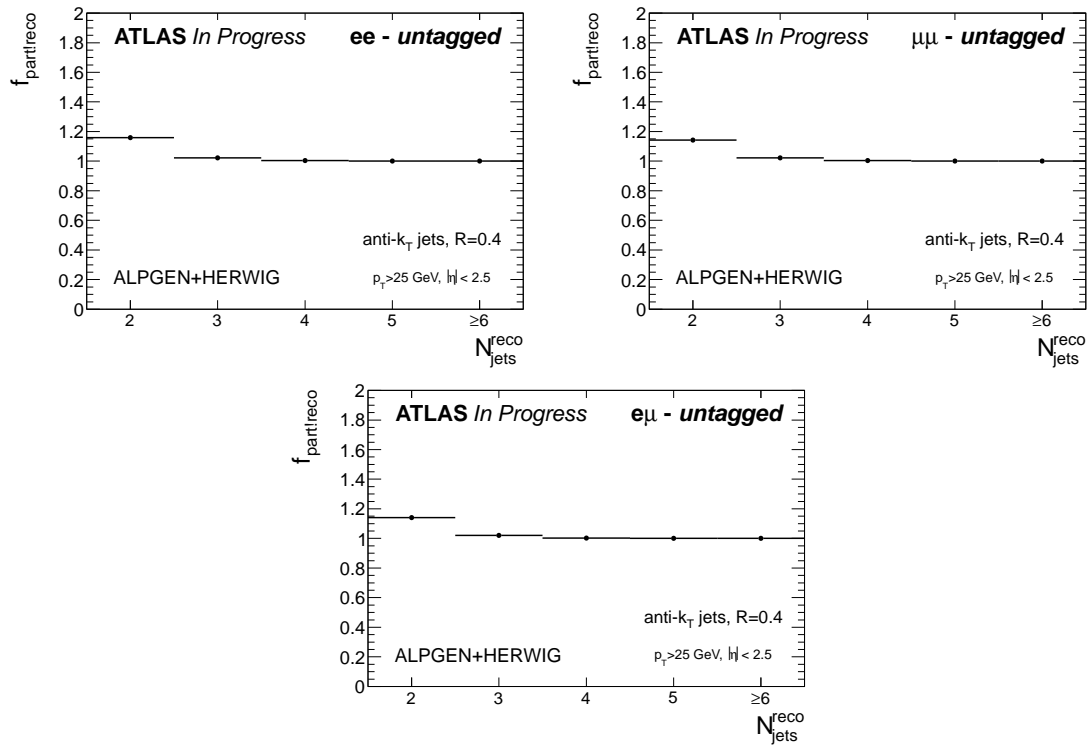


Figure 6.4: The  $f_{\text{part}|\text{reco}}$  scale factors as a function of  $N_{\text{jets}}^{\text{part}}$  for the  $ee$  (top left),  $\mu\mu$  (top right), and  $e\mu$  (bottom) channels for the  $p_T > 25$  GeV threshold.

In equation form, given a reconstructed jet multiplicity distribution on the data,  $F(N_{\text{jets}}^{\text{reco}})$ , the unfolded particle-level distribution  $G(N_{\text{jets}}^{\text{part}})$  can be obtained via:

$$G(N_{\text{jets}}^{\text{part}}) = f_{\text{part!reco}} M_{\text{reco}}^{\text{part}-1} ((1 - f_{\text{reco!part}}) f_{\text{accept}} (1 - f_{\text{bkg}}) F(N_{\text{jets}}^{\text{reco}})), \quad (6.4)$$

where  $M_{\text{reco}}^{\text{part}-1}$  is the iterative unsmearing procedure with four iterations discussed above.

### 6.2.3 Closure

The validity of the method is tested by so-called closure tests. The distributions in Figure 6.5 is obtained by performing the unfolding with corrections derived from the ALPGEN+HERWIG generator on its own reconstruction-level distribution. To simulate statistical independence, pseudo-experiments are performed whereby the unfolding corrections are smeared by their statistical uncertainties (correctly accounting for correlations in overlapping regions). The mean is taken as the central value and the RMS as the statistical uncertainty. Near perfect closure is achieved when using the same generator for both the reconstruction and unfolding, with small differences due to a limited number of pseudo-experiments (10,000 in this case). Comparing different generators for the reconstruction and unfolding is done as part of the systematic uncertainty estimation and is discussed in Chapter 7.

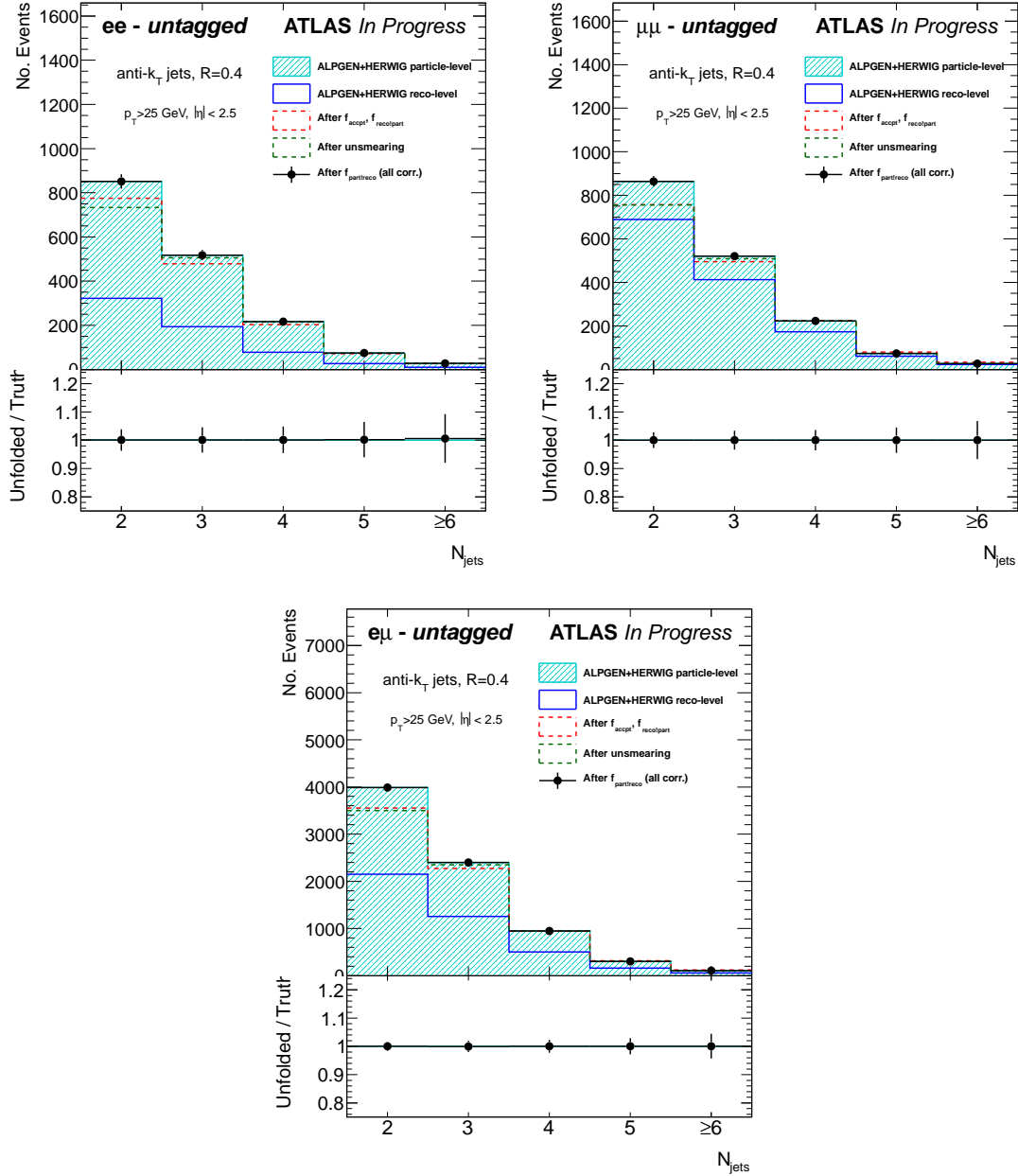


Figure 6.5: Closure tests for unfolding of  $p_T > 25$  GeV jet multiplicity distributions for the  $ee$  (top left),  $\mu\mu$  (top right), and  $e\mu$  (bottom) channels. The distribution after each individual correction is also shown.

### 6.2.4 $Z$ +jets unfolding

Unfolding on  $Z$ +jets events proceeds using the same method as in  $t\bar{t}$ , however since there is no jet multiplicity requirement, no  $(1 - f_{\text{reco!part}})$  or  $f_{\text{part!reco}}$  correction is needed. The features of the  $f_{\text{accept}}$  correction and the migration matrix are very similar to those observed in the  $t\bar{t}$  corrections histograms, with the largest contribution to the acceptance corrections due to lepton inefficiency and small differences in the  $Z \rightarrow ee$  and  $Z \rightarrow \mu\mu$  migration matrices due to the overlap removal between reconstructed jets and particle-level electrons in cases where the electrons fail the reconstruction-level cuts. Closure is demonstrated in Figure 6.6.

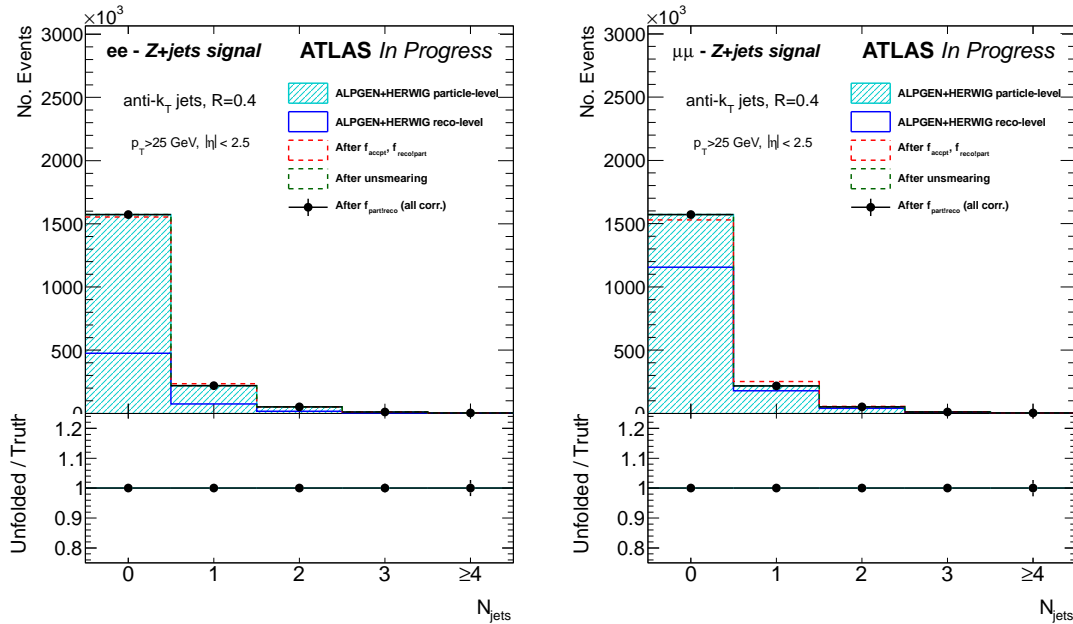


Figure 6.6: Closure tests for unfolding of  $p_T > 25$  GeV jet multiplicity distributions for the  $ee$  (left) and  $\mu\mu$  (right) channels. The distribution after each individual correction is also shown.

## Chapter 7

# Systematic Uncertainties on the Measurement

### 7.1 Sources of uncertainty

**Statistics** The cross-section measurements of this analysis are sensitive to statistical uncertainties in the data yields. The  $ee$  channel is particularly limited by statistical uncertainties at high jet multiplicity due to its lower efficiency. A combined measurement is made to reduce these sensitivities. There are also smaller statistical uncertainties on the MC estimates of the unfolding corrections and the backgrounds.

**Jets** Jet reconstruction leads to several important sources of systematic uncertainty. The jet energy scale (JES) measurement is based on a combination of MC and *in situ* techniques documented in Ref. [140]. The JES includes some  $\sim 60$  sources of uncertainty which are grouped into 21 nuisance parameters expected to be relatively uncorrelated. These nuisance parameters include statistical, modeling, and detector related uncertainties in the *in situ* JES measurements as well as accounting for additional uncertainties due to pile-up effects, non-closure<sup>1</sup>, close-by jets, and response dependence on jet flavor (that is, jets induced

---

<sup>1</sup>The *in situ* techniques were tested on the simulation and difference between the measured and true jet energy is taken as an additional source of uncertainty. This results in an uncertainty of less than 1 permil in most jet multiplicity bins for this analysis

from light quarks,  $b$  quarks, or gluons). Most *in situ* techniques involve measuring energies of jets predominantly induced from light quarks balancing photons or  $Z$  bosons. Quarks induced from gluons therefore have additional uncertainties and propagating their impact to the final results requires estimating the fraction of gluon induced jets in the signal sample. This is documented in Appendix C.1. The total JES uncertainty is usually dominant in this analysis, except in low statistics bins where statistical uncertainties dominate. In addition to the uncertainty on the jet energy scale, there are smaller uncertainties due to the jet energy resolution, the jet reconstruction efficiency, and the efficiency of the jet vertex fraction (JVF) selection used to reject pile-up jets.

**Leptons** Uncertainties due to electron and muon selection and reconstruction include the lepton energy/momentum scale, momentum resolution, and the trigger, reconstruction, identification, and isolation efficiency estimates. The muon momentum resolution is split between the uncertainty due to the Inner Detector measurement and the Muon Spectrometer measurement. Lepton measurements are relatively precise in the ATLAS experiment, so these have a small impact on the final results.

**Missing transverse momentum,  $E_T^{\text{miss}}$**  Uncertainties on the missing transverse momentum are mostly due to the uncertainties affecting the reconstructed objects input into the  $E_T^{\text{miss}}$  algorithm. The energy and resolution uncertainties on electrons, muons, and jets outlined above are also propagated to the  $E_T^{\text{miss}}$ . There is an additional uncertainty due to softer energy deposits in the calorimeter. Finally, an uncertainty due to the contribution of pile-up to the  $E_T^{\text{miss}}$  algorithm is also estimated. Both of these uncertainties are relatively small compared to the uncertainty on jet measurements.

**Backgrounds** Backgrounds estimated with MC simulation are affected by uncertainties on the object reconstruction described above. Several additional sources of uncertainty affect only the backgrounds. Due to the good purity of the  $t\bar{t}$  and  $Z$ +jets signal regions, uncertainties on the backgrounds have a small impact on the uncertainties of the final measurements.

Input cross-section uncertainties affect the normalization of the MC backgrounds. In

general these are included in a jet multiplicity dependent way, starting with  $\pm 4\%$  and adding 24% in quadrature for each  $p_T > 25$  GeV jet in the event. The exception is the  $t\bar{t}$  MC background to the  $Z$ +jets signal region in the ratio, where a 100% uncertainty is applied.

Luminosity uncertainties mainly affect absolute cross-section measurements. The results of this analysis are either presented as a ratio to the  $t\bar{t}$  inclusive cross-section ( $1/\sigma d\sigma/dN_{\text{jets}}$ ), or as a ratio to the  $Z$ +jets jet multiplicity, in order to increase sensitivity to the shape of the distributions. Therefore, the luminosity cancels and its effects are mitigated. The luminosity measurement does affect the MC background normalization. The estimated luminosity uncertainty on the 2011 dataset is 1.8%.

Uncertainties on the  $t\bar{t}$  fake lepton estimation are due to the uncertainties on the measured efficiencies and fake rates which are input into the matrix method calculation. These are varied independently by their one sigma shifts and the fake estimate is re-performed for their propagation to the jet multiplicity distribution.

The object reconstruction and cross-section normalization uncertainties are propagated to the MC component of the data-driven Drell-Yan estimation. Their effects are mitigated since the method constrains the total yields to the data (though the shape can change). Potential differences in the modeling of the shape of the MC distribution and the data lead to an additional uncertainty in the Drell-Yan background estimation. This is estimated by re-performing the estimate with events simulated with the SHERPA generator in place of ALPGEN+HERWIG.

The object reconstruction and cross-section normalization uncertainties are propagated to the MC signal templates in the QCD fake estimation for  $Z$ +jets events. The estimate is also performed with coarser binning and the difference between this and the nominal estimate is included as an uncertainty on the method.

**Unfolding** Aside from the statistical uncertainties in the unfolding corrections, two additional sources of uncertainty need to be considered for the unfolding. The first is possible systematic differences between the data and the MC in the response matrix used to define the unfolding corrections. Several choices are made in any MC model including the finite

order in perturbation theory in which the matrix element (ME) was calculated, the parton shower and fragmentation algorithms used, how probable it is for the parton shower to add additional radiation to the partonic final state, the simplified color reconnection scheme between final state partons, and the parton distribution functions (PDFs) used. The assumptions in each of these approximations leads to uncertainties which are estimated by comparing the simulated response matrices of two different generators (described in the next section). The comparison is always between generators which use the same methods of approximation in all but the assumption being tested (e.g. the parton shower algorithm used in order to estimate the parton shower systematic).

A second, much smaller source of uncertainty is that associated with the unfolding algorithm. This uncertainty is due to the method's sensitivity to the shape of MC jet multiplicity distribution used to define the unfolding corrections (i.e. the unfolding bias discussed in Chapter 6). With the unfolding method used in this analysis, this uncertainty is typically much smaller than the uncertainties in the response matrix. Also, it is already included in the response matrix uncertainty calculations due to the way they are estimated (see Section 7.2). Thus, they are not independently included in the total uncertainty estimate. They are however estimated as a cross-check (see Appendix B).

The uncertainty due to the fragmentation model is estimated by comparing the response matrices of the nominal ALPGEN+HERWIG generator and ALPGEN+PYTHIA. The HERWIG model uses an angular ordered parton shower with cluster-based fragmentation and the PYTHIA model uses a  $k_T$  ordered shower with string fragmentation. The uncertainty due to the ME calculation is estimated by comparing the ALPGEN generator, with its leading order multi-leg ME calculation, and the POWHEG generator with its next-to-leading order ME, both showered using PYTHIA. The ALPGEN+PYTHIA generator was re-tuned for more and less radiation by varying  $\alpha_s$ , for both the ME and the parton shower, by replacing  $\alpha_s(k_T)$  (that is, the value of the running coupling calculated at the scale of the transverse momentum carried away by the emitted parton,  $k_T$ ) by  $\alpha_s(0.5k_T)$  for more radiation or  $\alpha_s(2k_T)$  for less. Their simulated response matrices are compared to assess the uncertainty due to the effects of more or less initial/final state radiation (I/FSR) on the unfolding. Color reconnection refers to the interference between nearby colored systems and can perturb

the final state configuration. Simplified models are used in MC generators to account for the effects of color reconnection. To assess the uncertainty on the model, the response matrices of the POWHEG+PYTHIA generator both with and without color reconnection effects included are compared. Finally, the uncertainty on the PDF used to generate signal MC events which define the unfolding corrections must also be considered. This uncertainty is estimated by reweighting events to match the PDFs in the CT10, MSTWNLO2008, and NNPDF2.3 sets and their corresponding uncertainties. An envelope covering the extremes of the results from all reweighted distributions is taken as the systematic uncertainty.

## 7.2 Propagation of uncertainties

In order to check the effect of the statistical and systematic uncertainties on the unfolded results, the propagation of uncertainties proceeds using pseudo-experiments. For each source of uncertainty, 1000 pseudo-experiments are performed. In each pseudo-experiment, the nominal (un-varied) background is subtracted from varied pseudo-data before unfolding with the nominal corrections. The exception is the estimation of the statistical uncertainty affecting the signal MC where the unfolding corrections are varied.

Statistical uncertainties are propagated by independently smearing each bin of the reconstructed results, or the histograms used to derive the unfolding corrections in the case of the signal MC. The impact of limited data statistics is calculated by smearing each bin in the data according to a Poisson distribution about the observed number of events before subtracting the nominal background and applying the nominal unfolding. For the statistical uncertainty in the signal MC, the histograms defining the unfolding corrections are smeared according to Gaussian distributions (correctly accounting for statistical correlations of overlapping regions) before unfolding a pseudo-data defined by an unsmeared signal MC reconstruction-level distribution. For the backgrounds, the reconstruction-level MC background jet multiplicity distributions are smeared according to Gaussian distributions and added to the signal MC distribution before subtracting the nominal background and unfolding. For all statistical uncertainties, after all pseudo-experiments are performed, the bin-to-bin covariance can be statistically estimated using the equation:

$$C_{ij} = E[(x_i - E[x_i])(x_j - E[x_j])] \quad (7.1)$$

where  $x_i$  is the unfolded content in bin  $i$  and  $E[x_i]$  is the mean of all experiments. The statistical uncertainty on a single bin is quoted as the square-root of the variance,  $\sigma_i = \sqrt{C_{ii}}$ .

Individual sources of systematic uncertainty (nuisance parameters) are assumed to be uncorrelated with each other, but to lead to fully correlated bin-to-bin and sample-to-sample uncertainties in the jet multiplicity distributions. These uncertainties are estimated by varying the nuisance parameter up and down by one sigma (defined by the 68% confidence interval of the best estimate of the parameter). The object and event selections are re-performed on the signal and background MC samples to produce one sigma variations in the jet multiplicity. The statistical pseudo experiments described above are performed on the one sigma shifted distributions. The difference between the means of the shifted pseudo experiments and the nominal is taken as the systematic uncertainty. In cases where the up and down one sigma systematic uncertainties are different, the larger uncertainty is kept and symmetrized.

Systematic uncertainties on the response matrix are estimated using a relative bias method. The goal of this method is to measure the effect of unfolding with a response matrix which is potentially different than the “true” response due to signal modeling assumptions. This is accomplished by unfolding a reconstruction-level distribution of one generator with the unfolding corrections defined by a different model, and comparing to the case where the distribution is unfolded with its own response. The difference between the two unfolded results is taken as the systematic uncertainty. Due to some generators having low statistics, elements of the response matrices from each channel are combined (where appropriate) before performing the test.

## Chapter 8

# Results and Conclusions

### 8.1 $t\bar{t}$ measurement

The unfolded results for the  $p_T > 25, 40, 60$  and  $80$  GeV thresholds are shown for the  $ee$ ,  $\mu\mu$ , and  $e\mu$  channels in Figures 8.1, 8.2, and 8.3, respectively. The total number of events is normalized to unity, that is, the results are presented as  $\frac{1}{\sigma_{t\bar{t}}} \frac{d\sigma_{t\bar{t}}}{dN_{\text{jets}}}$ . A breakdown of systematic uncertainties for each distribution is shown in Tables 8.1-8.12. More details on the systematic uncertainties are available in Appendix C.2.

In order to compare their performance, the predictions of several generators are superimposed on the data, together with their statistical uncertainties (no theoretical uncertainties are included on the predictions). The ALPGEN+HERWIG generator shows generally good agreement with the unfolded result with a small systematic trend towards an over estimate of the data at high jet multiplicity. This difference is consistent within the statistical and systematic uncertainties in most cases. The MC@NLO+HERWIG generator also agrees well with the data at low jet multiplicity, but systematically underestimates the data at high jet multiplicity. This is not unexpected, since MC@NLO only explicitly calculates matrix elements for  $t\bar{t}$  plus up to one additional hard parton. This also confirms observations of the performance of MC@NLO in several other analyses in describing jet multiplicity distributions [25, 149]. The predictions of the POWHEG+PYTHIA and SHERPA generators are similar to those of ALPGEN+HERWIG. Like ALPGEN, SHERPA is a multi-leg matrix element generator, so similar predictions are expected for those two generators. It is surprising

that the predictions of POWHEG, an NLO generator (which, like MC@NLO, only explicitly calculates one real emission), performs similarly to the multi-leg generators. The predictions of the ALPGEN+PYTHIA generator along with tunings for more/less initial/final state radiation will be compared with the combined measurement in Section 8.3.

The  $ee$  and  $\mu\mu$  channels are statistically limited in many bins, with the statistical uncertainties becoming dominant for events with more than  $\sim 4$  jets. The largest systematic uncertainty in all channels at high jet multiplicity comes from the JES (part of the “Jets” uncertainties in the tables). Several studies briefly discussed in this thesis have been performed which attempt to reduce the JES uncertainty as much as possible. Additional effort to reduce this systematic uncertainty for this analysis by considering the ratio of the jet multiplicities in  $t\bar{t}$  and  $Z$ +jets events will be discussed in the next section.

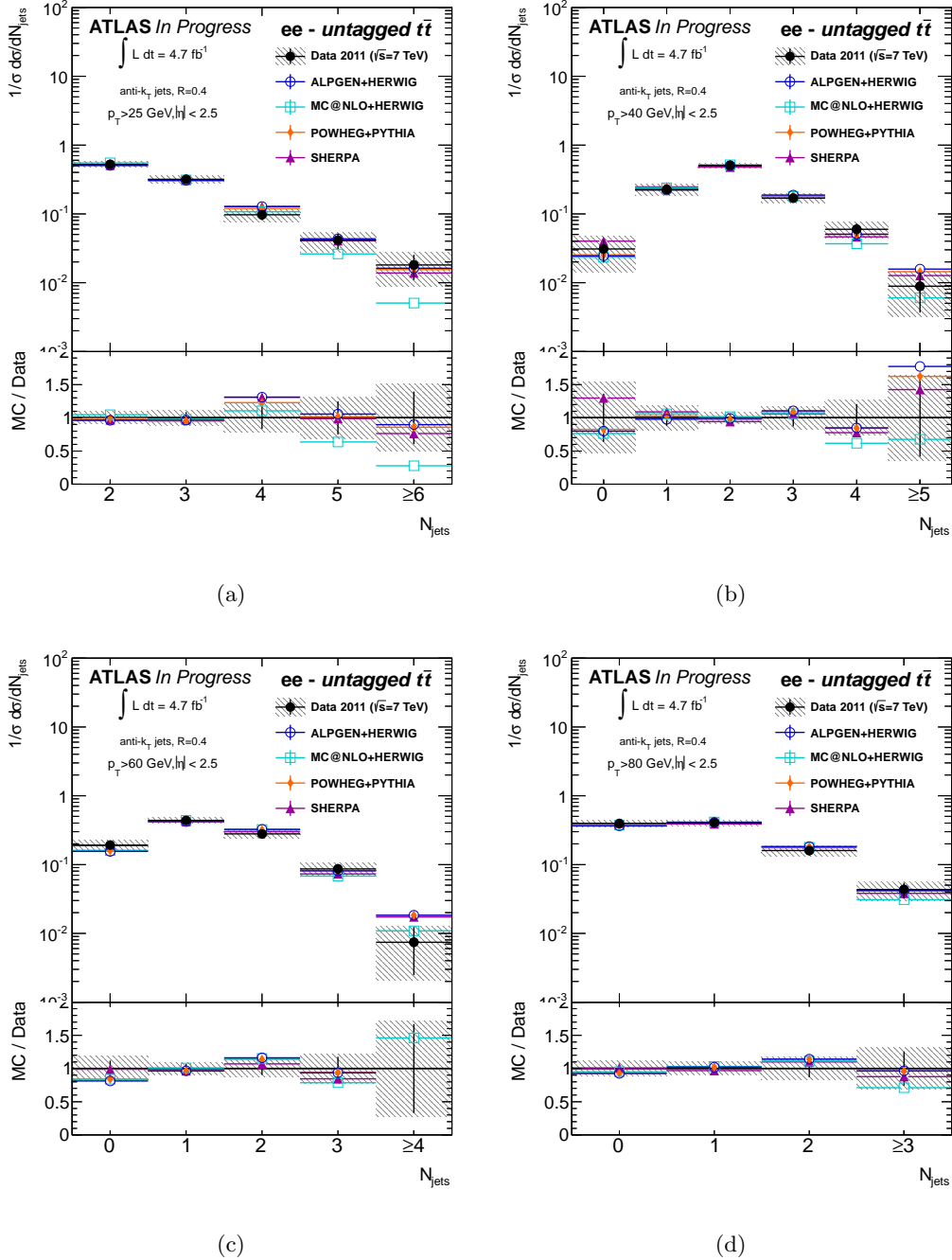


Figure 8.1: The unfolded di-electron  $t\bar{t}$  particle-level jet multiplicity differential cross-sections for the (a) 25, (b) 40, (c) 60, and (d) 80 GeV  $p_T$ -thresholds.

Table 8.1: Relative uncertainties (in %) for the  $ee$ -channel for the  $p_T > 25$  GeV threshold measurement.

	2 jets	3 jets	4 jets	5 jets	$\geq 6$ jets
Statistics	$\pm 6.4$	$\pm 10.3$	$\pm 18.1$	$\pm 26.4$	$\pm 41.6$
Backgrounds	$\pm 0.7$	$\pm 0.6$	$\pm 2.9$	$\pm 3.0$	$\pm 3.4$
Jets	$\pm 6.8$	$\pm 4.7$	$\pm 9.8$	$\pm 17.4$	$\pm 28.4$
Leptons	$\pm 0.5$	$\pm 0.8$	$\pm 1.1$	$\pm 1.2$	$\pm 1.7$
$E_T^{\text{miss}}$	$\pm 0.3$	$\pm 0.6$	$\pm 1.6$	$\pm 0.9$	$\pm 1.1$
Unfolding	$\pm 1.0$	$\pm 2.0$	$\pm 2.6$	$\pm 2.7$	$\pm 5.1$
All Syst	$\pm 6.9$	$\pm 5.3$	$\pm 10.8$	$\pm 17.9$	$\pm 29.1$
Syst + Stat	$\pm 9.4$	$\pm 11.6$	$\pm 21.0$	$\pm 31.9$	$\pm 50.8$

Table 8.2: Relative uncertainties (in %) for the  $ee$ -channel for the  $p_T > 40$  GeV threshold measurement.

	0 jets	1 jet	2 jets	3 jets	4 jets	$\geq 5$ jets
Statistics	$\pm 47.1$	$\pm 14.5$	$\pm 7.2$	$\pm 14.7$	$\pm 22.6$	$\pm 60.4$
Backgrounds	$\pm 6.9$	$\pm 3.6$	$\pm 1.7$	$\pm 1.2$	$\pm 2.8$	$\pm 7.1$
Jets	$\pm 20.1$	$\pm 9.8$	$\pm 3.8$	$\pm 6.8$	$\pm 12.0$	$\pm 21.1$
Leptons	$\pm 1.9$	$\pm 1.4$	$\pm 0.7$	$\pm 1.0$	$\pm 1.3$	$\pm 1.4$
$E_T^{\text{miss}}$	$\pm 1.0$	$\pm 0.8$	$\pm 0.4$	$\pm 1.1$	$\pm 1.2$	$\pm 3.4$
Unfolding	$\pm 14.3$	$\pm 4.0$	$\pm 1.2$	$\pm 4.0$	$\pm 4.8$	$\pm 3.6$
All Syst	$\pm 25.7$	$\pm 11.3$	$\pm 4.4$	$\pm 8.1$	$\pm 13.3$	$\pm 22.9$
Syst + Stat	$\pm 53.7$	$\pm 18.4$	$\pm 8.5$	$\pm 16.8$	$\pm 26.2$	$\pm 64.6$

Table 8.3: Relative uncertainties (in %) for the  $ee$ -channel for the  $p_T > 60$  GeV threshold measurement.

	0 jets	1 jet	2 jets	3 jets	$\geq 4$ jets
Statistics	$\pm 15.3$	$\pm 8.5$	$\pm 11.0$	$\pm 20.2$	$\pm 69.4$
Backgrounds	$\pm 3.6$	$\pm 0.6$	$\pm 2.6$	$\pm 1.9$	$\pm 3.2$
Jets	$\pm 8.3$	$\pm 3.4$	$\pm 4.9$	$\pm 7.9$	$\pm 18.4$
Leptons	$\pm 1.8$	$\pm 0.8$	$\pm 0.8$	$\pm 1.8$	$\pm 2.7$
$E_T^{\text{miss}}$	$\pm 0.8$	$\pm 0.4$	$\pm 0.6$	$\pm 2.3$	$\pm 2.6$
Unfolding	$\pm 3.7$	$\pm 2.9$	$\pm 3.5$	$\pm 2.5$	$\pm 6.7$
All Syst	$\pm 10.0$	$\pm 4.6$	$\pm 6.7$	$\pm 9.0$	$\pm 20.2$
Syst + Stat	$\pm 18.3$	$\pm 9.6$	$\pm 12.9$	$\pm 22.1$	$\pm 72.3$

Table 8.4: Relative uncertainties (in %) for the  $ee$ -channel for the  $p_T > 80$  GeV threshold measurement.

	0 jets	1 jet	2 jets	$\geq 3$ jets
Statistics	$\pm 8.7$	$\pm 8.9$	$\pm 15.1$	$\pm 27.9$
Backgrounds	$\pm 4.0$	$\pm 3.9$	$\pm 2.2$	$\pm 3.2$
Jets	$\pm 4.8$	$\pm 2.9$	$\pm 6.2$	$\pm 12.7$
Leptons	$\pm 0.8$	$\pm 0.4$	$\pm 1.2$	$\pm 1.8$
$E_T^{\text{miss}}$	$\pm 0.8$	$\pm 0.5$	$\pm 0.6$	$\pm 1.4$
Unfolding	$\pm 3.1$	$\pm 2.4$	$\pm 3.2$	$\pm 5.5$
All Syst	$\pm 7.1$	$\pm 5.5$	$\pm 7.4$	$\pm 14.4$
Syst + Stat	$\pm 11.2$	$\pm 10.4$	$\pm 16.8$	$\pm 31.4$

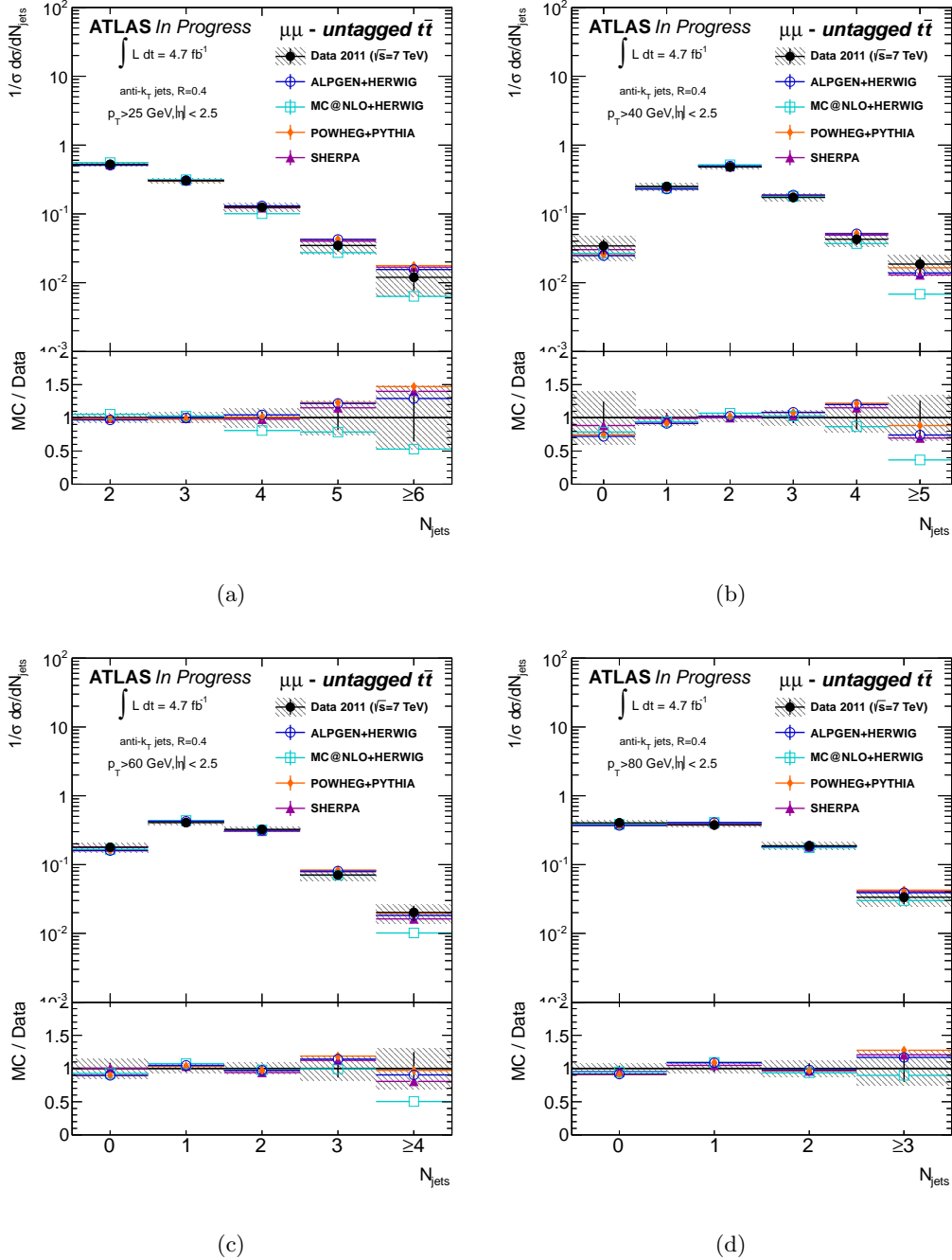


Figure 8.2: The unfolded di-muon  $t\bar{t}$  particle-level jet multiplicity differential cross-sections for the (a) 25, (b) 40, (c) 60, and (d) 80 GeV  $p_T$ -thresholds.

Table 8.5: Relative uncertainties (in %) for the  $\mu\mu$ -channel for the  $p_T > 25$  GeV threshold measurement.

	2 jets	3 jets	4 jets	5 jets	$\geq 6$ jets
Statistics	$\pm 4.4$	$\pm 7.2$	$\pm 11.1$	$\pm 19.6$	$\pm 37.3$
Backgrounds	$\pm 0.8$	$\pm 1.6$	$\pm 2.4$	$\pm 3.3$	$\pm 4.8$
Jets	$\pm 5.0$	$\pm 2.8$	$\pm 7.8$	$\pm 14.7$	$\pm 28.2$
Leptons	$\pm 0.3$	$\pm 0.4$	$\pm 0.4$	$\pm 1.0$	$\pm 2.2$
$E_T^{\text{miss}}$	$\pm 0.1$	$\pm 0.5$	$\pm 0.4$	$\pm 0.8$	$\pm 1.1$
Unfolding	$\pm 0.7$	$\pm 1.7$	$\pm 1.9$	$\pm 7.2$	$\pm 7.4$
All Syst	$\pm 5.2$	$\pm 3.7$	$\pm 8.4$	$\pm 16.7$	$\pm 29.6$
Syst + Stat	$\pm 6.8$	$\pm 8.1$	$\pm 13.9$	$\pm 25.7$	$\pm 47.6$

Table 8.6: Relative uncertainties (in %) for the  $\mu\mu$ -channel for the  $p_T > 40$  GeV threshold measurement.

	0 jets	1 jet	2 jets	3 jets	4 jets	$\geq 5$ jets
Statistics	$\pm 33.4$	$\pm 9.4$	$\pm 5.3$	$\pm 9.7$	$\pm 18.6$	$\pm 28.0$
Backgrounds	$\pm 3.5$	$\pm 2.6$	$\pm 0.8$	$\pm 1.0$	$\pm 1.7$	$\pm 1.6$
Jets	$\pm 14.3$	$\pm 6.4$	$\pm 3.2$	$\pm 6.4$	$\pm 8.2$	$\pm 16.7$
Leptons	$\pm 1.8$	$\pm 0.5$	$\pm 0.2$	$\pm 0.2$	$\pm 0.4$	$\pm 0.9$
$E_T^{\text{miss}}$	$\pm 2.1$	$\pm 0.6$	$\pm 0.4$	$\pm 0.6$	$\pm 0.6$	$\pm 0.9$
Unfolding	$\pm 15.0$	$\pm 4.0$	$\pm 1.5$	$\pm 2.3$	$\pm 7.1$	$\pm 7.7$
All Syst	$\pm 21.2$	$\pm 8.0$	$\pm 3.6$	$\pm 7.0$	$\pm 11.0$	$\pm 18.5$
Syst + Stat	$\pm 39.6$	$\pm 12.4$	$\pm 6.4$	$\pm 11.9$	$\pm 21.6$	$\pm 33.6$

Table 8.7: Relative uncertainties (in %) for the  $\mu\mu$ -channel for the  $p_T > 60$  GeV threshold measurement.

	0 jets	1 jet	2 jets	3 jets	$\geq 4$ jets
Statistics	$\pm 11.3$	$\pm 6.1$	$\pm 6.8$	$\pm 15.5$	$\pm 27.0$
Backgrounds	$\pm 1.7$	$\pm 2.2$	$\pm 2.2$	$\pm 3.6$	$\pm 3.3$
Jets	$\pm 9.1$	$\pm 1.6$	$\pm 4.1$	$\pm 8.0$	$\pm 12.6$
Leptons	$\pm 0.8$	$\pm 0.1$	$\pm 0.4$	$\pm 1.1$	$\pm 1.4$
$E_T^{\text{miss}}$	$\pm 1.4$	$\pm 0.3$	$\pm 0.6$	$\pm 1.1$	$\pm 0.8$
Unfolding	$\pm 3.3$	$\pm 2.8$	$\pm 2.2$	$\pm 3.5$	$\pm 4.4$
All Syst	$\pm 10.0$	$\pm 3.9$	$\pm 5.2$	$\pm 9.6$	$\pm 13.8$
Syst + Stat	$\pm 15.1$	$\pm 7.2$	$\pm 8.5$	$\pm 18.2$	$\pm 30.4$

Table 8.8: Relative uncertainties (in %) for the  $\mu\mu$ -channel for the  $p_T > 80$  GeV threshold measurement.

	0 jets	1 jet	2 jets	$\geq 3$ jets
Statistics	$\pm 5.7$	$\pm 6.2$	$\pm 9.6$	$\pm 22.0$
Backgrounds	$\pm 2.5$	$\pm 1.9$	$\pm 4.4$	$\pm 4.5$
Jets	$\pm 4.9$	$\pm 2.7$	$\pm 4.8$	$\pm 11.1$
Leptons	$\pm 0.4$	$\pm 0.2$	$\pm 0.3$	$\pm 1.5$
$E_T^{\text{miss}}$	$\pm 0.4$	$\pm 0.4$	$\pm 0.5$	$\pm 1.2$
Unfolding	$\pm 1.3$	$\pm 0.7$	$\pm 3.5$	$\pm 4.9$
All Syst	$\pm 5.7$	$\pm 3.4$	$\pm 7.4$	$\pm 13.1$
Syst + Stat	$\pm 8.1$	$\pm 7.1$	$\pm 12.1$	$\pm 25.6$

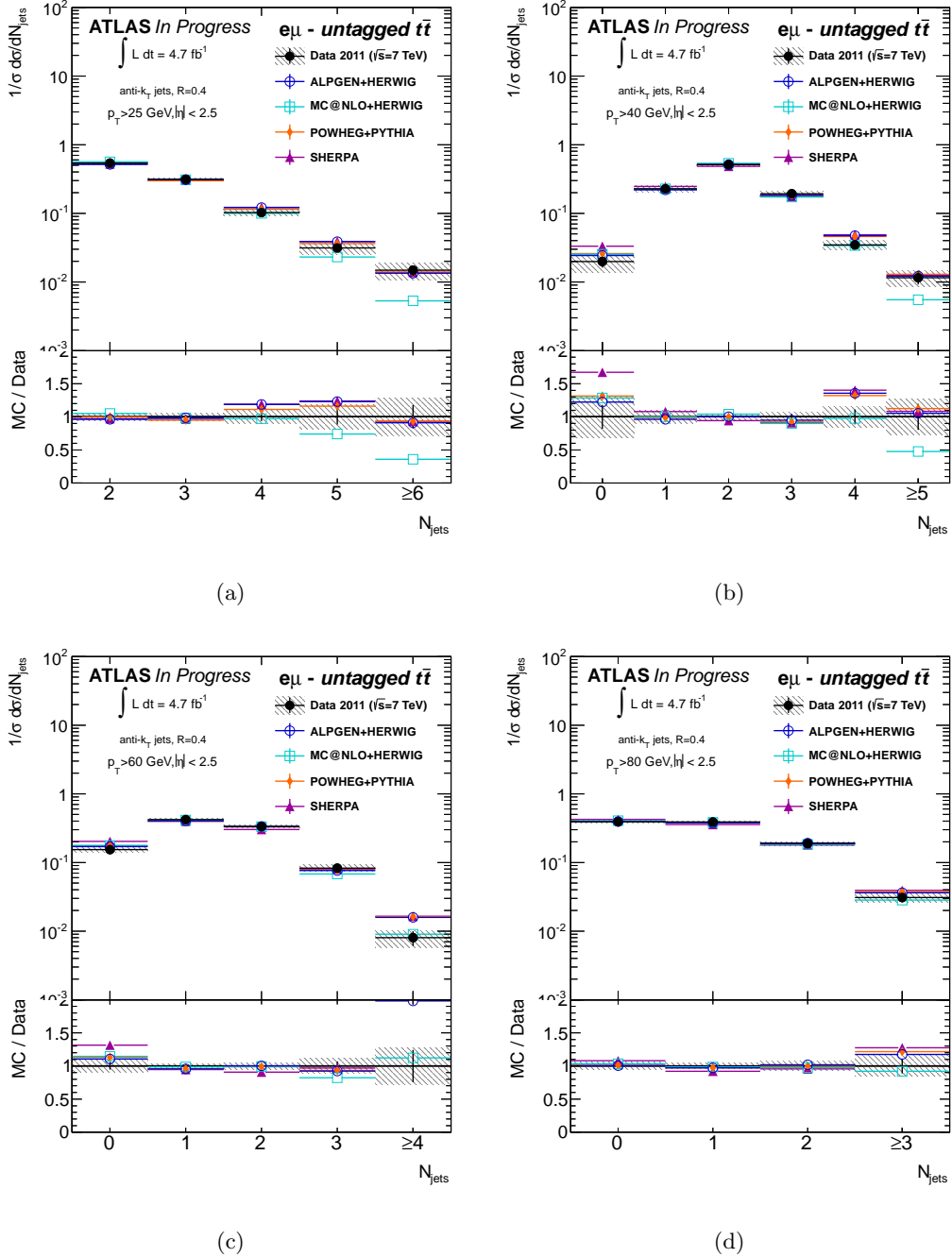


Figure 8.3: The unfolded  $e\mu$ -channel  $t\bar{t}$  particle-level jet multiplicity differential cross-sections for the (a) 25, (b) 40, (c) 60, and (d) 80 GeV  $p_T$ -thresholds.

Table 8.9: Relative uncertainties (in %) for the  $e\mu$ -channel for the  $p_T > 25$  GeV threshold measurement.

	2 jets	3 jets	4 jets	5 jets	$\geq 6$ jets
Statistics	$\pm 2.4$	$\pm 4.1$	$\pm 7.2$	$\pm 12.2$	$\pm 18.6$
Backgrounds	$\pm 0.3$	$\pm 0.4$	$\pm 1.5$	$\pm 0.8$	$\pm 1.5$
Jets	$\pm 4.8$	$\pm 2.9$	$\pm 7.4$	$\pm 14.0$	$\pm 20.8$
Leptons	$\pm 0.1$	$\pm 0.1$	$\pm 0.3$	$\pm 0.4$	$\pm 0.3$
Unfolding	$\pm 1.0$	$\pm 1.6$	$\pm 1.0$	$\pm 4.2$	$\pm 5.2$
All Syst	$\pm 4.9$	$\pm 3.3$	$\pm 7.6$	$\pm 14.7$	$\pm 21.5$
Syst + Stat	$\pm 5.4$	$\pm 5.3$	$\pm 10.5$	$\pm 19.1$	$\pm 28.4$

Table 8.10: Relative uncertainties (in %) for the  $e\mu$ -channel for the  $p_T > 40$  GeV threshold measurement.

	0 jets	1 jet	2 jets	3 jets	4 jets	$\geq 5$ jets
Statistics	$\pm 22.4$	$\pm 5.6$	$\pm 2.9$	$\pm 5.3$	$\pm 12.1$	$\pm 20.8$
Backgrounds	$\pm 5.8$	$\pm 1.1$	$\pm 0.4$	$\pm 0.8$	$\pm 0.7$	$\pm 1.3$
Jets	$\pm 17.7$	$\pm 7.3$	$\pm 2.0$	$\pm 4.8$	$\pm 8.9$	$\pm 15.9$
Leptons	$\pm 1.1$	$\pm 0.4$	$< \pm 0.1$	$\pm 0.2$	$\pm 0.3$	$\pm 0.4$
Unfolding	$\pm 11.7$	$\pm 3.1$	$\pm 1.1$	$\pm 1.4$	$\pm 2.8$	$\pm 5.4$
All Syst	$\pm 22.0$	$\pm 8.0$	$\pm 2.3$	$\pm 5.0$	$\pm 9.4$	$\pm 16.8$
Syst + Stat	$\pm 31.4$	$\pm 9.8$	$\pm 3.7$	$\pm 7.3$	$\pm 15.3$	$\pm 26.8$

Table 8.11: Relative uncertainties (in %) for the  $e\mu$ -channel for the  $p_T > 60$  GeV threshold measurement.

	0 jets	1 jet	2 jets	3 jets	$\geq 4$ jets
Statistics	$\pm 6.8$	$\pm 3.4$	$\pm 3.9$	$\pm 8.2$	$\pm 25.2$
Backgrounds	$\pm 1.7$	$\pm 0.2$	$\pm 0.4$	$\pm 1.1$	$\pm 1.8$
Jets	$\pm 7.1$	$\pm 0.9$	$\pm 2.5$	$\pm 7.3$	$\pm 10.6$
Leptons	$\pm 0.4$	$< \pm 0.1$	$\pm 0.1$	$\pm 0.3$	$\pm 0.4$
Unfolding	$\pm 1.1$	$\pm 1.4$	$\pm 1.9$	$\pm 0.9$	$\pm 3.4$
All Syst	$\pm 7.4$	$\pm 1.7$	$\pm 3.2$	$\pm 7.5$	$\pm 11.3$
Syst + Stat	$\pm 10.0$	$\pm 3.8$	$\pm 5.0$	$\pm 11.1$	$\pm 27.7$

Table 8.12: Relative uncertainties (in %) for the  $e\mu$ -channel for the  $p_T > 80$  GeV threshold measurement.

	0 jets	1 jet	2 jets	$\geq 3$ jets
Statistics	$\pm 3.4$	$\pm 3.6$	$\pm 5.3$	$\pm 12.6$
Backgrounds	$\pm 0.1$	$\pm 0.4$	$\pm 0.6$	$\pm 0.5$
Jets	$\pm 4.1$	$\pm 1.8$	$\pm 4.0$	$\pm 8.5$
Leptons	$< \pm 0.1$	$< \pm 0.1$	$\pm 0.1$	$\pm 0.3$
Unfolding	$\pm 1.5$	$\pm 1.0$	$\pm 2.5$	$\pm 4.0$
All Syst	$\pm 4.4$	$\pm 2.1$	$\pm 4.8$	$\pm 9.4$
Syst + Stat	$\pm 5.5$	$\pm 4.2$	$\pm 7.1$	$\pm 15.7$

## 8.2 Ratio to $Z$ +jets

Figure 8.4 shows the unfolded  $Z \rightarrow (ee, \mu\mu)$  jet multiplicity distributions, and compares them with the predictions of several generators. As can be seen in the figure, the predictions of the ALPGEN+HERWIG sample agree reasonably well with the data, as do the predictions of the other multi-leg generator, SHERPA. MC@NLO+HERWIG and POWHEG+PYTHIA badly mismodel the shape of the jet multiplicity distribution according to these results. Since the goal of this analysis is to measure the  $t\bar{t}$  distribution, the predictions of ALPGEN+HERWIG are used for MC@NLO+HERWIG and POWHEG+PYTHIA as the denominator for their ratio predictions.

The unfolded ratio for each channel for the  $p_T > 25$  GeV threshold is shown in Figure 8.5. Note that for the  $e\mu$  channel, a ratio of the  $t\bar{t}$  jet multiplicity is taken with twice the square-root of the  $Z \rightarrow ee$  unfolded jet multiplicity multiplied by that of  $Z \rightarrow \mu\mu$  as the denominator. The breakdown of systematic uncertainties is shown in Tables 8.13-8.15. The ratio measurement shows a large reduction in systematic uncertainties associated with jet measurements, dropping from nearly 30% in the  $ee$  and  $\mu\mu$  channels in the highest jet multiplicity bin to less than 15% in most bins. The ratio analysis is therefore largely statistics limited.

The predictions of ALPGEN+HERWIG agree very well with the data, as do the predictions of POWHEG+PYTHIA when ALPGEN+HERWIG is used to model the  $Z$ +jets denominator. With the uncertainties reduced, the performance of MC@NLO+HERWIG is shown to be worse than observed in the pure  $t\bar{t}$  measurement. Though SHERPA performed reasonably well at predicting the pure  $t\bar{t}$  distribution, it performs poorly for the ratio measurement.

Some care should be taken when interpreting the agreement between the predictions and the unfolded results for the ratio. The trend towards predicting more events with higher jet multiplicities than is observed in the data (but typically within the uncertainties) is present in both the  $t\bar{t}$  and  $Z$ +jets predictions for ALPGEN+HERWIG. This might be due to biases in the object measurements (e.g. the JES) which would cancel in the ratio and indeed was the purpose of making this measurement. However, it may also be due to mismodeling of the particle-level jet multiplicity distributions of both processes. It should be noted that biases present in the modeling of each process need not go in the same direction. For example,

SHERPA predicts a slightly higher number of events with high jet multiplicity for  $t\bar{t}$ , but a slightly lower number of high jet multiplicity events in  $Z$ +jets and this is the reason it performs poorly in the ratio measurement. Additionally, POWHEG performs reasonably well for  $t\bar{t}$ , but does remarkably badly at modeling the  $Z$ +jets distribution.

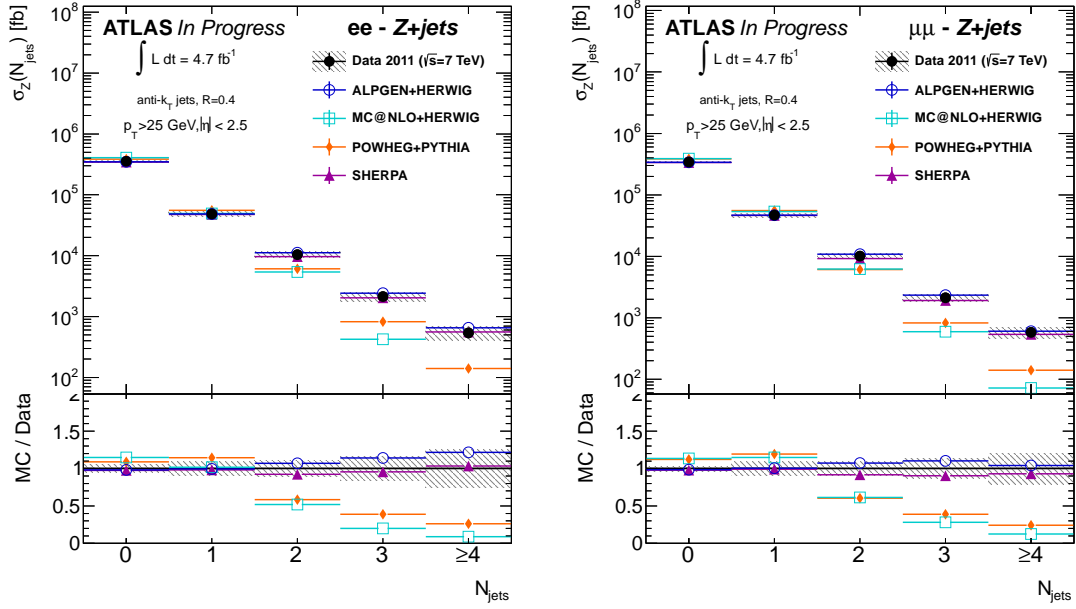


Figure 8.4: The unfolded  $Z \rightarrow ee$  (left) and  $Z \rightarrow \mu\mu$  (right) results.

Table 8.13: Relative uncertainties (in %) broken down by source for the  $ee$ -channel for ratio of the  $t\bar{t}$  to  $Z$ +jets jet multiplicities.

	2 jets	3 jets	4 jets	5 jets	$\geq 6$ jets
Statistics	$\pm 8.9$	$\pm 11.2$	$\pm 18.4$	$\pm 26.7$	$\pm 42.2$
Backgrounds	$\pm 3.3$	$\pm 3.2$	$\pm 6.0$	$\pm 5.4$	$\pm 6.7$
Jets	$\pm 5.7$	$\pm 6.2$	$\pm 7.1$	$\pm 10.0$	$\pm 12.7$
Leptons	$\pm 3.1$	$\pm 2.7$	$\pm 2.8$	$\pm 2.7$	$\pm 2.8$
$E_T^{\text{miss}}$	$\pm 1.1$	$\pm 1.3$	$\pm 1.4$	$\pm 0.8$	$\pm 1.3$
Unfolding	$\pm 1.2$	$\pm 2.2$	$\pm 4.0$	$\pm 5.2$	$\pm 3.2$
All Syst	$\pm 7.4$	$\pm 7.9$	$\pm 10.6$	$\pm 12.8$	$\pm 15.0$
Syst + Stat	$\pm 11.6$	$\pm 13.7$	$\pm 21.2$	$\pm 29.7$	$\pm 44.8$

Table 8.14: Relative uncertainties (in %) broken down by source for the  $\mu\mu$ -channel for ratio of the  $t\bar{t}$  to  $Z$ +jets jet multiplicities.

	2 jets	3 jets	4 jets	5 jets	$\geq 6$ jets
Statistics	$\pm 6.2$	$\pm 8.0$	$\pm 11.4$	$\pm 19.9$	$\pm 37.7$
Backgrounds	$\pm 2.1$	$\pm 3.3$	$\pm 2.1$	$\pm 4.1$	$\pm 8.0$
Jets	$\pm 2.7$	$\pm 7.5$	$\pm 4.9$	$\pm 6.7$	$\pm 15.9$
Leptons	$\pm 0.8$	$\pm 0.8$	$\pm 0.8$	$\pm 1.7$	$\pm 2.6$
$E_T^{\text{miss}}$	$\pm 0.7$	$\pm 0.8$	$\pm 0.6$	$\pm 0.7$	$\pm 1.4$
Unfolding	$\pm 1.0$	$\pm 1.8$	$\pm 2.3$	$\pm 8.2$	$\pm 7.1$
All Syst	$\pm 3.7$	$\pm 8.4$	$\pm 5.9$	$\pm 11.5$	$\pm 19.4$
Syst + Stat	$\pm 7.2$	$\pm 11.6$	$\pm 12.8$	$\pm 23.0$	$\pm 42.5$

Table 8.15: Relative uncertainties (in %) broken down by source for the  $e\mu$ -channel for ratio of the  $t\bar{t}$  to  $Z$ +jets jet multiplicities.

	2 jets	3 jets	4 jets	5 jets	$\geq 6$ jets
Statistics	$\pm 3.4$	$\pm 4.5$	$\pm 7.4$	$\pm 12.4$	$\pm 19.1$
Backgrounds	$\pm 2.3$	$\pm 1.7$	$\pm 3.1$	$\pm 3.1$	$\pm 5.7$
Jets	$\pm 2.8$	$\pm 6.1$	$\pm 5.3$	$\pm 5.8$	$\pm 7.9$
Leptons	$\pm 1.5$	$\pm 1.3$	$\pm 1.2$	$\pm 1.2$	$\pm 1.2$
Unfolding	$\pm 0.6$	$\pm 0.5$	$\pm 3.6$	$\pm 5.9$	$\pm 6.6$
All Syst	$\pm 3.9$	$\pm 6.4$	$\pm 7.2$	$\pm 9.0$	$\pm 11.8$
Syst + Stat	$\pm 5.2$	$\pm 7.9$	$\pm 10.3$	$\pm 15.3$	$\pm 22.5$

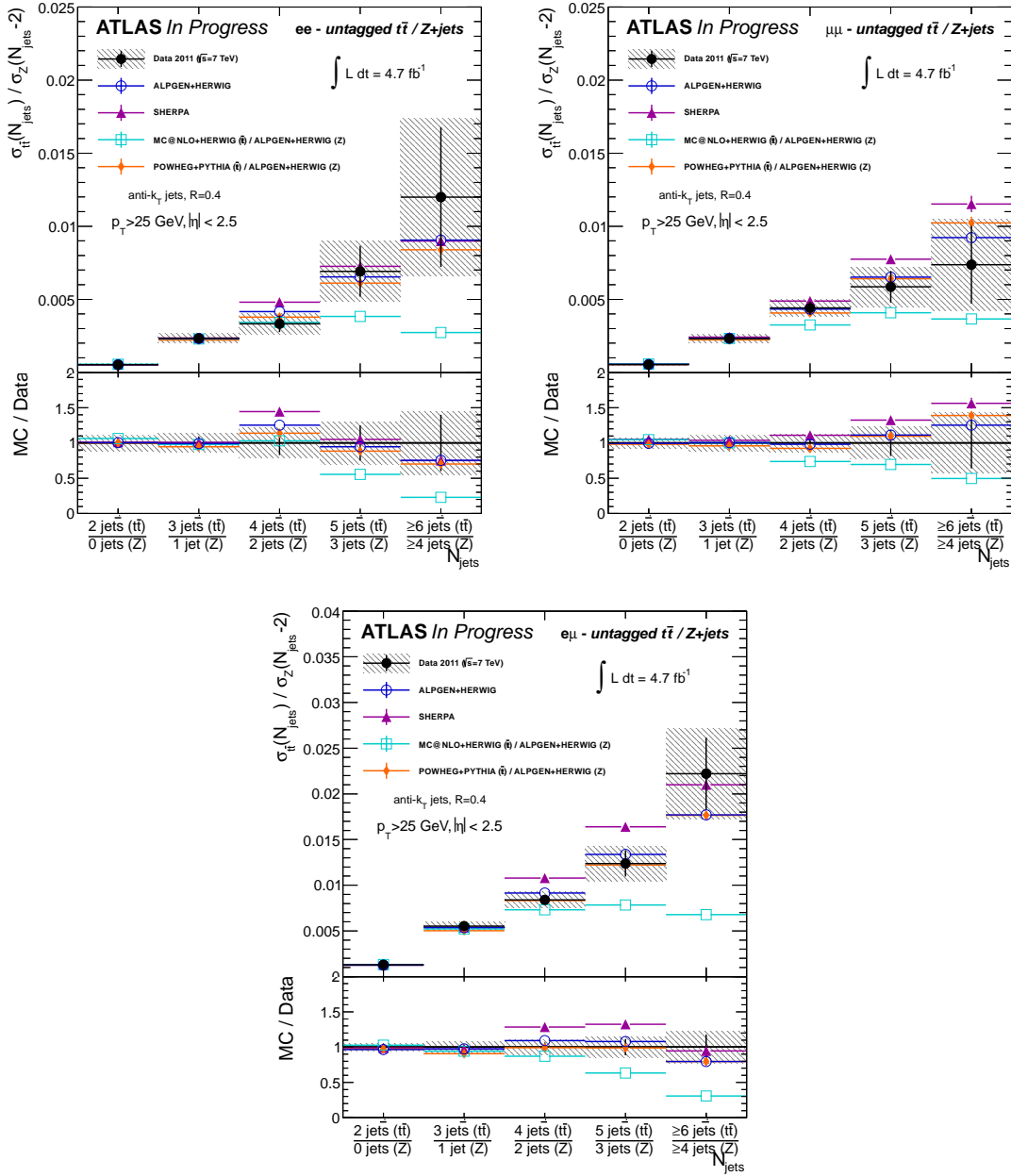


Figure 8.5: The unfolded ratio of the  $t\bar{t}$  to  $Z$ +jets jet multiplicities for the  $ee$  (top left),  $\mu\mu$  (top right), and  $e\mu$  (bottom) channels.

### 8.3 Combination of all channels

In order to further reduce sensitivity to some uncertainties, a combination of the results from each channel has been performed for this analysis and is presented in this section. In order to perform the combination in a straight-forward manner, the particle-level selections have been modified so that each channel has the same selections at the particle-level (as mentioned in Section 6.1). Specifically:

- The  $E_T^{\text{miss}}$  cut applied in the same-flavor channels has been removed.
- The  $M_{\ell\ell}$  cuts applied in the same-flavor channels have been removed.
- The  $H_T$  cut applied in the  $e\mu$  channel has been removed.

Note that these changes only apply to the particle-level selections. This results in some extrapolation in the unfolding corrections. Appendix A discusses the validation of this extrapolation.

The combination is performed by adding the unnormalized unfolded numbers of events per bin in each channel and then normalizing the total number of events to 1. For the ratio, the unnormalized unfolded numbers of events in each  $t\bar{t}$  channel are added for the numerator. For the denominator, the unfolded numbers of  $Z \rightarrow ee$  and  $Z \rightarrow \mu\mu$  events are added to twice the square-root of the number of  $Z \rightarrow ee$  events multiplied by the number of  $Z \rightarrow \mu\mu$  events.

To propagate uncertainties, this combination is performed in each pseudo experiment in order to calculate the final covariance. The results of the combination are shown in Figures 8.6 and 8.7 and the systematic uncertainties are summarized in Tables 8.16-8.19. These tables show a small reduction with respect to the  $e\mu$ -channel results in both the statistical and total systematic uncertainties in all bins. The final bin-to-bin correlations are shown in Figure 8.8.

The plots in Figure 8.6 show that the nominal ALPGEN+HERWIG generator agrees reasonably well with the data. Its predictions in general predict slightly higher numbers of events with high jet multiplicity, near the edge of the uncertainty bands (and in some cases outside the uncertainty attributed partially to fluctuations, see Appendix A).

Figure 8.7 shows the same unfolded data distributions compared with the predictions of the nominal ALPGEN+PYTHIA generator as well as when the strong coupling  $\alpha_s$  is varied up and down for more and less additional radiation. The nominal ALPGEN+PYTHIA performs similarly to ALPGEN+HERWIG. The low  $\alpha_s$  ALPGEN+PYTHIA variation shows the best performance according to this analysis, in agreement with what was observed in the ATLAS single lepton  $t\bar{t}$  jet multiplicity analysis [150]. The high  $\alpha_s$  variation badly describes the jet multiplicity in  $t\bar{t}$  events.

The results for the combination for the ratio are shown in Figure 8.9. Its relative uncertainties are shown in Table 8.20. The bin-to-bin error correlation matrix is shown in Figure 8.10. Despite the combination, these results are also statistics limited due to large reductions in the systematic uncertainties in the ratio with respect to the pure  $t\bar{t}$  measurement. ALPGEN+HERWIG generator performs best. POWHEG+PYTHIA performs well using ALPGEN+HERWIG to model the  $Z$ +jets denominator of the ratio. ALPGEN+PYTHIA and SHERPA overestimate the ratio at high jet multiplicity and MC@NLO underestimates it with ALPGEN+HERWIG used for the  $Z$ +jets denominator.

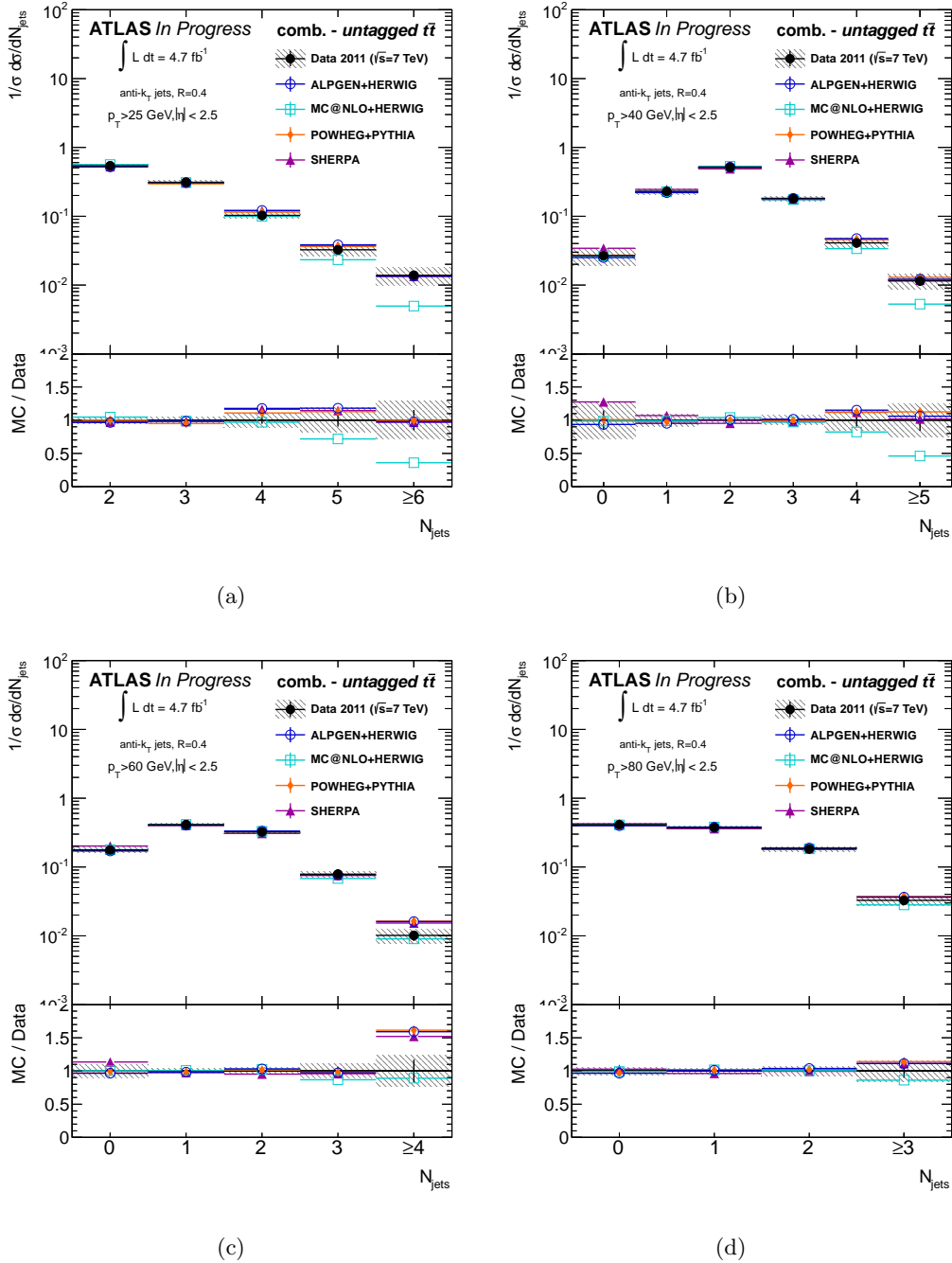


Figure 8.6: The unfolded  $t\bar{t}$  particle-level jet multiplicity normalized differential cross-sections for the combination of all channels for the (a) 25, (b) 40, (c) 60, and (d) 80 GeV  $p_T$ -thresholds. The predictions of the ALPGEN, MC@NLO, POWHEG, and SHERPA generators are also shown.

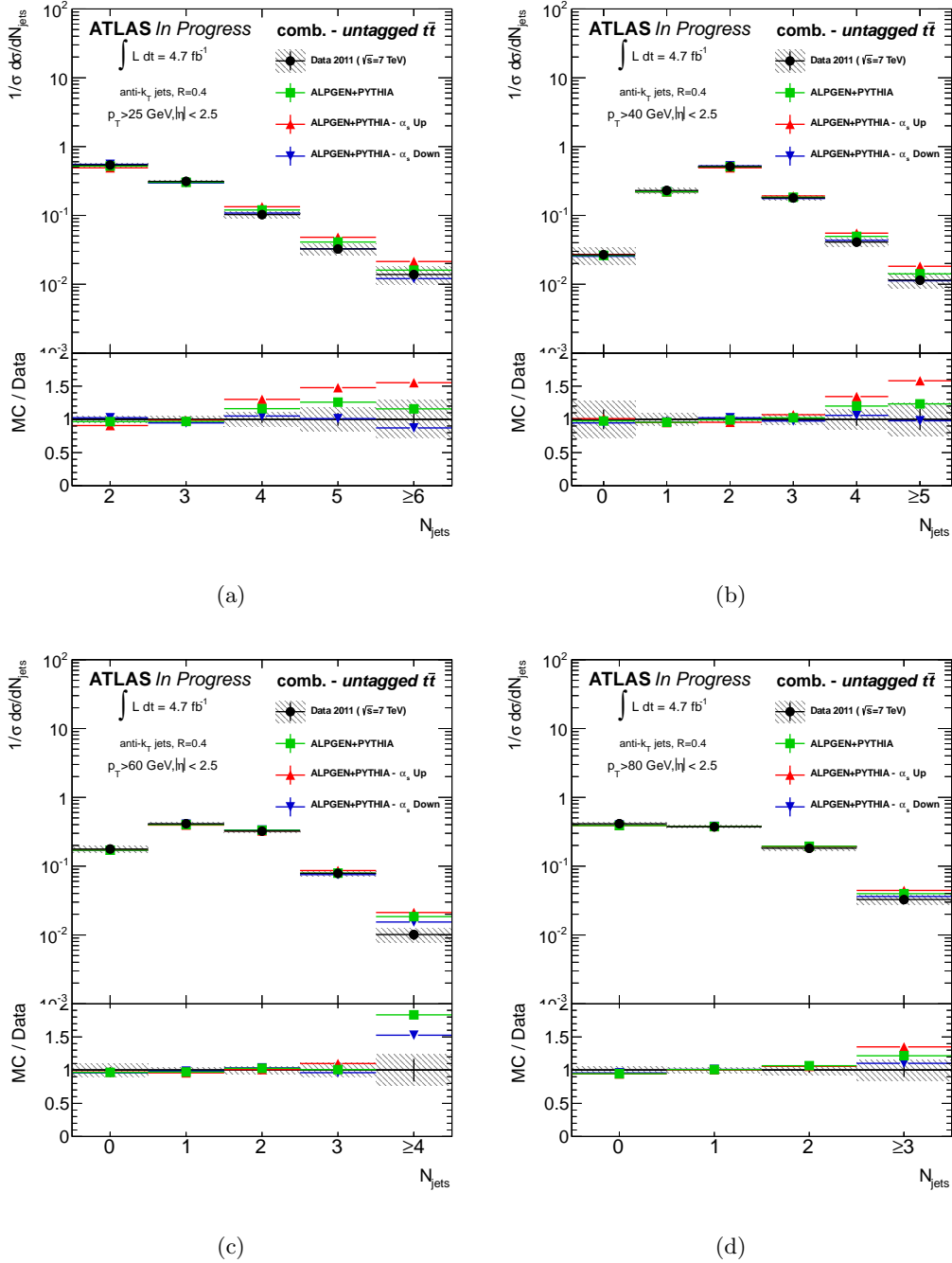


Figure 8.7: The unfolded  $t\bar{t}$  particle-level jet multiplicity normalized differential cross-sections for the combination of all channels for the (a) 25, (b) 40, (c) 60, and (d) 80 GeV  $p_T$ -thresholds. The predictions of the nominal ALPGEN+PYTHIA generator as well as its tunings for more or less radiation also shown.

Table 8.16: Relative uncertainties (in %) for the combination for the  $p_T > 25$  GeV threshold measurement.

	2 jets	3 jets	4 jets	5 jets	$\geq 6$ jets
Statistics	$\pm 2.3$	$\pm 3.9$	$\pm 6.2$	$\pm 10.3$	$\pm 16.2$
Backgrounds	$\pm 0.4$	$\pm 0.5$	$\pm 1.4$	$\pm 1.3$	$\pm 2.0$
Jets	$\pm 5.0$	$\pm 3.0$	$\pm 7.8$	$\pm 14.7$	$\pm 23.0$
Leptons	$\pm 0.1$	$\pm 0.2$	$\pm 0.4$	$\pm 0.5$	$\pm 0.7$
$E_T^{\text{miss}}$	$< \pm 0.1$	$\pm 0.2$	$\pm 0.4$	$\pm 0.3$	$\pm 0.4$
Unfolding	$\pm 0.4$	$\pm 1.4$	$\pm 2.0$	$\pm 4.2$	$\pm 5.2$
All Syst	$\pm 5.0$	$\pm 3.4$	$\pm 8.2$	$\pm 15.3$	$\pm 23.7$
Syst + Stat	$\pm 5.5$	$\pm 5.1$	$\pm 10.2$	$\pm 18.5$	$\pm 28.7$

Table 8.17: Relative uncertainties (in %) for the combination for the  $p_T > 40$  GeV threshold measurement.

	0 jets	1 jet	2 jets	3 jets	4 jets	$\geq 5$ jets
Statistics	$\pm 19.2$	$\pm 5.2$	$\pm 2.6$	$\pm 4.8$	$\pm 10.2$	$\pm 16.8$
Backgrounds	$\pm 1.9$	$\pm 0.9$	$\pm 0.3$	$\pm 0.6$	$\pm 1.0$	$\pm 1.6$
Jets	$\pm 15.7$	$\pm 7.1$	$\pm 2.2$	$\pm 5.3$	$\pm 9.3$	$\pm 16.2$
Leptons	$\pm 0.8$	$\pm 0.5$	$\pm 0.2$	$\pm 0.2$	$\pm 0.3$	$\pm 0.6$
$E_T^{\text{miss}}$	$\pm 0.6$	$\pm 0.3$	$\pm 0.1$	$\pm 0.4$	$\pm 0.4$	$\pm 0.7$
Unfolding	$\pm 11.8$	$\pm 3.1$	$\pm 1.0$	$\pm 1.8$	$\pm 6.5$	$\pm 7.1$
All Syst	$\pm 19.7$	$\pm 7.8$	$\pm 2.4$	$\pm 5.7$	$\pm 11.3$	$\pm 17.8$
Syst + Stat	$\pm 27.6$	$\pm 9.4$	$\pm 3.5$	$\pm 7.4$	$\pm 15.3$	$\pm 24.5$

Table 8.18: Relative uncertainties (in %) for the combination for the  $p_T > 60$  GeV threshold measurement.

	0 jets	1 jet	2 jets	3 jets	$\geq 4$ jets
Statistics	$\pm 6.1$	$\pm 3.2$	$\pm 3.6$	$\pm 7.4$	$\pm 18.2$
Backgrounds	$\pm 0.7$	$\pm 0.5$	$\pm 0.6$	$\pm 1.2$	$\pm 5.1$
Jets	$\pm 7.5$	$\pm 1.3$	$\pm 3.3$	$\pm 7.1$	$\pm 12.4$
Leptons	$\pm 0.5$	$\pm 0.2$	$\pm 0.2$	$\pm 0.5$	$\pm 0.8$
$E_T^{\text{miss}}$	$\pm 0.4$	$\pm 0.1$	$\pm 0.3$	$\pm 0.7$	$\pm 0.5$
Unfolding	$\pm 1.8$	$\pm 1.6$	$\pm 2.2$	$\pm 1.0$	$\pm 5.5$
All Syst	$\pm 7.8$	$\pm 2.1$	$\pm 4.0$	$\pm 7.4$	$\pm 14.5$
Syst + Stat	$\pm 9.9$	$\pm 3.9$	$\pm 5.4$	$\pm 10.5$	$\pm 23.3$

Table 8.19: Relative uncertainties (in %) for the combination for the  $p_T > 80$  GeV threshold measurement.

	0 jets	1 jet	2 jets	$\geq 3$ jets
Statistics	$\pm 3.0$	$\pm 3.3$	$\pm 5.0$	$\pm 11.5$
Backgrounds	$\pm 1.2$	$\pm 1.4$	$\pm 1.3$	$\pm 1.6$
Jets	$\pm 4.1$	$\pm 2.1$	$\pm 4.3$	$\pm 9.7$
Leptons	$\pm 0.1$	$< \pm 0.1$	$\pm 0.4$	$\pm 0.6$
$E_T^{\text{miss}}$	$\pm 0.2$	$\pm 0.1$	$\pm 0.3$	$\pm 0.6$
Unfolding	$\pm 1.9$	$\pm 1.6$	$\pm 2.5$	$\pm 3.9$
All Syst	$\pm 4.7$	$\pm 3.0$	$\pm 5.2$	$\pm 10.7$
Syst + Stat	$\pm 5.6$	$\pm 4.4$	$\pm 7.2$	$\pm 15.7$

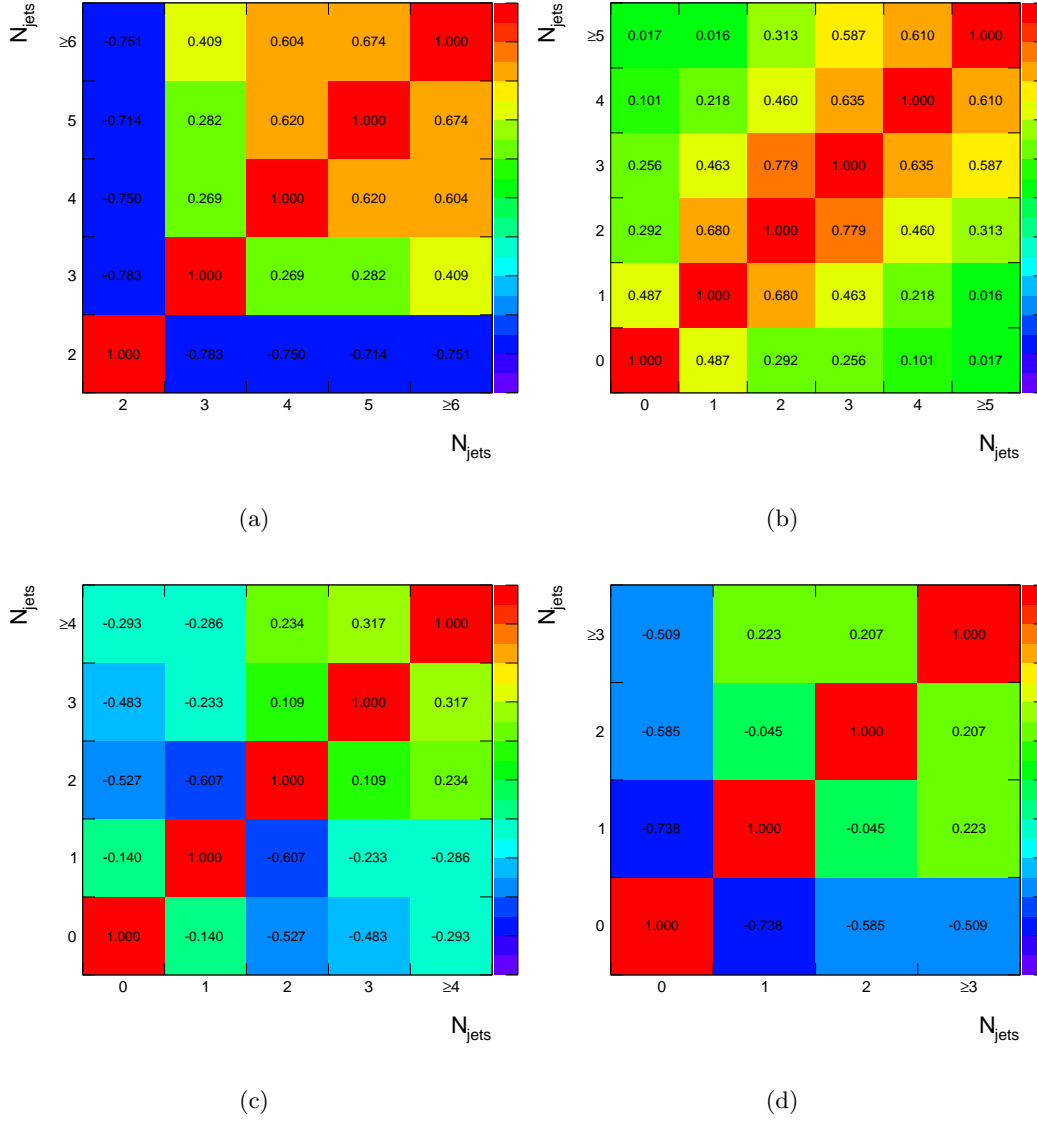


Figure 8.8: The bin-to-bin correlation matrices for the uncertainty on the unfolded  $t\bar{t}$  particle-level jet multiplicity cross-sections for the combination of all channels for the (a) 25, (b) 40, (c) 60, and (d) 80 GeV  $p_T$  thresholds.

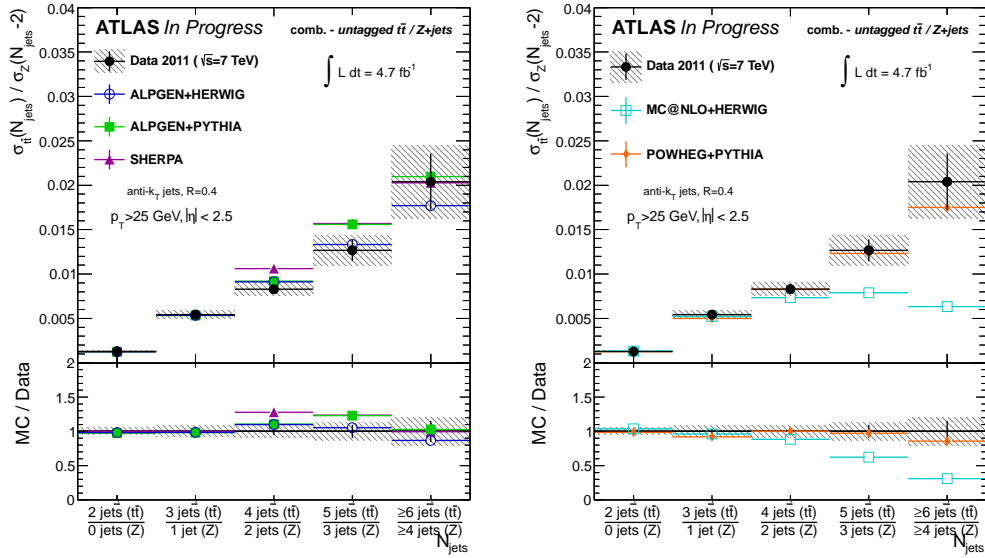


Figure 8.9: The unfolded ratio of the  $t\bar{t}$  to Z+jets jet multiplicities ( $p_T > 25 \text{ GeV}$ ) for the all channel combination compared to the predictions of the multi-leg (left) and NLO (right) generators.

Table 8.20: Relative uncertainties (in %) for the combination of all channels for the ratio of the  $t\bar{t}$  to  $Z$ +jets jet multiplicities ( $p_T > 25$  GeV).

	2 jets	3 jets	4 jets	5 jets	$\geq 6$ jets
Statistics	$\pm 3.3$	$\pm 4.1$	$\pm 6.4$	$\pm 10.5$	$\pm 16.7$
Backgrounds	$\pm 2.2$	$\pm 2.2$	$\pm 3.1$	$\pm 3.5$	$\pm 6.0$
Jets	$\pm 2.9$	$\pm 6.2$	$\pm 5.2$	$\pm 6.2$	$\pm 7.9$
Leptons	$\pm 1.5$	$\pm 1.3$	$\pm 1.2$	$\pm 1.4$	$\pm 1.4$
$E_T^{\text{miss}}$	$\pm 0.4$	$\pm 0.4$	$\pm 0.3$	$\pm 0.2$	$\pm 0.8$
Unfolding	$\pm 0.8$	$\pm 1.3$	$\pm 1.6$	$\pm 3.3$	$\pm 4.9$
All Syst	$\pm 4.0$	$\pm 6.9$	$\pm 6.5$	$\pm 8.4$	$\pm 11.3$
Syst + Stat	$\pm 5.2$	$\pm 8.0$	$\pm 9.1$	$\pm 13.5$	$\pm 20.2$

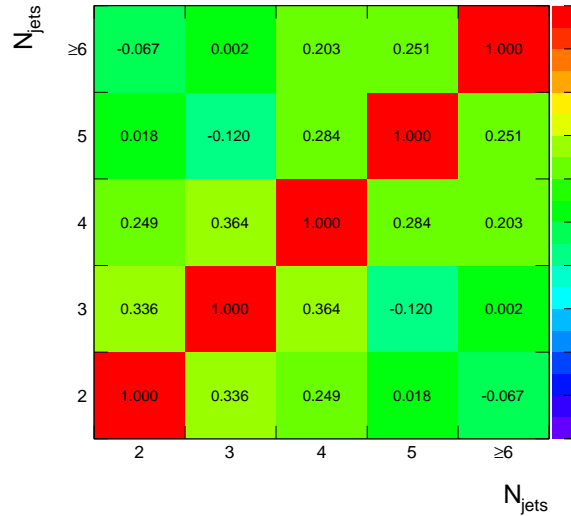


Figure 8.10: The bin-to-bin correlation matrices for the uncertainty on the unfolded  $t\bar{t}$  particle-level jet multiplicity ratio to  $Z$ +jets.

## 8.4 Conclusions

The jet multiplicity distribution in  $t\bar{t}$  events has been measured for several  $p_T$  thresholds for the  $ee$ ,  $\mu\mu$ , and  $e\mu$  channels using data collected with the ATLAS detector during the 2011 data-taking period. The results from each channel have been combined in order to reduce statistical uncertainties. The results have been compared with the predictions of several MC generators, showing good agreement for all at low jet multiplicity and generally good agreement at high jet multiplicity. The worst performing generators are MC@NLO+HERWIG and ALPGEN+PYTHIA, if the QCD coupling constant  $\alpha_s$  is varied up in both the matrix element calculation and in the calculation of the Sudakov form factors in the parton shower algorithm. The best performing generator is ALPGEN+PYTHIA with  $\alpha_s$  varied down. The nominal ALPGEN+PYTHIA, ALPGEN+HERWIG, POWHEG+PYTHIA, and SHERPA generators all perform reasonably well.

The uncertainty associated with the JES was found to be the largest systematic uncertainty in this analysis. In order to reduce this uncertainty, a ratio of the jet multiplicity in  $t\bar{t}$  events to  $Z$ +jets events was also measured. These results show large reductions in the systematic uncertainties. The results are also compared with several generators. ALPGEN+HERWIG performs best in that comparison.

## Part I

# Appendices

## Appendix A

# Data/MC agreement

### A.1 General discussion

ALPGEN+HERWIG is the primary generator used to estimate systematic uncertainties and unfolding corrections for the  $t\bar{t}$  sample. In order to ensure that these estimations are accurate, it is important to check that the ALPGEN sample adequately reproduces  $t\bar{t}$  events in data. Several distributions were shown in Section 5.3 and in general good agreement between the data and ALPGEN MC was observed. This appendix provides a more comprehensive comparison.

Event selections at the reconstruction-level are made on the di-lepton mass, the  $E_{\text{T}}^{\text{miss}}$ , and the  $H_{\text{T}}$ , depending on the channel. Figures A.1 and A.2 show the  $H_{\text{T}}$  and the di-lepton mass distributions. A bias is observed in Figure A.1, where the  $H_{\text{T}}$  distribution in the predictions of the ALPGEN+HERWIG generator is generally harder than that observed in data. Near the  $H_{\text{T}} = 130$  GeV threshold of the selection for the  $e\mu$  channel, the data and MC agree within their uncertainties, suggesting that the analysis should not be sensitive to this bias due to this selection. The analysis is potentially sensitive to the bias at the unfolding-level, if this is due to mismodeling of the jet kinematics, however, jet kinematic distributions show good agreement between the data and MC (see below). Additionally, the effect of this on the unfolded jet multiplicity results bias was checked by reweighting events to better match the  $H_{\text{T}}$  distribution in data. The response from the reweighted events was used to unfold the nominal distribution and the bias was measured. It was found to

lead to at most a 2% difference at high jet multiplicity between the unfolded and truth distributions. This difference is covered by the unfolding systematic uncertainties and is dwarfed by the statistical and JES systematic uncertainties.

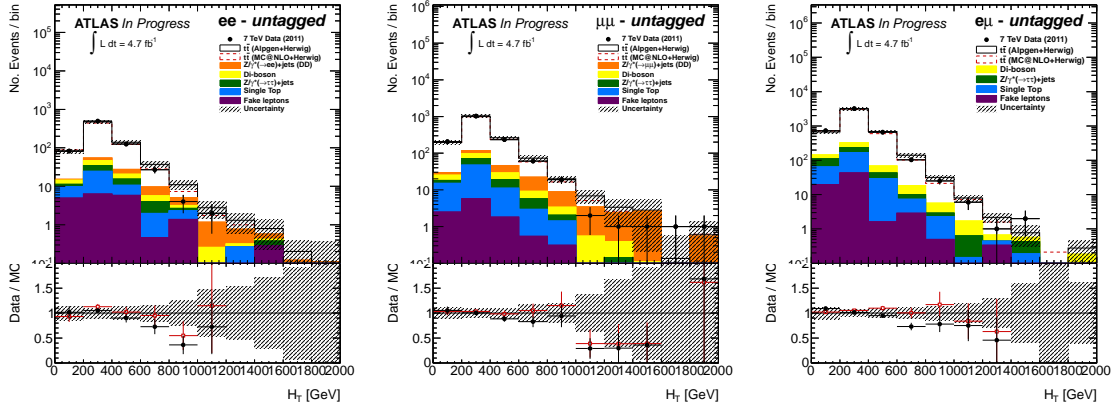


Figure A.1:  $H_T$  distributions for the  $ee$  (left),  $\mu\mu$  (center),  $e\mu$  (right) channels.

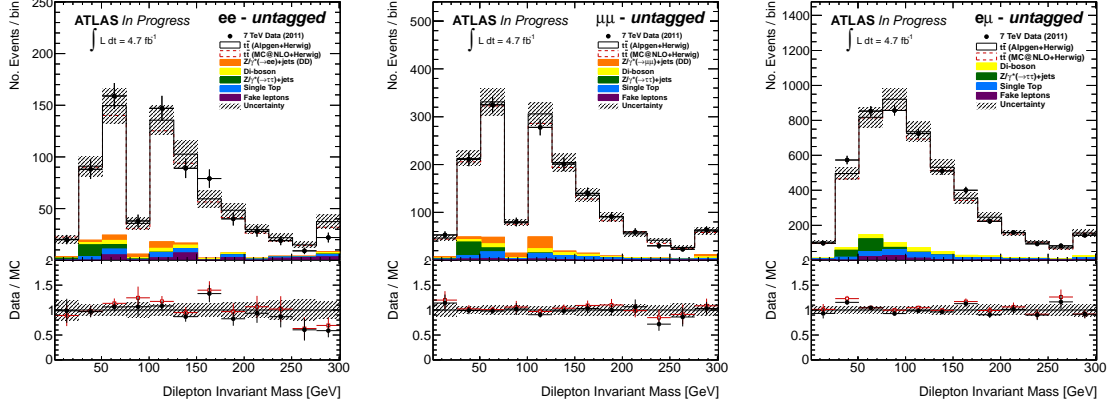


Figure A.2: Di-lepton mass distributions for the  $ee$  (left),  $\mu\mu$  (center),  $e\mu$  (right) channels.

The lepton kinematics show a similar bias as is observed in the  $H_T$ . Lepton  $p_T$  and  $\eta$  distributions are shown in Figures A.3-A.6. In general, the bias is observed in the high  $p_T$  tail region, far from the  $p_T = 25$  GeV threshold used for lepton selection in this analysis. The bias is observed for both electrons and muons, indicating that it's likely due to generator (as opposed to instrumental) modeling. The lepton  $\eta$  distributions are modeled reasonably well. As observed in Figure A.2, this bias does not seem to significantly affect the di-lepton

mass. The  $H_T$  reweighting method described above also corrects this bias, so the sensitivity of the results to this bias is addressed there.

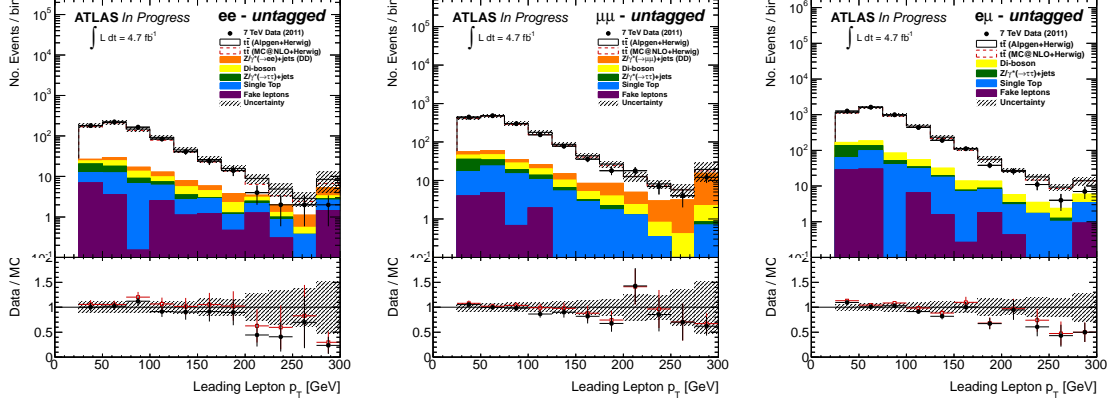


Figure A.3: Leading lepton  $p_T$  distributions for the  $ee$  (left),  $\mu\mu$  (center),  $e\mu$  (right) channels.

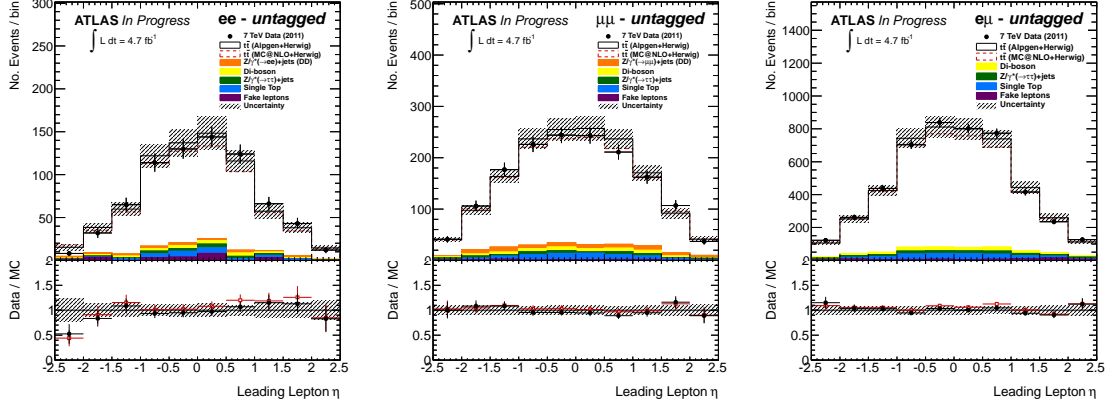


Figure A.4: Leading lepton  $\eta$  distributions for the  $ee$  (left),  $\mu\mu$  (center),  $e\mu$  (right) channels.

Since unfolding acceptance corrections are applied as a function of  $N_{\text{jets}}$ , it is also important to check these distributions in each jet multiplicity bin. In particular, the  $E_T^{\text{miss}}$  distributions for each  $p_T > 25$  GeV jet multiplicity bin are shown in Figures A.7-A.9. Agreement within the uncertainties between the data and MC is observed for the ALPGEN generator.

A model-dependent extrapolation is performed in the combination for the  $ee$  and  $\mu\mu$  channels. It is especially important to check the performance of the generator used for

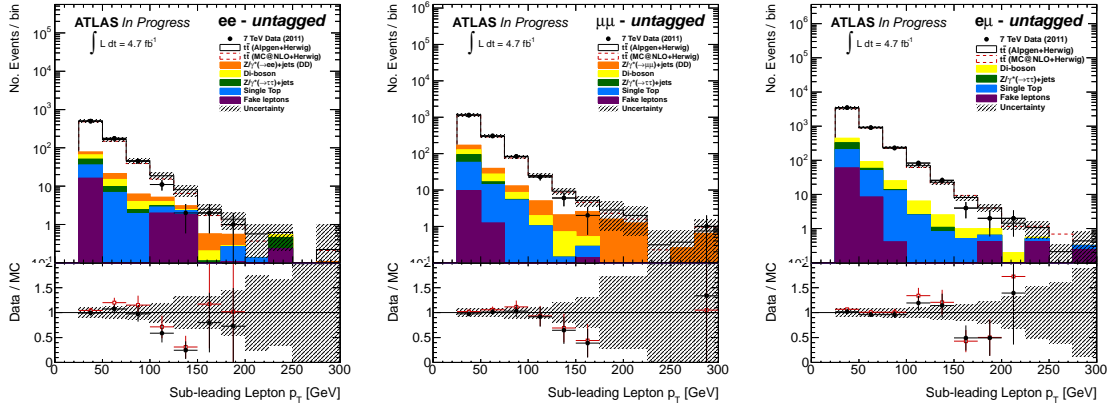


Figure A.5: Sub-leading lepton  $p_T$  distributions for the  $ee$  (left),  $\mu\mu$  (center),  $e\mu$  (right) channels.

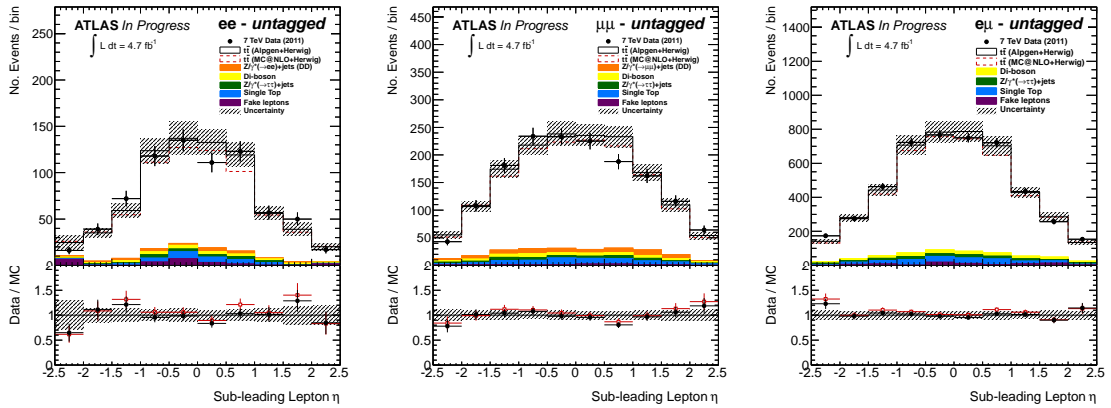


Figure A.6: Sub-leading lepton  $\eta$  distributions for the  $ee$  (left),  $\mu\mu$  (center),  $e\mu$  (right) channels.

unfolding in the low  $E_T^{\text{miss}}$  region(s). Since the Drell-Yan background is significantly reduced in the  $e\mu$  channel, the  $E_T^{\text{miss}}$  distributions shown in Figure A.9 are particularly useful for validating this correction. In addition, the low  $E_T^{\text{miss}}$  region of  $t\bar{t}$  events can be compared with the data for the  $ee$  and  $\mu\mu$  channels by dropping the  $E_T^{\text{miss}}$  requirement and requiring two  $b$ -tagged jets in order to reject Drell-Yan. These distributions are shown in Figures A.10 and A.11. Again, agreement with the data within the uncertainties is observed for the ALPGEN+HERWIG generator.

As the largest systematic uncertainty associated with counting jets in  $t\bar{t}$  events is the JES uncertainty, it is also important to check data/MC agreement in the kinematic distributions of the jets from this sample. Additionally, jet modeling drives the unsmearing correction and any disagreement outside of the uncertainties could indicate potential problems with modeling the response. Figures A.12 and A.13 show the jet  $p_T$  and  $\eta$  distributions ordered by  $p_T$  for all channels combined in order to increase the statistical power of these checks. The data show good agreement with the MC within the uncertainties.

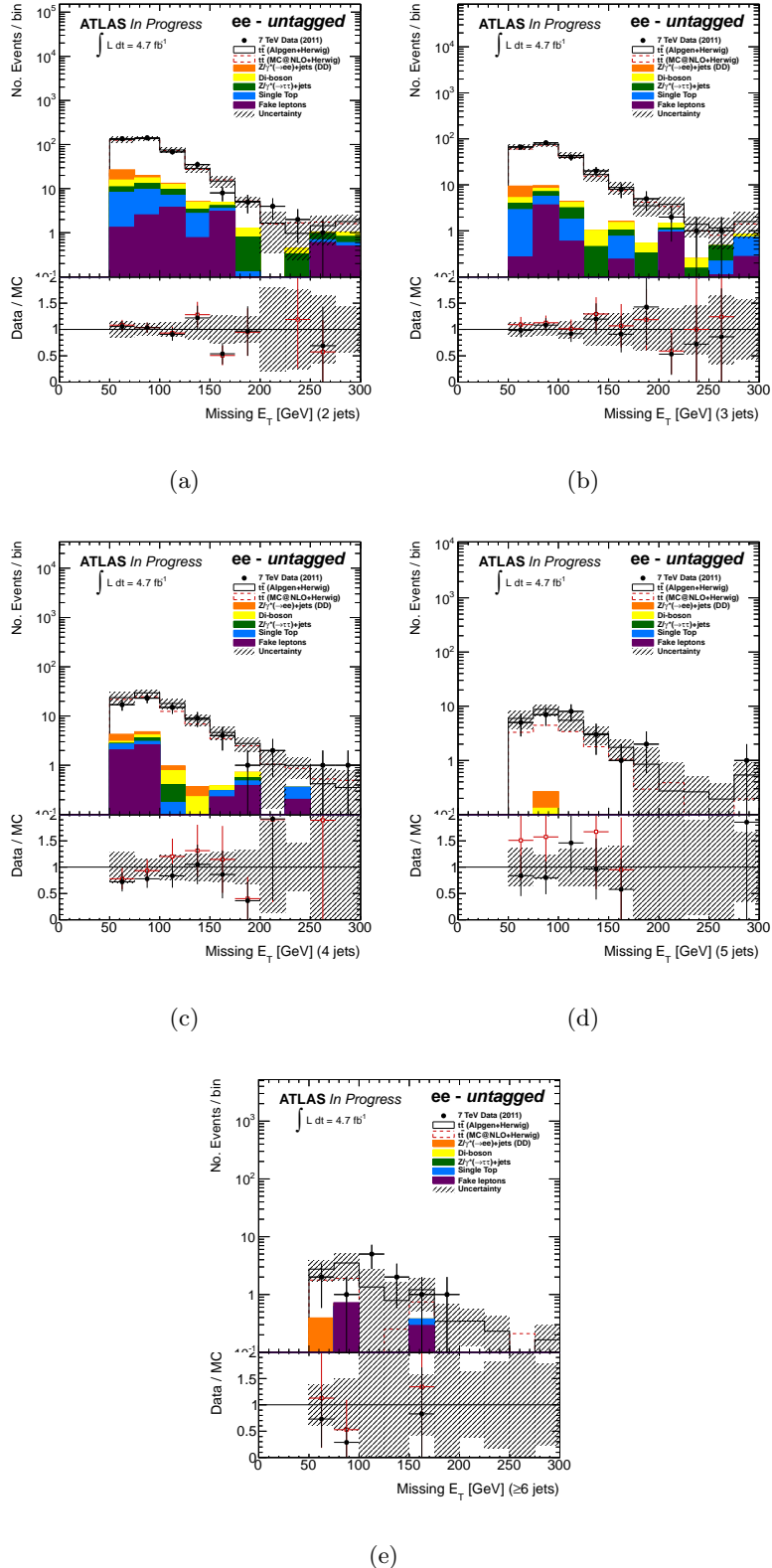
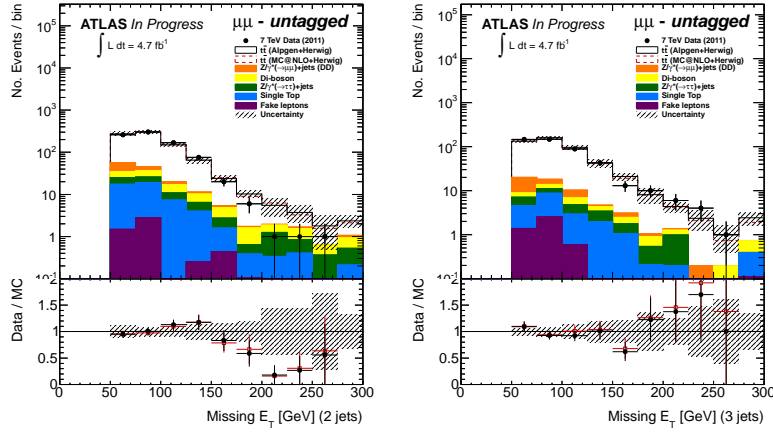
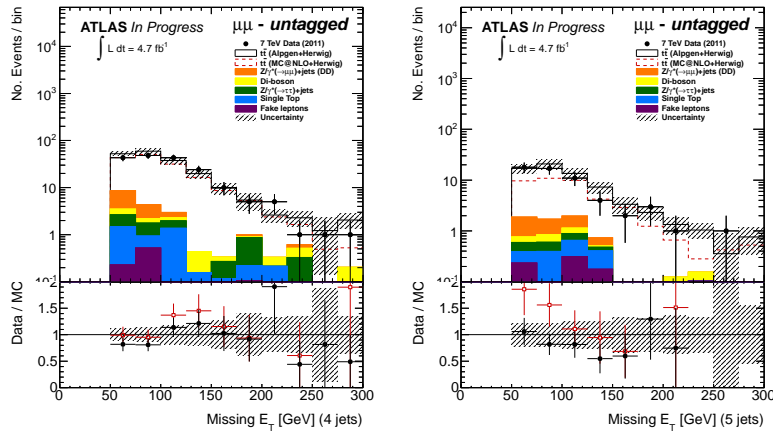


Figure A.7: The  $E_T^{\text{miss}}$  distribution of the di-electron channel for the exclusive (a) 2, (b) 3, (c) 4, (d) 5, and (e) inclusive 6 jet bins for a  $p_T > 25$  GeV jet threshold.



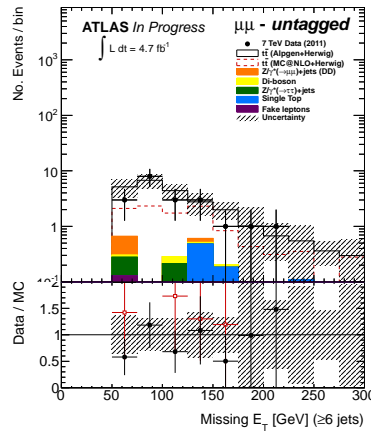
(a)

(b)



(c)

(d)



(e)

Figure A.8: The  $E_T^{\text{miss}}$  distribution of the di-muon channel for the exclusive (a) 2, (b) 3, (c) 4, (d) 5, and (e) inclusive 6 jet bins for a  $p_T > 25$  GeV jet threshold.

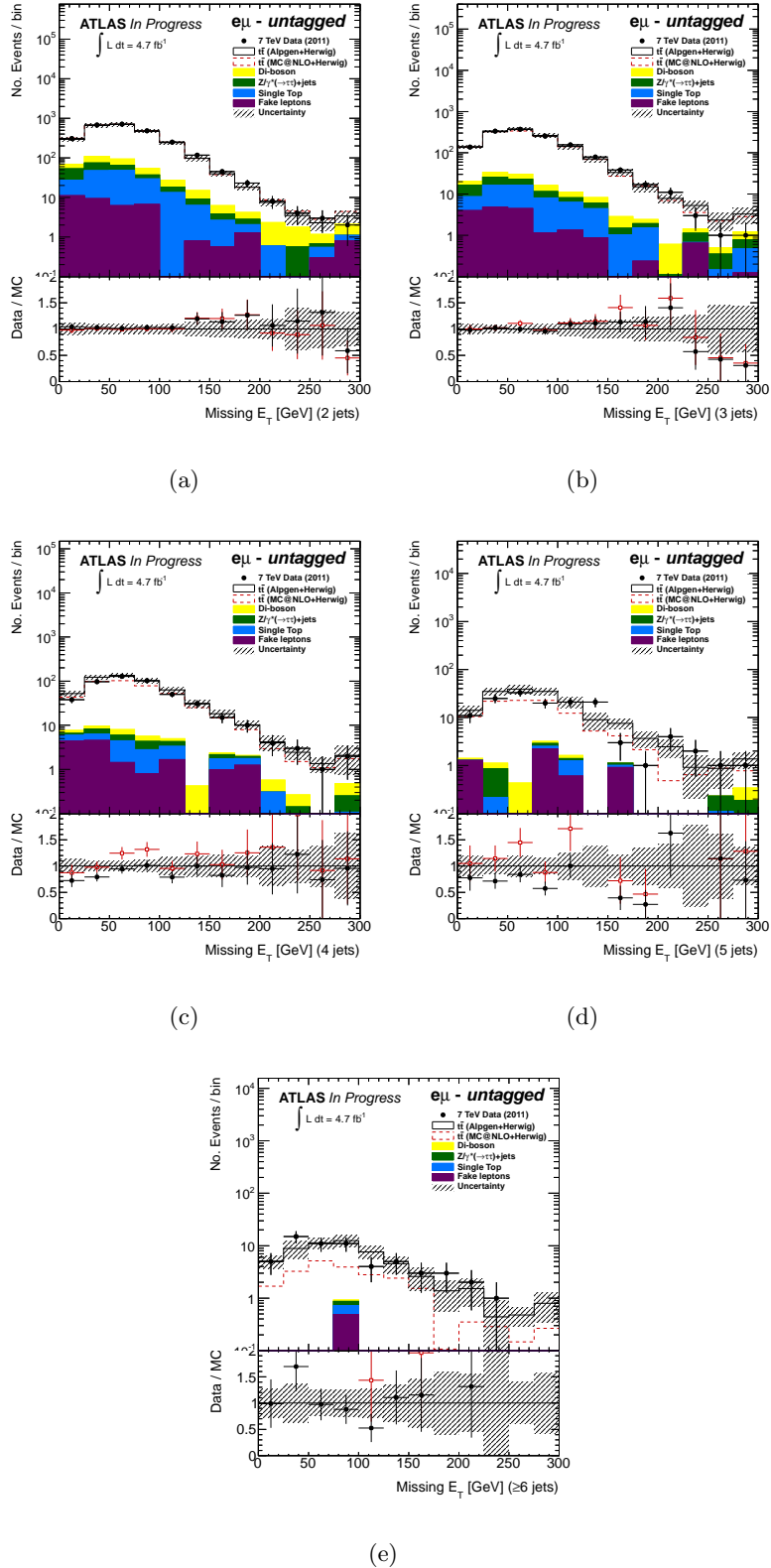


Figure A.9: The  $E_T^{\text{miss}}$  distribution of the  $e\mu$  channel for the exclusive (a) 2, (b) 3, (c) 4, (d) 5, and (e) inclusive 6 jet bins for a  $p_T > 25$  GeV jet threshold.

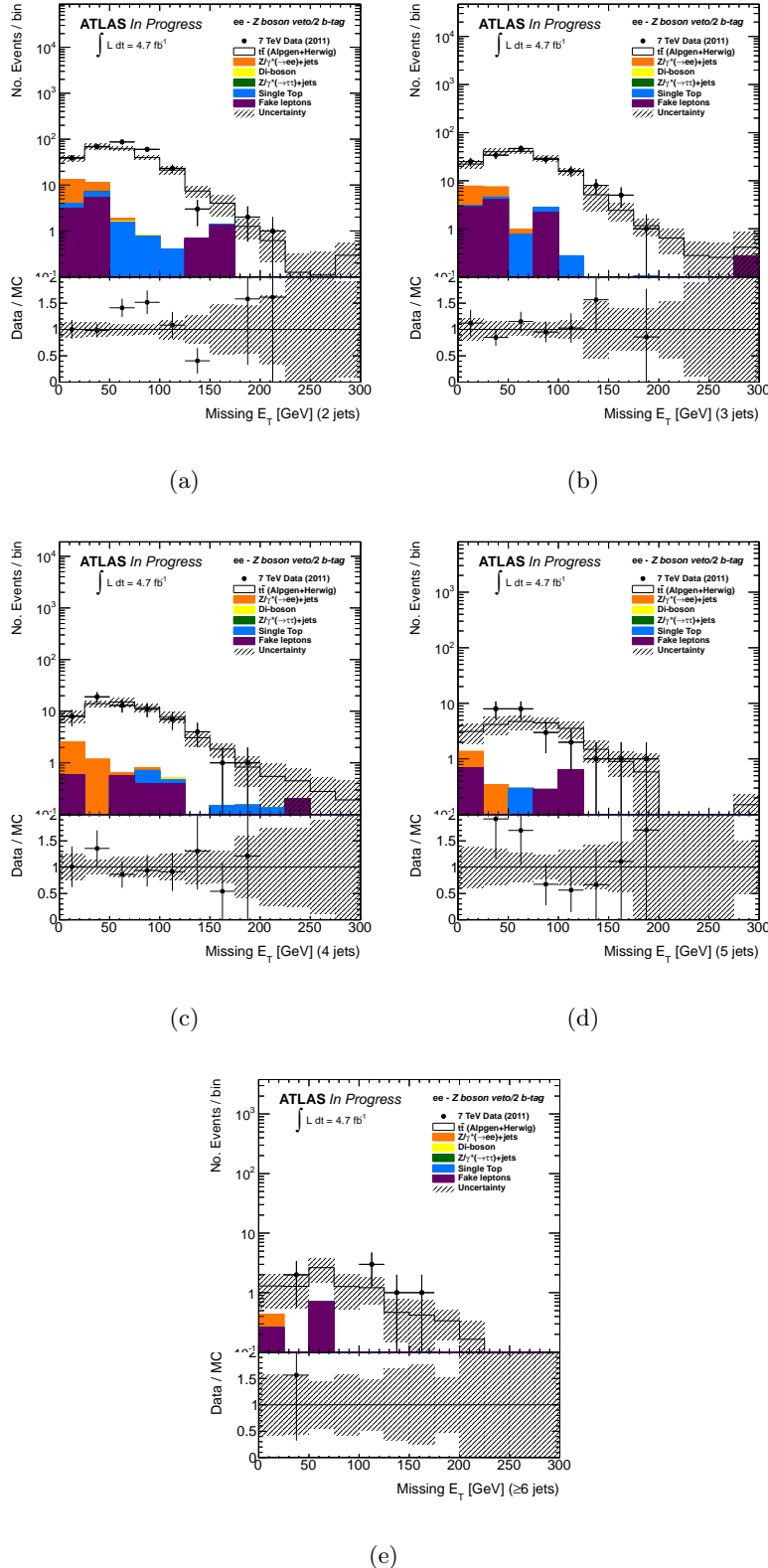


Figure A.10: The  $E_T^{\text{miss}}$  distributions of the di-electron channel with the requirement that at least two jets pass the  $b$ -tagging selections in place of a  $E_T^{\text{miss}}$  cut for the exclusive (a) 2, (b) 3, (c) 4, (d) 5, and (e) inclusive 6 jet bins for a  $p_T > 25$  GeV jet threshold.

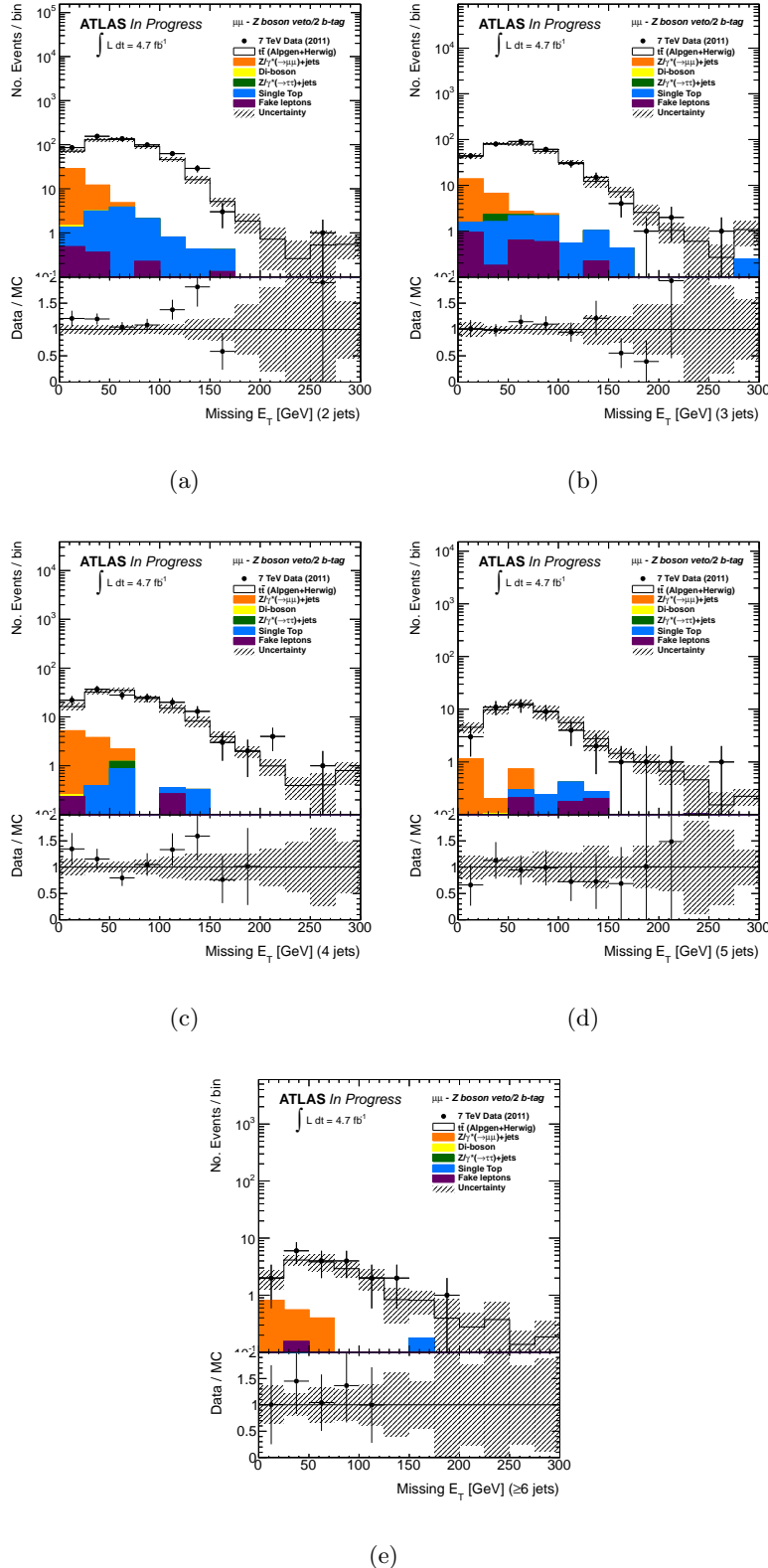


Figure A.11: The  $E_T^{\text{miss}}$  distribution of the di-muon channel with the requirement that at least two jets pass the  $b$ -tagging selections in place of a  $E_T^{\text{miss}}$  cut for the exclusive (a) 2, (b) 3, (c) 4, (d) 5, and (e) inclusive 6 jet bins for a  $p_T > 25$  GeV jet threshold.

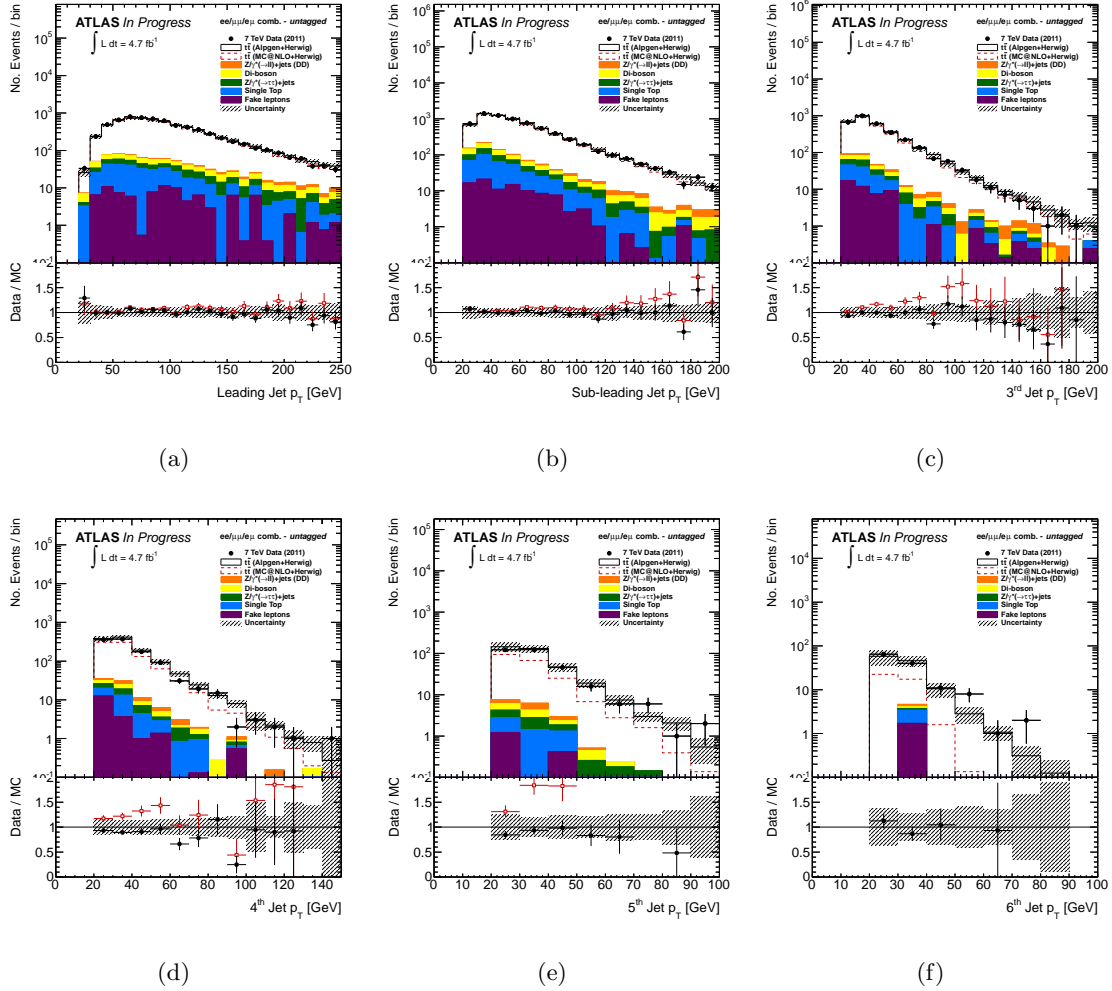


Figure A.12: The  $p_T$  distributions for all channels combined for the (a) leading, (b) sub-leading, (c) 3<sup>rd</sup>, (d) 4<sup>th</sup>, (e) 5<sup>th</sup>, and (f) 6<sup>th</sup> (inclusive) jets.

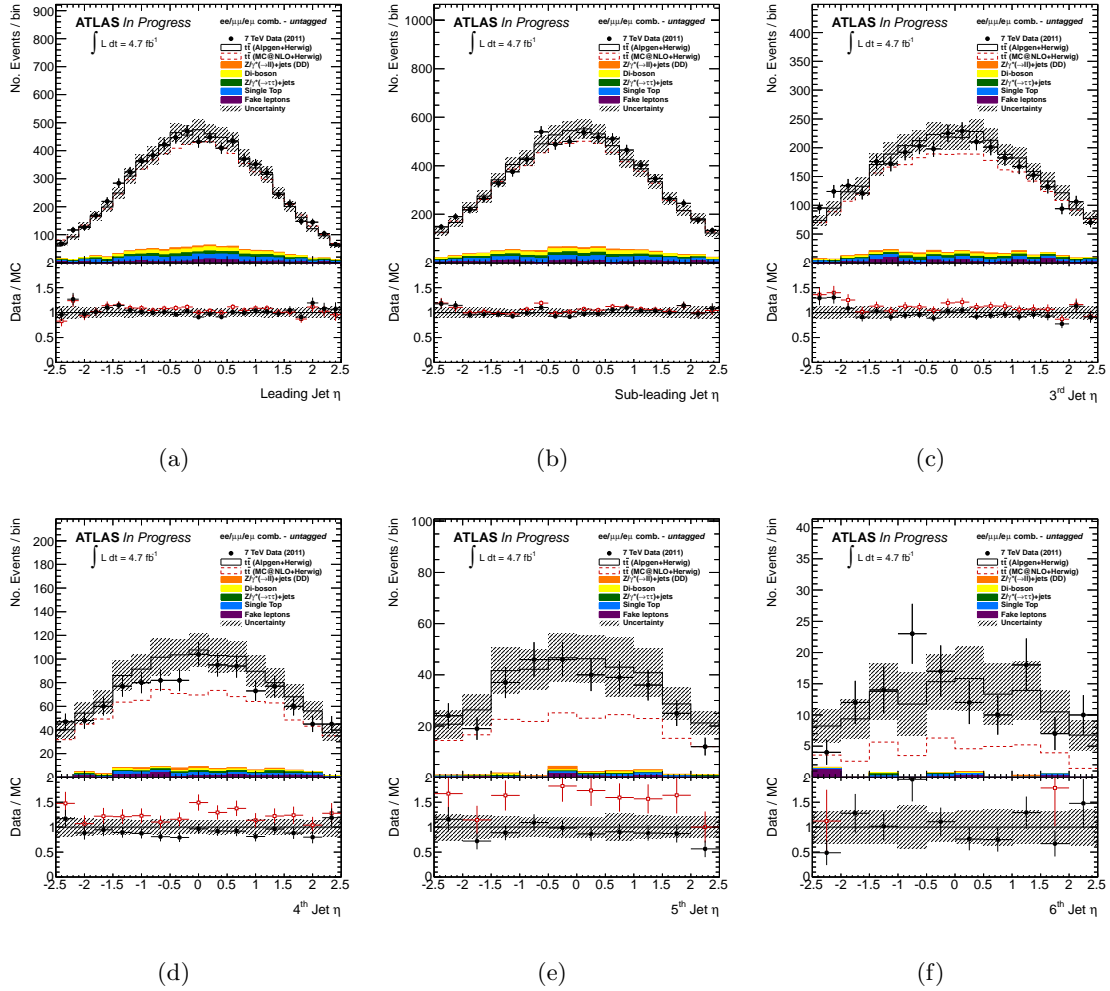


Figure A.13: The  $\eta$  distributions for all channels combined for the (a) leading, (b) sub-leading, (c) 3<sup>rd</sup>, (d) 4<sup>th</sup>, (e) 5<sup>th</sup>, and (f) 6<sup>th</sup> (inclusive) jets.

## A.2 Reconstructed jet multiplicity results and modeling

The reconstruction-level jet multiplicity results were shown in Section 5.3. In general, the predicted yields showed good agreement with the data within the uncertainties in most bins for the ALPGEN+HERWIG generator (with observed data yields in many of the high jet multiplicity bins on the edge of the uncertainty band). One exception to this observation is in the  $e\mu$  channel in the four jet bin for the 60 GeV threshold (and to a lesser extent, the same bin in the same channel for the 40 GeV threshold as well), where a significant deviation is observed. Though the analysis is designed to be insensitive to the predictions of the generator used to unfold the reconstruction-level distribution, large disagreements between the data and MC should be investigated, and this is the subject of this section. The statistical significance of the disagreement in this bin is  $S = 3.1\sigma$  when taking the Poisson uncertainty on the expectation as the statistical uncertainty. Including systematics, the significance is  $S = 2.2\sigma$ .

In total, there are 60 jet multiplicity bins with non-trivial statistical correlations in all channels and all thresholds, so the issue is to determine the probability (or  $p$ -value) for observing a fluctuation of the observed size in any one of these bins. This is essentially accounting for the look-elsewhere effect [151, 152], usually discussed in the literature in the context of searches for new resonances, where the largest disagreement with the background only hypothesis in the tested parameter space is considered as potential new physics.

Due to the relatively small disagreement observed in this analysis (compared to the  $\sim 5\sigma$  deviations which need to be evaluated in searches for new physics), the  $p$ -value for this fluctuation is easily estimated using the pseudo-experiments, using the same method outlined in Section 7.2. Ten thousand pseudo-experiments are performed in order to simulate fluctuations which are potentially at the permil level. In each pseudo-experiment, the largest fluctuation is recorded and used to determine a probability distribution. The pseudo-experiments use statistical uncertainties and correlations based on Poisson distributions about the expectation (MC signal plus backgrounds). The statistical error matrix for the ALPGEN+HERWIG  $t\bar{t}$  MC plus all estimated backgrounds is shown in Figure A.14 for the  $e\mu$  channel analysis. The probability distribution is estimated both for statistical fluctuations only, and including systematics, with all systematics outlined in Section 7.1

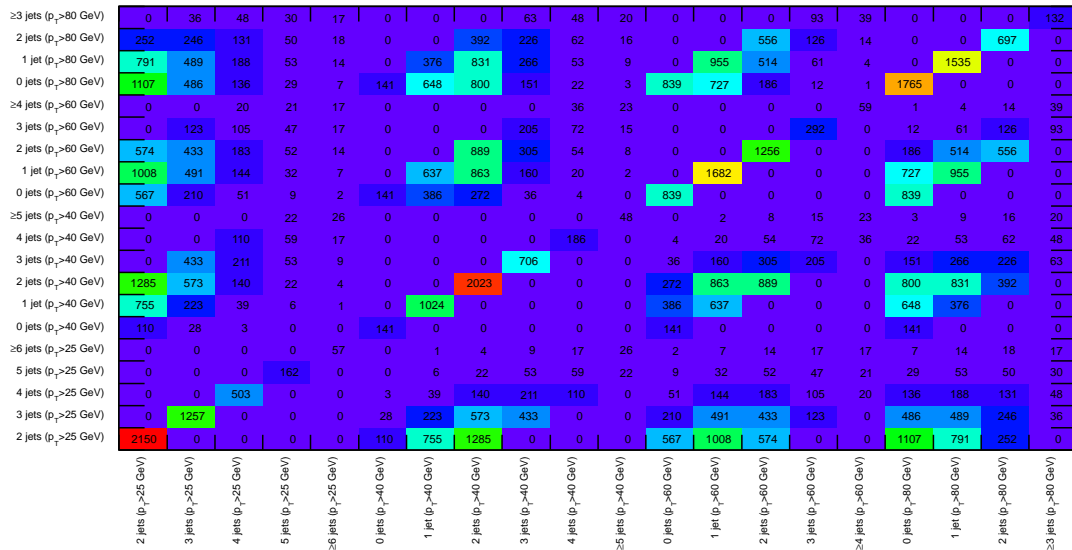


Figure A.14: Statistical covariance matrix for the  $e\mu$  channel. Cross-referencing bins in separate jet multiplicity distributions with different  $p_T$  thresholds shows the number of events that are in both bins.

considered except the unfolding uncertainties (since reconstruction-level disagreement is considered here).

Figure A.15 shows the distribution of the largest statistical fluctuation in each pseudo-experiment and the  $p$ -value for a given fluctuation, as measured by this distribution. Figure A.16 shows the same distributions when including systematic uncertainties. These results show that a  $3.1\sigma$  ( $2.2\sigma$ ) statistical (plus systematic) fluctuation in a single bin corresponds to a  $1.7\sigma$  ( $0.6\sigma$ ) fluctuation of the data, when considering all bins for all jet multiplicity distributions for all  $p_T$  thresholds and channels. The deviation of the ALPGEN+HERWIG reconstruction-level predictions for this bin is therefore not inconsistent with the ATLAS dataset.

The  $p_T > 40$  GeV jet multiplicity distribution in the  $e\mu$  channel also has a significant disagreement corresponding to a  $2.9\sigma$  ( $1.6\sigma$ ) statistical (plus systematic) fluctuation, when considering the bin in isolation. As can be seen in Figure A.14, there is some statistical correlation between this bin, and the corresponding bin in the  $p_T > 60$  GeV distribution, so this is not too surprising. The analysis described above is also used to estimate the

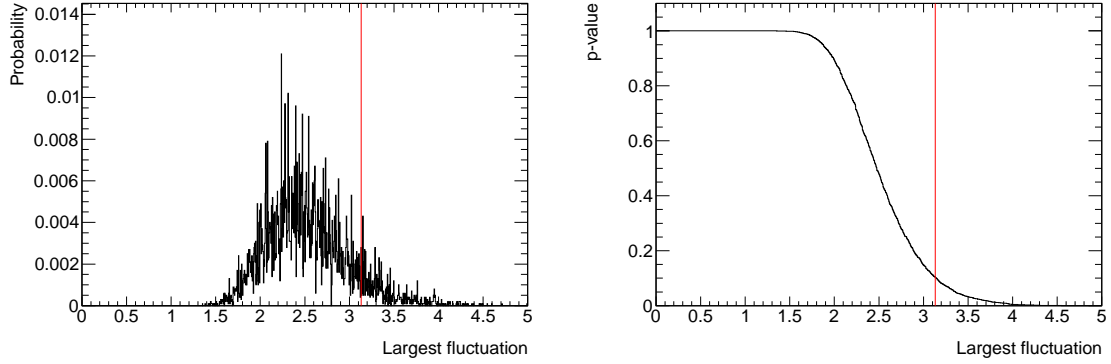


Figure A.15: Probability distribution for the largest statistical fluctuation in a given pseudo-experiment (left) and the corresponding  $p$ -value for a given fluctuation (right). The red line shows statistical significance of the observed deviation in the four 60 GeV jet bin in the  $e\mu$  channel, the largest deviation of the ATLAS dataset with respect to the ALPGEN+HERWIG  $t\bar{t}$  MC plus backgrounds in this analysis.

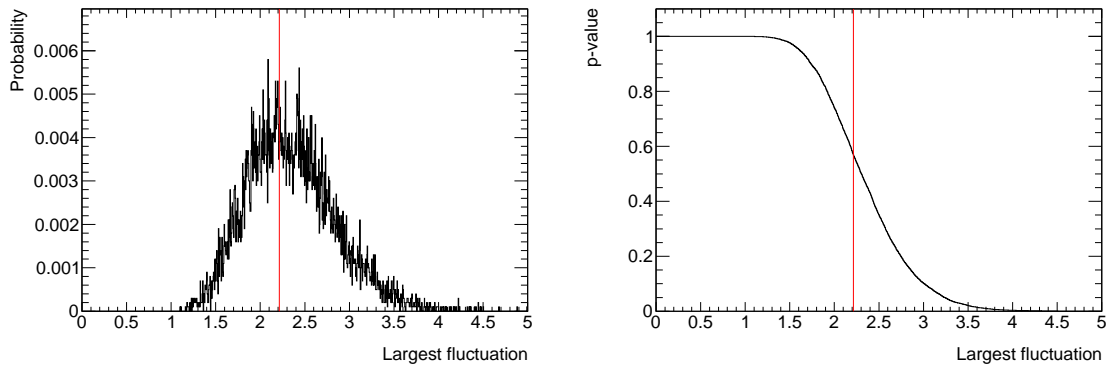


Figure A.16: Probability distribution for the largest statistical plus systematic fluctuation in a given pseudo-experiment (left) and the corresponding  $p$ -value for a given fluctuation (right). The red line shows significance of the observed deviation in the four 60 GeV jet bin in the  $e\mu$  channel, the largest deviation of the ATLAS dataset with respect to the ALPGEN+HERWIG  $t\bar{t}$  MC plus backgrounds in this analysis.

$p$ -value for the second largest fluctuation when taking into account all bins, which shows that this fluctuation is equivalent to a  $2.3\sigma$  ( $0.8\sigma$ ) statistical (plus systematic) fluctuation of the data. This is also not inconsistent when including systematics.

As a more comprehensive test of the consistency of the ALPGEN+HERWIG predictions (as well as other models) with the ATLAS 7 TeV dataset, a generalized  $\chi^2$  test statistic distribution is used to calculate a  $p$ -value for all considered jet multiplicity bins in all channels. The statistic is defined as:

$$\chi^2 = (v - \mu)^T C (v - \mu) \quad (\text{A.1})$$

where  $v$  is the vector of data yields (over all 60 bins considered),  $\mu$  is the expectation of the model, and  $C$  is the error (covariance) matrix, including both statistical and systematic uncertainties. The  $\chi^2$  distribution is estimated by throwing pseudo-experiments for a pseudo-data  $v_{\text{pseudo}}$  in order to evaluate the  $p$ -value for the deviation of the ATLAS dataset with respect to a given model  $\mu$ . The statistical uncertainties are again based on Poisson distributions about the expectation of the model being tested and include statistical correlations between bins in the different  $p_T$  thresholds. Systematic uncertainties are evaluated for a given model using independent Gaussian variations of nuisance parameters for each source. Each source is treated as fully correlated sample-to-sample and bin-to-bin and uncorrelated with any other source.

The results of the generalized  $\chi^2$  tests for each of the fully simulated generators used in this analysis are shown in Figure A.17 and summarized in Table A.1. Defining inconsistency at the 95% confidence level, the main generators used for the nominal unfolding and evaluating systematics (ALPGEN+HERWIG, ALPGEN+PYTHIA, and POWHEG+PYTHIA) are all consistent with the data, whereas MC@NLO+HERWIG is not.

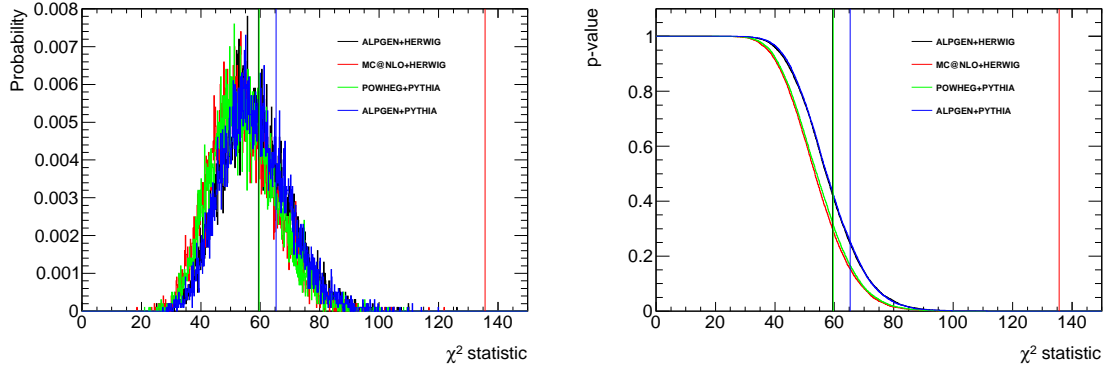


Figure A.17: Probability distribution for the  $\chi^2$  test statistic for a given pseudo-experiment (left) and the corresponding  $p$ -value (right). The vertical lines show the observed  $\chi^2$  test statistics for each model with respect to the ATLAS dataset.

Table A.1: Table showing the observed generalized  $\chi^2$  test statistics of each fully simulated model used in this analysis with respect to the ATLAS dataset, as well as the  $p$ -value that the dataset is consistent with each model. The  $p$ -value in each case is determined using the pseudo-experiment method described in this section, with the exception of MC@NLO which is estimated assuming a standard  $\chi^2$  distribution with 60 degrees of freedom for each bin considered in this analysis.

Model	$\chi^2$	$\chi^2/\text{n.d.f.}$	$p$ -value
ALPGEN+HERWIG	59.5	0.992	0.42
MC@NLO+HERWIG	134	2.23	$\sim 10^{-7}$
POWHEG+PYTHIA	59.3	0.988	0.31
ALPGEN+PYTHIA	64.8	1.08	0.25

## Appendix B

# Unfolding

As mentioned in Chapter 6, the unfolding corrections also have potential biases which are sensitive to differences between the “true”  $N_{\text{jets}}^{\text{part}}$  spectrum and the spectrum in the MC used to define the corrections. In the iterative unsmearing method, this bias comes from the fact that the method starts with a set of priors equal to the MC sample defining the unfolding and iteratively moves away from that towards an unbiased result, but stopping before that in order to reduce sensitivity to statistical fluctuations. This bias is present even if the response matrix is correct, but the true particle-level p.d.f. is different from the one used as an initial prior. The size of the bias is therefore a function of how different the priors are from the true value and how many iterations are used. In addition to the bias from the unsmearing, several of the other corrections are potentially sensitive to biases coming from the  $N_{\text{jets}}^{\text{part}}$  spectrum used to define the unfolding (for example, the  $f_{\text{reco!part}}$  correction depends somewhat on how many events are generated with less than 2 jets).

The potential bias is estimated by changing the ALPGEN particle-level distribution to match the one from MC@NLO before folding, unfolding, and measuring the difference with respect to MC@NLO. The folding is applied by re-weighting ALPGEN events to match the particle-level distribution of MC@NLO. Figure B.1 shows the bias estimates as well as the statistical uncertainties for the  $p_{\text{T}} > 25$  GeV threshold for several numbers of iterations. The statistical uncertainty is shown by the dotted lines and the bias is shown by the dashed. The solid line shows the two added in quadrature.

The goal is to make use of the iterative method to reduce sensitivity to statistical

fluctuations while maintaining control of the bias. Since the analysis aims to compare results between different generators, a choice of the number of iterations with a relatively small bias is favored. Therefore, final number of iterations was chosen such that the bin with the largest bias estimation as a percentage of the statistical uncertainty (considering all  $p_T$  thresholds) is less than 20%, which in this analysis was determined to be 4 iterations. The bias uncertainty estimate on the unfolded result determined from this method is no more than 5% of the measured values (and less than 1% in most bins). With the choice of 4 iterations, the figures show that the statistical uncertainty is reduced, while the bias is kept small. The “uncertainty” due to the bias added in quadrature with the statistical uncertainty is nearly identical to the uncertainty due to statistics alone, indicating that any bias uncertainty would not have a strong relative influence on the final results. Note that the bias uncertainty is included indirectly with the other unfolding uncertainties, as discussed in Section 7.2.

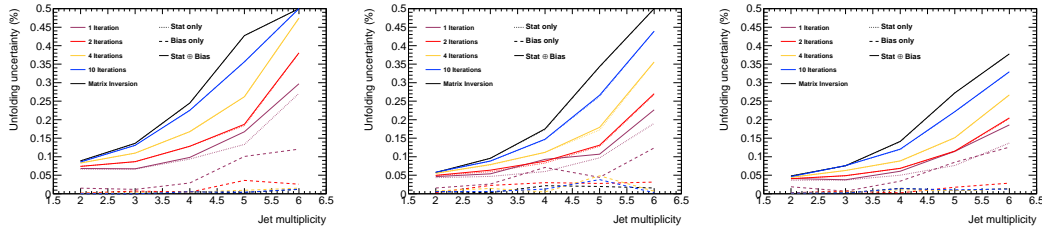


Figure B.1: Estimated unfolding biases for the  $ee$  (left),  $\mu\mu$  (center), and  $e\mu$  channels for the  $p_T > 25$  GeV threshold, for different numbers of iterations, as well as the matrix inversion method for comparison. The dashed line represents the estimated relative error on the measurement due to the unfolding bias and the dotted line is the statistical uncertainty. The solid line is the two uncertainties added in quadrature.

## Appendix C

# Details of systematic uncertainties

### C.1 Jet Energy Scale

As has been mentioned numerous times throughout this note, the uncertainty associated with the JES is dominant in this analysis. Several steps have been taken to reduce this uncertainty. In addition to the 11 nuisance parameters describing the uncertainty on the baseline estimate, additional uncertainties come from effects due to pile-up, close-by jets, and jet flavor. In the final estimate of the uncertainty on the  $t\bar{t}$  jet multiplicity analysis, each individual nuisance parameter is varied independently in the pseudo-experiments.

The processes used to estimate the JES in the *in situ* techniques are dominated by jets induced from high  $p_T$  light quarks. Therefore, additional uncertainties need to be considered for samples containing jets induced from  $b$ -quarks and/or gluons. Uncertainties applied to  $b$ -jets are derived from MC studies and validated using  $b$ -tagged jets on data. The uncertainty is applied to jets which match to true  $b$ -quarks in the MC.

Uncertainties on gluon induced jets are not added on a jet-by-jet basis as they are with  $b$ -jets. Instead, additional uncertainties are applied to all non- $b$ -jets based on an uncertainty of the fraction of jets estimated to be induced from gluons, as well as the uncertainty of the gluon-jet response estimated by comparing different Monte Carlos. The gluon fraction estimate for this analysis is the topic of this appendix.

For the purposes of the gluon fraction estimate, the flavor of a true particle-level jet is defined as the hardest parton (including light quarks,  $b$ -quarks, and gluons) matched to

the jet within a cone of  $\Delta R < 0.4$ . The flavor of a reconstructed jet is taken as the flavor of the closest particle-level jet within  $\Delta R < 0.35$ . Unmatched reconstructed jets are not considered in the gluon fraction estimation. Since additional flavor-related uncertainties on  $b$ -jets are applied separately,  $b$ -jets are also not considered in the fraction. Taking all matched non- $b$ -jets, the gluon fraction  $f_g$  is defined as:

$$f_g = \frac{N_g}{N_g + N_q} \quad (\text{C.1})$$

$f_g$  is estimated using the nominal ALPGEN+HERWIG sample, parametrized vs. jet  $p_T$ ,  $\eta$ , and the number of jets in the event. An uncertainty  $\sigma_{f_g}$  is estimated by comparing the estimate from the nominal sample to the same fraction estimated on MC@NLO. To be conservative on this purely MC-based estimate, an additional 10% added in quadrature. In bins with low statistics, a 50% gluon fraction is considered, with a 50% uncertainty. The final quark-gluon uncertainty applied to all non- $b$ -jets is given by:

$$\sigma_{\text{quark-gluon}} = \frac{\sigma_{f_g}(R_q - R_g)}{(1 - f_g)R_q + f_g R_g} \oplus \sigma_{R_g} f_g \quad (\text{C.2})$$

where  $R_q$  and  $R_g$  are the responses for quark and gluon jets, respectively.

Figure C.1 shows the estimated gluon fraction and Figure C.2 shows its uncertainty for jets in di-lepton  $t\bar{t}$  events passing the signal selections outlined in Section 5.1. As can be seen in the figures, gluon fractions are typically higher in the  $p_T$ -range of interest to this analysis than the  $50 \pm 50\%$  assumed by the tool used to apply the JES uncertainty in the absence of analysis specific inputs. The flavor fraction uncertainty, however, is significantly lower, so while the gluon-response component of the uncertainty is higher than the default assumption, the flavor fraction component is much lower leading to an overall decrease in the total JES uncertainty of about 0.5% between  $15 \text{ GeV} < p_t < 100 \text{ GeV}$ , as can be seen by comparing the default uncertainty in Figure C.3 and the corresponding uncertainty using the estimated flavor fraction inputs in Figure C.4.

This analysis is repeated for the  $Z$ +jets sample in its signal region to get a gluon fraction for  $Z$ +jets events. The gluon fraction in  $Z$ +jets events in the  $p_T$  range of interest is found to be significantly higher, at around 30%. The uncertainties on each gluon fraction are

assumed to be uncorrelated. This leads to some residual uncertainty due to the JES at high jet multiplicity in the ratio measurement.

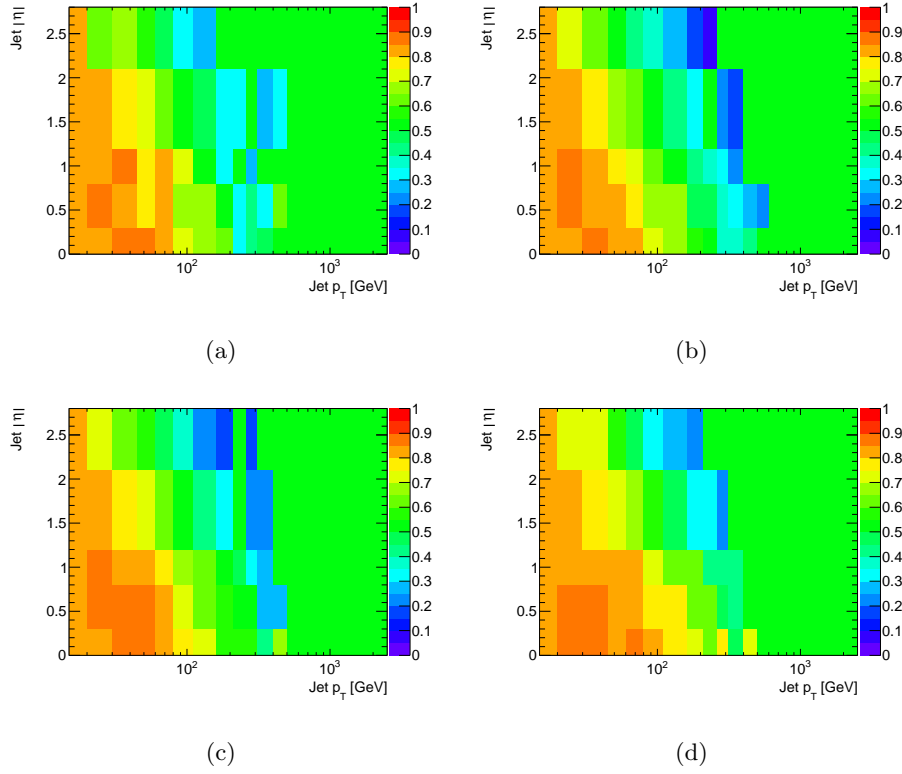


Figure C.1: The gluon fraction estimate used in the di-lepton  $t\bar{t}$  jet multiplicity for events with (a) 2, (b) 3, (c) 4, and (d)  $\geq 5$  jets, used for the JES uncertainty.

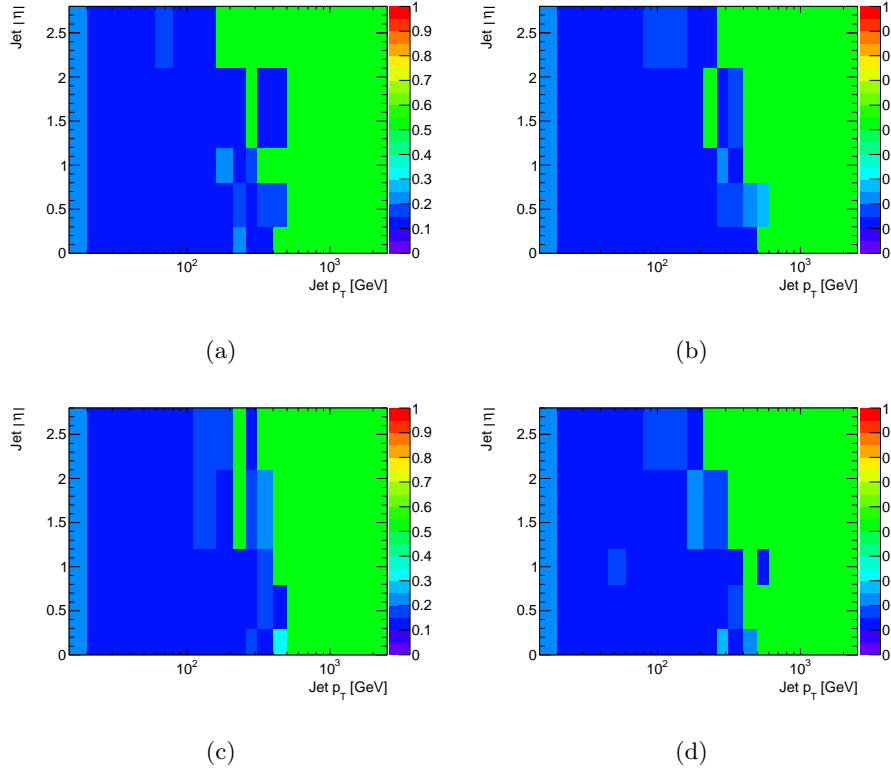


Figure C.2: The gluon fraction uncertainty estimate used in the di-lepton  $t\bar{t}$  jet multiplicity for events with (a) 2, (b) 3, (c) 4, and (d)  $\geq 5$  jets, used for the JES uncertainty.

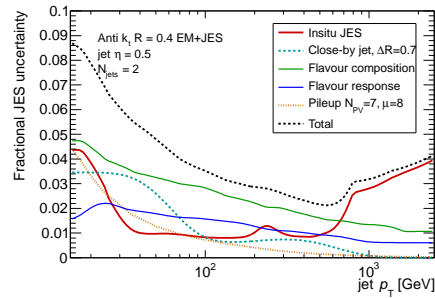


Figure C.3: The default JES uncertainty by component as a function of jet  $p_T$  for jets with  $\eta < 0.8$ .

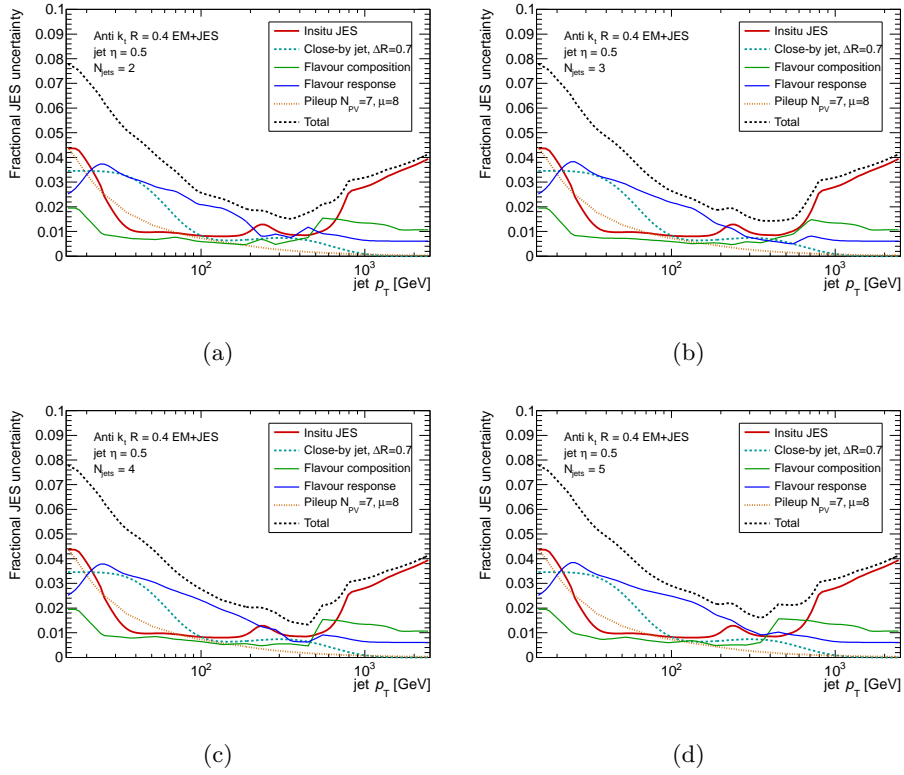


Figure C.4: The JES uncertainty by component using the estimated flavor fraction inputs, as a function of jet  $p_T$  for events with (a) 2, (b) 3, (c) 4, and (d)  $\geq 5$  jets, and for jets with  $\eta < 0.8$ .

## C.2 Full systematic uncertainty tables

For brevity, the systematics tables shown throughout this note have been grouped together by objects/procedures. Detailed tables listed by source are available here for the 25 GeV threshold for the all channel combination for both the pure  $t\bar{t}$  measurement in Tables ??-C.6. The JES uncertainty is also broken down by nuisance parameter. Since most of the cancellation of systematic uncertainties occurs for nuisance parameters in the jet energy scale, the JES uncertainty broken down by nuisance parameter is also shown for the combination of all channels in the ratio measurement in Table C.7.

Table C.1: Statistical uncertainties (in %) for the combination of all channels for the  $p_T > 25$  GeV threshold.

	2 jets	3 jets	4 jets	5 jets	$\geq 6$ jets
Stat(Data)	$\pm 1.8$	$\pm 3.1$	$\pm 5.5$	$\pm 9.6$	$\pm 15.3$
Stat(MC)	$\pm 1.4$	$\pm 2.3$	$\pm 2.8$	$\pm 3.8$	$\pm 5.3$
All Syst. (Statistics)	$\pm 2.3$	$\pm 3.9$	$\pm 6.2$	$\pm 10.3$	$\pm 16.2$

Table C.2: Background specific uncertainties (in %) for the combination of all channels for the  $p_T > 25$  GeV threshold.

	2 jets	3 jets	4 jets	5 jets	$\geq 6$ jets
Lumi (1.8%)	$< \pm 0.1$	$< \pm 0.1$	$\pm 0.1$	$\pm 0.1$	$\pm 0.2$
Fakes( $\epsilon_{real}$ )	$< \pm 0.1$	$< \pm 0.1$	$\pm 0.6$	$\pm 0.3$	$\pm 0.4$
Fakes( $\epsilon_{fake}$ )	$\pm 0.2$	$\pm 0.1$	$\pm 1.0$	$\pm 1.0$	$\pm 0.5$
Shape(DY)	$\pm 0.2$	$\pm 0.4$	$\pm 0.5$	$\pm 0.2$	$\pm 1.4$
Background $\sigma_{t\bar{t}}$ (Theory)	$< \pm 0.1$	$< \pm 0.1$	$< \pm 0.1$	$< \pm 0.1$	$< \pm 0.1$
Background $\sigma_{Drell-Yan}$ (Theory)	$\pm 0.1$	$< \pm 0.1$	$\pm 0.3$	$\pm 0.5$	$\pm 0.1$
$\sigma_{Z \rightarrow \tau\tau}$ (Theory)	$< \pm 0.1$	$< \pm 0.1$	$\pm 0.1$	$\pm 0.2$	$\pm 0.9$
$\sigma_{VV}$ (Theory)	$\pm 0.2$	$\pm 0.2$	$\pm 0.3$	$\pm 0.3$	$\pm 0.7$
$\sigma_t$ (Theory)	$\pm 0.1$	$\pm 0.1$	$\pm 0.2$	$\pm 0.3$	$\pm 0.3$
$\sigma_{W+jets}$ (Theory)	$< \pm 0.1$	$< \pm 0.1$	$< \pm 0.1$	$< \pm 0.1$	$< \pm 0.1$
All Syst. (Backgrounds)	$\pm 0.4$	$\pm 0.5$	$\pm 1.4$	$\pm 1.3$	$\pm 2.0$

Table C.3: Lepton specific uncertainties (in %) for the combination of all channels for the  $p_T > 25$  GeV threshold.

	2 jets	3 jets	4 jets	5 jets	$\geq 6$ jets
SF(Mu.ID)	$< \pm 0.1$	$< \pm 0.1$	$< \pm 0.1$	$< \pm 0.1$	$< \pm 0.1$
SF(Mu.Trig)	$< \pm 0.1$	$< \pm 0.1$	$< \pm 0.1$	$< \pm 0.1$	$< \pm 0.1$
SF(El.ID)	$< \pm 0.1$	$< \pm 0.1$	$\pm 0.2$	$\pm 0.2$	$\pm 0.3$
SF(El.Trig)	$< \pm 0.1$	$< \pm 0.1$	$< \pm 0.1$	$< \pm 0.1$	$< \pm 0.1$
Mu.ES	$< \pm 0.1$	$< \pm 0.1$	$< \pm 0.1$	$\pm 0.2$	$\pm 0.2$
Mu.ER(MS)	$< \pm 0.1$	$< \pm 0.1$	$\pm 0.1$	$\pm 0.2$	$\pm 0.2$
Mu.ER(ID)	$< \pm 0.1$	$< \pm 0.1$	$< \pm 0.1$	$< \pm 0.1$	$\pm 0.3$
El.ES	$< \pm 0.1$	$\pm 0.1$	$\pm 0.2$	$< \pm 0.1$	$\pm 0.3$
El.ER	$\pm 0.1$	$\pm 0.2$	$\pm 0.2$	$\pm 0.4$	$\pm 0.3$
All Syst. (Leptons)	$\pm 0.1$	$\pm 0.2$	$\pm 0.4$	$\pm 0.5$	$\pm 0.7$

Table C.4:  $E_T^{\text{miss}}$  specific uncertainties (in %) for the combination of all channels for the  $p_T > 25$  GeV threshold.

	2 jets	3 jets	4 jets	5 jets	$\geq 6$ jets
MET(CellOut)	$< \pm 0.1$	$\pm 0.2$	$\pm 0.3$	$\pm 0.3$	$\pm 0.4$
MET(PileUp)	$< \pm 0.1$	$< \pm 0.1$	$\pm 0.3$	$\pm 0.1$	$\pm 0.2$
All Syst. ( $E_T^{\text{miss}}$ )	$< \pm 0.1$	$\pm 0.2$	$\pm 0.4$	$\pm 0.3$	$\pm 0.4$

Table C.5: Jet specific uncertainties (in %) for the combination of all channels for the  $p_T > 25$  GeV threshold.

	2 jets	3 jets	4 jets	5 jets	$\geq 6$ jets
JES (Eff. NP - Stat. 1)	$\pm 0.8$	$\pm 0.4$	$\pm 1.4$	$\pm 2.3$	$\pm 3.9$
JES (Eff. NP - Stat. 2)	$< \pm 0.1$	$< \pm 0.1$	$< \pm 0.1$	$< \pm 0.1$	$\pm 0.3$
JES (Eff. NP - Stat. 3)	$\pm 0.1$	$\pm 0.1$	$\pm 0.2$	$\pm 0.2$	$\pm 0.6$
JES (Eff. NP - Modeling 1)	$\pm 1.4$	$\pm 0.7$	$\pm 2.3$	$\pm 4.4$	$\pm 6.5$
JES (Eff. NP - Modeling 2)	$\pm 0.1$	$< \pm 0.1$	$\pm 0.2$	$\pm 0.2$	$\pm 0.5$
JES (Eff. NP - Modeling 3)	$< \pm 0.1$	$< \pm 0.1$	$\pm 0.2$	$\pm 0.1$	$\pm 0.3$
JES (Eff. NP - Modeling 4)	$< \pm 0.1$	$< \pm 0.1$	$< \pm 0.1$	$\pm 0.1$	$\pm 0.4$
JES (Eff. NP - Detector 1)	$\pm 0.5$	$\pm 0.2$	$\pm 1.1$	$\pm 1.7$	$\pm 2.6$
JES (Eff. NP - Detector 2)	$< \pm 0.1$	$< \pm 0.1$	$\pm 0.1$	$\pm 0.2$	$\pm 0.4$
JES (Eff. NP - Mixed 1)	$< \pm 0.1$	$< \pm 0.1$	$\pm 0.1$	$\pm 0.2$	$\pm 0.3$
JES (Eff. NP - Mixed 2)	$\pm 0.3$	$\pm 0.2$	$\pm 0.5$	$\pm 0.8$	$\pm 0.9$
JES ( $\eta$ -inter. - stat)	$\pm 0.4$	$\pm 0.3$	$\pm 0.8$	$\pm 0.8$	$\pm 1.4$
JES ( $\eta$ -inter. - MC)	$\pm 1.2$	$\pm 0.7$	$\pm 2.1$	$\pm 3.1$	$\pm 4.2$
JES (High $p_T$ extr.)	$< \pm 0.1$	$< \pm 0.1$	$< \pm 0.1$	$< \pm 0.1$	$< \pm 0.1$
JES (Non-closure)	$< \pm 0.1$	$< \pm 0.1$	$< \pm 0.1$	$< \pm 0.1$	$< \pm 0.1$
JES (Pile-up - $\mu$ )	$\pm 1.7$	$\pm 0.9$	$\pm 2.8$	$\pm 4.9$	$\pm 7.3$
JES (Pile-up - $N_{PV}$ )	$\pm 1.6$	$\pm 0.9$	$\pm 2.6$	$\pm 4.5$	$\pm 6.9$
JES (Close-by)	$\pm 1.4$	$\pm 0.6$	$\pm 2.4$	$\pm 4.8$	$\pm 9.1$
JES (Flavor Comp. - $t\bar{t}$ )	$\pm 0.7$	$\pm 0.4$	$\pm 1.3$	$\pm 2.0$	$\pm 2.8$
JES (Flavor Comp. - $Z$ +jets)	$< \pm 0.1$	$< \pm 0.1$	$< \pm 0.1$	$\pm 0.1$	$\pm 0.5$
JES (Flavor Comp. - other)	$< \pm 0.1$	$< \pm 0.1$	$\pm 0.2$	$\pm 0.4$	$\pm 1.1$
JES (Flavor Resp.)	$\pm 2.9$	$\pm 1.5$	$\pm 4.7$	$\pm 8.5$	$\pm 12.7$
JES ( $b$ -jets)	$\pm 0.2$	$\pm 0.3$	$\pm 0.3$	$\pm 0.4$	$\pm 0.8$
JER	$\pm 2.0$	$\pm 1.8$	$\pm 1.5$	$\pm 5.7$	$\pm 9.5$
Jet Eff.	$< \pm 0.1$	$< \pm 0.1$	$< \pm 0.1$	$\pm 0.2$	$\pm 0.3$
JVF	$< \pm 0.1$	$< \pm 0.1$	$< \pm 0.1$	$< \pm 0.1$	$< \pm 0.1$
All Syst. (Jets)	$\pm 5.0$	$\pm 3.0$	$\pm 7.8$	$\pm 14.7$	$\pm 23.0$

Table C.6: Unfolding/signal modeling specific uncertainties (in %) for the combination of all channels for the  $p_T > 25$  GeV threshold.

	2 jets	3 jets	4 jets	5 jets	$\geq 6$ jets
Generator	$\pm 0.2$	$\pm 0.8$	$\pm 0.7$	$\pm 1.9$	$\pm 1.9$
Fragmentation	$\pm 0.3$	$\pm 0.9$	$\pm 1.3$	$\pm 2.4$	$\pm 2.4$
I/FSR	$\pm 0.1$	$\pm 0.4$	$\pm 1.1$	$\pm 0.9$	$\pm 3.1$
Color Reconnection	$\pm 0.1$	$\pm 0.6$	$\pm 0.7$	$\pm 2.6$	$\pm 2.6$
PDF	$\pm 0.1$	$\pm 0.1$	$\pm 0.5$	$\pm 1.0$	$\pm 1.0$
All Syst. (Unfolding)	$\pm 0.4$	$\pm 1.4$	$\pm 2.0$	$\pm 4.2$	$\pm 5.2$

Table C.7: Jet specific uncertainties (in %) for the combination of all channels for the  $p_T > 25$  GeV threshold ratio measurement.

	2 jets	3 jets	4 jets	5 jets	$\geq 6$ jets
JES (Eff. NP - Stat. 1)	$\pm 0.3$	$\pm 0.7$	$\pm 0.5$	$\pm 0.7$	$\pm 0.6$
JES (Eff. NP - Stat. 2)	$\pm 0.3$	$\pm 0.3$	$\pm 0.3$	$\pm 0.5$	$\pm 0.4$
JES (Eff. NP - Stat. 3)	$\pm 0.3$	$\pm 0.3$	$\pm 0.5$	$\pm 0.5$	$\pm 0.5$
JES (Eff. NP - Modeling 1)	$\pm 0.3$	$\pm 1.1$	$\pm 0.4$	$\pm 1.4$	$\pm 1.0$
JES (Eff. NP - Modeling 2)	$\pm 0.3$	$\pm 0.3$	$\pm 0.5$	$\pm 0.6$	$\pm 0.5$
JES (Eff. NP - Modeling 3)	$\pm 0.3$	$\pm 0.4$	$\pm 0.5$	$\pm 0.5$	$\pm 0.3$
JES (Eff. NP - Modeling 4)	$< \pm 0.1$	$< \pm 0.1$	$< \pm 0.1$	$< \pm 0.1$	$\pm 0.3$
JES (Eff. NP - Detector 1)	$\pm 0.3$	$\pm 0.6$	$\pm 0.4$	$\pm 0.5$	$\pm 0.9$
JES (Eff. NP - Detector 2)	$< \pm 0.1$	$< \pm 0.1$	$< \pm 0.1$	$< \pm 0.1$	$\pm 0.3$
JES (Eff. NP - Mixed 1)	$< \pm 0.1$	$< \pm 0.1$	$< \pm 0.1$	$< \pm 0.1$	$\pm 0.3$
JES (Eff. NP - Mixed 2)	$\pm 0.2$	$\pm 0.2$	$\pm 0.2$	$\pm 0.2$	$\pm 0.4$
JES ( $\eta$ -inter. - stat)	$\pm 0.4$	$\pm 0.4$	$\pm 0.7$	$\pm 0.5$	$\pm 0.4$
JES ( $\eta$ -inter. - MC)	$\pm 0.3$	$\pm 0.6$	$\pm 0.9$	$\pm 1.2$	$\pm 0.6$
JES (High $p_T$ extr.)	$< \pm 0.1$	$< \pm 0.1$	$< \pm 0.1$	$< \pm 0.1$	$< \pm 0.1$
JES (Non-closure)	$< \pm 0.1$	$< \pm 0.1$	$< \pm 0.1$	$< \pm 0.1$	$< \pm 0.1$
JES (Pile-up - $\mu$ )	$\pm 0.4$	$\pm 1.0$	$\pm 0.7$	$\pm 1.2$	$\pm 1.1$
JES (Pile-up - $N_{PV}$ )	$\pm 0.2$	$\pm 1.0$	$\pm 0.8$	$\pm 1.5$	$\pm 1.2$
JES (Close-by)	$\pm 0.4$	$\pm 0.8$	$\pm 1.6$	$\pm 2.2$	$\pm 3.2$
JES (Flavor Comp. - $t\bar{t}$ )	$\pm 0.6$	$\pm 0.6$	$\pm 1.6$	$\pm 2.2$	$\pm 3.1$
JES (Flavor Comp. - $Z$ +jets)	$\pm 0.7$	$\pm 1.7$	$\pm 2.2$	$\pm 2.8$	$\pm 3.8$
JES (Flavor Comp. - other)	$\pm 0.4$	$\pm 0.5$	$\pm 0.6$	$\pm 0.7$	$\pm 1.2$
JES (Flavor Resp.)	$\pm 1.5$	$\pm 2.5$	$\pm 0.4$	$\pm 1.9$	$\pm 2.5$
JES ( $b$ -jets)	$\pm 0.7$	$\pm 1.1$	$\pm 1.2$	$\pm 1.4$	$\pm 0.7$
JER	$\pm 1.9$	$\pm 4.7$	$\pm 3.4$	$\pm 2.3$	$\pm 3.6$
Jet Eff.	$< \pm 0.1$	$< \pm 0.1$	$< \pm 0.1$	$\pm 0.1$	$\pm 0.3$
JVF	$< \pm 0.1$	$< \pm 0.1$	$< \pm 0.1$	$< \pm 0.1$	$< \pm 0.1$
All Syst. (Jets)	$\pm 2.9$	$\pm 6.2$	$\pm 5.2$	$\pm 6.2$	$\pm 7.9$

## Part II

# Bibliography

# Bibliography

- [1] G. P. Salam, *Towards Jetography* arXiv, 0906.1833[hep-ph, ], Eur.Phys.J. **C67** (2010), 637–686.
- [2] M. E. Peskin and D. V. Schroeder, *An Introduction to Quantum Field Theory*, Perseus Books, Cambridge, Massachusetts, 1995.
- [3] F. Halzen and A. Martin, *Quarks & Leptons: An introductory course in modern particle physics*, John Wiley & Sons, New York, USA, 1984.
- [4] D. Perkins, *Introduction to High Energy Physics*, Addison-Wesley, Reading, USA, 1982.
- [5] D. Griffiths, *Introduction to Elementary Particles*, John Wiley & Sons, New York, USA, 1987.
- [6] G. Aad et al. (ATLAS Collaboration), *Observation of a new particle in the search for the Standard Model Higgs boson with the ATLAS detector at the LHC* arXiv, 1207.7214[hep-ex, ], Phys.Lett. **B716** (2012), 1–29.
- [7] S. Chatrchyan et al. (CMS Collaboration), *Observation of a new boson at a mass of 125 GeV with the CMS experiment at the LHC* arXiv, 1207.7235[hep-ex, ], Phys.Lett. **B716** (2012), 30–61.
- [8] R. Brock et al. (CTEQ Collaboration), *Handbook of perturbative QCD: Version 1.0*, Rev.Mod.Phys. **67** (1995), 157–248.
- [9] D. E. Soper, *Basics of QCD perturbation theory* arXiv, hep-ph/9702203[hep-ph, ], (1996).

- [10] M. Kobayashi and T. Maskawa, *CP-Violation in the Renormalizable Theory of Weak Interaction*, Progress of Theoretical Physics **49** (1973), 652–657.
- [11] N. Cabibbo, *Unitary Symmetry and Leptonic Decays*, Physical Review Letters **10** (1963), 531–533.
- [12] F. Abe et al. (CDF Collaboration), *Observation of top quark production in  $\bar{p}p$  collisions* arXiv, hep-ex/9503002[hep-ex, ], Phys.Rev.Lett. **74** (1995), 2626–2631.
- [13] S. Abachi et al. (D0 Collaboration), *Search for high mass top quark production in  $p\bar{p}$  collisions at  $\sqrt{s} = 1.8$  TeV* arXiv, hep-ex/9411001[hep-ex, ], Phys.Rev.Lett. **74** (1995), 2422–2426.
- [14] T. Aaltonen et al. (CDF Collaboration), *Measurement of the top quark forward-backward production asymmetry and its dependence on event kinematic properties* arXiv, 1211.1003[hep-ex, ], (2012).
- [15] V. M. Abazov et al. (D0 Collaboration), *Forward-backward asymmetry in top quark-antiquark production* arXiv, 1107.4995[hep-ex, ], Phys.Rev. **D84** (2011), 112005.
- [16] Tevatron Electroweak Working Group, CDF Collaboration, D0 Collaboration, *Combination of CDF and D0 results on the mass of the top quark using up to 5.8 fb<sup>-1</sup> of data* arXiv, 1107.5255[hep-ex, ], (2011).
- [17] *Measurement of the top quark mass from 2011 ATLAS data using the template method*, Tech. Report ATLAS-CONF-2011-120, CERN, Geneva, Aug 2011.
- [18] S. Chatrchyan et al. (CMS Collaboration), *Measurement of the  $t\bar{t}$  production cross section and the top quark mass in the dilepton channel in  $pp$  collisions at  $\sqrt{s} = 7$  TeV* arXiv, 1105.5661[hep-ex, ], JHEP **1107** (2011), 049.
- [19] B. Lillie, J. Shu, and T. M. Tait, *Kaluza-Klein Gluons as a Diagnostic of Warped Models* arXiv, hep-ph/0706.3960, Phys. Rev. D **76** (2007).
- [20] A. Djouadi, G. Moreau, and R. K. Singh, *Kaluza-Klein excitations of gauge bosons at the LHC* arXiv, hep-ph/0706.4191, Nucl. Phys. B **797** (2007), 1–26.

- [21] S. P. Martin, *Exploring compressed supersymmetry with same-sign top quarks at the Large Hadron Collider* arXiv, 0807.2820[hep-ph, ], Phys.Rev. **D78** (2008), 055019.
- [22] S. Dittmaier, P. Uwer, and S. Weinzierl, *Hadronic top-quark pair production in association with a hard jet at next-to-leading order QCD: Phenomenological studies for the Tevatron and the LHC* arXiv, 0810.0452[hep-ph, ], Eur.Phys.J. **C59** (2009), 625–646.
- [23] G. Aad et al. (ATLAS Collaboration), *Measurement of the production cross section for  $Z/\gamma^*$  in association with jets in pp collisions at  $\sqrt{s} = 7$  TeV with the ATLAS detector* arXiv, 1111.2690[hep-ex, ], Phys.Rev. **D85** (2012), 032009.
- [24] G. Aad et al. (ATLAS Collaboration), *Study of jets produced in association with a W boson in pp collisions at  $\sqrt{s} = 7$  TeV with the ATLAS detector* arXiv, 1201.1276[hep-ex, ], Phys.Rev. **D85** (2012), 092002.
- [25] K. Bierwagen, U. Blumenschein, J. F. Grivaz, T. Kanno, S. Meeham, M. Sandhoff, J. Sauvan, and A. Quadt, *Measurement of the cross section for jets produced in association with Z bosons*, Tech. Report ATL-COM-PHYS-2012-735, CERN, Geneva, Jun 2012.
- [26] *Combination of ATLAS and CMS top-quark pair cross section measurements using up to 1.1 fb<sup>-1</sup> of data at 7 TeV*, Tech. Report ATLAS-CONF-2012-134, CERN, Geneva, Sep 2012.
- [27] M. Cacciari, M. Czakon, M. Mangano, A. Mitov, and P. Nason, *Top-pair production at hadron colliders with next-to-next-to-leading logarithmic soft-gluon resummation* arXiv, 1111.5869[hep-ph, ], Phys.Lett. **B710** (2012), 612–622.
- [28] M. Czakon and A. Mitov, *Top++: A Program for the Calculation of the Top-Pair Cross-Section at Hadron Colliders* arXiv, 1112.5675[hep-ph, ], (2011).
- [29] H. Yukawa, *On the interaction of elementary particles*, Proc.Phys.Math.Soc.Jap. **17** (1935), 48–57.
- [30] C. Lattes, H. Muirhead, G. Occhialini, and C. Powell, *Processes Involving Charged Mesons*, Nature **159** (1947), 694–697.

- [31] C. Lattes, G. Occhialini, and C. Powell, *OBSERVATIONS ON THE TRACKS OF SLOW MESONS IN PHOTOGRAPHIC EMULSIONS. 1*, Nature **160** (1947), 453–456.
- [32] C. Lattes, G. Occhialini, and C. Powell, *OBSERVATIONS ON THE TRACKS OF SLOW MESONS IN PHOTOGRAPHIC EMULSIONS. 2*, Nature **160** (1947), 486–492.
- [33] M. Gell-Mann, *A Schematic Model of Baryons and Mesons*, Phys.Lett. **8** (1964), 214–215.
- [34] G. Zweig, *An  $SU_3$  model for strong interaction symmetry and its breaking; Part II*, (1964), no. CERN-TH-412, 80 p.
- [35] M. Han and Y. Nambu, *Three Triplet Model with Double  $SU(3)$  Symmetry*, Phys.Rev. **139** (1965), B1006–B1010.
- [36] O. Greenberg, *Spin and Unitary Spin Independence in a Paraquark Model of Baryons and Mesons*, Phys.Rev.Lett. **13** (1964), 598–602.
- [37] E. D. Bloom, D. Coward, H. DeStaebler, J. Drees, G. Miller, et al., *High-Energy Inelastic  $e p$  Scattering at 6-Degrees and 10-Degrees*, Phys.Rev.Lett. **23** (1969), 930–934.
- [38] J. I. Friedman and H. W. Kendall, *Deep inelastic electron scattering*, Ann.Rev.Nucl.Part.Sci. **22** (1972), 203–254.
- [39] R. P. Feynman, *Very high-energy collisions of hadrons*, Phys.Rev.Lett. **23** (1969), 1415–1417.
- [40] J. Bjorken and E. A. Paschos, *Inelastic Electron Proton and gamma Proton Scattering, and the Structure of the Nucleon*, Phys.Rev. **185** (1969), 1975–1982.
- [41] D. Gross and F. Wilczek, *Ultraviolet Behavior of Nonabelian Gauge Theories*, Phys.Rev.Lett. **30** (1973), 1343–1346.

- [42] H. D. Politzer, *Asymptotic Freedom: An Approach to Strong Interactions*, Phys.Rept. **14** (1974), 129–180.
- [43] K. G. Wilson, *Nonlagrangian models of current algebra*, Phys.Rev. **179** (1969), 1499–1512.
- [44] J. Callan, Curtis G., *Broken scale invariance in scalar field theory*, Phys.Rev. **D2** (1970), 1541–1547.
- [45] K. Symanzik, *Small distance behavior in field theory and power counting*, Commun.Math.Phys. **18** (1970), 227–246.
- [46] N. Christ, B. Hasslacher, and A. H. Mueller, *Light-Cone Behavior of Perturbation Theory*, Phys. Rev. D **6** (1972), 3543–3562.
- [47] Y. Frishman, *Light cone and short distances*, Physics Reports **13** (1974), no. 1, 1 – 52.
- [48] H. Fritzsche, M. Gell-Mann, and H. Leutwyler, *Advantages of the Color Octet Gluon Picture*, Phys.Lett. **B47** (1973), 365–368.
- [49] D. J. Gross and F. Wilczek, *Asymptotically Free Gauge Theories. I*, Phys. Rev. D **8** (1973), 3633–3652.
- [50] S. Weinberg, *Non-Abelian Gauge Theories of the Strong Interactions*, Phys. Rev. Lett. **31** (1973), 494–497.
- [51] K. G. Wilson, *Confinement of quarks*, Phys. Rev. D **10** (1974), 2445–2459.
- [52] J. Kogut and L. Susskind, *Hamiltonian formulation of Wilson’s lattice gauge theories*, Phys. Rev. D **11** (1975), 395–408.
- [53] R. K. Ellis, W. J. Stirling, and B. Webber, *QCD and collider physics*, Camb.Monogr.Part.Phys.Nucl.Phys.Cosmol. **8** (1996), 1–435.
- [54] D. Stump, J. Huston, J. Pumplin, W.-K. Tung, H. Lai, et al., *Inclusive jet production, parton distributions, and the search for new physics* arXiv, hep-ph/0303013[hep-ph, ], JHEP **0310** (2003), 046.

- [55] H.-L. Lai, M. Guzzi, J. Huston, Z. Li, P. M. Nadolsky, et al., *New parton distributions for collider physics* arXiv, 1007.2241[hep-ph, ], Phys.Rev. **D82** (2010), 074024.
- [56] A. Martin, W. Stirling, R. Thorne, and G. Watt, *Parton distributions for the LHC* arXiv, 0901.0002[hep-ph, ], Eur.Phys.J. **C63** (2009), 189–285.
- [57] V. Gribov and L. Lipatov, *Deep inelastic  $e p$  scattering in perturbation theory*, Sov.J.Nucl.Phys. **15** (1972), 438–450.
- [58] Y. L. Dokshitzer, *Calculation of the Structure Functions for Deep Inelastic Scattering and  $e^+ e^-$  Annihilation by Perturbation Theory in Quantum Chromodynamics.*, Sov.Phys.JETP **46** (1977), 641–653.
- [59] G. Altarelli and G. Parisi, *Asymptotic Freedom in Parton Language*, Nucl.Phys. **B126** (1977), 298.
- [60] L. Lipatov, *Reggeization of the Vector Meson and the Vacuum Singularity in Non-abelian Gauge Theories*, Sov.J.Nucl.Phys. **23** (1976), 338–345.
- [61] I. Balitsky and L. Lipatov, *The Pomeron Singularity in Quantum Chromodynamics*, Sov.J.Nucl.Phys. **28** (1978), 822–829.
- [62] A. Buckley, J. Butterworth, S. Gieseke, D. Grellscheid, S. Hoche, et al., *General-purpose event generators for LHC physics* arXiv, 1101.2599[hep-ph, ], Phys.Rept. **504** (2011), 145–233.
- [63] M. Dobbs, S. Frixione, E. Laenen, K. Tollefson, H. Baer, et al., *Les Houches guidebook to Monte Carlo generators for hadron collider physics* arXiv, hep-ph/0403045[hep-ph, ], (2004), 411–459.
- [64] G. 't Hooft, *Dimensional regularization and the renormalization group*, Nucl.Phys. **B61** (1973), 455–468.
- [65] S. Weinberg, *New approach to the renormalization group*, Phys.Rev. **D8** (1973), 3497–3509.

- [66] J. C. Collins, *Renormalization. An Introduction to Renormalization, the Renormalization Group, and the Operator Product Expansion*, (1984).
- [67] V. Sudakov, *Vertex parts at very high-energies in quantum electrodynamics*, Sov.Phys.JETP **3** (1956), 65–71.
- [68] T. Sjostrand, *A Model for Initial State Parton Showers*, Phys.Lett. **B157** (1985), 321.
- [69] G. Marchesini and B. Webber, *Monte Carlo Simulation of General Hard Processes with Coherent QCD Radiation*, Nucl.Phys. **B310** (1988), 461.
- [70] J. C. Collins, *Sudakov form-factors* arXiv, hep-ph/0312336[hep-ph, ], Adv.Ser.Direct.High Energy Phys. **5** (1989), 573–614.
- [71] G. Gustafson and U. Pettersson, *Dipole Formulation of QCD Cascades*, Nucl.Phys. **B306** (1988), 746.
- [72] B. Andersson, G. Gustafson, G. Ingelman, and T. Sjostrand, *Parton Fragmentation and String Dynamics*, Phys.Rept. **97** (1983), 31–145.
- [73] B. Webber, *A QCD Model for Jet Fragmentation Including Soft Gluon Interference*, Nucl.Phys. **B238** (1984), 492.
- [74] D. Lange, *The EvtGen particle decay simulation package*, Nucl.Instrum.Meth. **A462** (2001), 152–155.
- [75] P. Golonka, B. Kersevan, T. Pierzchala, E. Richter-Was, Z. Was, et al., *The Tauola photos F environment for the TAUOLA and PHOTOS packages: Release. 2.* arXiv, hep-ph/0312240[hep-ph, ], Comput.Phys.Comm. **174** (2006), 818–835.
- [76] G. F. Sterman and S. Weinberg, *Jets from Quantum Chromodynamics*, Phys.Rev.Lett. **39** (1977), 1436.
- [77] G. Arnison et al. (UA1 Collaboration), *Hadronic Jet Production at the CERN Proton - anti-Proton Collider*, Phys.Lett. **B132** (1983), 214.
- [78] G. C. Blazey, J. R. Dittmann, S. D. Ellis, V. D. Elvira, K. Frame, et al., *Run II jet physics* arXiv, hep-ex/0005012[hep-ex, ], (2000), 47–77.

- [79] M. Cacciari, G. P. Salam, and G. Soyez, *The Catchment Area of Jets* arXiv, 0802.1188[hep-ph, ], JHEP **0804** (2008), 005.
- [80] M. H. Seymour and C. Tevlin, *A Comparison of two different jet algorithms for the top mass reconstruction at the LHC* arXiv, hep-ph/0609100[hep-ph, ], JHEP **0611** (2006), 052.
- [81] G. P. Salam and G. Soyez, *A Practical Seedless Infrared-Safe Cone jet algorithm* arXiv, 0704.0292[hep-ph, ], JHEP **0705** (2007), 086.
- [82] S. Moretti, L. Lonnblad, and T. Sjostrand, *New and old jet clustering algorithms for electron - positron events* arXiv, hep-ph/9804296[hep-ph, ], JHEP **9808** (1998), 001.
- [83] W. Bartel et al. (JADE Collaboration), *Experimental Studies on Multi-Jet Production in  $e^+ e^-$  Annihilation at PETRA Energies*, Z.Phys. **C33** (1986), 23.
- [84] S. Bethke et al. (JADE Collaboration), *Experimental Investigation of the Energy Dependence of the Strong Coupling Strength*, Phys.Lett. **B213** (1988), 235.
- [85] M. Cacciari, G. P. Salam, and G. Soyez, *The Anti- $k(t)$  jet clustering algorithm* arXiv, 0802.1189[hep-ph, ], JHEP **0804** (2008), 063.
- [86] T. Sjostrand, S. Mrenna, and P. Z. Skands, *PYTHIA 6.4 Physics and Manual* arXiv, hep-ph/0603175[hep-ph, ], JHEP **0605** (2006), 026.
- [87] G. Corcella, I. Knowles, G. Marchesini, S. Moretti, K. Odagiri, et al., *HERWIG 6: An Event generator for hadron emission reactions with interfering gluons (including supersymmetric processes)* arXiv, hep-ph/0011363[hep-ph, ], JHEP **0101** (2001), 010.
- [88] T. Gleisberg, S. Hoeche, F. Krauss, M. Schonherr, S. Schumann, et al., *Event generation with SHERPA 1.1* arXiv, 0811.4622[hep-ph, ], JHEP **0902** (2009), 007.
- [89] J. Butterworth, J. R. Forshaw, and M. Seymour, *Multiparton interactions in photoproduction at HERA* arXiv, hep-ph/9601371[hep-ph, ], Z.Phys. **C72** (1996), 637–646.
- [90] *First tuning of HERWIG/JIMMY to ATLAS data*, (2010).

- [91] *Further ATLAS tunes of PYTHIA6 and Pythia 8*, (2011).
- [92] P. Z. Skands, *Tuning Monte Carlo Generators: The Perugia Tunes* arXiv, 1005.3457[hep-ph, ], Phys.Rev. **D82** (2010), 074018.
- [93] B. P. Kersevan and E. Richter-Was, *The Monte Carlo event generator AcerMC version 2.0 with interfaces to PYTHIA 6.2 and HERWIG 6.5* arXiv, hep-ph/0405247[hep-ph, ], (2004).
- [94] J. C. Collins, *Subtraction method for NLO corrections in Monte Carlo event generators for leptoproduction* arXiv, hep-ph/0001040[hep-ph, ], JHEP **0005** (2000), 004.
- [95] S. Frixione and B. R. Webber, *Matching NLO QCD computations and parton shower simulations* arXiv, hep-ph/0204244[hep-ph, ], JHEP **0206** (2002), 029.
- [96] S. Frixione, F. Stoeckli, P. Torrielli, B. R. Webber, and C. D. White, *The MCanLO 4.0 Event Generator* arXiv, 1010.0819[hep-ph, ], (2010).
- [97] S. Alioli, P. Nason, C. Oleari, and E. Re, *A general framework for implementing NLO calculations in shower Monte Carlo programs: the POWHEG BOX* arXiv, 1002.2581[hep-ph, ], JHEP **1006** (2010), 043.
- [98] S. Catani, F. Krauss, R. Kuhn, and B. Webber, *QCD matrix elements + parton showers* arXiv, hep-ph/0109231[hep-ph, ], JHEP **0111** (2001), 063.
- [99] F. Krauss, *Matrix elements and parton showers in hadronic interactions* arXiv, hep-ph/0205283[hep-ph, ], JHEP **0208** (2002), 015.
- [100] S. Hoeche, F. Krauss, N. Lavesson, L. Lonnblad, M. Mangano, et al., *Matching parton showers and matrix elements* arXiv, hep-ph/0602031[hep-ph, ], (2006).
- [101] M. L. Mangano, M. Moretti, F. Piccinini, R. Pittau, and A. D. Polosa, *ALPGEN, a generator for hard multiparton processes in hadronic collisions* arXiv, hep-ph/0206293[hep-ph, ], JHEP **0307** (2003), 001.
- [102] M. M., *The so-called MLM prescription for ME/PS matching*, (October, 4, 2002).

- [103] B. Cooper, J. Katzy, M. Mangano, A. Messina, L. Mijovic, et al., *Importance of a consistent choice of  $\alpha(s)$  in the matching of AlpGen and Pythia* arXiv, 1109.5295[hep-ph, ], Eur.Phys.J. **C72** (2012), 2078.
- [104] S. Chatrchyan et al. (CMS Collaboration), *The CMS experiment at the CERN LHC*, JINST **3** (2008), S08004.
- [105] J. Alves, A. Augusto et al. (LHCb Collaboration), *The LHCb Detector at the LHC*, JINST **3** (2008), S08005.
- [106] K. Aamodt et al. (ALICE Collaboration), *The ALICE experiment at the CERN LHC*, JINST **3** (2008), S08002.
- [107] G. Anelli et al. (TOTEM Collaboration), *The TOTEM experiment at the CERN Large Hadron Collider*, JINST **3** (2008), S08007.
- [108] O. Adriani et al. (LHCf Collaboration), *The LHCf detector at the CERN Large Hadron Collider*, JINST **3** (2008), S08006.
- [109] e. Evans, Lyndon and e. Bryant, Philip, *LHC Machine*, JINST **3** (2008), S08001.
- [110] G. Jackson and G. W. Foster, *Storage Ring for Enhanced Antiproton Production at Fermilab*, (1995).
- [111] G. Aad et al. (ATLAS), *The ATLAS Experiment at the CERN Large Hadron Collider*, JINST **3** (2008), S08003.
- [112] G. Aad et al. (The ATLAS), *Expected Performance of the ATLAS Experiment - Detector, Trigger and Physics* arXiv, 0901.0512[hep-ex, ], (2009).
- [113] *Performance of the ATLAS Inner Detector Track and Vertex Reconstruction in the High Pile-Up LHC Environment*, Tech. Report ATLAS-CONF-2012-042, CERN, Geneva, Mar 2012.
- [114] W. E. Cleland and E. G. Stern, *Signal Processing Considerations for Liquid Ionization Calorimeters in a High Rate Environment*, Nucl. Instrum. Methods Phys. Res., A **338** (1994), 467–497.

- [115] G. Aad et al. (ATLAS Collaboration), *Luminosity Determination in pp Collisions at  $\sqrt{s} = 7$  TeV Using the ATLAS Detector at the LHC* arXiv, 1101.2185[hep-ex, ], Eur.Phys.J. **C71** (2011), 1630.
- [116] S. van der Meer, *Calibration of the effective beam height in the ISR*, Tech. Report CERN-ISR-PO-68-31. ISR-PO-68-31, CERN, Geneva, 1968.
- [117] V. Cindro, D. Dobos, I. Dolenc, H. Fraiss-Kolbl, H. Fraiss-Koelbl, et al., *The ATLAS beam conditions monitor*, JINST **3** (2008), P02004.
- [118] P. Jenni, M. Nordberg, M. Nessi, and K. Jon-And, *ATLAS Forward Detectors for Measurement of Elastic Scattering and Luminosity*, Technical Design Report, CERN, Geneva, 2008.
- [119] G. Aad et al. (Atlas Collaboration), *Performance of the ATLAS Trigger System in 2010* arXiv, 1110.1530[hep-ex, ], Eur.Phys.J. **C72** (2012), 1849.
- [120] C. Eck, J. Knobloch, L. Robertson, I. Bird, K. Bos, N. Brook, D. Dillmann, I. Fisk, D. Foster, B. Gibbard, C. Grandi, F. Grey, J. Harvey, A. Heiss, F. Hemmer, S. Jarp, R. Jones, D. Kelsey, M. Lamanna, H. Marten, P. Mato-Vila, F. Ould-Saada, B. Panzer-Steindel, L. Perini, Y. Schutz, U. Schwickerath, J. Shiers, and T. Wenaus, *LHC computing Grid: Technical Design Report. Version 1.06 (20 Jun 2005)*, Technical Design Report LCG, CERN, Geneva, 2005.
- [121] *Performance of the Electron and Photon Trigger in p-p Collisions at  $\sqrt{s} = 7$  TeV*, Tech. Report ATLAS-CONF-2011-114, CERN, Geneva, Aug 2011.
- [122] T. Matsushita, *Performance of the ATLAS muon trigger in 2011*, Tech. Report ATL-DAQ-PROC-2012-008, CERN, Geneva, Jun 2012.
- [123] C. Cuenca Almenar, A. Corso-Radu, H. Hadavand, Y. Ilchenko, S. Kolos, et al., *ATLAS online data quality monitoring*, Nucl.Phys.Proc.Suppl. **215** (2011), 304–306.
- [124] J. Adelman, M. Baak, N. Boelaert, M. D’Onofrio, J. Frost, et al., *ATLAS offline data quality monitoring*, J.Phys.Conf.Ser. **219** (2010), 042018.

- [125] G. Aad et al. (ATLAS Collaboration), *The ATLAS Simulation Infrastructure* arXiv, 1005.4568[physics.ins-det, ], Eur.Phys.J. **C70** (2010), 823–874.
- [126] S. Agostinelli et al. (GEANT4), *GEANT4: A Simulation toolkit*, Nucl.Instrum.Meth. **A506** (2003), 250–303.
- [127] E. Abat, J. Abdallah, T. Addy, P. Adragna, M. Aharrouche, et al., *Response and shower topology of 2 to 180 GeV pions measured with the ATLAS barrel calorimeter at the CERN test-beam and comparison to Monte Carlo simulations*, (2010).
- [128] G. Aad et al. (ATLAS Collaboration), *Commissioning of the ATLAS Muon Spectrometer with Cosmic Rays* arXiv, 1006.4384[physics.ins-det, ], Eur.Phys.J. **C70** (2010), 875–916.
- [129] D. Adams, S. Asai, D. Cavalli, M. Dhrssen, K. Edmonds, S. Elles, M. Fehling, U. Felzmann, L. Gladilin, L. Helary, M. Hohlfeld, S. Horvat, K. Jakobs, M. Kaneda, G. Kirsch, S. Kuehn, J. F. Marchand, C. Pizio, X. Portell, D. Rebutzi, E. Schmidt, A. Shibata, I. Vivarelli, S. Winkelmann, and S. Yamamoto, *The ATLFAST-II performance in release 14 -particle signatures and selected benchmark processes-*, Tech. Report ATL-PHYS-INT-2009-110, CERN, Geneva, Dec 2009.
- [130] G. Aad et al. (ATLAS Collaboration), *Charged-particle multiplicities in pp interactions measured with the ATLAS detector at the LHC* arXiv, 1012.5104[hep-ex, ], New J.Phys. **13** (2011), 053033.
- [131] G. Aad et al. (ATLAS Collaboration), *Electron performance measurements with the ATLAS detector using the 2010 LHC proton-proton collision data* arXiv, 1110.3174[hep-ex, ], Eur.Phys.J. **C72** (2012), 1909.
- [132] *Expected electron performance in the ATLAS experiment*, Tech. Report ATL-PHYS-PUB-2011-006, CERN, Geneva, Apr 2011.
- [133] T. Lagouri, D. Adams, K. Assamagan, M. Biglietti, G. Carlino, et al., *A Muon Identification and Combined Reconstruction Procedure for the ATLAS Detector at the LHC at CERN*, IEEE Trans.Nucl.Sci. **51** (2004), 3030–3033.

- [134] *Muon reconstruction efficiency in reprocessed 2010 LHC proton-proton collision data recorded with the ATLAS detector*, Tech. Report ATLAS-CONF-2011-063, CERN, Geneva, Apr 2011.
- [135] *Muon Momentum Resolution in First Pass Reconstruction of pp Collision Data Recorded by ATLAS in 2010*, Tech. Report ATLAS-CONF-2011-046, CERN, Geneva, Mar 2011.
- [136] W. Lampl, S. Laplace, D. Lelas, P. Loch, H. Ma, S. Menke, S. Rajagopalan, D. Rousseau, S. Snyder, and G. Unal, *Calorimeter Clustering Algorithms: Description and Performance*, Tech. Report ATL-LARG-PUB-2008-002. ATL-COM-LARG-2008-003, CERN, Geneva, Apr 2008.
- [137] G. Aad et al. (ATLAS Collaboration), *Jet energy measurement with the ATLAS detector in proton-proton collisions at  $\sqrt{s} = 7$  TeV* arXiv, 1112.6426[hep-ex, ], (2011).
- [138] *Pile-up corrections for jets from proton-proton collisions at  $\sqrt{s} = 7$  TeV in ATLAS in 2011*, Tech. Report ATLAS-CONF-2012-064, CERN, Geneva, Jul 2012.
- [139] *Jet energy scale and its systematic uncertainty in proton-proton collisions at  $\sqrt{s}=7$  TeV in ATLAS 2010 data*, Tech. Report ATLAS-CONF-2011-032, CERN, Geneva, Mar 2011.
- [140] *Jet energy scale and its systematic uncertainty in proton-proton collisions at  $\sqrt{s}=7$  TeV with ATLAS 2011 data*, Tech. Report ATLAS-CONF-2013-004, CERN, Geneva, Jan 2013.
- [141] *Jet energy resolution and selection efficiency relative to track jets from in-situ techniques with the ATLAS Detector Using Proton-Proton Collisions at a Center of Mass Energy  $\sqrt{s} = 7$  TeV*, Tech. Report ATLAS-CONF-2010-054, CERN, Geneva, Jul 2010.
- [142] *Performance of Missing Transverse Momentum Reconstruction in ATLAS with 2011 Proton-Proton Collisions at  $\sqrt{s} = 7$  TeV*, Tech. Report ATLAS-CONF-2012-101, CERN, Geneva, Jul 2012.

- [143] The ATLAS Collaboration, *Measurement of the top quark pair production cross section in pp collisions at  $\sqrt{s} = 7$  TeV in dilepton final states with ATLAS*, (2011), ATLAS-CONF-2011-100.
- [144] G. Cowan, *A Survey Of Unfolding Methods For Particle Physics*.
- [145] G. Choudalakis (ATLAS Collaboration), *Unfolding in ATLAS* arXiv, 1104.2962[hep-ex, ], (2011).
- [146] G. D'Agostini, *A Multidimensional unfolding method based on Bayes' theorem*, Nucl. Instrum. Meth. **A362** (1995), 487–498.
- [147] V. Blobel, *An Unfolding method for high-energy physics experiments* arXiv, hep-ex/0208022[hep-ex, ], (2002), 258–267.
- [148] A. Hocker and V. Kartvelishvili, *SVD approach to data unfolding* arXiv, hep-ph/9509307[hep-ph, ], Nucl.Instrum.Meth. **A372** (1996), 469–481.
- [149] G. Aad et al. (ATLAS Collaboration), *Measurement of  $t\bar{t}$  production with a veto on additional central jet activity in pp collisions at  $\sqrt{s} = 7$  TeV using the ATLAS detector* arXiv, 1203.5015[hep-ex, ], Eur. Phys. J. **C72** (2012), 2043.
- [150] *Measurement of the jet multiplicity in top anti-top final states produced in 7 TeV proton-proton collisions with the ATLAS detector*, Tech. Report ATLAS-CONF-2012-155, CERN, Geneva, Nov 2012.
- [151] R. B. Davies, *Hypothesis testing when a nuisance parameter is present only under the alternative*, Biometrika **74** (1987), 33–43.
- [152] L. Lyons, *Open statistical issues in Particle Physics*, Ann.Appl.Stat. **2** (2008), 887–915.